

DEVELOPMENT AND CHARACTERISATION OF STEREOLITHOGRAPHIC  
3D PRINTED SOLID ORAL DOSAGE FORMS

**CARLO CURTI**

Doctor of Philosophy

ASTON UNIVERSITY

December 2021

©Carlo Curti, 2021

Carlo Curti asserts his moral right to be identified as the author of this thesis.

This copy of the thesis has been supplied on condition that anyone who consults it is understood to recognise that its copyright belongs to its author and that no quotation from the thesis and no information derived from it may be published without appropriate permission or acknowledgement.

DEVELOPMENT AND CHARACTERISATION OF STEREOLITHOGRAPHIC  
3D PRINTED SOLID ORAL DOSAGE FORMS

CARLO CURTI

Doctor of Philosophy

December 2021

Thesis Summary

The recent years have witnessed the rise of three-dimensional printing (3DP) technologies in several fields, spanning from healthcare to automotive and construction. In particular, 3DP has aroused much interest in pharmaceuticals, mainly for its potential to deliver personalised drug products on-demand, thus revolutionising the way medicines are designed, manufactured, and dispensed.

Among the several 3DP technologies currently available, stereolithography (SLA) is particularly attractive because of key advantages such as offering an unrivalled printing resolution and compatibility with thermolabile drugs. On the other hand, since conventional SLA 3D printers are designed to operate with large volumes of a single material, significant throughput limitations remain. This, coupled with the limited choice of biocompatible polymers and photoinitiators available, hold back the pharmaceutical development of such technology. Furthermore, limited data on SLA 3D printed tablets physical properties are available. Therefore, this research project aimed to address the abovementioned problems using a step-by-step approach.

First, a novel SLA apparatus was developed to enhance throughput and improve formulation development cost-effectiveness, thus enabling to use up to 12 different materials simultaneously and reducing sample amount by 20 times. As a result, formulation development cost was reduced by 95%. Then, such high-throughput SLA apparatus was used to conduct a systematic printability screening on 156 novel photopolymer formulations, to identify candidates with optimal printability for the subsequent drug loading studies. Polyethylene glycol diacrylate 700 and diphenyl-(2,4,6-trimethylbenzoyl)-phosphine oxide were identified as lead photopolymer and photoinitiator, respectively, while propylene glycol was found to be a suitable liquid filler to be incorporated in the photopolymer resin formulations. Lastly, 43 drug-loaded formulations containing theophylline, warfarin, or warfarin sodium were 3D printed into solid oral dosage forms and thoroughly characterised. Dosage forms' physical properties, namely hardness and friability, were found to be compliant with current Pharmacopoeia standards. Furthermore, potassium bicarbonate was incorporated, for the first time, in the photopolymerisable resin to tune drug release via effervescence in the acidic simulated gastric medium.

In conclusion, the findings of this research indicate that SLA 3D printing can be successfully used to manufacture quality solid oral dosage forms loaded with clinically relevant drug dosages, with the potential to deliver personalised medicine at the point of care.

Key Words:

Personalised Medicine; Printability; Biocompatible Photopolymers; Solid Oral Dosage Forms; Warfarin.

*To my parents Titti and Paolo, and to my sister Valentina,  
whose unconditional love allowed me to complete this long journey.*

*To my grandfather and pharmacist Carlo Curti,  
who would be amazed to see a 3D printer making medicines.*

## - Acknowledgments -

---

First and foremost, I would like to thank my academic supervisors, Dr Craig Russell and Dr Daniel Kirby, for their guidance and support throughout my PhD.

Craig, thank you in particular for the enormous amount of time and energy you have invested in our project and into my professional and personal development.

I would like to thank Aston University for funding my studies and all aspects of this project. Thank you to all members of staff in the School of Pharmacy, and in particular thank you to Daniel Burrell and Rachel Heath for providing the amazing technical support necessary for my research work and for cheering me up when I needed it.

Thank you to all colleagues in research lab MB328 for sharing moments of joy and gloom, for teaching me, and for allowing me to get to know new amazing cultures.

Thank you to all the wonderful people I met in Birmingham. Shital, Fede, Nic, Jimmy, May, Lorenzo, Alfredo, Claudia, Marco, Ire, Ila, Marti, Spencer, you all have enriched my life and I feel blessed to have met you.

Thank you to all my old friends for creating a fantastic support network around me. Diego, Janto, Luca, Federico, Fefo, Anto, Willi, Ale, Mariano, Marcello, Antonio, Valeria, Tizi, Marco, Connie, Benny, to name a few, I am proud to stand by your side.

Above all, thank you to all my family for their unconditional support and for inspiring me to become a scientist. In particular, thank you to aunt Mary and to uncle Bob for mentoring me since I was a kid.

Thank you, Mum and Dad, for your patience and understanding, your teachings, and your love. Thank you, Sister, for being my beacon of light and strength. I dedicate this Thesis to you all.

## - Impact Statement -

---

The restrictions in place to contain the spread of the Coronavirus pandemic in early 2020 led to the reconsideration of some aspects of this research project.

Closure of research laboratories coincided with the transition into the third year of my PhD, delaying the last phases of experimental work. As a result, some areas of the research project, including cell-culture work to investigate the biocompatibility of SLA 3D printed dosage forms, were no longer possible.

Additionally, attendance at prestigious international conferences, including the Controlled Release Society annual meeting and the GPEN meeting where my research had been accepted for presentation, did not go ahead as planned.

Nevertheless, the project continued shifting the focus to use time in the most efficient way possible. During the first period of lockdown, the opportunity was taken to produce an article for publication. Once research could reconvene, planned tablet characterisation was completed in order to complete data collection for this thesis.

I am enormously grateful to my Supervisors, who have guided and supported me during those difficult times.

## - Research Output -

---

### *Publications*

- ❖ Published review article: *Curti, C., Kirby, D.J. & Russell, C.A., 2020. Current formulation approaches in design and development of solid oral dosage forms through three-dimensional printing. Progress in Additive Manufacturing, 5, p. 111.*
- ❖ Published research article: *Curti, C., Kirby, D.J. & Russell, C.A., 2021. Stereolithography Apparatus Evolution: Enhancing Throughput and Efficiency of Pharmaceutical Formulation Development. Pharmaceutics, 13(5), p.616.*

### *Conference Contributions*

- ❖ UKICRS Belfast 2018 - Poster Presentation: *Development of a biocompatible SLA printable resin for controlled release 3D printed tablets.*
- ❖ Aston University 3MT - Three Minute Thesis competition: *Enhancing personalised medicine through Stereolithography 3D printing.*
- ❖ Aston University Research Day 2018 Podium presentation: *Development of a biocompatible SLA printable resin for controlled release 3D printed tablets - identification of suitable photopolymerisable excipients and photoinitiators.*
- ❖ APS Glasgow 2018 Poster Presentation: *Enhancing 3D printing in personalised medicine: development of a biocompatible resin for sla 3d printed tablets.*
- ❖ UKICRS Liverpool 2019 Poster Presentation & 1<sup>st</sup> Poster award: *Design, development and characterisation of stereolithographic 3D printed controlled release theophylline solid oral dosage forms.*
- ❖ UKICRS 2020 Virtual symposium oral presentation: *Systematic evaluation of photopolymer formulations for stereolithography 3D printing of solid oral dosage forms.*

## - List of Contents -

---

Title page.....	1
Thesis summary.....	2
Acknowledgments.....	4
Impact statement.....	5
Research output.....	6
List of contents.....	7
List of abbreviations.....	13
List of tables.....	16
List of figures.....	19
Chapter I – Introduction.....	32
1.1 Background.....	33
1.2 The oral route for drug administration.....	34
1.2.1 The gastrointestinal tract: anatomy, physiology, and drug absorption.....	34
1.2.2 Oral dosage forms.....	37
1.2.2.1 Solid oral pharmaceutical formulations.....	37
1.2.2.2 Liquid oral pharmaceutical formulations.....	40
1.3 Pharmaceutical additive manufacturing.....	41
1.3.1 Computer-aided design of solid oral dosage forms.....	43
1.3.2 Tuning dosage form properties through digital design.....	44
1.3.3 3D printing technologies in pharmaceuticals.....	46
1.3.3.1 Binder jetting 3D printing.....	46
1.3.3.2 Semi-solid extrusion 3D printing.....	50
1.3.3.3 Fused deposition modelling 3D printing.....	53
1.3.3.4 Selective laser sintering 3D printing.....	56
1.3.3.5 Stereolithography 3D printing.....	58

1.4 Rationale of drug selection for 3D printed individualised therapies.....	62
1.5 Research aim and objectives.....	63
Chapter II – Development of a novel stereolithography apparatus designed for pharmaceutical application.....	64
2.1 Introduction.....	65
2.2 Chapter aim and objectives.....	66
2.3 Materials and Methods.....	67
2.3.1 Materials.....	67
2.3.2 Methods.....	67
2.3.2.1 Computer-aided design.....	67
2.3.2.2 Stereolithography apparatus.....	67
2.3.2.3 Stereolithography 3D printing.....	68
2.3.2.4 Tablet uniformity testing.....	68
2.3.2.5 Material waste determination.....	69
2.3.2.6 Resin recovery efficiency evaluation.....	69
2.3.2.7 Statistical analysis.....	70
2.4 Results and Discussion.....	70
2.4.1 Computer-aided design of solid oral dosage forms.....	70
2.4.2 Printability assessment of solid oral dosage forms models.....	71
2.4.3 Proof of concept design and development.....	73
2.4.4 Design and fabrication of a low volume multi-compartment resin tank.....	76
2.4.5 Design and fabrication of a multi-spot build platform.....	77
2.4.6 Novel stereolithography apparatus validation.....	83
2.4.7 Assessment of printing supports related waste generation.....	88
2.4.8 Material recovery efficacy assessment.....	89
2.5 Conclusion.....	92

Chapter III – Printability screening of photopolymer resin formulations for stereolithography 3D printing of solid oral dosage forms.....	94
3.1 Introduction.....	95
3.2 Chapter aim and objectives.....	98
3.3 Materials and Methods.....	99
3.3.1 Materials.....	99
3.3.2 Methods.....	99
3.3.2.1 Photoinitiators selection.....	99
3.3.2.2 UV-visible spectrophotometry.....	99
3.3.2.3 Formulation of photopolymer resins.....	100
3.3.2.4 Stereolithography 3D printing.....	100
3.3.2.5 Printability evaluation.....	100
3.4 Results and Discussion.....	101
3.4.1 Photoinitiator selection.....	101
3.4.2 Design of photopolymer formulations for photoinitiator screening.....	104
3.4.3 Photoinitiator suitability for stereolithography 3D printing.....	105
3.4.4 Systematic printability screening of photopolymer formulations.....	108
3.4.4.1 Materials selection and formulation design.....	108
3.4.4.2 Stereolithography 3D printing and printability evaluation.....	115
3.4.4.3 Polyethylene glycol diacrylate influence on printability.....	125
3.4.4.4 Liquid fillers influence on printability.....	126
3.4.4.5 N-vinyl pyrrolidone influence on printability.....	130
3.4.4.6 Evaluation of photoinitiator concentration on printability.....	131

3.4.4.7 Evaluation of printing resolution on printability outcomes.....	132
3.5 Conclusion.....	133
Chapter IV – Stereolithography 3D printing of solid oral dosage forms.....	134
4.1 Introduction.....	135
4.2 Chapter aim and objectives.....	137
4.3 Materials and methods.....	138
4.3.1 Materials.....	138
4.3.2 Development and validation of a HPLC method for theophylline detection.....	138
4.3.3 Development and validation of a HPLC method for warfarin detection.....	139
4.3.4 Size reduction of solid fillers.....	139
4.3.5 Particle size distribution analysis of solid fillers.....	140
4.3.6 Preparation of drug loaded photopolymer resins.....	140
4.3.7 Determination of drug solubility in polyethylene glycol diacrylate.....	140
4.3.8 Determination of drug concentration in photopolymer resin.....	141
4.3.9 Computer-aided design of solid oral dosage forms.....	141
4.3.10 Stereolithography 3D printing of solid oral dosage forms.....	141
4.3.11 Determination of drug concentration in 3D printed dosage forms.....	142
4.3.12 Tablet weight uniformity.....	142
4.3.13 Tablet friability testing.....	142
4.3.14 Tablet hardness testing.....	142
4.3.15 Dissolution testing of 3D printed dosage forms.....	143
4.3.16 Swelling ratio and sol-fraction determination.....	144
4.3.17 Determination of liquid fillers leakage.....	145

4.3.18 Weight uniformity determination of manually split tablets.....	146
4.3.19 Optical microscopy imaging.....	146
4.3.20 Fourier-transform infrared spectroscopy.....	147
4.3.21 Differential scanning calorimetry.....	147
4.3.22 X-ray powder diffractometry.....	147
4.3.23 Scanning electron microscopy imaging.....	148
4.3.24 Raman spectroscopy imaging.....	148
4.4 Results and Discussion.....	149
4.4.1 Development and validation of a HPLC method for theophylline detection.....	149
4.4.2 Development and validation of a HPLC method for warfarin detection.....	158
4.4.3 Particle size reduction and distribution analysis of solid fillers.....	165
4.4.4 Preparation of drug loaded photopolymer resins.....	169
4.4.5 Determination of drug solubility in polyethylene glycol diacrylate.....	173
4.4.6 Determination of drug concentration in photopolymer resin.....	174
4.4.7 Computer-aided design of solid oral dosage forms.....	176
4.4.8 Stereolithography 3D printing of solid oral dosage forms.....	177
4.4.9 Determination of drug concentration in 3D printed dosage forms.....	195
4.4.10 Tablet weight uniformity.....	198
4.4.11 Mechanical characterisation of stereolithographic 3D printed dosage forms.....	200
4.4.12 Dissolution testing of 3D printed dosage forms.....	202
4.4.13 Swelling ratio and sol-fraction determination.....	218
4.4.14 Determination of liquid fillers leachates.....	220

4.4.15 Weight uniformity determination of manually split tablets.....	222
4.4.16 Fourier-transform infrared spectroscopy.....	224
4.4.17 Differential scanning calorimetry.....	228
4.4.18 X-ray powder diffractometry.....	229
4.4.19 Scanning electron microscopy imaging.....	230
4.4.20 Raman spectroscopy imaging.....	240
4.5 Conclusion.....	245
Chapter V – Closing commentary and future work.....	246
List of References.....	252

## - List of Abbreviations -

---

- $\%E_r$  – Percent Relative Error
- .stl – Stereolithographic File
- 3D – Three-dimensional
- 3DP – Three-dimensional Printing
- AM – Additive Manufacturing
- API – Active Pharmaceutical Ingredient
- ATR – Attenuated Total Reflectance
- BF – Best Formulation
- BJ – Binder Jetting
- BP – Build Platform
- BRm – BioRelevant Media
- CAD – Computer-aided Design
- $C_d$  – Curing Depth
- CNC – Computerised Numerical Control
- $C_w$  – Curing Width
- DC – Degree of Conversion
- DL – Detection Limit
- DLP – Digital Light Processing
- DSC – Differential Scanning Calorimetry
- FaSSGF – Fasted State Simulated Gastric Fluid
- FaSSIF – Fasted State Simulated Intestinal Fluid
- FDA – Food and Drug Administration
- FDM – Fused Deposition Modelling
- FTIR – Fourier-transform Infrared Spectroscopy
- GBP – Pound Sterling

GI – Gastrointestinal

GRAS – Generally Recognised As Safe

HME – Hot-melt Extrusion

HPLC – High Performance Liquid Chromatography

HPMC – Hydroxypropyl Methylcellulose

INR – International Normalised Ratio

MANOVA – Multivariate Analysis of Variance

MIT – Massachusetts Institute of Technology

$M_n$  – Molecular Number

NNLS – Non-negative Least Squares

NTI – Narrow Therapeutic Index

N-VP – N-vinyl Pyrrolidone

O/W – Oil-in-water

ODF – Orodispersible Film

ODS – Octadecyl-silica

ODT – Orally Disintegrating Tablet

PEG – Polyethylene Glycol

PEGDA – Polyethylene Glycol Diacrylate

PEGDME – Polyethylene Glycol Dimethyl Ether

PF – Printable Formulation

PG – Propylene Glycol

PI – Photoinitiator

PS – Printability Score

PVA – Polyvinyl Alcohol

PVP – Polyvinyl Pyrrolidone

QL – Quantification Limit

RPM – Revolutions Per Minute

RSD – Relative Standard Deviation

RT – Retention Time

SD – Standard Deviation

SEM – Scanning Electron Microscopy

SF – Sol-fraction

SLA – Stereolithography

SLS – Selective Laser Sintering

SR – Swelling Ratio

SSE – Semi-solid Extrusion

TEOA – Triethanolamine

TGDA – Triglycerol Dicarylate

TPO – Diphenyl-(2,4,6-trimethylbenzoyl)-phosphine Oxide

USP – United States Pharmacopoeia

UV – Ultraviolet

VMD – Volume Mean Diameter

VP – Vat Photopolymerisation

VWD – Variable Wavelength Detector

XRPD – X-ray Powder Diffraction

## - List of Tables -

---

Table 2.1. RSD of tablet weight, thickness, and diameter for tablets 3D printed using supports.....	87
Table 2.2. RSD of tablet weight, thickness, and diameter for tablets 3D printed without using supports.....	87
Table 2.3. Material waste associated to the use of printing supports, expressed as the % ratio between Wps and Wt.....	89
Table 3.1. List of PI systems selected for a preliminary printability screening. Triethanolamine was used as a synergist with both camphorquinone and riboflavin (Norrish type II PIs).....	102
Table 3.2. Measured $\lambda$ max values of the photoinitiators selected for efficacy screening.....	104
Table 3.3. % w/w composition of 12 photopolymer resin formulations designed to evaluate the efficacy of 6 photoinitiator systems (PIa - PIf).....	105
Table 3.4. Printability score (PS) assigned to photopolymer formulations used for photoinitiator screening.....	106
Table 3.5. % w/w composition of the 156 photopolymer formulations designed and prepared to carry out a systematic printability screening.....	111
Table 3.6. Printability score (PS) and classification group assigned to each photopolymer formulation screened. Group A indicates formulations with PS $\neq$ 5 (n = 96); group B reports formulations with a PS = 5 or PS = * at least at one printing resolution (n = 60); groups B1 (n = 35) and B2 (n = 5) list formulations with a PS = 5* at least at one or at each printing resolution used, respectively.....	121
Table 4.1. Linear regression analysis results of the calibration curve reported in figure 4.8.....	154
Table 4.2. Theophylline formulations spiked with TPO tested for recovery accuracy. All the formulations were prepared using mobile phase.....	154
Table 4.3. Theophylline HPLC method accuracy data. Accuracy was assessed using nine determinations over three concentration levels. Results are reported as percent recovery in accordance with the ICH Q2(R1) guidelines.....	156
Table 4.4. Theophylline HPLC method precision assessment. Results are expressed as analyte concentration found, standard deviation, relative standard deviation, and	

confidence interval. Concentrations values are expressed as $\mu\text{g/mL}$ .....	156
Table 4.5. Theophylline method validation procedure.....	158
Table 4.6. Linear regression analysis results of the calibration curve reported in figure 4.13.....	162
Table 4.7. Warfarin recovery from formulations containing 0.05% TPO w/w. Recovery results excluded interferences due to the presence of the photoinitiator.....	162
Table 4.8. Warfarin HPLC method accuracy data. Accuracy was assessed using nine determinations over three concentration levels. Results are reported as percent recovery in accordance with the ICH Q2(R1) guidelines.....	163
Table 4.9. Warfarin HPLC method precision assessment. Results are expressed as analyte concentration found, standard deviation, relative standard deviation, and confidence interval. Concentrations values are expressed as $\mu\text{g/mL}$ .....	164
Table 4.10. Warfarin method validation procedure.....	165
Table 4.11. Composition of drug-loaded photopolymer resins formulated for 3D printing.....	171
Table 4.12. Theophylline, warfarin, and warfarin sodium solubility in PEGDA 700 at 20°C. Results are expressed as solubility $\pm$ SD.....	173
Table 4.13. Drug recovery in photopolymer resin. Measurements were taken on freshly prepared samples (n = 3). Drug loading percentages are expressed as w/v %.....	175
Table 4.14. Individual cost of drug loaded photopolymer formulations. Results are expressed in GBP for 200 g (formulation amount required in the original Form 2 3D printer) and 10 g (formulation amount required in the modified SLA apparatus).....	178
Table 4.15. Printability evaluation of drug loaded photopolymer formulations.....	182
Table 4.16. Drug content uniformity evaluation of SLA 3D printed dosage forms.....	197
Table 4.17. Weight uniformity determination of SLA 3D printed dosage forms. Results are expressed as mean $\pm$ SD, and % RSD (n = 10).....	199
Table 4.18. % Weight loss and tablet breaking force values of SLA 3D printed drug loaded formulations. Tablet breaking force data are reported as mean $\pm$ SD (n = 3).....	201

Table 4.19. Swelling ratio and sol-fraction values of 3D printed dosage forms. Results are expressed as mean value $\pm$ SD (n=3).....	218
Table 4.20. Percent weight and volume variation, and estimated drug loss resulting from leaching liquid fillers. Measurements were taken immediately after 3D printing and after 1 week (n = 3). Dosage forms were kept at room condition, protected from light.....	221
Table 4.21. Weight accuracy of whole tablets (weight1), halves (weight2) and quarters (weight3). Results are expressed as mean weight $\pm$ standard deviation (SD) and relative standard deviation (RSD).....	223
Table 4.22. Percent weight loss of tablet halves and quarters. Results are expressed as mean % weight loss $\pm$ standard deviation (SD) and relative standard deviation (RSD).....	223
Table 4.23. Percent dose accuracy calculated for tablet halves and quarters. Results are expressed as mean % dose accuracy and relative standard deviation (RSD).....	224

## - List of Figures -

---

Figure 1.1. The gastrointestinal tract anatomy. Figure reproduced from Aulton (2017).....	35
Figure 1.2. Number of peer-reviewed research articles related to 3D printing of solid oral dosage forms published within the years 1996–2010 (grouped as pre-2010) to 2021 (data lastly updated in November 2021). Coloured bars represent different 3DP technologies: stereolithography (SLA), digital light processing (DLP), selective laser sintering (SLS), fused deposition modelling (FDM), semi-solid extrusion (SSE), binder jetting (BJ). 3DP technologies less represented have been classified as ‘other’ or ‘other UV’ in case of products containing photopolymers. Google scholar, Science direct and PubMed search engines were used to find relevant manuscripts. Key words for searching were ‘3D printing’, ‘solid oral dosage forms’, ‘tablets’ and ‘personalised medicine’. Figure readapted from Curti, Kirby and Russell, 2020.....	43
Figure 1.3. Schematic diagram representing examples of two different approaches to tune dosage forms’ properties through CAD: (A) multi-material 3DP and (B) engineering strategies (channelled tablets). Figure reproduced from (Curti, Kirby and Russell, 2020).....	45
Figure 1.4. Schematic diagram of binder jetting 3D printing working principle.....	46
Figure 1.5. Drug delivery devices designed and fabricated by Rowe (2000); (a) breakaway tablet, (b) pulsatory release tablet, (c) immediate-extended release device and (d) enteric dual pulse release tablet. Figure reproduced from (Curti, Kirby and Russell, 2020).....	47
Figure 1.6. Schematic representation of a material gradients tablet. A different porosity degree allows a faster erosion when the surface area decreases resulting in a constant drug release. Figure reproduced from (Curti, Kirby and Russell, 2020).....	48
Figure 1.7. Schematic representation of a fast disintegrating tablet. Partially printed regions consist in loose powder that allows faster disintegration and dissolution. Figure reproduced from (Curti, Kirby and Russell, 2020).....	48
Figure 1.8. Spritam®, the first 3D printed medicine to receive FDA approval. Picture reproduced from Basulto, 2015.....	49
Figure 1.9. Schematic diagram of semi-solid extrusion 3D printing working principle.....	50

Figure 1.10. (A) Chewable isoleucine 3D printed tablets in different sizes, colours, and flavours (Goyanes et al., 2019); (B) Paediatric-friendly chocolate-based 3D printed dosage forms (Karavasili et al., 2020); (C) 3D printed drug loaded gummies (Herrada-Manchón et al., 2020).....	52
Figure 1.11. Schematic diagram of fused deposition modelling 3D printing working principle.....	54
Figure 1.12. (A) FDM 3D printed tablets with different infill percentages (Fina et al., 2020); (B) Comparison between a tablet fabricated through direct compression (left) and a FDM 3D printed dosage form (right) (Shi et al., 2021).....	55
Figure 1.13. Schematic diagram of selective laser sintering 3D printing working principle.....	57
Figure 1.14. (A) SLS 3D printed cylindrical tablets; (B) SLS 3D printed gyroid lattice solid dosage forms. Figure reproduced from Fina, Goyanes, et al., 2018.....	58
Figure 1.15. Schematic diagram of stereolithography 3D printing working principle.....	59
Figure 1.16. (A) Paracetamol and (B) 4-ASA SLA 3D printed torus shaped tablets consisting of PEGDA 700 and PEG300. Figure reproduced from (Wang et al., 2016).....	60
Figure 1.17. (A) Cylindrical and (B) ring shape SLA 3D printed polypills. Figure reproduced from Robles Martinez et al., 2019.....	61
Figure 2.1. Schematic diagram of the method developed to evaluate photopolymer resin wastage due to adherence on the BP after the completion of a print. Image reproduced from (Curti, Kirby and Russell, 2021).....	70
Figure 2.2. (A) Front and (B) top views of the tablet models designed using TinkerCAD. Each square on the blue background corresponds to a surface area of 1 cm <sup>2</sup> .....	71
Figure 2.3. 3D printed dosage forms models based on the design in figure 2.2. Image readapted from (Curti, Kirby and Russell, 2020).....	71
Figure 2.4. (Top) CAD models and (bottom) 3D printed spherical solid oral dosage forms. Design on the left features a hollow cavity (white arrow indicates an air bubble floating on liquid resin), while the design on the right is a solid sphere.....	72
Figure 2.5. CAD model of the rectangular resin tank insert used as a proof of concept. Each square on the blue background corresponds to a surface area of 1 cm <sup>2</sup> .....	73
Figure 2.6. Front, bottom, and side views of the CAD model (left) and 3D printed prototype (right) of the modified BP.....	74

Figure 2.7. Successful 3DP test of a supported cylindrical tablet model fabricated using the modified BP.....	75
Figure 2.8. (A) Top and (B) front view of the multi-compartment resin tank insert CAD model. Each square on the blue background corresponds to a surface area of 1 cm <sup>2</sup> . Image reproduced from (Curti, Kirby and Russell, 2021).....	76
Figure 2.9. (A) 3D printed multi-compartment resin tank insert fixed onto the silicon layer of the original resin tank. (B) Sealing test of an individual compartment. Image readapted from (Curti, Kirby and Russell, 2021).....	77
Figure 2.10. (A) Top and (B) bottom views of the 3DP12BP (Mk I) CAD model. Each square on the blue background corresponds to a surface area of 1 cm <sup>2</sup> .....	77
Figure 2.11. (A) Top and (B) bottom views of the 3DP12BP (Mk I).....	78
Figure 2.12. (A) Cam handle of the Form 2 3D printer; (B) single-spot BP prototype and (C) 3DP12BP (Mk I) coupled with the original BP fixture.....	78
Figure 2.13. (A) Detailed view of the 3 holes designed at the bottom side of each build spot in the CAD model. (B) Front and (C) side views of a 3D printed build spot model featuring 3 aluminium rods (indicated by white arrows) used to hold the aluminium foil.....	79
Figure 2.14. (A) Top and (B) bottom views of the 3DP12BP (Mk II) CAD model. The new version features a component (coloured in blue) designed to fit tight into the locking mechanism securing the BP to the 3D printer. Each square on the blue background corresponds to a surface area of 1 cm <sup>2</sup> . Image reproduced from (Curti, Kirby and Russell, 2021).....	80
Figure 2.15. (A) Top and (B) bottom views of the 3DP12BP(Mk II). Image readapted from (Curti, Kirby and Russell, 2021).....	80
Figure 2.16. Bending of the 3DP 12BP Mk. I leading to misalignment of the BP in the SLA apparatus. Image reproduced from (Curti, Kirby and Russell, 2021).....	81
Figure 2.17. (A) Top and (B) bottom views of the Alu 12BP fabricated through CNC milling. The novel design includes hollow build-spots, thus reducing the weight of the platform. (C) Detail of the bead-blasted surface of the Alu 12BP. Such finish was selected to optimise the adhesion of objects during 3D printing and to facilitate their release after completion. Image reproduced from (Curti, Kirby and Russell, 2021) .....	81
Figure 2.18. Detailed view of the 3D printed fixture used to firmly hold the Alu 12BP to the SLA apparatus.....	82

Figure 2.19. Stereolithography apparatus evolution: comparison of (A) the original Form 2 SLA apparatus, (B) the modified apparatus equipped with the 3DP 12BP Mk. II and the 12-vats resin tank, and (C) the final version equipped with the Alu 12BP. Image readapted from (Curti, Kirby and Russell, 2021) .....	83
Figure 2.20. (A) CAD model of a cylindrical test tablet (12 mm × 4 mm). Test tablet were 3D printed either (B) directly on the BP or (C) using supports. (D) Printing support after manual removal of a 3D printed test tablet. Image reproduced from (Curti, Kirby and Russell, 2021) .....	83
Figure 2.21. Test tablets 3D printed on the Alu 12BP (A) using supports and (B) directly on the BP. Test tablets were 3D printed using Clear resin photopolymer.....	84
Figure 2.22. Tablet weight uniformity assessment. Yellow and blue bars represent data of tablets 3D printed with and without supports, respectively. Black dashed line indicates the theoretical weight of an individual tablet (0.493 g). Results are reported as mean (n = 30). Error bars indicate standard deviation of the measurements. Image readapted from (Curti, Kirby and Russell, 2021) .....	84
Figure 2.23. Tablet thickness uniformity assessment. Yellow and blue bars represent data of tablets 3D printed with and without supports, respectively. Black dashed line indicates the theoretical tablet thickness (4.00 mm). Results are reported as mean (n = 30). Error bars indicate standard deviation of the measurements. Image readapted from (Curti, Kirby and Russell, 2021) .....	85
Figure 2.24. Tablet diameter uniformity assessment. Yellow and blue bars represent data of tablets 3D printed with and without supports, respectively. Black dashed line indicates the theoretical tablet diameter (12.00 mm). Results are reported as mean (n = 30). Error bars indicate standard deviation of the measurements. Image readapted from (Curti, Kirby and Russell, 2021).....	86
Figure 2.25. Comparison of photopolymer resin waste generated by adherence onto the original BP and the Alu 12BP over a period of 1 hour. Straight and dashed curves indicate the economic loss using the original and the modified SLA apparatus, respectively. Error bars indicate standard deviation of the measurement (n = 3). Image readapted from (Curti, Kirby and Russell, 2021) .....	90
Figure 3.1. Example of a simplified free-radical photopolymerisation sequence. PI molecules, mixed with the reactive monomers, are exposed to a UV source of actinic photons (hv). PIs absorb photons and yield an excited PI species (PI*). Then, a fraction of PI* is converted into free radicals (PI•) able to react with a monomer molecule (chain initiation step). The addition of other monomers allows the chain to grow (chain	

propagation step), until the reaction between two radical species terminates the polymerisation process (chain termination step). Figure readapted from Jacobs, 1996....96

Figure 3.2. Points-based printability scale developed to evaluate printability outcomes based on visual observation of the 3D printed tablet samples.....101

Figure 3.3. Test tablets 3D printed with (A) 0.1% w/w and (B) 1% w/w PIa. (B) Tablet on the top right shows extended and uncontrolled polymerisation resulting in poor geometrical accuracy. (C) Failed print of a test tablet made using 0.1% w/w PIe/TEOA: inaccuracies are visible on the tablet sides, while the arrow indicates a partially printed edge. (D) Polymerised fragments originated from formulation PIsF12, containing 1% w/w PIf/TEOA.....107

Figure 3.4. Generation of radical fragments resulting from TPO photolysis.....108

Figure 3.5. Chain initiation reaction between radical fragments ( $R_1$  and  $R_2$ ) produced following PI photocleavage and C=C double bonds of PEGDA.....109

Figure 3.6. Partial representation of a chain propagation reaction involving the radical PEGDA molecule showed in figure 3.5, and 2 unreacted PEGDA molecules. The reaction can then propagate further.....109

Figure 3.7. Simplified representation of the addition of a radical linear chain of PVP to a PEGDA molecule, resulting in the formation of a growing network of crosslinked PVP.  $R_1$  represents the radical fragment originally provided by the PI.....110

Figure 3.8. Structures of (A) Polyethylene glycol, (B) propylene glycol, and (C) glycerol.....110

Figure 3.9. From top left to bottom right: formulations F1-F12, 3D printed setting the layer thickness to (A) 25  $\mu\text{m}$ , (B) 50  $\mu\text{m}$ , and (C) 100  $\mu\text{m}$ .....116

Figure 3.10. From top left to bottom right: formulations F13-F24, 3D printed setting the layer thickness to (A) 25  $\mu\text{m}$ , (B) 50  $\mu\text{m}$ , and (C) 100  $\mu\text{m}$ .....116

Figure 3.11. From top left to bottom right: formulations F25-F36, 3D printed setting the layer thickness to (A) 25  $\mu\text{m}$ , (B) 50  $\mu\text{m}$ , and (C) 100  $\mu\text{m}$ .....116

Figure 3.12. From top left to bottom right: formulations F37-F48, 3D printed setting the layer thickness to (A) 25  $\mu\text{m}$ , (B) 50  $\mu\text{m}$ , and (C) 100  $\mu\text{m}$ .....117

Figure 3.13. From top left to bottom right: formulations F49-F60, 3D printed setting the layer thickness to (A) 25  $\mu\text{m}$ , (B) 50  $\mu\text{m}$ , and (C) 100  $\mu\text{m}$ .....117

Figure 3.14. From top left to bottom right: formulations F61-F72, 3D printed setting the layer thickness to (A) 25  $\mu\text{m}$ , (B) 50  $\mu\text{m}$ , and (C) 100  $\mu\text{m}$ .....117

Figure 3.15. From top left to bottom right: formulations F73-F84, 3D printed setting the layer thickness to (A) 25 $\mu\text{m}$ , (B) 50 $\mu\text{m}$ , and (C) 100 $\mu\text{m}$ .....	118
Figure 3.16. From top left to bottom right: formulations F85-F96, 3D printed setting the layer thickness to (A) 25 $\mu\text{m}$ , (B) 50 $\mu\text{m}$ , and (C) 100 $\mu\text{m}$ .....	118
Figure 3.17. From top left to bottom right: formulations F97-F108, 3D printed setting the layer thickness to (A) 25 $\mu\text{m}$ , (B) 50 $\mu\text{m}$ , and (C) 100 $\mu\text{m}$ .....	118
Figure 3.18. From top left to bottom right: formulations F109-F120, 3D printed setting the layer thickness to (A) 25 $\mu\text{m}$ , (B) 50 $\mu\text{m}$ , and (C) 100 $\mu\text{m}$ .....	119
Figure 3.19. From top left to bottom right: formulations F121-F132, 3D printed setting the layer thickness to (A) 25 $\mu\text{m}$ , (B) 50 $\mu\text{m}$ , and (C) 100 $\mu\text{m}$ .....	119
Figure 3.20. From top left to bottom right: formulations F133-F144, 3D printed setting the layer thickness to (A) 25 $\mu\text{m}$ , (B) 50 $\mu\text{m}$ , and (C) 100 $\mu\text{m}$ .....	119
Figure 3.21. From top left to bottom right: formulations F145-F156, 3D printed setting the layer thickness to (A) 25 $\mu\text{m}$ , (B) 50 $\mu\text{m}$ , and (C) 100 $\mu\text{m}$ .....	120
Figure 3.22. Group classification of photopolymer formulations screened. Group A indicates formulations with $\text{PS} \neq 5$ ( $n = 96$ ); group B reports formulations with a $\text{PS} = 5$ or $\text{PS} = *$ at least at one printing resolution ( $n = 60$ ); groups B1 ( $n = 35$ ) and B2 ( $n = 5$ ) list formulations with a $\text{PS} = 5^*$ at least at one or at each printing resolution used, respectively.....	125
Figure 3.23. Number of formulations containing PEGDA 250, 575, and 700 classified as PFs and BFs.....	126
Figure 3.24. Number of formulations containing PEG300 classified as PFs and BFs.....	127
Figure 3.25. Number of formulations containing propylene glycol classified as PFs and BFs.....	128
Figure 3.26. Number of formulations containing glycerol classified as PFs and BFs.....	129
Figure 3.27. Number of formulations containing N-VP classified as PFs and BFs.....	130
Figure 3.28. Number of formulations containing 1%, 0.5%, 0.1% and 0.05% w/w TPO classified as PFs and BFs.....	131
Figure 3.29. Number of formulations classified among PFs and BFs for each 3D printing resolution used.....	132

Figure 4.1. (A) 6 mm Magness-Taylor probe mounted on a Brookfield CT3 texture analyser; (B) 3D printed tablet placed on the testing plate; (C-D) 3D printed shield designed to fit on the testing plate and protect the operator from any fragments.....	143
Figure 4.2. 3D printed dosage form placed on filter paper to investigate potential leakage of the liquid fillers from the crosslinked structure.....	145
Figure 4.3. HPLC chromatogram of 0.500 mg/mL theophylline in mobile phase showing a retention time of 9.208 minutes produced following the method described by Kanakal (2014) using a mobile phase consisting in a mixture of water, acetonitrile, and methanol (90:03:07).....	149
Figure 4.4. Calibration curve produced modifying the method reported by Kanakal running six calibration standards. The mobile phase used consisted in a mixture of water, acetonitrile, and methanol (80:06:14); flow rate was set at 1.5 mL/min. The calibration range was 15.625-500 µg/mL. Results were generated from triplicates (n=3). Error bars indicate standard deviation.....	150
Figure 4.5. Chromatogram of six calibrations standards produced modifying the method reported by Kanakal. The mobile phase used consisted in a mixture of water, acetonitrile, and methanol (80:06:14); flow rate was set at 1.5mL/min. Overlaid peaks highlight inconsistency in retention time.....	151
Figure 4.6. Chromatogram of six calibrations standards produced modifying the method reported by Kanakal (2014) and using a brand new Phenomenex reverse phase C18 HPLC column. The mobile phase used was a mixture of water, acetonitrile, and methanol (80:06:14); flow rate was set at 1.5mL/min. Consistency in retention time was observed.....	152
Figure 4.7. Chromatogram of six calibrations standards produced using a mobile phase of water, acetonitrile, and methanol (90:03:07) as described by Kanakal (2014), and a flow rate of 1.5mL/min. The chromatogram shows a consistent retention time of 5.665 min.....	152
Figure 4.8. Calibration curve for HPLC detection of theophylline produced using a mobile phase consisting in a mixture of water, acetonitrile, and methanol (90:03:07) and a flow rate set at 1.5 mL/min. Results were generated from triplicates (n=3). Error bars indicate standard deviation.....	153
Figure 4.9. Regression residuals from calibration curve in figure 4.8. Regression residuals were used to determinate the uncertainty of the regression line.....	154

Figure 4.10. Comparison of the chromatograms produced by running blank mobile phase (A) and 0.500 mg/mL theophylline in mobile phase (B).....	155
Figure 4.11. HPLC chromatogram of 500 µg/mL warfarin in mobile phase (20 mM phosphoric acid and methanol, 30:70) showing a retention time of 2.543 minutes.....	159
Figure 4.12. HPLC chromatogram of 500 µg/mL warfarin in mobile phase (20 mM phosphoric acid and methanol, 30:70) showing a retention time of 4.272 minutes. This was obtained by lowering column temperature to 20°C.....	160
Figure 4.13. Calibration curve from warfarin standards analysis. Results were generated from triplicates (n=3). Error bars indicate standard deviation.....	161
Figure 4.14. Regression residuals from calibration curve in figure 4.13. Regression residuals were used to determinate the uncertainty of the regression line.....	161
Figure 4.15. Comparison of the chromatograms produced by running blank mobile phase (A) and 0.500 mg/mL warfarin in mobile phase (B).....	163
Figure 4.16. Particle size distribution analysis of coarse NaCl (VMD = 291.72 µm) and ball milled NaCl (VMD = 140.12 µm). Error bars indicate standard deviation of the measurement (n=3).....	166
Figure 4.17. Particle size distribution analysis of coarse KHCO <sub>3</sub> (VMD = 436.91 µm) and ball milled KHCO <sub>3</sub> (VMD = 45.44 µm). Error bars indicate standard deviation of the measurement (n=3).....	166
Figure 4.18. Light microscope image of coarse sodium chloride. Particle size within the sample was observed to be generally homogeneous.....	167
Figure 4.19. Light microscope image of coarse potassium bicarbonate. Particle size within the sample was observed to be heterogeneous, with large particles (top image) found together with small fragments (bottom image).....	168
Figure 4.20. CAD model used for 3D printing theophylline dosage forms.....	176
Figure 4.21. CAD model used for 3D printing warfarin and warfarin sodium dosage forms.....	177
Figure 4.22. FormLabs PreForm view of theophylline 3D models used for 3D printing solid oral dosage forms. One tablet was fabricated for each formulation in a single printing cycle. Each printing cycle required 56 min to be completed. Layer thickness was set at 100 µm.....	179
Figure 4.23. Formlabs PreForm view of warfarin and warfarin sodium 3D models used for 3D printing solid oral dosage forms. One tablet was fabricated for each formulation in a	

single printing cycle. To be completed, each printing cycle required 1 hour when 12 different formulations were used simultaneously (left), and 55 min when 4 different formulations were used simultaneously (right). Layer thickness was set at 100 $\mu\text{m}$ .....	180
Figure 4.24. FormLabs PreForm view of 3D models used for formulations TF1-TF3 (left) and WF1-WF40 (right). To be completed, each printing cycle would have required 1.45 hours for formulations TF1-TF3, and 1.15 hours for formulations WF1-WF40.....	181
Figure 4.25. Top view of a dosage form 3D printed using TF1 resin (drug loading = 0.5% w/v). Tablet geometry resulted accurate to the 3D model designed.....	183
Figure 4.26. Top view of three dosage forms 3D printed using TF2 resin (drug loading = 5% w/v). Geometrical accuracy was lost due to high broadening effect.....	184
Figure 4.27. (A) Top view of three dosage forms 3D printed using TF3 resin (drug loading = 50% w/v) and (B) detail of theophylline crystals on the 3D printed surface. Geometrical accuracy was lost due to substantial broadening effect.....	184
Figure 4.28. Optical microscope image of formulation TF2. Theophylline crystals in a size range between 26.35 $\mu\text{m}$ and 123.93 $\mu\text{m}$ were observed. Magnification was set at $\times 10$ .....	185
Figure 4.29. Optical microscope image of formulation TF2. Red arrow indicates an aggregate of theophylline crystals. Magnification was set at $\times 10$ .....	185
Figure 4.30. Optical microscope image of formulation TF3. It is visible the high density of theophylline crystals within the liquid photopolymer matrix. Magnification was set at $\times 10$ .....	186
Figure 4.31. From top left to bottom right: SLA 3D printed dosage forms from formulations WF1, WF2, WF3, WF4, WF5, and WF6.....	188
Figure 4.32. From left to right: SLA 3D printed dosage forms from formulations WF7, WF8, and WF9.....	189
Figure 4.33. From top left to bottom right: SLA 3D printed dosage forms from formulations WF10, WF11, WF12, WF13, WF14, and WF15.....	189
Figure 4.34. Failed print of formulation WF22. The layers sliding on each other are distinctly visible.....	190
Figure 4.35. From top left to bottom right: SLA 3D printed dosage forms from formulations WF17, WF20, WF21, WF35, WF36, and WF37.....	191

Figure 4.36. From left to right: SLA 3D printed dosage forms from formulations WF18, WF39, and WF40.....	192
Figure 4.37. From top left to bottom right: SLA 3D printed dosage forms from formulations WF23, WF25, WF27, WF29, WF31, and WF33.....	193
Figure 4.38. Optical microscope images of SLA 3D printed WF27. Tablet side facing the resin tank (A) does not allow the observation of potassium bicarbonate particles, distinctly visible at the tablet side facing the build platform (B).....	194
Figure 4.39. Optical microscope images of SLA 3D printed WF33. Tablet side facing the resin tank (A) does not allow the observation of sodium bicarbonate particles, distinctly visible at the tablet side facing the build platform (B).....	194
Figure 4.40. From top left to bottom right: SLA 3D printed dosage forms from formulations WF24, WF26, WF28, WF30, WF32, and WF34. Figure 4.40. From top left to bottom right: SLA 3D printed dosage forms from formulations WF24, WF26, WF28, WF30, WF32, and WF34.....	195
Figure 4.41. Protocol followed to pulverise SLA 3D printed dosage forms using a mortar and pestle. The 3DP tablet (A) is sliced into smaller fragments (B). Then, one fragment is transferred to the mortar containing grinded inert solid material (C) and finely grounded to avoid escape of fragments (D).....	196
Figure 4.42. (A) USP apparatus II (paddle) and (B) apparatus I (basket) in operation during in-vitro dissolution testing.....	202
Figure 4.43. Theophylline release from SLA 3D printed dosage forms. Dissolution medium was simulated gastric fluid (pH 1.2) for the first hour followed by phosphate buffer (pH 6.0) for the subsequent 7 hours. Data points represent mean $\pm$ SD (n = 3).....	203
Figure 4.44. Warfarin and warfarin sodium release profiles in water from formulations WF1-WF6. Data points represent mean $\pm$ SD (n = 3).....	204
Figure 4.45. Warfarin and warfarin sodium release profiles in BioRelevant media from formulations WF1-WF6. Dissolution testing was carried out in FaSSGF (pH 1.6) for the first 3 hours and in FaSSIF (pH 6.5) for the subsequent 5 hours. Data points represent mean $\pm$ SD (n = 3).....	205
Figure 4.46. Warfarin sodium release profiles in water from formulations WF7-WF15. Data points represent mean $\pm$ SD (n = 3).....	206
Figure 4.47. Warfarin sodium release profiles in BioRelevant media from formulations WF7-WF15. Dissolution testing was carried in FaSSGF (pH 1.6) for the first 3 hours and	

in FaSSIF (pH 6.5) for the subsequent 5 hours. Data points represent mean $\pm$ SD (n = 3).....	206
Figure 4.48. Warfarin sodium release profiles in BioRelevant media from formulations WF35-WF37. Dissolution testing was carried in FaSSGF (pH 1.6) for the first 3 hours and in FaSSIF (pH 6.5) for the subsequent 5 hours. Data points represent mean $\pm$ SD (n=3).....	207
Figure 4.49. Warfarin sodium release profiles in BioRelevant media from formulations WF20-WF21. Dissolution testing was carried in FaSSGF (pH 1.6) for the first 3 hours and in FaSSIF (pH 6.5) for the subsequent 5 hours. Data points represent mean $\pm$ SD (n=3).....	208
Figure 4.50. Warfarin sodium release profiles in BioRelevant media from formulations WF17-WF18. Dissolution testing was carried in FaSSGF (pH 1.6) for the first 3 hours and in FaSSIF (pH 6.5) for the subsequent 5 hours. Data points represent mean $\pm$ SD (n=3).....	209
Figure 4.51. Warfarin sodium release profiles in BioRelevant media from formulations WF39-WF40. Dissolution testing was carried in FaSSGF (pH 1.6) for the first 3 hours and in FaSSIF (pH 6.5) for the subsequent 5 hours. Data points represent mean $\pm$ SD (n=3).....	210
Figure 4.52. Images of swollen SLA 3DP dosage forms taken immediately after dissolution testing in BioRelevant media. A: WF1, B: WF2, C: WF3, D: WF4, E: WF5, F: WF6, G:WF7, H: WF8, I: WF9, J: (from top left to bottom right) WF10-WF11-WF12-WF13-WF14-WF15, K: (from top left to bottom right) WF17-WF20-WF21-WF35-WF36-WF37, L: (from left to right) WF18-WF39-WF40.....	211
Figure 4.53. Images of SLA 3DP dosage forms fractured after drying at room condition for 24 hours. A: WF1, B: WF2, C: WF3, D: WF4, E: WF5, F: WF6, G:WF7, H: WF8, I: WF9, J: (from top left to bottom right) WF10-WF11-WF12-WF13-WF14-WF15, K: (from top left to bottom right) WF17-WF20-WF21-WF35-WF36-WF37, L: (from left to right) WF18-WF39-WF40.....	212
Figure 4.54. Warfarin sodium release profiles in BioRelevant media from formulations WF23-WF28. Dissolution testing was carried in FaSSGF (pH 1.6) for the first 3 hours and in FaSSIF (pH 6.5) for the subsequent 5 hours. Data points represent mean $\pm$ SD (n=3).....	213
Figure 4.55. Warfarin sodium release profiles in BioRelevant media from formulations WF29-WF34. Dissolution testing was carried in FaSSGF (pH 1.6) for the first 3 hours and	

in FaSSiF (pH 6.5) for the subsequent 5 hours. Data points represent mean $\pm$ SD (n=3).....	214
Figure 4.56. SLA 3D printed dosage forms produced from formulations WF23 (A), WF25 (B), WF27 (C), WF29 (D), WF31 (E), WF33 (F). Images were taken immediately after dissolution testing and show the fragments collected from the basket.....	215
Figure 4.57. SLA 3D printed dosage forms produced from formulations WF24 (A), WF26 (B), WF28 (C), WF30 (D), WF32 (E), WF34 (F). Images were taken immediately after dissolution testing and show the fragments collected from the basket.....	216
Figure 4.58. Optical microscope image of two fragments originating from a SLA 3D printed dosage form. Images were taken on the fragments dispersed in dissolution medium setting the magnification to $\times 10$ .....	217
Figure 4.59. 1 mg (top) and 5 mg (bottom) commercially available warfarin sodium manually split tablets.....	223
Figure 4.60. From top to bottom: FTIR spectra of uncured PEGDA 700, warfarin, warfarin sodium, 3D printed warfarin (WF3), 3D printed warfarin sodium (WF6). PEGDA chemical structure is reported in the top-right corner as a reference.....	225
Figure 4.61. From top to bottom: FTIR spectra of 3D printed WF9, WF12 and WF15.....	226
Figure 4.62. From top to bottom: FTIR spectra of 3D printed WF35, WF36 and WF37.....	226
Figure 4.63. DSC thermograms of warfarin sodium, warfarin, 3D printed 5.0% w/v warfarin sodium (WF6) and 3D printed 5.0% w/v warfarin (WF3).....	228
Figure 4.64. X-ray powder diffractograms of pure warfarin and warfarin sodium and 3D printed dosage forms. Signals were acquired over a $2\theta$ range of 5-70 degrees.....	230
Figure 4.65. SEM images of cross-sectional view of a dosage form 3D printed from WF3.....	231
Figure 4.66. SEM images of cross-sectional view of a dosage form 3D printed from WF6.....	232
Figure 4.67. SEM images of top view of a dosage form 3D printed from WF25 before (A-B) and after (C-D) dissolution testing.....	233
Figure 4.68. SEM images of cross-sectional view of a dosage form 3D printed from WF25 before (A-B) and after (C-D) dissolution testing.....	234

Figure 4.69. SEM images of top view of a dosage form 3D printed from WF28 before (A-B) and after (C-D) dissolution testing.....	235
Figure 4.70. SEM images of cross-sectional view of a dosage form 3D printed from WF28 before (A-B) and after (C-D) dissolution testing.....	236
Figure 4.71. SEM images of top view of a dosage form 3D printed from WF31 before (A-B) and after (C-D) dissolution testing.....	237
Figure 4.72. SEM images of cross-sectional view of a dosage form 3D printed from WF31 before (A-B) and after (C-D) dissolution testing.....	238
Figure 4.73. SEM images of top view of a dosage form 3D printed from WF34 before (A-B) and after (C-D) dissolution testing.....	239
Figure 4.74. SEM images of cross-sectional view of a dosage form 3D printed from WF34 before (A-B) and after (C-D) dissolution testing.....	240
Figure 4.75. Raman spectra of (A) pure warfarin sodium and (B) drug free PEGDA 700 SLA 3D printed tablet (red) compared to PEGDA spectrum from Renishaw database (blue).....	241
Figure 4.76. Raman map (top) and spectra (bottom) collected from the surface of a warfarin sodium loaded SLA 3D printed tablet before dissolution testing. Warfarin sodium and PEGDA 700 spectra are coloured in blue and red, respectively.....	242
Figure 4.77. Raman map (top) and spectra (bottom) collected from the core of a warfarin sodium loaded SLA 3D printed tablet before dissolution testing. Warfarin sodium and PEGDA 700 spectra are coloured in blue and red, respectively.....	242
Figure 4.78. Raman map (top) and spectra (bottom) collected from the surface of a warfarin sodium loaded SLA 3D printed tablet after dissolution testing. PEGDA 700 spectrum (red) was compared to PEGDA reference spectrum from Renishaw database (blue).....	244
Figure 4.79. Raman map (top) and spectra (bottom) collected from the core of a warfarin sodium loaded SLA 3D printed tablet before dissolution testing. Warfarin sodium and PEGDA 700 spectra are coloured in blue and red, respectively.....	244

# - Chapter I -

## INTRODUCTION

---

### **Publications arising from the work in this chapter:**

Curti, C., Kirby, D.J. & Russell, C.A., 2020. Current formulation approaches in design and development of solid oral dosage forms through three-dimensional printing. *Progress in Additive Manufacturing*, 5, p. 111.

## 1.1 Background

The 20<sup>th</sup> century was marked by revolutionary breakthroughs in the medical field, that allowed humanity to effectively fight diseases previously left untreated. The introduction of drugs capable of preventing or treating infectious, cardiovascular, and oncological diseases, to mention a few, has led to a significant increase in life expectancy, representing a remarkable triumph for scientific progress. Today, the advent of digital healthcare opens the doors to a new era in the history of medicine. Advanced pharmaceutical products and cutting-edge technologies are driving a paradigm shift in pharmacotherapy, moving from a one-size-fits-most approach to patient-centred personalised medicine. This concept is increasingly being embraced by Health Services, which acknowledge the link between personalised medicine and improved therapeutic outcomes (Graham, 2016). Clearly, every innovation requires the right technology, and the digital revolution offers a unique opportunity for the development of a novel, integrated model of healthcare, spanning from smart diagnosis to the manufacturing of tailored medicines. Within this broad context, three-dimensional printing (3DP) has aroused much interest due to its large flexibility, making it an effective tool to fabricate bespoke drug delivery devices (Goole and Amighi, 2016). As such, this research project aims to shed light on the pharmaceutical application of Stereolithography (SLA) 3D printing, with a focus on solid oral dosage forms. Such advantageous technology holds the potential to revolutionise the way medicines are designed and fabricated, and it is of particular importance to understand what challenges need to be addressed to allow its deployment for the preparation of personalised drug products in a clinical setting, and what opportunities can be seized to fulfil the most important of all tasks: improving people's lives.

## **1.2 The oral route for drug administration**

Effective pharmacotherapy requires that adequate concentrations of the administered drug(s) reach the target site. This is the main focus of drug delivery; the science offering a wide range of solutions, spanning from pharmaceutical formulation to manufacturing techniques and storage systems, to ensure efficacy and safety of medicines. To be effective, medicinal products must be designed specifically, and administered through appropriate routes.

For most drugs, the oral route can be often employed with success. It is a natural way to introduce medicines in the human body and is well-established in clinical practice due to its convenience; it is, in fact, pain-free and easy to use and therefore is well accepted by patients.

When a medicine is administered *per os* (from Latin ‘by mouth’), drug molecules are released and absorbed in the gastrointestinal (GI) tract. Such processes, crucial for good therapeutic efficacy, are in some cases prevented. For example, degradation in the acidic environment of the stomach, and first-pass effect are typical causes of reduced efficacy. This points out how important it is to design and develop dosage forms after careful consideration of the physicochemical properties of the active pharmaceutical ingredients (API).

The following subsections provide an overview of oral drug delivery, with a focus on dosage forms available for oral administration.

### ***1.2.1 The gastrointestinal tract: anatomy, physiology, and drug absorption***

Food, drinks, and any product that is ingested necessarily pass through the GI tract. This also applies to medicinal products which, taken orally, exploit the sophisticated physiology of the GI tract for the absorption of the APIs. In fact, unlike other routes of administration (e.g., the parenteral route), drugs taken orally must be absorbed in order to reach the

systemic circulation and be distributed to the body tissues to accomplish their therapeutic action.

The human GI tract consists of a muscular tube with an approximate length of 6-9 meters and a rough lumen increasing the surface area for absorption (Hounnou *et al.*, 2002; Aulton and Taylor, 2017; Hua, 2020). The GI tract originates in the mouth and terminates with the anal cavity and is made up of four main anatomical areas known as oesophagus, stomach, small intestine, and large intestine (figure 1.1).

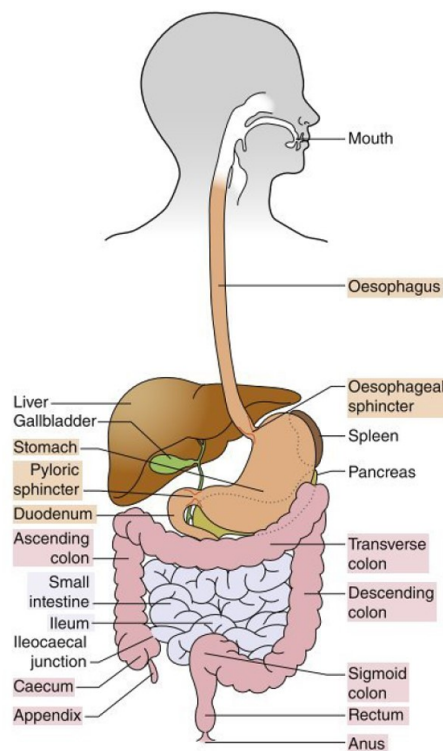


**Figure 1.1.** The gastrointestinal tract anatomy. Figure reproduced from Aulton (2017).

The oesophagus connects the mouth to the stomach via the cardiac orifice, and allows for rapid transit of dosage forms, usually within 20 seconds (Channer, K. S., & Virjee, J. P., 1985).

The stomach follows the oesophagus, thus acting as a receiver compartment of swallowed food and medicines. It has a capacity of approximately 1.5 L and contains varying volumes

of secretions. Such secretions include hydrochloric acid (keeping the pH between 1.0 and 3.5 in the fasted state), gastrin (stimulating the secretion of acid and pepsinogen), pepsin, and mucus (protecting the gastric mucosa from the erosive action of acids and pepsin) (Schubert, M. L., 2016). Gastric absorption of drugs is limited due to the reduced surface area available. A certain extent of delayed release action is accountable to the gastric emptying rate, which is highly variable depending on the fasted/fed state of the stomach and the type of dosage form administered. In general, gastric residence time spans between 5 minutes and 2 hours (Kumar and Philip, 2007).

Partially digested gastric content reaches the small intestine via the pyloric sphincter. The small intestine consists of three sections named duodenum, jejunum, and ileum, and is responsible for digestion and absorption. Indeed, it has a huge surface area (circa 200 m<sup>2</sup>) magnificently obtained thanks to structures like the folds of Kerckring, villi and microvilli, and is richly supplied by blood vessels (Brocchi, E., Corazza, G. R., Caletti, G., Treggiari, E. A., Barbara, L., & Gasbarrini, G., 1988). As a result, the small intestine is the best site available for absorption of both food nutrients and drug molecules. Compared to the stomach, the pH in the small intestine is kept between 6.0 and 7.5 by the secretion of bicarbonate (from Brunner's glands), mucus, enzymes, pancreatic secretions, and bile, while the typical transit time ranges between 3 and 4 hours (Krause, 2000).

The final portion of the GI tract is represented by the large intestine, also known as colon. The colon, characterized by a smaller surface area than the small intestine, is mainly responsible for the absorption of sodium and chlorine ions, and water, and for the storage and compaction of faeces (Sandle, G. I., 1998). The pH of the first portion of the colon is between 6.0 and 6.5 due to the presence of acid metabolites produced by the local microbiome and increases up to 7.0 - 7.5 in the distal tract. Transit time throughout the colon is typically between 12 and 36 hours, although it can be highly variable (Arhan, P., Devroede, G., Jehannin, B., Lanza, M., Faverdin, C., Dornic, C., ... & Pellerin, D. 1981).

### ***1.2.2 Oral dosage forms***

Oral dosage forms are mainly classified as solid and liquid formulations. In general, solid dosage forms share the advantage of offering high dosing accuracy, ease of transport and storage, and greater stability, while liquid formulations provide good dose flexibility and are easy to swallow (Mohammed and Russell, 2012; Lajoinie *et al.*, 2017).

#### ***1.2.2.1 Solid oral pharmaceutical formulations***

Principal solid oral dosage forms include powders, granulates, tablets and capsules, which will herein briefly described.

Powders are defined as blends of at least one API and one or more excipients, and they represent both a finite and an intermediate dosage form (Stranzinger *et al.*, 2021). Powders can be packaged in sachets or bottles for extemporaneous preparations such as solutions or suspensions (Mohammed and Russell, 2012).

Granulates, similarly to powders, are both a finite and an intermediate dosage form. They are produced via dry or wet granulation, and are mostly used in the manufacturing of tablets to avoid flow properties issues typical of powders (Prescott and Barnum, 2000).

Tablets refer instead to a wide range of solid oral dosage forms offering patients an easy form of self-medication. They are designed in different shapes and colours to be easily distinguished, which is particularly important for specific patient groups such as the elderly, carrying the burden of polypharmacy (Hajjar, Cafiero and Hanlon, 2007; Z. B. Shariff *et al.*, 2020). Tablets are mainly produced by compression of powders or granulates (Herting, M. G., & Kleinebudde, P., 2007) and can subsequently be subjected to further processes (e.g. coating). According to their processing and destination of use, tablets can be classified as following:

- Compressed tablets, produced by compression of granulates and designed to immediately release the API. Once swallowed, such tablets disaggregate in the stomach enabling the API to dissolve and be absorbed to pass through the blood stream.
- Direct compressed tablets, manufactured by simply compressing an homogeneous mixture of powders, thus representing a more convenient process with fewer steps besides the elimination of heat and moisture related issues (Jivraj, Martini and Thomson, 2000).
- Effervescent tablets, designed to be placed in water where they disintegrate quickly to produce a solution of the API. The effervescence is obtained using a mixture of organic acids and (bi)carbonates reacting in water. As they are not intended for swallowing, the size of effervescent tablets is typically larger than conventional tablets, therefore higher amounts of API can be loaded. Their main advantage relies in avoiding the disintegration and dissolution steps to happen in the human body so the API can be rapidly absorbed, resulting in a faster onset of action (Rygnestad, Zahlse and Samdal, 2000).
- Coated tablets, featuring several advantages including easiness of swallowing, masking of unpleasant odour and taste, protection of the API from degradation, and targeted drug release. Sugar coating was the first method to be introduced, aiming to provide tablets with an elegant appearance and to mask bitter taste (Ohmori *et al.*, 2004), while film-coating represented its evolution. With its excellent properties, such as limited size increase and good taste masking, film-coating is currently the 'gold standard' in coating of solid oral dosage forms. By varying the selection of polymers, film-coated tablets with different properties can be obtained. For example, methacrylic acid/methyl methacrylate copolymer is used to formulate enteric-coated tablets because it is only soluble in the alkaline environment of the intestinal lumen (Ozturk *et al.*, 1988). This allows to deliver acid-labile APIs, and to protect the gastric mucosa from drug induced irritation (Ozturk *et al.*, 1988).
- Orally disintegrating tablets (ODTs), specifically formulated to rapidly disintegrate when placed on the tongue. Naturally, this is a substantial advantage for patients

suffering from dysphagia, and ODTs popularity is increasing because they can be taken without water (Hirani, Rathod and Vadalía, 2009). ODTs also enable for a fast onset of action, which makes them particularly appealing to treat specific conditions (Guhmann *et al.*, 2015).

- Buccal tablets, designed to release their drug content in the mouth, and are generally used for local treatments (Khanna, Agarwal and Ahuja, 1996). They are normally placed between the lip and the gum, where they adhere by forming a gel allowing these dosage forms to remain in position releasing the drug for 1-2 hours (Aulton and Taylor, 2017).
- Sublingual tablets, placed under the tongue and are used to provide a rapid systemic drug effect without first-pass liver metabolism. Sublingual administration is generally limited to lipophilic molecules that can be rapidly absorbed without causing irritation of the oral mucosa (Reisfield and Wilson, 2007; Bilbault *et al.*, 2016).

Medicinal capsules are instead dosage forms consisting of a 'shell' containing a single dose of the API generally in the form of powder or granules (Podczeck and Jones, 2007). Capsules are mainly destined to oral use, and are classified in 'hard' (or two-piece) and 'soft' (or one-piece). Hard capsules are normally used to encapsulate powders or granulates, while soft capsules are filled with non-aqueous liquid where the API is solubilised or suspended (Podczeck and Jones, 2007).

Tablets and capsules can be engineered to deliver the API at desired rates, predefined time points, or in specific sites of the GI tract. This is based on the need to slow the release profile of certain APIs in specific diseases, or to prolong their effect. Delayed-release, gastro-resistant, and extended-release dosage forms represent the most important approaches to modified-release drug delivery, and allow significant advantages for patients, such as maintaining the drug in the therapeutics range, keeping drug levels overnight, reducing side effects, and improving patient adherence (Aulton and Taylor, 2017).

### 1.2.2.2 Liquid oral pharmaceutical formulations

Liquid formulations designed for oral administration generally contain water as a solvent, sweeteners, and flavourings as taste masking excipients. Liquid formulations are historically considered to be most appropriate for paediatric use, due to their ease to swallow and high dosing flexibility (Lajoinie *et al.*, 2017). Indeed, the main advantage of liquid oral formulations is the ability to provide dose flexibility by administering accurately measured volumes. Due to their minor stability compared to solid dosage forms, liquid formulations can be prepared extemporaneously (Jadhav, N. R. *et al.*, 2021). Main liquid oral formulations include solutions, suspensions, emulsions, syrups, and elixirs, and are herein described:

- Pharmaceutical solutions, homogeneous mixtures of two or more components, namely a solute and a solvent. Commonly, the solute is represented by the API and any solid excipients, while the solvent system is generally water based, although organic solvents such as alcohols and glycols can be used (Seedher and Bhatia, 2003).
- Suspensions, which are heterogeneous systems where the solid API does not dissolve in the liquid vehicle to any appreciable extent, and is therefore distributed throughout the vehicle (Patel, N. K. *et al.*, 1986). Suspension dosage forms are commonly employed to formulate hydrophobic drugs, to avoid the use of co-solvents, and to prevent degradation of drugs due to hydrolysis, oxidation or microbial activity (Nutan and Reddy, 2010). However, suspensions are unstable systems their formulation can be challenging (Patel, N. K. *et al.*, 1986).
- Oral emulsions, dispersions of at least two immiscible liquids, conventionally described as ‘oil’ and ‘water’. Oil-in-water emulsions (o/w) are most common in oral drug delivery, and enable the formulation of poorly water soluble APIs (Mohammed and Russell, 2012).
- Syrups, aqueous solutions containing high concentrations of sucrose, normally 66.7%. Such high concentration of sugar increases the osmotic pressure of the solution avoiding microbial growth (Alshammari *et al.*, 2021). Sugar free syrups are also

available, and are formulated using mannitol, sorbitol, xylitol, etc. Syrups are generally added with flavouring agents and they are particularly common among paediatric medicaments due to their good taste masking properties (Mohammed and Russell, 2012).

- Elixirs, which are clear, sweetened and flavoured hydroalcoholic solutions. They can contain significant amounts of ethanol used to promote solubilisation of the API, but alternatives such as propylene glycol or glycerol can be employed (Amorosa, 1986).

Other liquid oral formulations, nowadays less commonly used in clinical practice, are aromatic waters, spirits, and tinctures (Amorosa, 1986).

### **1.3 Pharmaceutical additive manufacturing**

The most popular way to administer drugs is through the oral route, with nearly 50% of medicines being taken *per os* (Alqahtani, M. S. *et al.*, 2021). In addition to excellent patient acceptability, the popularity of oral drug delivery is mainly due to the undemanding manufacture of oral dosage forms since they do not require sterilisation and can be produced economically in large amounts by automated systems. Tablet manufacturing, accounting for nearly 80% of all marketed formulations (Chen, Aburub and Sun, 2019), is based on automatic machines since the early 1800s (Augsburger and Hoag, 2008) and throughout the decades it has been enhanced by increasing the production rate up to 500,000 units per hour (Augsburger and Hoag, 2008), improving tablet uniformity, and introducing multi-layer tableting (Conte *et al.*, 1993). Nevertheless, tablet production is still based on tableting machines whose design has not essentially changed since the introduction of automated rotary tablet presses (Sastry, Nyshadham and Fix, 2000). Furthermore, despite the technological advances, conventional tableting still suffers from limitations caused by flowability, compactability, and compression properties of pharmaceutical powders, making techniques such as direct compression challenging.

Most importantly, an emerging weakness of conventional tableting relies on the increasing demand for personalised treatments, which is likely to represent a significant change in future medicine (Graham, 2016; Sarah J. Trenfield *et al.*, 2018). Indeed, rotary presses are designed for the mass production market and are inherently lacking in flexibility; in contrast, a more flexible manufacturing technology would facilitate to design, produce and dispense bespoke medicines (Pritchard *et al.*, 2017). However, it is of particular importance to consider that the introduction of alternative manufacturing methods to allow the personalisation of medicines does not aim to compete with the well-established conventional tableting techniques (Hopkinson and Dickens, 2003; Awad, Sarah J Trenfield, *et al.*, 2018), whose throughput remains undoubtedly superior. Rather, it should be considered that the loss in productivity is gained as improved therapeutic outcomes and patient acceptability (Dumpa *et al.*, 2021).

In less than a decade, additive manufacturing (AM), an umbrella term used to indicate a wide set of technologies including 3D printing, has aroused much interest in pharmaceuticals (figure 1.2) due to its large flexibility making it a promising tool to bring a paradigm shift in healthcare allowing the on-demand production of safe, effective, and quality personalised medicines (Goole and Amighi, 2016).

In the next sections, the state-of-the-art of 3D printing in the development and manufacture of solid oral dosage forms will be described in detail, with a focus on the opportunities and areas of development of SLA 3DP.

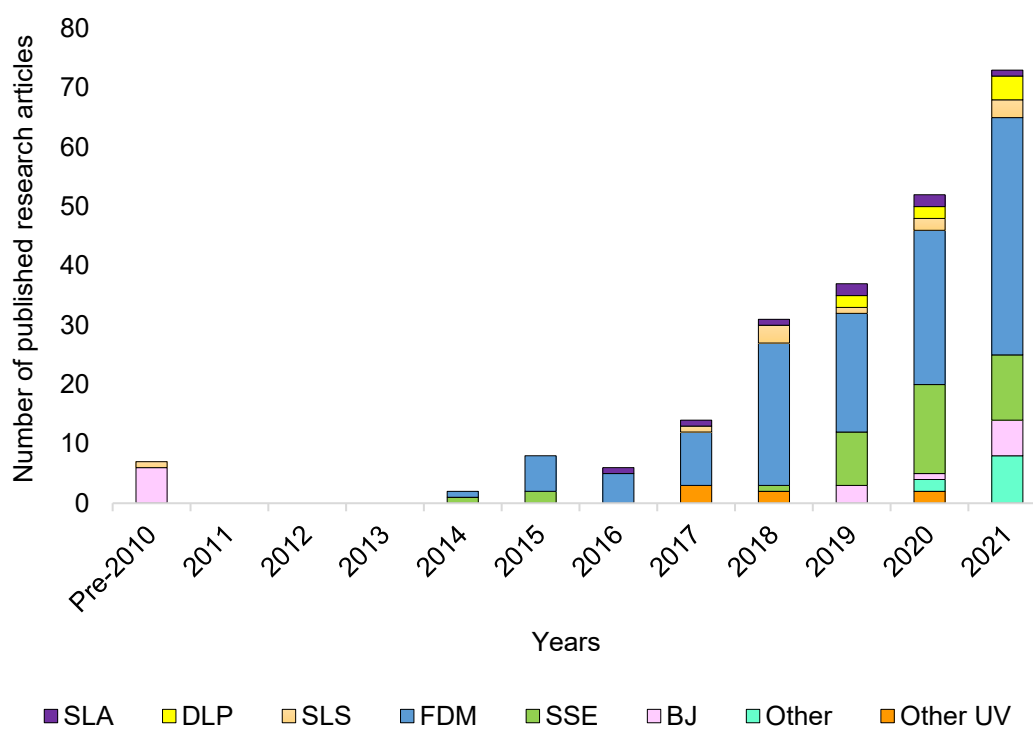


**Figure 1.2.** Number of peer-reviewed research articles related to 3D printing of solid oral dosage forms published within the years 1996–2010 (grouped as pre-2010) to 2021 (data lastly updated in November 2021). Coloured bars represent different 3DP technologies: stereolithography (SLA), digital light processing (DLP), selective laser sintering (SLS), fused deposition modelling (FDM), semi-solid extrusion (SSE), binder jetting (BJ). 3DP technologies less represented have been classified as ‘other’ or ‘other UV’ in case of products containing photopolymers. Google scholar, Science direct and PubMed search engines were used to find relevant manuscripts. Key words for searching were ‘3D printing’, ‘solid oral dosage forms’, ‘tablets’ and ‘personalised medicine’. Figure readapted from Curti, Kirby and Russell, 2020.

### 1.3.1 Computer-aided design of solid oral dosage forms

Prior to 3D printing a solid oral dosage form, it is essential to produce its digital model through computer-aided design (CAD) software (Curti, Kirby and Russell, 2020). Digital modelling allows freedom of design such that the production of tablets, for instance, is no longer dependent on size and shape of dies and punches, eventually making the same equipment suitable for producing a potentially unlimited variety of geometries (Fina, Goyanes, *et al.*, 2018).

### ***1.3.2 Tuning dosage form properties through digital design***

Following oral administration, solid dosage forms generally disintegrate and dissolve to allow the API to be absorbed and pass to the bloodstream. Dosage forms' disintegration and dissolution are dependent upon a wide range of formulation and manufacturing parameters. While the type of 3DP technology used mainly affects tablet disintegration, dissolution time is influenced by formulation composition and tablet geometry (Curti, Kirby and Russell, 2020). Conventional tablet shapes are limited by the geometry of dies and punches available for use in tablet presses, and complex shapes might be virtually impossible to realise (Martinez *et al.*, 2018). In contrast, 3DP allows formulation scientists to introduce tablet digital design as a novel stage in pharmaceutical development. Tuning dosage form properties through digital design mainly relies on fabricating devices with different excipients and/or APIs deposited in specific regions (multi-material 3DP), and engineering approaches (figure 1.3).

Multi-material 3DP of drug loaded devices was firstly introduced by Rowe (2000), who reported the fabrication of oral dosage forms with different drug release profiles obtained by including specific excipients in different sections. In subsequent years, more applications of multi-material 3DP of dosage forms were found, mainly involving the fabrication of 'polypills', dosage units containing more APIs. In this context, Khaled and colleagues (2015) developed a hybrid dosage form featuring an osmotic pump and a sustained release compartment, while in another work the potential of 3D printing to fabricate novel complex geometry 'five-drugs-in-one' polypills with immediate and sustained release was demonstrated (Khaled, 2015a). Pereira and colleagues (2019) used a low temperature fused deposition modelling (FDM) process to produce individualised multi-drug units for the treatment of cardiovascular diseases, whereas Okwuosa (2018) modified a dual-extrusion FDM 3D printer to fabricate liquid capsules containing drugs as solution or suspension, and achieving both immediate and extended release profiles. Other relevant applications of multi-material 3DP include the formulation of composite tablets (Tagami, Nagata, *et al.*, 2018) and personalised supplements (Goh *et al.*, 2021).

Engineering approaches are instead used to modify dosage form properties by simply varying their geometries, with no need to alter the formulation (Curti, Kirby and Russell, 2020). For example, Sadia and colleagues (2018) introduced perforating channels within the dosage form design to increase tablet surface area, facilitating medium flow, and ultimately accelerating drug release, whereas Arafat (2018) developed a multi-block tablet design resulting in quick fragmentation compared to no-gaps devices, thus avoiding the need for a disintegrant. Another approach consists in varying the infill percentage in FDM 3D printed tablets, thus altering tablet density and achieving different drug release profiles without modifying the formulation (Chai *et al.*, 2017; Goyanes, Fina, *et al.*, 2017). Tuning drug release through engineering approaches brings significant advantages, since dosage forms tailored on the needs of individual patients can be manufactured using the same equipment and feedstock material, benefitting treatments costs.

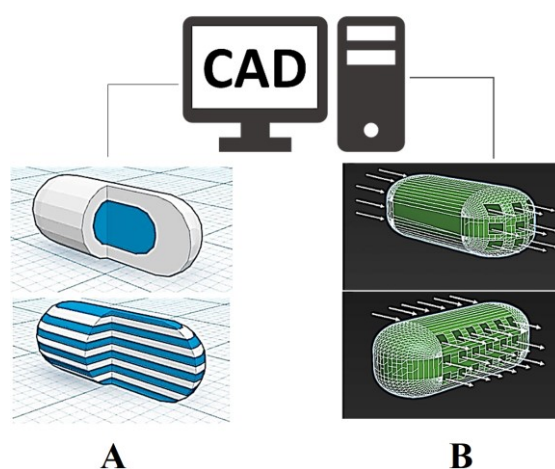


**Figure 1.3.** Schematic diagram representing examples of two different approaches to tune dosage forms' properties through CAD: (A) multi-material 3DP and (B) engineering strategies (channelled tablets). Figure reproduced from (Curti, Kirby and Russell, 2020).

### 1.3.3 3D printing technologies in pharmaceuticals

#### 1.3.3.1 Binder jetting 3D printing

In binder jetting (BJ) 3DP, objects are fabricated binding selected regions of a thin layer of a powdered material using a binder solution sprayed from an inkjet type nozzle. Once bound, the powder bed is lowered by a piston and the process is repeated until the whole part is produced (figure 1.4). From a pharmaceutical perspective, such process implies the formulation of both a powder mixture and a liquid binder, where the latter represents the most challenging step due to potential nozzle clogging issues (Infanger *et al.*, 2019). The API can be either solubilised in the liquid binder or blended with the powder mixture. When the drug is dissolved in the liquid binder, it can be loaded at very low concentrations in the tablets; this would benefit the formulation of drug products requiring ultra-low dosages (Hong *et al.*, 2021), while dispersing the API in the powder blend requires reduced excipients (Curti, Kirby and Russell, 2020).

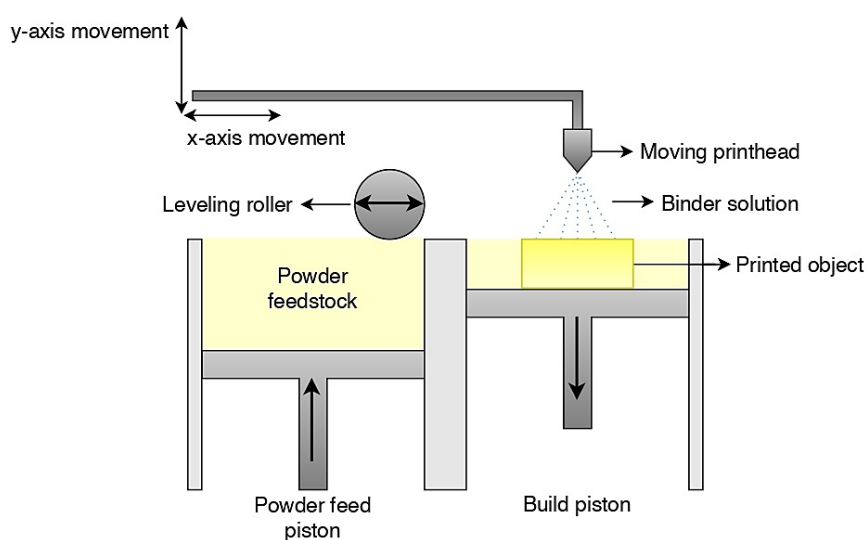


**Figure 1.4.** Schematic diagram of binder jetting 3D printing working principle.

3DP potential in drug delivery was first explored in 1996 at the Massachusetts Institute of Technology (MIT), when a desktop 3D printer (developed at the MIT itself) was used to produce a device featuring internal cells made of polymeric material (Wu *et al.*, 1996). The

ability of controlling drug release profiles was demonstrated by depositing dyes only in selected cells, thus introducing a new feature in solid dosage form design and development: microstructural control.

Following this proof of concept, 3D printed dosage forms with both erosion and diffusion drug release mechanism were realised by using specific tablets design and conventional pharmaceutical excipients (Katstra *et al.*, 2000).

The introduction of more sophisticated technologies, such as the TheriForm™ process, also made it possible to tune tablet properties through spatial control of composition. Immediate-extended release, breakaway, enteric dual pulsatory and dual pulsatory tablets are examples of dosage forms produced following digital design modelling (figure 1.5), highlighting a flexibility which is unachievable with conventional tablet pressing techniques (Rowe *et al.*, 2000).

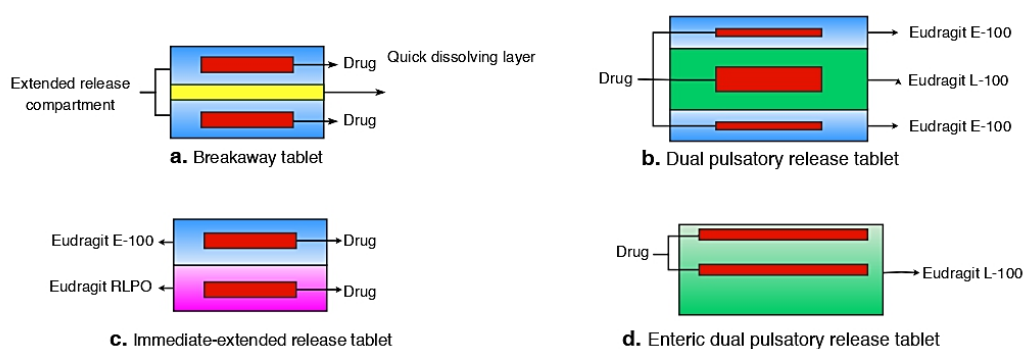


**Figure 1.5.** Drug delivery devices designed and fabricated by Rowe (2000); **(a)** breakaway tablet, **(b)** pulsatory release tablet, **(c)** immediate-extended release device and **(d)** enteric dual pulse release tablet. Figure reproduced from (Curti, Kirby and Russell, 2020).

Another appealing application of BJ 3DP is designing zero-order drug release devices (Yu *et al.*, 2007). Zero-order release kinetics, defined as constant drug release over time, is a desirable attribute for oral formulations containing APIs with short half-life or narrow therapeutic index because this allows for minimum fluctuations in drug plasma levels (Gokhale, 2014; Paarakh *et al.*, 2018). Yu (2007) described devices based on hydrophobic

top and bottom layers to limit drug release from the sides of the tablets, and tablets consisting of a middle compartment formed by annular sections with a porosity gradient achieved by printing a lower amount of binder solution (figure 1.6); the porosity gradient was exploited to have a stable erosion volume, thus resulting in a linear drug release. Another approach to achieve linear drug release proposed by Yu was based on torus shaped tablets, designed to release drug molecules only from the outer and inner surfaces (Yu, Branford-White, *et al.*, 2009).

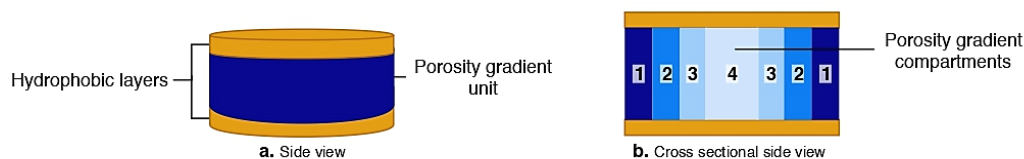


**Figure 1.6.** Schematic representation of a material gradients tablet. A different porosity degree allows a faster erosion when the surface area decreases resulting in a constant drug release. Figure reproduced from (Curti, Kirby and Russell, 2020).

Moreover, Yu and co-workers employed BJ 3DP to produce fast-disintegrating tablets binding powdered material in a gradient fashion, resulting in dosage forms with inner compartments of loose powder and highly porous structures (figure 1.7) (Yu, Shen, *et al.*, 2009).

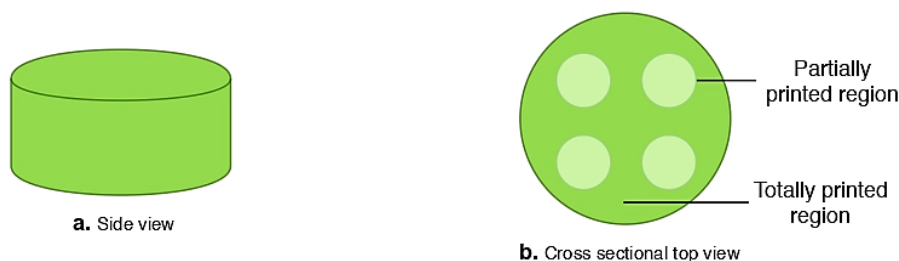


**Figure 1.7.** Schematic representation of a fast disintegrating tablet. Partially printed regions consist in loose powder that allows faster disintegration and dissolution. Figure reproduced from (Curti, Kirby and Russell, 2020).

High porosity also characterises Spritam<sup>®</sup> (figure 1.8), the first medicine fabricated through a 3D printing process - known as ZipDose<sup>®</sup> - to gain Food and Drug Administration (FDA) approval in 2015, and marketed by Aprelia Pharmaceuticals (Fitzgerald S, 2015). Spritam<sup>®</sup> is an ODT containing the drug levetiracetam and the rationale behind its development is that the highly porous structure allows the tablet to disintegrate in a mean of 11 seconds, allowing a fast onset of action (Boudriau *et al.*, 2016). As expected, the approval of Spritam<sup>®</sup> promoted the investigation of BJ 3DP, predominantly to produce ODTs. Tian and colleagues (2018) described the formulation of warfarin sodium ODTs while, more recently, Hong and co-workers (2021) reported the development of multi-compartmental structure dispersible tablets to deliver photolabile APIs.



**Figure 1.8.** Spritam<sup>®</sup>, the first 3D printed medicine to receive FDA approval. Picture reproduced from Basulto, 2015.

Although BJ 3DP allowed fundamental advances in 3D printing pharmaceuticals, demonstrating flexibility of the technique as well as the feasibility of using conventional excipients, its application remains underrepresented. The use of powders is related to several challenges, such as wettability, consolidation, and flowability (Van Den Heuvel, De Wit and Dickhoff, 2021), that can affect both the process and the final product (Prescott and Barnum, 2000) and require thorough optimisation (Antic *et al.*, 2021). For example, poor powder flowability can cause the deposition of non-uniform layers, thus affecting

dosing homogeneity (Infanger *et al.*, 2019), while highly porous structures can fail Pharmacopoeia friability tests (Yu, Shen, *et al.*, 2009; ‘British Pharmacopoeia, Appendix XVII G; Friability of Uncoated Tablets; Ph. Eur. method (2.9.7)’, 2011; Infanger *et al.*, 2019). Also, drug molecules with a high partition coefficient can complicate the manufacture process (Kozakiewicz *et al.*, 2021). Patient acceptability should be well assessed, since BJ 3D printed dosage forms usually result in a rough surface finishing, which might require coating processes to gain an appealing look, while unpleasant taste could reduce compliance of 3D printed ODTs (Wang *et al.*, 2021).

### 1.3.3.2 Semi-solid extrusion 3D printing

Semi-solid extrusion (SSE) 3DP was introduced in 2006 and represented a breakthrough point in the accessibility of affordable multi-material 3D printers (Malone and Lipson, 2007). SSE 3D printers are equipped with one or multiple syringes that can deposit a variety of materials, including liquids, gels or paste (figure 1.9).

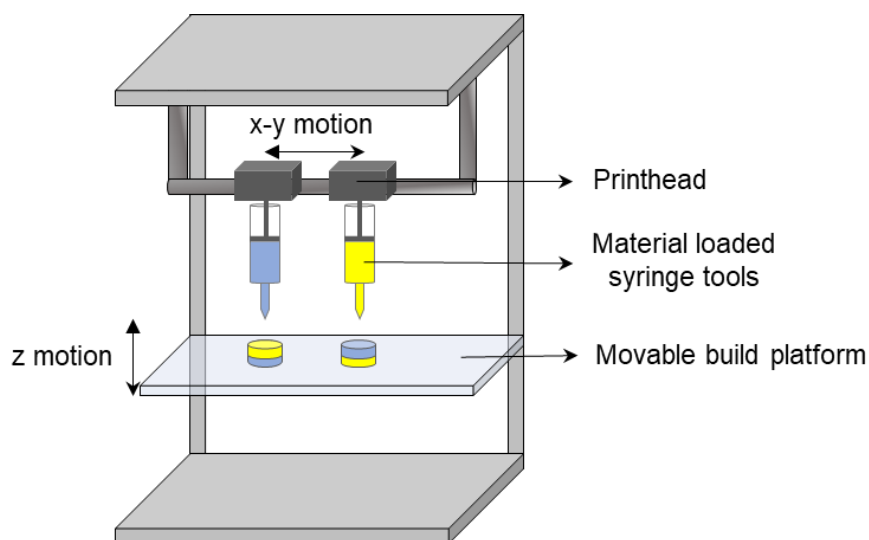


**Figure 1.9.** Schematic diagram of semi-solid extrusion 3D printing working principle.

The wide choice of materials compatible with SSE 3DP and its multi-material nature provide this technology with great manufacturing flexibility, enabling the fabrication of

polypills, immediate and controlled release tablets, chewable tablets, orodispersible films (ODFs) (Seoane-Viaño *et al.*, 2021). Using SSE 3DP, Khaled (2014) developed for the first time bilayer tablets featuring immediate and sustained release. Later, the design of polypills containing more APIs with different release profiles was introduced (Khaled *et al.*, 2015a, 2015b). Engineered polypills with programmed release profiles (Haring *et al.*, 2018), and controlled release fixed dose combination dosage forms (Siyawamwaya *et al.*, 2018) were also reported. This is intriguing, since the concept of polypills has aroused much interest in the development of personalised therapies, especially in geriatric patients suffering from polypharmacy (Hajjar, Cafiero and Hanlon, 2007; Rosted, Schultz and Sanders, 2016). In the development of a polypill, it is of particular importance to consider the APIs allocation in the different layers; the top and the bottom layers will expose a larger area to the media and, therefore, drugs in those layers will be released faster. Generally, less soluble APIs are included in the external layer, and the more soluble in the inner ones (Robles Martinez *et al.*, 2019).

SSE 3DP was successfully used to manufacture immediate (Khaled, Alexander, Wildman, *et al.*, 2018a; Conceição *et al.*, 2019; Croitoru-Sadger *et al.*, 2019; Cui, Li, *et al.*, 2019; El Aita, Breitreutz and Quodbach, 2019; Cui *et al.*, 2020; El Aita *et al.*, 2020; Yang *et al.*, 2020; Zheng *et al.*, 2020) and controlled release dosage forms (Khaled *et al.*, 2014; Li *et al.*, 2018; Tagami, Ando, *et al.*, 2018; Cui, Yang, *et al.*, 2019; Cheng *et al.*, 2020; El Aita, Breitreutz and Quodbach, 2020; Real *et al.*, 2020; Yang *et al.*, 2020), and it was found particularly suitable to produce chewable tablets including the first 3D printed formulations prepared and administered in a clinical setting (Goyanes *et al.*, 2019) (figure 1.10A), paediatric-friendly chocolate-based dosage forms (Karavasili *et al.*, 2020) (figure 1.10B), and drug loaded gummies (Rycerz *et al.*, 2019; Herrada-Manchón *et al.*, 2020; Tagami *et al.*, 2021) (figure 1.10C).

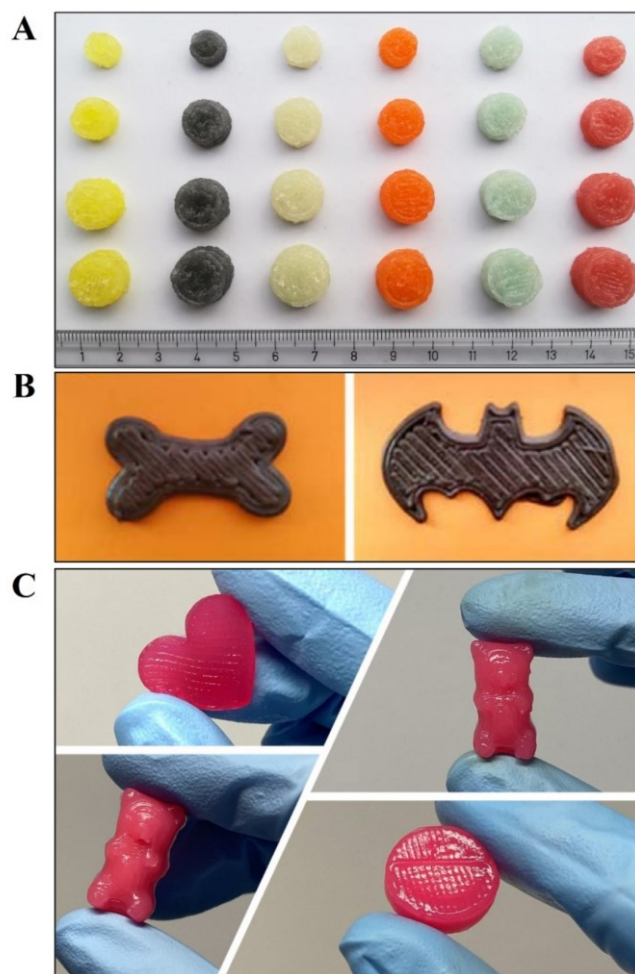


**Figure 1.10.** (A) Chewable isoleucine 3D printed tablets in different sizes, colours, and flavours (Goyanes *et al.*, 2019); (B) Paediatric-friendly chocolate-based 3D printed dosage forms (Karavasili *et al.*, 2020); (C) 3D printed drug loaded gummies (Herrada-Manchón *et al.*, 2020).

Although the advantages of SSE 3DP are clear, some limitations remain and need to be addressed before this technology can be implemented (Seoane-Viaño *et al.*, 2021). Despite SSE offers high printing speed, the resolution is often low (Vithani *et al.*, 2019). To obtain printable feedstock, it is essential to optimise material viscosity by altering temperature, pH, or excipients, but this can cause changes in the physical state of the API and requires more attention (Basit and Gaisford, 2018). A further issue is related to the drying step required after production. Indeed, preliminary development of SSE 3D printed dosage forms involved the use of solvents such as ethanol, acetone, and dimethyl sulfoxide to produce printable feedstock. Besides any toxicity concerns, which require the final product

to be compliant with the ICH Guideline Q3C (R6) (2016), effective drying is required if solvents are used, leading to the possible degradation of thermolabile APIs when heat is used. Drying is also a time-consuming process (Khaled *et al.*, 2015b), and if water is used to replace organic solvents to reduce drying time (Khaled, Alexander, Wildman, *et al.*, 2018) it should be considered that residual moisture in the final product could cause APIs hydrolytic degradation and promote microbial growth (Carstensen, 1988). Furthermore, stability concerns should also entail pre-filled syringes containing ready-to-print materials (Seoane-Viaño *et al.*, 2021).

#### ***1.3.3.3 Fused deposition modelling 3D printing***

FDM currently represents the most widely used 3DP technique in solid oral dosage form development (figure 1.2); this is attributed to the availability of inexpensive equipment that could be coupled to conventional pharmaceutical processes such as hot-melt extrusion (HME) and film coating (Goyanes, Chang, *et al.*, 2015). Introduced in 1988 (Crump, 1992), FDM became affordable to the general public in 2005 due to the RepRap (replicating rapid prototyper) project (Jones *et al.*, 2011). In FDM 3D printers, the feedstock material is a thermoplastic filament, which is melted and extruded through a heated nozzle; once extruded, the material returns to a solid, giving the object the desired geometry (figure 1.11).

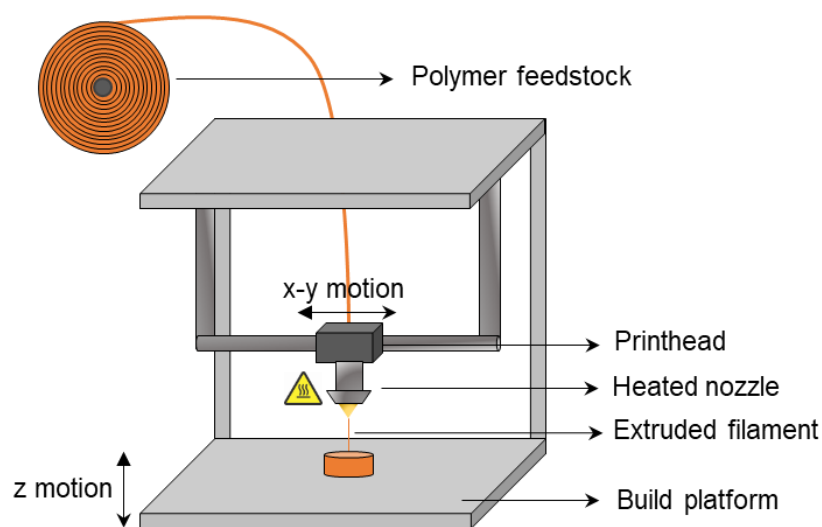


**Figure 1.11.** Schematic diagram of fused deposition modelling 3D printing working principle.

Similarly to SSE, FDM 3DP offers high flexibility resulting from the wide choice of available materials and numerous settings that can be programmed. An example is the ‘infill percentage’, defining the printing density of a certain patterned structure inside the object, which was found a valid approach to tune drug release from 3D printed dosage forms (Tagami *et al.*, 2017; Yang *et al.*, 2018; Fuenmayor *et al.*, 2019; Venâncio *et al.*, 2021) (figure 1.12A).

Early attempts of using FDM to manufacture solid oral dosage forms reported polyvinyl alcohol (PVA) filaments loaded with model drugs by passive diffusion (Goyanes *et al.*, 2014; Goyanes, Buanz, *et al.*, 2015; Skowrya, Pietrzak and Alhnan, 2015). PVA was advantageous as it is both a GRAS listed excipient (Martin, 2003) and a well-established material for FDM 3DP (Ligon *et al.*, 2017). However, drug loading of PVA filaments by passive diffusion is low, therefore limiting the application to low dosages of active ingredients (Goyanes *et al.*, 2014; Skowrya, Pietrzak and Alhnan, 2015; Ayyoubi, Cerda, Fernández-García, Knief, Lalatsa, Healy, *et al.*, 2021). To overcome such limitation, HME was coupled with FDM to produce printable filaments from pharmaceutical grade excipients. This allowed to improve drug loading and obtain devices with attractive design

(Goyanes, Wang, *et al.*, 2015), including 3D printed mesoporous carrier systems (Katsiotis *et al.*, 2021) (figure 1.12B).

Alongside PVA, other pharmaceutical grade polymers were investigated to produce printable filaments via HME (Melocchi *et al.*, 2016; Solanki *et al.*, 2018). Zhang (2017) used filaments made of hydroxypropyl methylcellulose (HPMC) and Soluplus® to fabricate zero-order drug release tablets, while immediate release tablets were produced by Sadia (2016) using Eudragit E-PO filaments. Berg (2021) used Eudragit RS to produce filaments for FDM 3D printing of pressure sensitive capsules for oral peptide delivery.

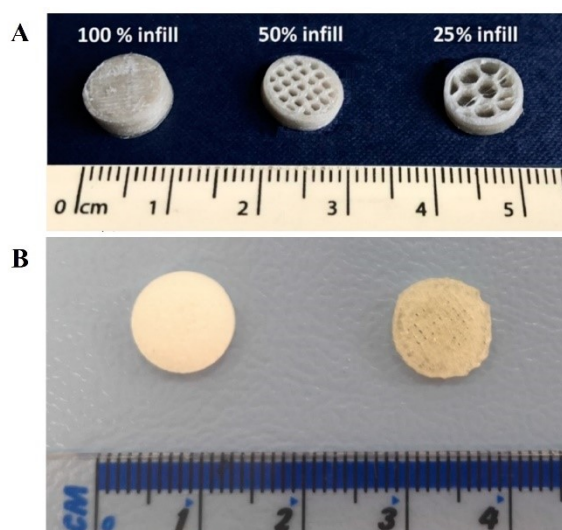


**Figure 1.12.** (A) FDM 3D printed tablets with different infill percentages (Fina *et al.*, 2020); (B) comparison between a tablet fabricated through direct compression (left) and a FDM 3D printed dosage form (right) (Shi *et al.*, 2021).

However, Sadia (2016) reported a significant decrease in drug content after printing at a temperature of 135°C, evidencing a major limitation of pharmaceutical FDM 3DP. Indeed, temperatures up to 200°C can be required for optimal printability, making FDM unsuitable for thermolabile APIs (Goyanes, Buanz, *et al.*, 2015; Nukala, Palekar, Solanki, *et al.*, 2019). Therefore, filaments extrudable at temperatures lower than 100°C are required

(Curti, Kirby and Russell, 2020), although FDM is inherently designed to work with thermoplastic materials extruded at higher temperatures.

Furthermore, the production of custom-made filaments introduces a more complex step to the relatively simple 3DP process, requiring several optimisation studies to assess properties like stiffness, toughness, melt viscosity and moisture uptake, usually altered by high drug loading (Zhang *et al.*, 2017; Öblom *et al.*, 2019); filaments with unsuited mechanical properties can cause nozzle blockage and result in printing failures (Nasereddin *et al.*, 2018), while the storage stability of drug loaded filaments remains debated (Okwuosa *et al.*, 2021).

#### ***1.3.3.4 Selective laser sintering 3D printing***

Another powder based 3DP technology recently introduced in pharmaceutical development is selective laser sintering (SLS). SLS 3DP works on similar principles as BJ 3DP, with the difference that powder particles are sintered by a high energy laser rather than bound by liquid solutions (figure 1.13). The laser writes a specific pattern on the surface of the powder bed, corresponding to each layer of the object to fabricate. A clear advantage of this is that organic solvents are not required, thus excluding toxicity concerns and further drying steps.

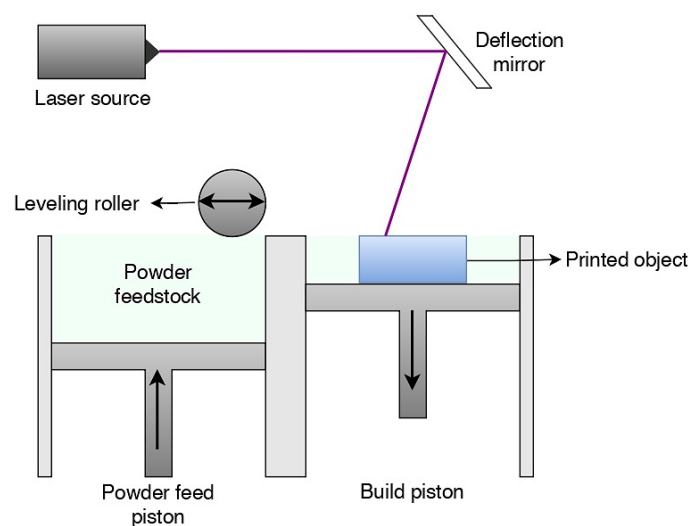


**Figure 1.13.** Schematic diagram of selective laser sintering 3D printing working principle.

The first pharmaceutical application of SLS 3DP consisted in the fabrication of polycaprolactone based drug delivery devices (Leong *et al.*, 2007). A decade later, Fina (2017) described the manufacturing of tablets by SLS using pharmaceutical polymers; Fina found that the presence of an additive absorbing light of the same wavelength as the laser was essential to obtain significant sintering of the powdered material, and Candurin<sup>®</sup> gold sheen was added to the polymer blend. Also, modulating laser scanning speed resulted effective to alter tablet porosity.

Later, the fabrication of SLS 3D printed ODTs disintegrating within four seconds was reported (Fina, Madla, *et al.*, 2018), and gyroid lattice constructs proved efficient in modulating the drug release profiles of different pharmaceutical polymers (Fina, Goyanes, *et al.*, 2018) (figure 1.14). Other application of SLS 3DP include ODTs containing mannitol as a taste masking agent (Allahham *et al.*, 2020), minitables (Awad *et al.*, 2019), and dosage forms for the visually-impaired (Awad *et al.*, 2020). Interestingly, in a recent work Gueche and colleagues (2021) found that a CO<sub>2</sub> laser was effective in sintering Kollidon<sup>®</sup> VA64 making the addition of an absorbance enhancer not necessary.

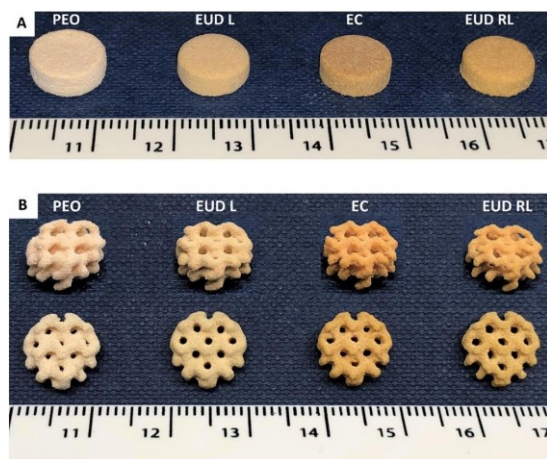


**Figure 1.14.** (A) SLS 3D printed cylindrical tablets; (B) SLS 3D printed gyroid lattice solid dosage forms. Figure reproduced from Fina, Goyanes, *et al.*, 2018.

Despite the appealing applications, SLS 3DP of pharmaceuticals remains challenging, with many process parameters to optimise (Kulinowski *et al.*, 2021; Madžarevi, 2021; Thakkar *et al.*, 2021). It should be considered that in most of the studies involving SLS 3D printed dosage forms, paracetamol was the only drug used and evidence that thermolabile APIs can be safely employed is lacking (Alhnan *et al.*, 2016; Curti, Kirby and Russell, 2020; Gueche *et al.*, 2021). In fact, when the laser hits a specific point of the powder bed, it increases the temperature; the local rise in temperature reaches a value between the melting point of the powdered material  $T_m$  and  $T_m/2$ , otherwise sintering would not occur. Despite no evidence of degradation of thermostable drug being observed (Fina *et al.*, 2017), high heating developed during operation as well as the effect of high-power lasers may affect thermolabile APIs and further investigation is required (Gueche *et al.*, 2021). Also, sintering powdered materials makes tablets' appearance considerably rough and that should be considered from a patient acceptability perspective (Januskaite *et al.*, 2020).

### 1.3.3.5 Stereolithography 3D printing

Stereolithography (SLA) 3DP is classified as a vat photopolymerisation (VP) technique, a generic term used to define a number of 3DP technologies (including digital light processing – DLP) whose working principle is based on the use of light radiation to induce

computer-spatially-controlled polymerisation of a liquid resin into a solid object (Xu *et al.*, 2021).

SLA represented a milestone in the history of 3DP as it was the first technology to be ever introduced in the field, thanks to the ingenuity of Chuck Hull, who coined the term stereolithography himself (Hull, 1984). In SLA, photopolymerisation is achieved when a focused laser beam hits a liquid photosensitive resin contained in a vat (figure 1.15); a mirror galvanometer system directs the laser beam onto the liquid resin, drawing a pattern corresponding to each single layer of the digital model (Curti, Kirby and Russell, 2020).

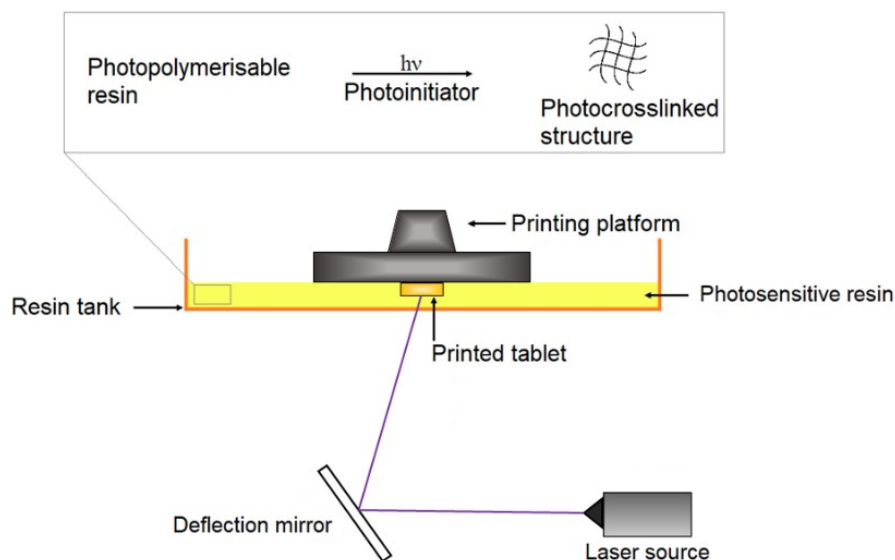


**Figure 1.15.** Schematic diagram of stereolithography 3D printing working principle.

SLA presents significant advantages, especially in terms of printing accuracy and resolution allowing the fabrication of complex geometries (Xu *et al.*, 2021), with micro SLA being able to reach 1  $\mu\text{m}$  layer thickness (Gardan, 2016). Since powders are not used to directly feed the machine, flowability and segregation issues are excluded, while the nature of the photopolymerisation process allows the fabrication of crosslinked structures with advantageous physical properties (Curti, Kirby and Russell, 2020). Furthermore, in SLA 3DP heating is not involved during operation, thus allowing to safely include thermolabile APIs (Curti, Kirby and Russell, 2021).

Generally, photopolymerisable resins for SLA 3DP are mixtures of reactive monomers and oligomers that crosslink when exposed to light of a certain wavelength in the presence of a photoinitiator (PI). Printable resins can also contain additives such as pigments, dyes, or light absorbers (Ligon *et al.*, 2017).

Pharmaceutical applications of SLA 3DP mostly relied on acrylate photopolymers to assemble biocompatible printable resins (Curti, Kirby and Russell, 2020). Wang (2016) investigated for the first time the feasibility of SLA 3DP in the formulation of solid oral dosage forms, that were produced in a torus geometry using polyethylene glycol diacrylate (PEGDA) 700 and diphenyl-(2,4,6-trimethylbenzoyl)-phosphine oxide (TPO) as a PI (figure 1.16). In the photopolymer resin, Wang also included polyethylene glycol (PEG) 300 as a drug release tuning agent (Wang *et al.*, 2016).

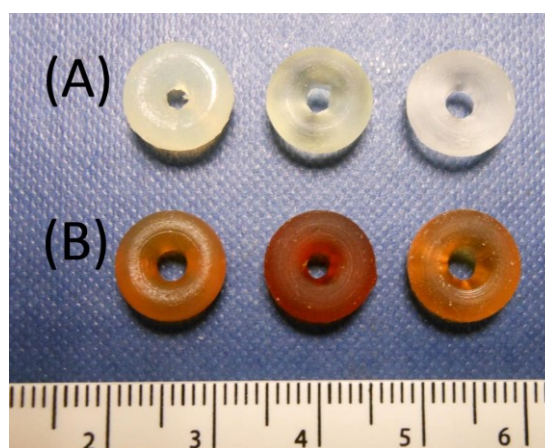


**Figure 1.16.** (A) Paracetamol and (B) 4-ASA SLA 3D printed torus shaped tablets consisting of PEGDA 700 and PEG 300. Figure reproduced from (Wang *et al.*, 2016).

Wang (2016) pioneering research stimulated further work on the topic, as evidenced by the studies of Martinez and colleagues on drug loaded hydrogels (2017), and on the influence of geometry on the drug release profiles of SLA 3DP dosage forms (2018). More intriguingly, Martinez (2019) and Xu (2020) also developed multi-layered polypills containing several APIs, thus introducing multi-material SLA 3DP (figure 1.17).



**Figure 1.17.** (A) Cylindrical and (B) ring shape SLA 3D printed polypills. Figure reproduced from Robles Martinez *et al.*, 2019.

Surprisingly, Xu (2020) described for the first time the incompatibility of PEGDA with one of the APIs used (amlodipine) resulting from the Michael addition reaction between the two compounds. Clearly, this highlights the need to screen for photopolymer resins compatible with drugs to be included in SLA 3D printed dosage forms (Xu *et al.*, 2020).

As a matter of fact, major challenges of pharmaceutical SLA 3DP can be attributed to the photopolymers required, because of the limited choice available (Wang *et al.*, 2016). Furthermore, none of them is currently GRAS listed (Curti, Kirby and Russell, 2021). Therefore, there remain significant limitations to be addressed before SLA 3DP can be implemented in clinical practice. In this context, the screening and the systematic evaluation of monomers, oligomers, and PIs to assemble a variety of photopolymer resins, could enlarge the pool of materials suitable for SLA 3DP of dosage forms (Curti, Kirby and Russell, 2021). A few studies have already demonstrated that non-toxic PIs can be successfully used (Martinez *et al.*, 2017; Karakurt *et al.*, 2020) to produce SLA 3D printed hydrogels, but evidence of the fabrication of tablets is lacking. Moreover, to progress the SLA 3DP of dosage forms, thorough investigation of tablet uniformity and physical properties such as hardness and friability is needed (Healy *et al.*, 2019).

#### **1.4 Rationale of drug selection for 3D printed individualised therapies**

The rationale of introducing 3DP in pharmaceutical manufacturing relies on providing an adaptable platform to produce and dispense tailored drug products (Trenfield *et al.*, 2018). Indeed, the availability of treatments designed to meet individual needs is considered a main objective of future medicine, thanks to continuous progress in pharmacogenomics and bioinformatics which can help to predict patients' response to medicinal products (Graham, 2016).

In this context, pharmaceutical 3DP offers its potential to manufacture dosage forms with adaptable properties, such as bespoke drug dosages or release profiles (Curti, Kirby and Russell, 2020). Personalising medicinal products also encompasses features as size, shape, texture, colour, and flavour of oral dosage forms influencing patient acceptability (Yoder *et al.*, 2014; Goyanes, Scarpa, *et al.*, 2017; Scoutaris, Ross and Douroumis, 2018). From a clinical perspective, personalisation of pharmacotherapies shows higher relevance when drugs with narrow therapeutic index (NTI) are used. NTI drugs are those APIs whose effective dose is so close to the toxic dose to represent a potential danger for the patient if badly managed. According to this, NTI drugs represent the ideal model compounds to include in 3D printed formulations aimed to investigate the potential to deliver safe, effective, and quality personalised medicines.

## 1.5 Research aim and objectives

The increasing need for patient-centric medicine has led to major breakthroughs in the pharmaceutical field. In recent years, three dimensional printing has aroused much interest in pharmaceuticals, due to the wide flexibility making such technology the ideal choice for the on-demand manufacture of personalised medicines. 3D printing pharmaceuticals allows to fabricate solid oral dosage forms in a virtually unlimited selection of geometries, while also encompassing features like texture, size, colour, taste, or drug release profile, thus enabling to truly deliver personalised medicine. Several 3DP technologies have been implemented for the production of pharmaceuticals, and stereolithography has emerged as a frontrunner for the design of solid oral dosage forms.

The following work entails the thorough investigation of pharmaceutical SLA 3D printing aimed to assess its potential in the development of a wide range of drug loaded dosage forms targeting individualised treatments.

In particular, the objectives of this research project are outlined as follows:

- Investigate the suitability of a desktop SLA 3D printer to manufacture solid oral dosage forms designs and assessment of any printability limitations. Repurpose the SLA 3D printer into a high-throughput platform designed to optimise pharmaceutical formulation screening cost-effectiveness.
- Design of novel photopolymer resin formulations and evaluation of their printability by conducting a systematic screening aimed to identify candidate formulations for SLA 3DP of drug loaded solid oral dosage forms.
- Fabrication of SLA 3D printed drug loaded solid oral dosage forms aimed to achieve clinically relevant drug dosages. Characterisation of the 3D printed dosage forms according to conventional Pharmacopoeia quality standards. Identification of potential areas of development and guide for future work.

## - Chapter II -

### DEVELOPMENT OF A NOVEL STEREOLITHOGRAPHY APPARATUS DESIGNED FOR PHARMACEUTICAL APPLICATION

---

#### **Publications arising from the work in this chapter:**

Curti, C., Kirby, D.J. & Russell, C.A., 2021. Stereolithography Apparatus Evolution: Enhancing Throughput and Efficiency of Pharmaceutical Formulation Development. *Pharmaceutics*, 13(5), p.616.

## 2.1 Introduction

Pharmaceutical formulation development is a thorough process requiring the testing of several drug-excipient blends to obtain an in depth understanding of the critical parameters affecting the quality of the final product, and to provide it with the desired characteristics (Aulton and Taylor, 2017).

Cost-effectiveness analyses suggest that the cost of excipients should be kept to a minimum in pharmaceutical development (Van Hoogevest and Wendel, 2014); clearly, this is even more significant when raw materials cost is high, as for photopolymers used in stereolithography (SLA) three-dimensional printing (3DP) (Yun *et al.*, 2016).

Commercially available SLA 3D printers are generally equipped with resin tanks requiring large resin volumes to operate (Kadry *et al.*, 2019). Such a concept is unsuitable for pharmaceutical development, where the ability to operate with small batches of different formulations is ideally preferred (Curti, Kirby and Russell, 2021). Indeed, currently available SLA 3D printers are not designed to simultaneously use different photopolymer formulations; despite multi-material SLA 3DP being described in recent work (Robles Martinez *et al.*, 2019), the method used was discontinuous and required the intervention of an operator to physically replace the resin tank.

As such, conventional SLA apparatus do not meet the requirements of cost-efficiency and flexibility of pharmaceutical formulation development processes. For example, to evaluate a novel photopolymer formulation by 3DP three cylindrical tablets measuring 12 × 4 mm (diameter × thickness), a total of 1.35 mL of resin would be required while an average resin tank needs to be filled with hundreds to thousands of millilitres (Kadry *et al.*, 2019). This would lead to an unsustainable waste of materials with a significant economic and environmental impact.

Therefore, in this Chapter were identified the throughput limitations of a desktop SLA 3D printer with the aim to repurpose it into a novel SLA apparatus with optimised cost-effectiveness. More precisely, such apparatus was designed to operate with low resin

volumes, and to simultaneously work with up to twelve different formulations, thus maximising the efficiency of pharmaceutical formulation development to ultimately fulfil the need for screening and systematically evaluating novel photopolymer resins for SLA 3DP of medicines.

## **2.2 Chapter aim and objectives**

The primary aim of this chapter was to assess the suitability of a commercially available desktop SLA 3D printer to manufacture solid oral dosage forms in a cost effective way. This was of particular importance since pharmaceutical grade SLA 3D printers are lacking. Therefore, it was essential to investigate the potential to fabricate solid oral dosage forms in a variety of geometries while assessing any printability limitations. Furthermore, with the view to conduct a high throughput printability screening on several photopolymer formulations, the commercially available desktop SLA 3D printer had to be repurposed into a novel platform specifically designed to maximise cost-effectiveness of pharmaceutical formulation development.

To achieve the abovementioned aim, the work presented in this chapter was essentially carried out in three different phases characterised by the following objectives:

- Computer aided design and 3D printing of solid oral dosage forms prototypes featuring various geometries for printability assessment.
- Design, fabrication, and optimisation of custom made 3D printer components to enable low-volume, multi-material SLA 3D printing.
- Validation of the novel SLA apparatus developed by evaluating tablet uniformity of weight, thickness, and diameter, aimed to guarantee a reliable manufacturing of 3D printed tablet batches.

## **2.3 Materials and Methods**

### ***2.3.1 Materials***

Clear resin V4.0 (Formlabs Inc, USA) was used as a commercially available photopolymer for SLA 3DP. Cyanoacrylate adhesive and clear silicon glue were respectively purchased from RS components (UK) and Loctite (Henkel Corp, Germany). Aluminium foil and tape were respectively acquired from VWR (VWR International LLC, USA) and 3M (3M Company, USA). Technical grade propan-2-ol used to wash 3D printed parts was obtained from Fisher Chemical (Fisher Scientific, UK). The aluminium used to produce the modified build platform (BP) was a 150 × 150 × 100 mm (W × D × H) H30-6082-T6 aluminium alloy block purchased from John Keatley Metals (Keatley Metals Ltd, UK).

### ***2.3.2 Methods***

#### ***2.3.2.1 Computer-aided design***

Three-dimensional (3D) models of solid oral dosage forms, the resin tank inserts, and the modified BPs were designed using the computer-aided design (CAD) software TinkerCAD (Autodesk Inc, USA). TinkerCAD was also used to generate the stereolithographic files (.stl) of the 3D models designed, that were later uploaded to the 3D printer software to initiate a print. The 3D model of the BP final version, used for computerised numerical control (CNC) manufacturing, was designed using SolidWorks (Dassault Systèmes, France).

#### ***2.3.2.2 Stereolithography apparatus***

A Form 2 SLA 3D printer (Formlabs Inc, USA) was used as a desktop stereolithography apparatus. The Form 2 is equipped with a 405 nm laser and has a build volume of 145 × 145 × 175 mm (W × D × H). The feedstock material consists of a photopolymer resin contained in a 200 mL vat. 3D printed objects are formed on a BP made of aluminium and

plastic, having a build area of 21,025 mm<sup>2</sup> and a weight of 635.18 g. The Form 2 was used to 3D print the resin tank inserts, the modified BPs, and the tablet models used for printability tests.

### ***2.3.2.3 Stereolithography 3D printing***

All 3D printed objects described in this Chapter were produced using Clear resin photopolymer. 3DP was initiated by using PreForm 2.20.0–Beta 1 (Formlabs Inc, USA) to upload the .stl files of the 3D models previously designed, and to set the layer thickness and the printing supports required for the design. After completion, all 3D printed objects were washed in a sonic bath using propan-2-ol for 20 minutes to remove the uncured resin, and then dried at room temperature. If present, printing supports were manually removed from the 3D printed model after drying.

### ***2.3.2.4 Tablet uniformity testing***

The original and the modified versions of the BP were used to fabricate cylindrical tablets to evaluate the influence of different BPs on tablet uniformity. Three batches of twelve tablets each were 3D printed on each BP. All tablets manufactured at this stage were composed of Clear resin photopolymer V4.0. After 3DP, ten tablets per batch were randomly picked to carry out tablet uniformity tests. Measurements were taken for tablet weight, thickness, and diameter. Tablets were printed both directly on the BP and oriented to 45° using printing supports to evaluate their impact on tablet uniformity. Tablet thickness and diameter were measured using a digital calliper, while weight of individual tablets was measured using a semi-micro balance (Sartorius AG, Germany) with a scale interval of 0.01 mg.

### 2.3.2.5 Material waste determination

The amount of material wasted consequently the use of printing supports was determined by fabricating 30 cylindrical tablets. Supports were automatically generated using PreForm 2.20.0–Beta 1 software. After 3DP, supports still attached to the respective tablets were weighed ( $W_i$ ). Then, supports were manually removed and weighed ( $W_{ps}$ ). Material waste was calculated as the percentage ratio between  $W_{ps}$  and  $W_i$ .

### 2.3.2.6 Resin recovery efficiency evaluation

The original BP and the Alu<sub>12</sub>BP were weighed separately. Each platform was connected to the 3D printer and a print was initiated. Once the platform was completely lowered in the resin tank and covered in photopolymer resin, the print was aborted to allow the BP to home. As soon as the initial position was reached, a timer was started, and the platform collected to be weighed again at given timepoints (Figure 2.1). The experimental procedure was carried out at room temperature. The volume of resin adhered to the BP at each timepoint was calculated using Equation (1):

$$V_n = (W_n - W_i) / \rho \quad (1)$$

where  $V_n$  indicates the volume of resin adhering to the BP at the n-time point,  $W_n$  is the weight of the BP at the n-time,  $W_i$  is the initial weight of the BP, and  $\rho$  is the resin relative density.

The economic loss relative to the wasted resin at the n-timepoint was calculated using Equation (2):

$$\text{Economic loss } (\mathcal{E}) = [(W_n - W_i) / \rho] \times \text{resin cost } (\mathcal{E}/\text{mL}) \quad (2)$$

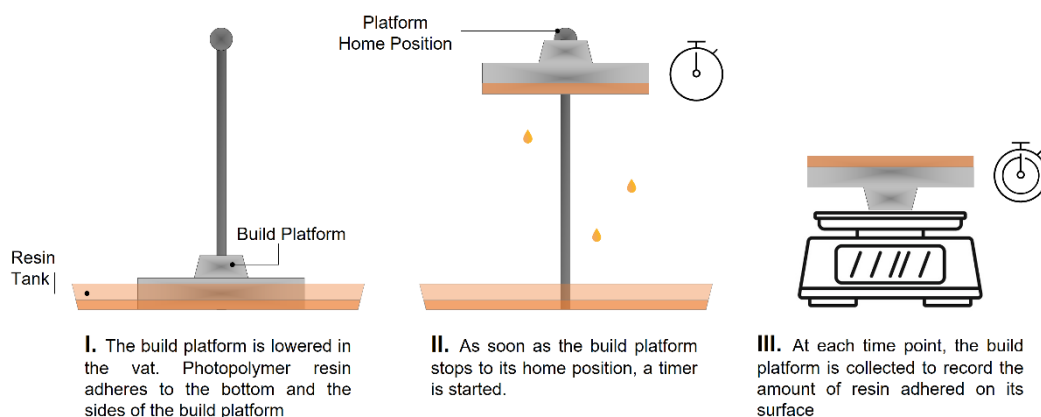


**Figure 2.1.** Schematic diagram of the method developed to evaluate photopolymer resin wastage due to adherence on the BP after the completion of a print. Image reproduced from (Curti, Kirby and Russell, 2021).

### 2.3.2.7 Statistical analysis

Tablet uniformity data were statistically analysed by performing a multivariate analysis of variance (MANOVA) coupled with a Tukey post-hoc test using SPSS Version 26.0.0.0 (IBM Corp, USA);  $p$ -values  $<0.05$  were considered statistically significant.

## 2.4 Results and Discussion

### 2.4.1 Computer-aided design of solid oral dosage forms

With the view to assess their respective printability, 3D models of 5 different tablet geometries were designed (figure 2.2). The 5 designs were based on a cylindrical, a biconvex, a torus, a biconical frustrum, and a capsule shape, thus resembling conventional solid oral dosage forms shapes. These different designs were chosen to identify potential 3DP limitations intrinsic of specific geometries.

Another reason for designing different tablet shapes was based on the potential future need to explore different geometries as ways to tune drug release (Goyanes, Robles Martinez, *et al.*, 2015; Martinez *et al.*, 2018), or to conduct patient-acceptability studies (Januskaite *et al.*, 2020; Z. B. Shariff *et al.*, 2020; Z. Shariff *et al.*, 2020)

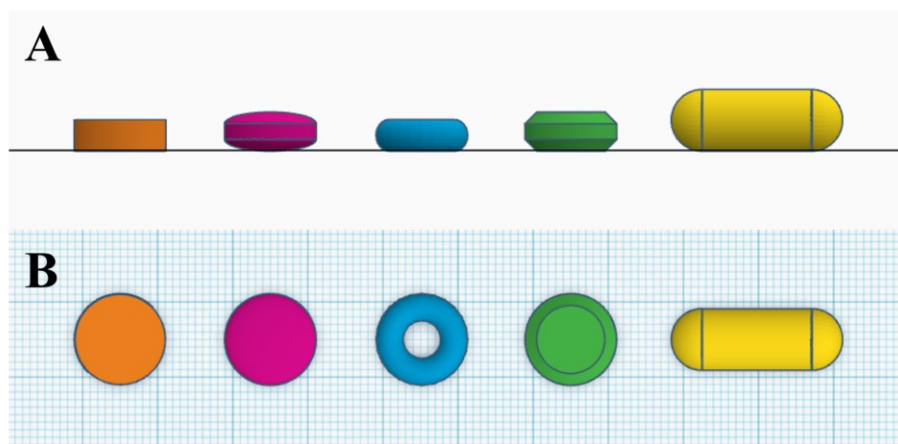


**Figure 2.2.** (A) Front and (B) top views of the tablet models designed using TinkerCAD. Each square on the blue background corresponds to a surface area of 1 cm<sup>2</sup>.

After designing the 3D models of tablet prototypes, the following step consisted in uploading the respective .stl files to the 3D printer software in order to set the first 3DP experiment.

#### *2.4.2 Printability assessment of solid oral dosage forms models*

The five tablet models were successfully 3D printed (figure 2.3) using printing supports and orienting the dosage forms to 45° with respect to the BP plane, indicating the suitability of SLA to accurately fabricate drug delivery devices with various geometries. However, when tablets were 3D printed with a 0° degrees orientation with respect to the BP plane, printability issues were encountered due to the accumulation of partially cured resin between the tablet surface and the supports' structure eventually causing a rough appearance. Therefore, tablets later described in this Chapter were all 3D printed with a 45° orientation with respect to the BP plane.



**Figure 2.3.** 3D printed dosage forms models based on the design in figure 2.2. Image readapted from (Curti, Kirby and Russell, 2020).

A further tablet model based on a spherical design was also fabricated (figure 2.4). More specifically, two spherical dosage form models were designed, one being hollow and the other being a whole solid. The hollow design was selected to assess the potential to SLA 3D print solid oral dosage forms acting as gastric-floating drug delivery devices (Li *et al.*, 2018; Chen *et al.*, 2020; Vo *et al.*, 2020), spherical mini-tablets (Ayyoubi, Cerda, Fernández-García, Knief, Lalatsa, Marie Healy, *et al.*, 2021), or as fillable shells (Okwuosa *et al.*, 2018).

For 3D printed hollow spheres, it was observed that the internal cavity of the design remained almost entirely filled with uncured resin, thus proving unfeasible to be safely fabricated. In fact, the liquid resin inside should be washed to be removed or undergo thermal or ultraviolet (UV) post processing aimed to reduce its toxicity before administration (Xu *et al.*, 2021).

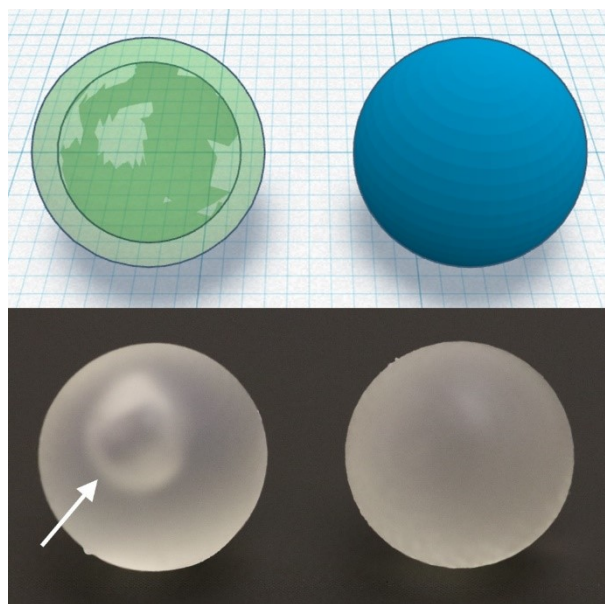


**Figure 2.4. (Top)** CAD models and **(bottom)** 3D printed spherical solid oral dosage forms. Design on the left features a hollow cavity (white arrow indicates an air bubble floating on liquid resin), while the design on the right is a solid sphere.

Having proved that various geometries can be successfully fabricated via SLA 3DP, the cylindrical shape was selected for the subsequent work presented in this Thesis. The rationale for this relied in its wide use as a standard shape in solid oral formulation development (Siepmann *et al.*, 2010; Ahmat, Ugail and Castro, 2011; Xu *et al.*, 2020), also allowing to reveal challenging formulation issues such as susceptibility to friability failures caused by the presence of sharp edges (Osei-Yeboah and Sun, 2015). Moreover, cylindrical shapes allow easy alteration of tablet volume by varying the thickness of the design, thus enabling to tailor drug dosage, with no need to alter the formulation (Curti, Kirby and Russell, 2020).

#### ***2.4.3 Proof of concept design and development***

The first step in developing a more efficient SLA apparatus consisted in demonstrating the feasibility of 3DP a dosage form model using a modified custom-made resin tank and BP.

In order to reduce the volume of photopolymer resin to be loaded in the original resin tank (circa 200 mL), a rectangular insert with internal sides measuring 100 × 40 mm, hence allowing to load 20 mL of resin, was designed using TinkerCAD (figure 2.5).

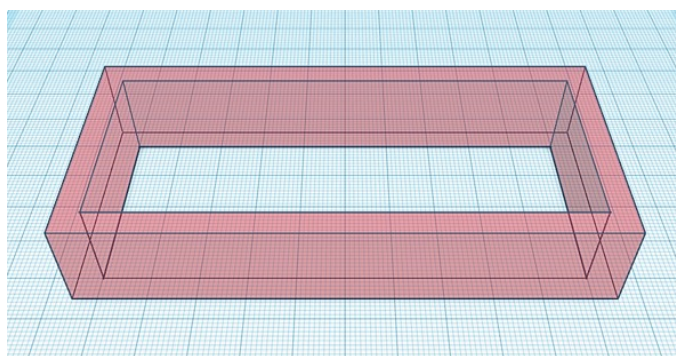


**Figure 2.5.** CAD model of the rectangular resin tank insert used as a proof of concept. Each square on the blue background corresponds to a surface area of 1 cm<sup>2</sup>.

The resin tank insert was 3D printed using Clear photopolymer resin. The design was fabricated in 6 hours and 15 minutes, using printing supports and setting the layer thickness of 100 µm. Once ready, the insert was attached to the silicon layer of the original resin tank

using silicon glue and allowed to dry for 24 hours. Afterwards, the modified resin tank was tested for being watertight by filling it with an aqueous solution of green food colouring and leaving it overnight to detect any leaks. Eventually, the modified resin tank prototype was loaded with 20 mL of photopolymer resin to carry out a 3D printing test, thus proving a 10-fold reduction of the amount of material required in comparison with the original resin vat.

Having successfully developed a low volume resin tank, the next step consisted in designing a functional BP matching the rectangular insert. The modified BP was designed with a build area of 400 mm<sup>2</sup> to allow 3DP of single tablet models, with or without supports. The top side of the BP was designed to match the geometry of the original component manufactured by Formlabs, to secure a perfect fit to the cam handle of the 3D printer (figure 2.6).

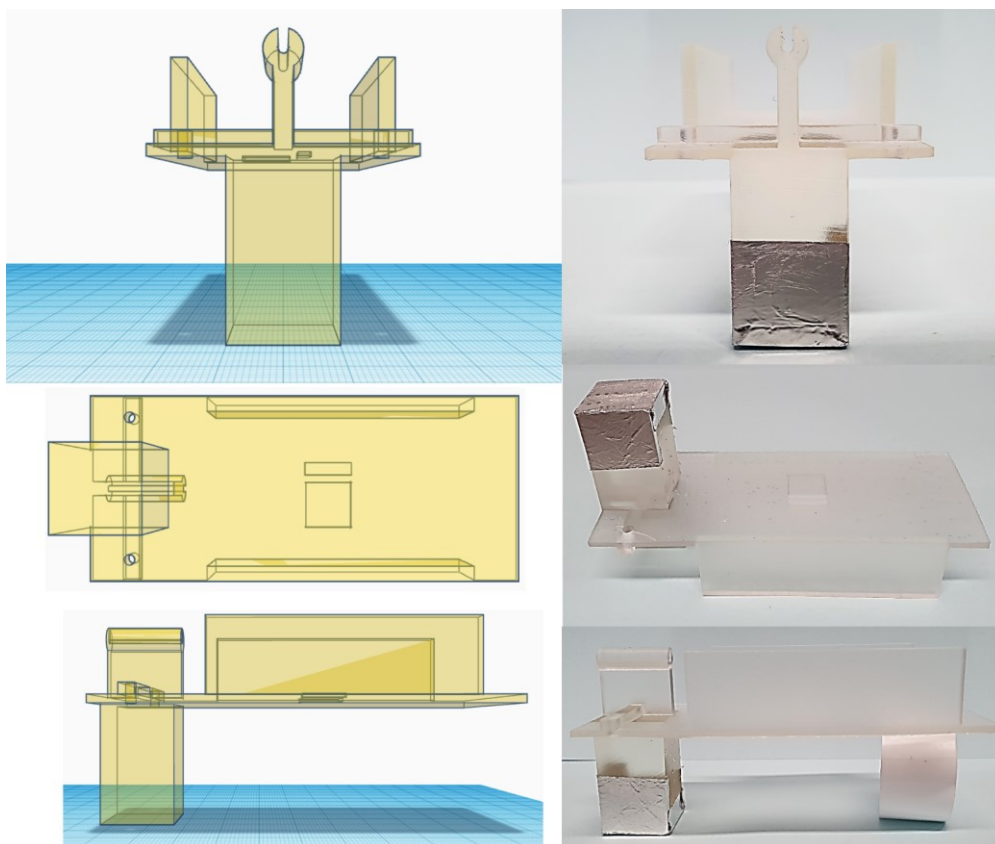


**Figure 2.6.** Front, bottom, and side views of the CAD model (**left**) and 3D printed prototype (**right**) of the modified BP.

The model was fabricated in 22 hours and 31 minutes setting layer thickness to 25  $\mu\text{m}$  to maximise geometrical accuracy and to ensure the smoothness of the build area. Once completed, the build spot was coated with 15  $\mu\text{m}$  thick aluminium foil fixed with clear plastic tape, to allow an easy removal of 3D printed objects, while the top of the BP was connected to the 3D printer using the original platform's fixture.

Having equipped the Form 2 SLA apparatus with the modified resin tank and BP prototypes, a 3D print test of a supported cylindrical tablet model was successfully performed, thus proving our concept (figure 2.7).



**Figure 2.7.** Successful 3DP test of a supported cylindrical tablet model fabricated using the modified BP.

Having effectively managed to use the Form 2 3D printer equipped with custom made components aimed to maximise process' efficiency, the next phase consisted in moving from a proof of concept to a more ambitious design focused to boost throughput.

#### 2.4.4 Design and fabrication of a low volume multi-compartment resin tank

A multi-compartment resin tank insert was designed as six modular elements combining each other to fit within the print area of the original resin tank (figure 2.8). Thickness of walls delimiting the outer perimeter of the insert was 5 mm, whereas internal partitions between each cell measured 4 mm.

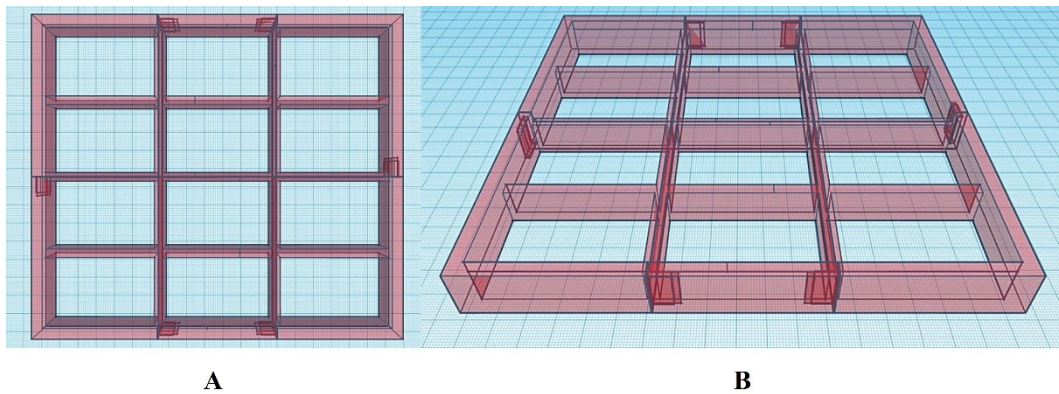


**Figure 2.8.** (A) Top and (B) front view of the multi-compartment resin tank insert CAD model. Each square on the blue background corresponds to a surface area of 1 cm<sup>2</sup>. Image reproduced from (Curti, Kirby and Russell, 2021).

After fabrication, the 6 modular elements were combined and fixed using cyanoacrylate adhesive, thus forming a structure hosting 12 resin vats. After drying, the insert was attached to the silicon layer of the original resin tank using silicon glue and allowed to dry for 24 hours (figure 2.9A). Then, the multi-compartment resin tank insert was tested for being watertight by alternately filling each cell with an aqueous solution of green food colouring and leaving it overnight to assess any leaks (figure 2.9B).

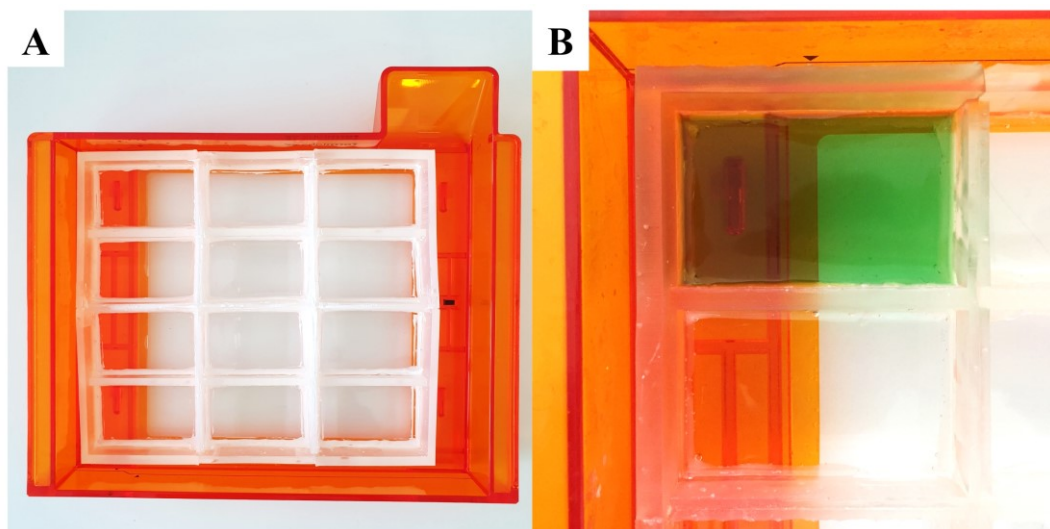


**Figure 2.9.** (A) 3D printed multi-compartment resin tank insert fixed onto the silicon layer of the original resin tank. (B) Sealing test of an individual compartment. Image readapted from (Curti, Kirby and Russell, 2021).

#### *2.4.5 Design and fabrication of a multi-spot build platform*

To match the 12-vats resin tank previously described, a first version of BP featuring 12 separate build areas, denominated 3DP<sub>12</sub>BP (Mk I), was designed and 3D printed (figures 2.10-2.11).

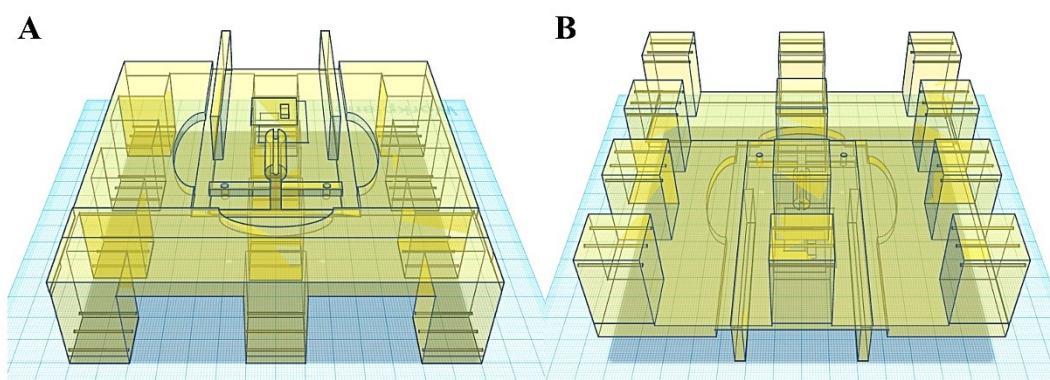


**Figure 2.10.** (A) Top and (B) bottom views of the 3DP<sub>12</sub>BP (Mk I) CAD model. Each square on the blue background corresponds to a surface area of 1 cm<sup>2</sup>.

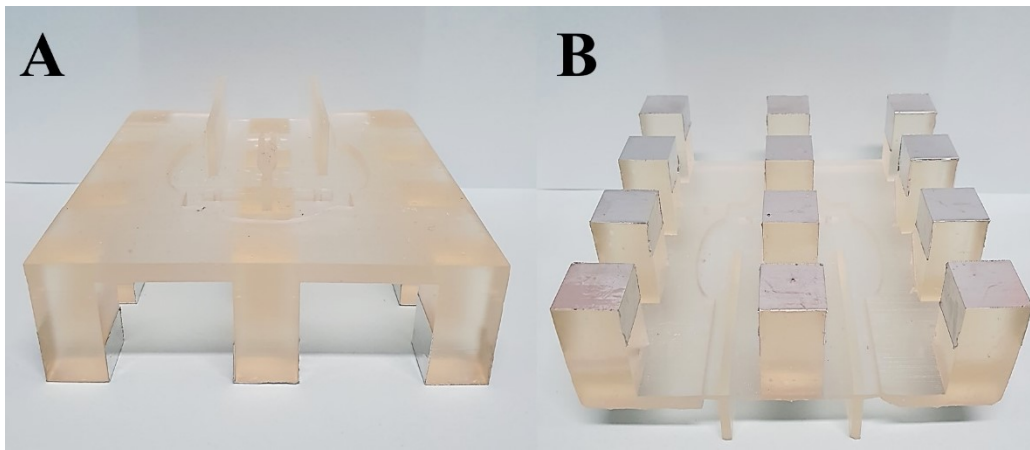


**Figure 2.11.** (A) Top and (B) bottom views of the 3DP<sub>12</sub>BP (Mk I).

The top side of the 3DP<sub>12</sub>BP (Mk I) design was based on the prototype previously described, which proved to be firmly connected to the cam handle of the Form 2 3D printer (figure 2.12).

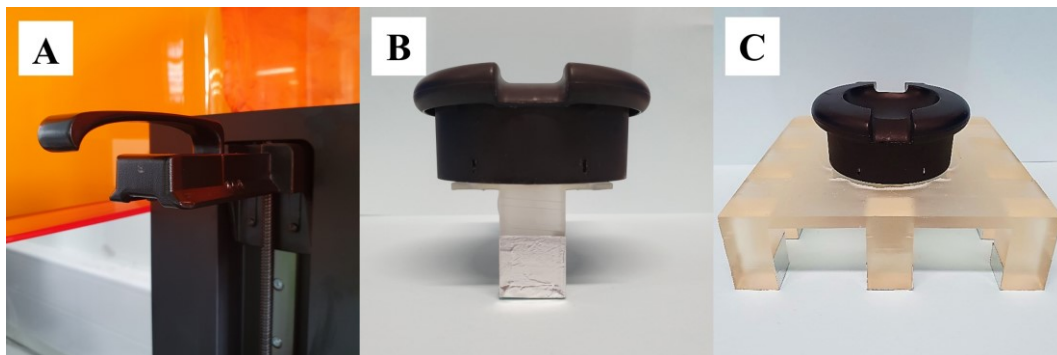


**Figure 2.12.** (A) Cam handle of the Form 2 3D printer; (B) single-spot BP prototype and (C) 3DP<sub>12</sub>BP (Mk I) coupled with the original BP fixture.

A new feature consisted in introducing in each build spot 3 holes having a diameter of 1.5 mm allowing the insertion of 3 aluminium rods. This was to ensure the aluminium foil was firmly held in place since it was observed that, after multiple prints, the chemicals contained in the photopolymer resin dissolved the glue on the tape. A detail of such artifice is visible in figure 2.13.

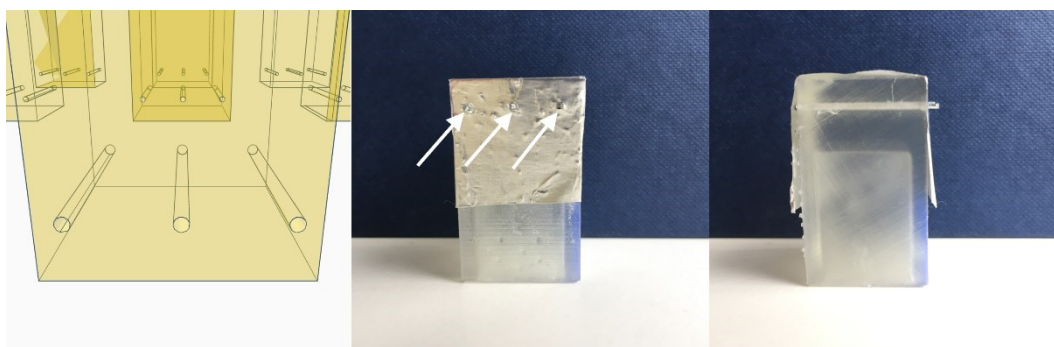


**Figure 2.13.** (A) Detailed view of the 3 holes designed at the bottom side of each build spot in the CAD model. (B) Front and (C) side views of a 3D printed build spot model featuring 3 aluminium rods (indicated by white arrows) used to hold the aluminium foil.

The 3DP<sub>12</sub>BP (Mk I) demonstrated the feasibility of 3DP dosage form models, with and without supports, in combination with the modified 12-vats resin tank. However, tablet uniformity data showed lack of accuracy and precision, as it will be discussed later in this Chapter (figures 2.22-2.24). Indeed, visual inspection of the 3DP<sub>12</sub>BP (Mk I) during the printing process proved that a poor hold of the BP onto the cam handle of the 3D printer caused an unstable positioning resulting in a non-uniform print. Such issue was not observed when the single build spot prototype was tested, as it is likely that it was caused by the higher weight of the 3DP<sub>12</sub>BP (Mk I).

To overcome such problem, an improved version of the 3D printed BP, denominated 3DP<sub>12</sub>BP (Mk II), was designed to directly fit the 3D printer support arm (figures 2.14-2.15). Furthermore, aluminium foil on the build spots was replaced by 75 µm thick aluminium tape with an adhesion strength of 12N/cm because of its improved firmness still allowing an easy substitution in case of damage.

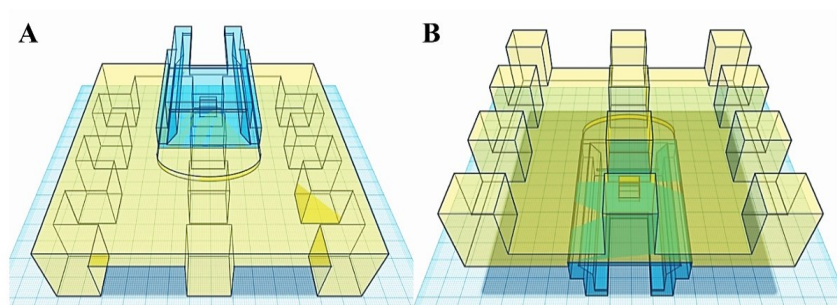


**Figure 2.14.** (A) Top and (B) bottom views of the 3DP<sub>12</sub>BP (Mk II) CAD model. The new version features a component (coloured in blue) designed to fit tight into the locking mechanism securing the BP to the 3D printer. Each square on the blue background corresponds to a surface area of 1 cm<sup>2</sup>. Image reproduced from (Curti, Kirby and Russell, 2021).

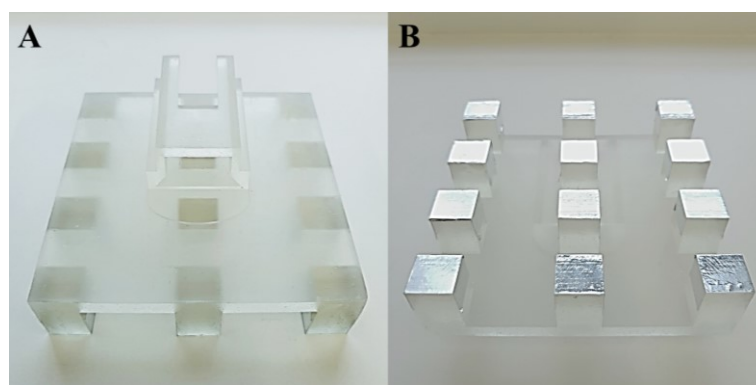


**Figure 2.15.** (A) Top and (B) bottom views of the 3DP<sub>12</sub>BP(Mk II). Image readapted from (Curti, Kirby and Russell, 2021).

Thanks to the improvements in the holding mechanism, the 3DP<sub>12</sub>BP(Mk II) proved to substantially improve tablet uniformity, as showed later (figures 2.22-2.24). Also, the introduction of aluminium tape proved valid in terms of resistance and firmness on the build spots. However, both the 3DP<sub>12</sub>BP(Mk I) and 3DP<sub>12</sub>BP(Mk II) suffered from intrinsic limitations typical of acrylates used in photopolymer resins. Indeed, SLA 3D printed parts are highly subjected to bending and shrinking phenomena whose extent increase over time and light exposure (Feng *et al.*, 2017; Jiang, Lou and Hu, 2019; Invernizzi *et al.*, 2020). This became clearly visible in the 3D printed BPs within one month from fabrication (figure 2.16) and it was found to be a major source of lack of uniformity in 3D printed tablet batches, thus highlighting the need for a BP made from a material with suitable mechanical

properties. Indeed, even a minimal change in the BP geometry could eventually result in a print with poor dimensional accuracy.

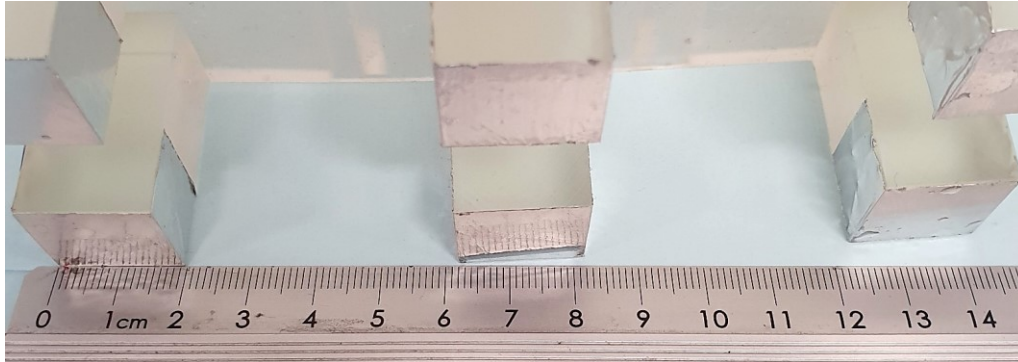


**Figure 2.16.** Bending of the 3DP <sub>12</sub>BP (Mk I) leading to misalignment of the BP in the SLA apparatus. Image reproduced from (Curti, Kirby and Russell, 2021).

To tackle such challenge, a final BP made of aluminium and so denominated Alu <sub>12</sub>BP was designed and fabricated through CNC milling (figure 2.17).

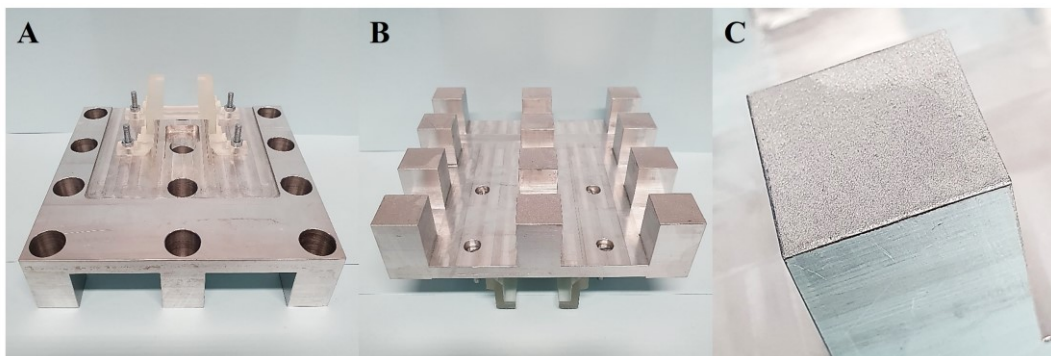


**Figure 2.17.** (A) Top and (B) bottom views of the Alu <sub>12</sub>BP fabricated through CNC milling. The novel design includes hollow build-spots, thus reducing the weight of the platform. (C) Detail of the bead-blasted surface of the Alu <sub>12</sub>BP. Such finish was selected to optimise the adhesion of objects during 3D printing and to facilitate their release after completion. Image reproduced from (Curti, Kirby and Russell, 2021).

Aluminium was selected due to its similarity to the original component and its density of  $2.70 \text{ g/cm}^3$ . The final weight of the fully assembled Alu<sub>12</sub>BP was 625.15 g, resulting in a 1.58% decrease in weight compared to the original BP. Such weight was estimated before manufacturing based on the CAD model volume and maintained by drilling holes in the aluminium block (visible in figure 2.17A) to obtain a finished product whose weight could not damage the moving parts of the SLA apparatus. After fabrication, the Alu<sub>12</sub>BP was fixed to the SLA apparatus using a 3D printed joint, designed to be easily replaceable in case of damage (figure 2.18).

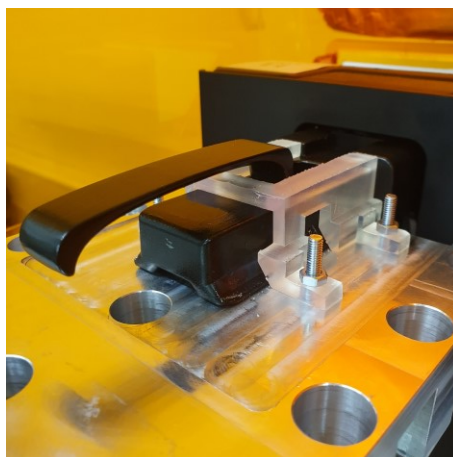


**Figure 2.18.** Detailed view of the 3D printed fixture used to firmly hold the Alu<sub>12</sub>BP to the SLA apparatus.

Having developed and optimised a novel resin tank and BP, a commercial stereolithography apparatus was converted into a more efficient piece of equipment able to operate using multiple photopolymer formulations at a single time with a fraction of the material originally required (figure 2.19). Such improved SLA apparatus was designed with the intention to conduct a high-throughput printability screening of photopolymer formulations aimed to identify suitable candidates to produce solid oral dosage forms.

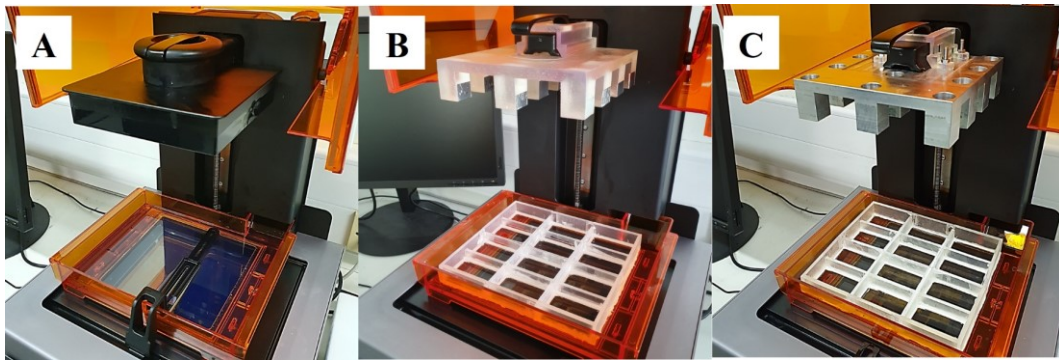


**Figure 2.19.** Stereolithography apparatus evolution: comparison of (A) the original Form 2 SLA apparatus, (B) the modified apparatus equipped with the 3DP <sub>12</sub>BP (Mk II) and the 12-vats resin tank, and (C) the final version equipped with the Alu <sub>12</sub>BP. Image readapted from (Curti, Kirby and Russell, 2021).

#### 2.4.6 Novel stereolithography apparatus validation

Having modified key structural components of the Form 2 SLA 3D printer, it was necessary to prove both reliability and consistency of the modified SLA apparatus. An investigation of 3DP accuracy and precision using the different equipment available was carried out by printing cylindrical test tablet models using a commercially available resin photopolymer (figures 2.20-2.21).

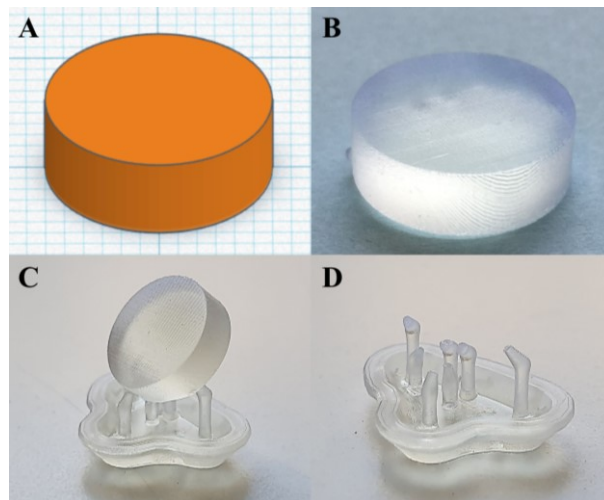


**Figure 2.20.** (A) CAD model of a cylindrical test tablet (12 mm × 4 mm). Test tablet were 3D printed either (B) directly on the BP or (C) using supports. (D) Printing support after

manual removal of a 3D printed test tablet. Image reproduced from (Curti, Kirby and Russell, 2021).

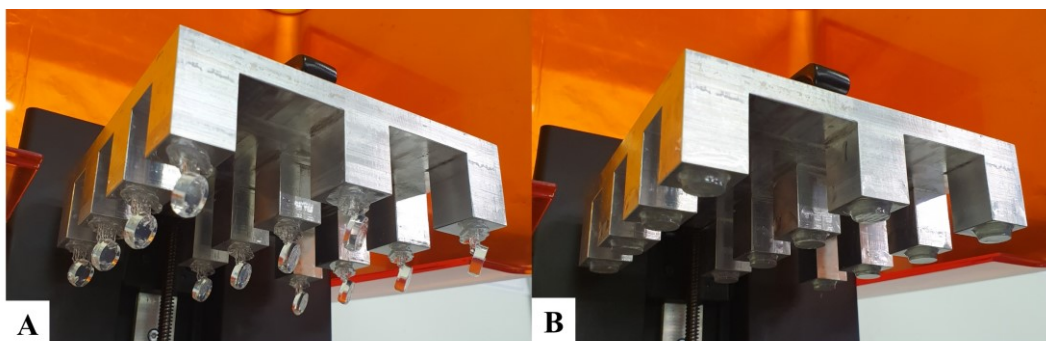


**Figure 2.21.** Test tablets 3D printed on the Alu<sub>12</sub>BP (A) using supports and (B) directly on the BP. Test tablets were 3D printed using Clear resin photopolymer.

Modified equipment validation was performed by fabricating 3 batches of 12 tablets each using the original BP, the 3DP<sub>12</sub>BP (Mk I) and (Mk II), and the Alu<sub>12</sub>BP. For each batch, test tablets were 3D printed both using printing supports and directly on the BP, in order to evaluate printing supports' impact on tablet uniformity. Results related to uniformity of weight, thickness, and diameter are shown in figures 2.22-2.24.

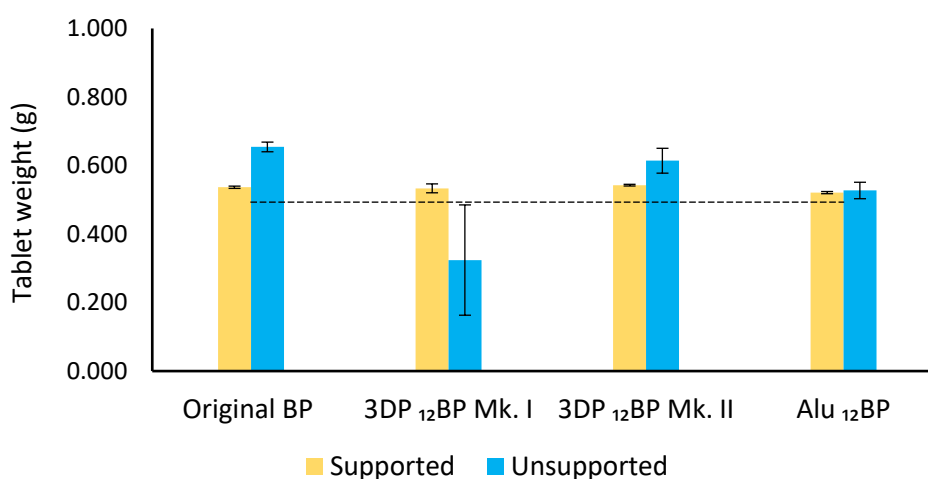


**Figure 2.22.** Tablet weight uniformity assessment. Yellow and blue bars represent data of tablets 3D printed with and without supports, respectively. Black dashed line indicates the theoretical weight of an individual tablet (0.493 g). Results are reported as mean (n = 30).

Error bars indicate standard deviation of the measurements. Image readapted from (Curti, Kirby and Russell, 2021).

Considering a theoretical tablet weight of 0.493 g, estimated from tablet volume and resin density, the tablet weight percent relative error ( $\%E_r$ ) calculated for the original BP, the 3DP<sub>12</sub>BP (Mk I), the 3DP<sub>12</sub>BP (Mk II), and the Alu<sub>12</sub>BP was 32.67%, -34.29%, 24.50% and 6.90%, respectively, for tablets printed directly on the BP (figure 2.22). The introduction of printing supports resulted instead in the fabrication of more accurate batches, as shown by a decrease of tablet weight  $\%E_r$  to 8.81%, 8.17%, 10.05%, and 5.64% in relation to the use of the original BP, the 3DP<sub>12</sub>BP (Mk I), the 3DP<sub>12</sub>BP (Mk II), and the Alu<sub>12</sub>BP, respectively (figure 2.22).

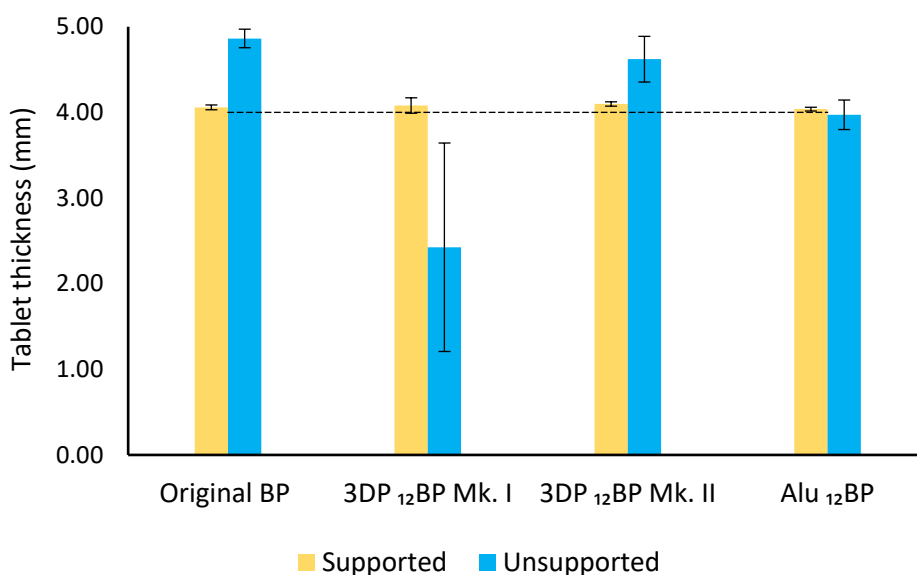


**Figure 2.23.** Tablet thickness uniformity assessment. Yellow and blue bars represent data of tablets 3D printed with and without supports, respectively. Black dashed line indicates the theoretical tablet thickness (4.00 mm). Results are reported as mean ( $n = 30$ ). Error bars indicate standard deviation of the measurements. Image readapted from (Curti, Kirby and Russell, 2021).

Similarly, thickness values of tablets 3D printed directly on the BP showed lack of accuracy depending on the BP used, with tablet thickness  $\%E_r$  of 21.57%, -39.38%, and 15.52% in relation to the use of the original BP, the 3DP<sub>12</sub>BP (Mk I), and the 3DP<sub>12</sub>BP (Mk II), respectively. However, tablet thickness  $\%E_r$  recorded when the Alu<sub>12</sub>BP was used was -0.71%, proving its reliability in comparison of both the original BP, the 3DP<sub>12</sub>BP (Mk I) and (Mk II) (figure 2.23).

As per tablet weight, introducing printing supports determined a general decrease of tablet thickness  $\%E_r$  to 1.46%, 2.00%, 2.44%, and 0.94%, in relation to the use of the original BP, the 3DP<sub>12</sub>BP (Mk I), the 3DP<sub>12</sub>BP (Mk II), and the Alu<sub>12</sub>BP, respectively (figure 2.23).

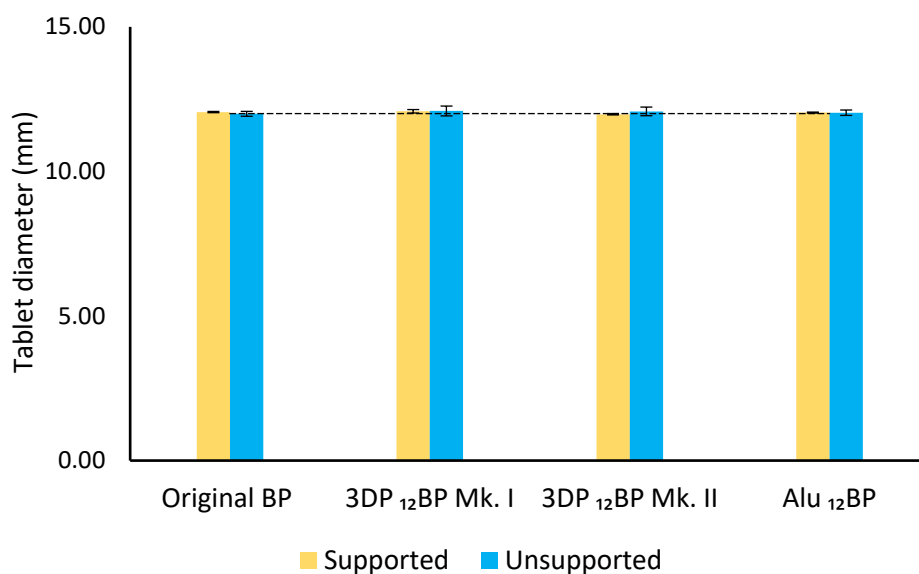


**Figure 2.24.** Tablet diameter uniformity assessment. Yellow and blue bars represent data of tablets 3D printed with and without supports, respectively. Black dashed line indicates the theoretical tablet diameter (12.00 mm). Results are reported as mean (n = 30). Error bars indicate standard deviation of the measurements. Image readapted from (Curti, Kirby and Russell, 2021).

The evaluation of tablet diameter uniformity allowed the observation of more homogeneous results, regardless of the BP used. Indeed, 3D printing tablets directly on the BP led to tablet diameter  $\%E_r$  of -0.07%, 0.75%, 0.63%, and 0.26% in relation to the use

of the original BP, the 3DP<sub>12</sub>BP (Mk I), the 3DP<sub>12</sub>BP (Mk II), and the Alu<sub>12</sub>BP, respectively (figure 2.24). When printing supports were introduced, tablet diameter %E<sub>r</sub> was 0.44%, 0.67, -0.19%, and 0.29%, in relation to the use of the original BP, the 3DP<sub>12</sub>BP (Mk I), the 3DP<sub>12</sub>BP (Mk II), and the Alu<sub>12</sub>BP, respectively (figure 2.24).

The relative standard deviation (RSD) related to the measurements of tablet weight, thickness, and diameter was also determined, and is reported in tables 2.1-2.2.

**Table 2.1.** RSD of tablet weight, thickness, and diameter for tablets 3D printed using supports.

<b>Build Platform type</b>	<b>Weight RSD (%)</b>	<b>Thickness RSD (%)</b>	<b>Diameter RSD (%)</b>
Original BP	0.613	0.691	0.176
3DP <sub>12</sub> BP (Mk I)	2.437	2.206	0.497
3DP <sub>12</sub> BP (Mk II)	0.457	0.617	0.198
Alu <sub>12</sub> BP	0.610	0.543	0.146

**Table 2.2.** RSD of tablet weight, thickness, and diameter for tablets 3D printed without using supports.

<b>Build Platform type</b>	<b>Weight RSD (%)</b>	<b>Thickness RSD (%)</b>	<b>Diameter RSD (%)</b>
Original BP	2.154	2.224	0.703
3DP <sub>12</sub> BP (Mk I)	49.691	50.186	1.406
3DP <sub>12</sub> BP (Mk II)	5.911	5.772	1.234
Alu <sub>12</sub> BP	4.557	4.336	0.777

A MANOVA coupled with a Tukey post-hoc test performed to evaluate the effect of the build platform used evidenced a statistically significant difference ( $p < 0.05$ ) in tablet weight, thickness, and diameter when the 3DP<sub>12</sub>BP (Mk II) was compared to the original

BP and tablets were printed directly on the BP. Comparing weight and thickness uniformity results of unsupported tablets fabricated with the Alu<sub>12</sub>BP and the original BP also resulted in a statistically significant difference ( $p < 0.05$ ), while no difference ( $p > 0.05$ ) was observed for tablet diameter.

The results firstly suggest that tablet thickness is the most susceptible factor to inhomogeneity; since it is generally observed that tablet thickness is higher than the expected value, it is likely that this also led to a gain in weight and therefore inhomogeneity in tablet weight uniformity. High differences were related to the use of the 3DP<sub>12</sub>BP (Mk II). It can be hypothesised that, as previously discussed, the loss of structural integrity due to bending phenomena observed in the 3DP<sub>12</sub>BP (Mk II) over time (figure 2.16) has determined variability in the results. As aluminium doesn't share such a limitation, this would explain the significant improvements in tablet uniformity when the Alu<sub>12</sub>BP was used.

Furthermore, it was demonstrated that the use of printing supports substantially improved tablet uniformity when using the original BP and the 3DP<sub>12</sub>BP (Mk II). In comparison with the original BP, no statistically significant difference ( $p > 0.05$ ) in weight and thickness uniformity was observed for tablets fabricated on the 3DP<sub>12</sub>BP (Mk II). Supported tablets printed on the Alu<sub>12</sub>BP also showed no significant difference in terms of uniformity of thickness and diameter when compared to tablets produced on the original BP. Such improvements are compatible with the general recommendation to use printing supports for fabricating objects with minimum risk of size inaccuracies (Jiang, Lou and Hu, 2019).

#### ***2.4.7 Assessment of printing supports related waste generation***

Having demonstrated that using printing supports affects tablet uniformity, it was important to assess their impact on waste generation. In fact, despite the better results in terms of uniformity and printability, it should be carefully considered that printing supports require extra material to be fabricated and are therefore a primary source of waste (table 2.3).

**Table 2.3.** Material waste associated to the use of printing supports, expressed as the % ratio between  $W_{ps}$  and  $W_t$ .

$W_t$	$W_{ps}$	Material waste
30.250 g	14.623 g	48.340 %

The results shown in table 2.3 indicate that 3DP tablets with supports can result in the waste of almost 50 % of the material used. Such a high figure is an indication of poor cost effectiveness and unsustainability, as the recycling of commonly used photopolymers is unfeasible. Indeed, the thermoset nature of SLA 3D printed materials makes them infusible and insoluble, therefore their recycle is complex and they are generally disposed by incineration or destined to landfills (Voet, Guit and Loos, 2021). Moreover, additional attention should be paid to the ethical and environmental concerns of disposing drug loaded material that could have been avoided in the first place.

In light of these considerations, the work described in Chapters III and IV of this Thesis was solely carried out on tablets produced without the use of printing supports.

#### ***2.4.8 Material recovery efficacy assessment***

A final assessment on potential areas of wastage intrinsic of SLA 3DP aimed to determinate the extent of photopolymer resin recovery over time following the completion of a print. In fact, once a 3D printing cycle is finished, the BP is automatically lifted and it is later removed by an operator to collect the fabricated dosage forms, while any uncured resin remaining on the platform is removed and disposed of. Attempts to manually recover resin adhered to the BP using metal tools could result in accidentally recovering partially cured resin debris, or in scratching the aluminium surface with risk to contaminate the feedstock material. Although manual removal determines most of the final resin loss, the amount of

material wasted, and its related cost, have not been defined before. As a variable amount of recoverable resin drops from the BP into the resin tank as soon as a print is finished, it was hypothesised that the time the platform was left in the 3D printer before being removed was a critical parameter to estimate the final material wastage. In fact, the longer the BP remains connected to the SLA apparatus, the more photopolymer resin is recovered and saved. Therefore, the impact of the time the BP is left in the 3D printer after a print is completed on the amount of resin eventually wasted was investigated (Figure 2.25). Both the original SLA apparatus and its modified version were compared to assess potential differences in their capacity to generate time-dependent resin waste. Cost implications of such waste generation were also assessed.

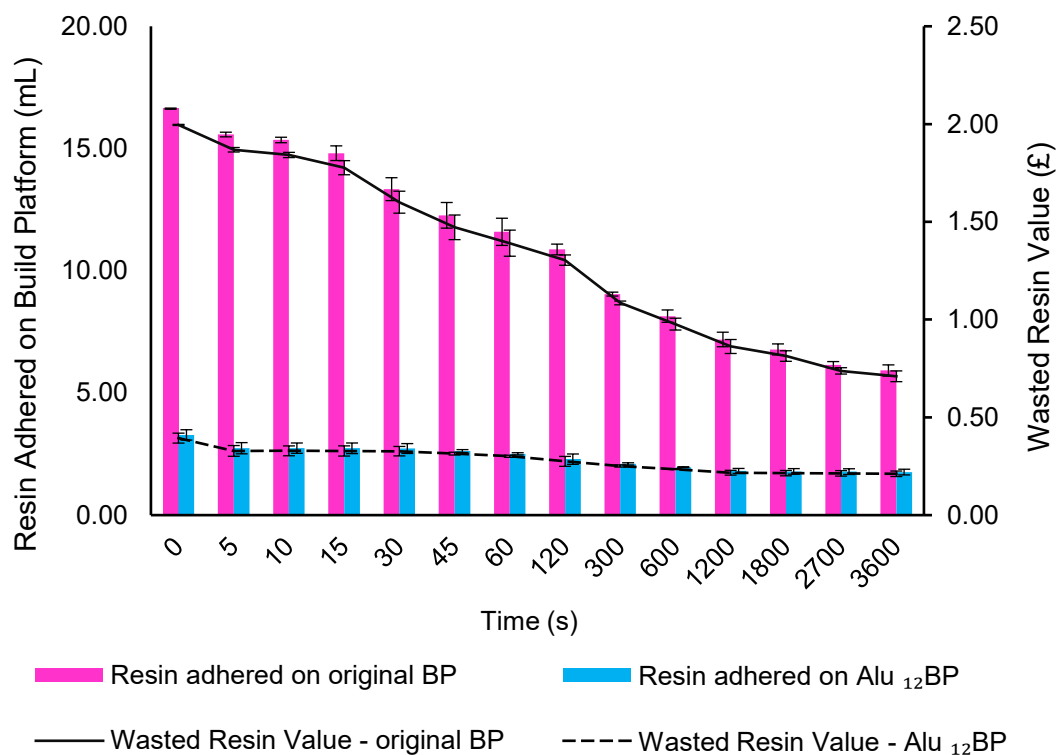


**Figure 2.25.** Comparison of photopolymer resin waste generated by adherence onto the original BP and the Alu<sub>12</sub>BP over a period of 1 hour. Straight and dashed curves indicate the economic loss using the original and the modified SLA apparatus, respectively. Error bars indicate standard deviation of the measurement (n = 3). Image readapted from (Curti, Kirby and Russell, 2021).

Measurements were taken at 14 time points covering a period of 1 h. At  $t = 0$  s, 16.63 mL of resin adhered to the original BP, while only 3.28 mL were recorded on the Alu<sub>12</sub>BP. At  $t = 3600$  s, the amount of adhered material was quantified as 5.92 and 1.76 mL for the original BP and the Alu<sub>12</sub>BP, respectively. According to the results, it can be seen that if the BP is left in the SLA apparatus at the end of a print for an increasing amount of time, a clear effect on reducing resin waste is observed. Furthermore, the Alu<sub>12</sub>BP used in the novel SLA apparatus has proven to reduce the amount of adhering resin by 70.27%, in comparison to the original BP; avoiding such waste would allow for the saving of enough material to produce an additional 11 and 3 tablets (based on a 0.5 mL tablet volume) using the original and the modified SLA apparatus, respectively. From a cost point of view, the effect of time on material saving, as well as differences between the use of the original and the modified SLA apparatus, are evident (figure 2.25). The economic loss due to the resin adhering on the BPs just returned in position after a print ( $t = 0$  s) was quantified as GBP 2.00 for the original SLA apparatus versus GBP 0.39 for the modified version. By leaving the BP above the tank until the end of the experiment ( $t = 3600$  s), wasted resin value decreased to GBP 0.71 and GBP 0.21 for the original and the modified BPs, respectively. It should be noted that the suggested model was based on the use of a commercial photopolymer resin not intended for pharmaceuticals applications. The lack of commercially available resins designed for pharmaceutical manufacturing necessitates the on-site production of photopolymer formulations consisting of polymers, photoinitiators, active pharmaceutical ingredients and other excipients, which eventually increase the final cost per mL. Ultimately, these findings aim to suggest a potential solution to minimise photopolymer resin wastage by avoiding the immediate removal of the BP after the completion of dosage forms of 3D printing. This would, in fact, allow a certain amount of resin to be time-dependently recovered and reused, with no need of operator intervention. While the effect of time and the type of BP used have been evaluated, other factors, such as photopolymer resins' viscosity and surface tension, should also be investigated, in order to establish a solid model to universally predict material wastage and identify the amount of time providing the highest recovery. In fact, it is likely that the production of

personalised dosage forms in clinical settings, such as hospital pharmacies, will have higher costs than the mass production of drugs at an industrial level, and it is, therefore, necessary to maximise process cost-effectiveness (Rautamo *et al.*, 2020).

## 2.5 Conclusion

Although a few studies on SLA 3D printing of solid oral dosage forms have been published in recent years, data on geometry-related printability limitations are lacking. Also, the lack of a pharmaceutical grade SLA 3D printer makes challenging both formulation development and the fabrication of reliable dosage forms' batches.

In this chapter, we have shown that a variety of tablet geometries can be successfully fabricated using a desktop SLA 3D printer, although printability issues may occur when dosage forms are printed with a flat orientation. As such, we have found that 3D printing dosage forms with an angle of 45° with respect to the build platform allows to achieve the best printability outcomes.

Moreover, with the view to conduct extensive formulation development work, we have repurposed a desktop SLA apparatus into a novel piece of equipment, specifically designed for pharmaceutical application. This was achieved by developing and optimising novel components for the SLA 3D printer, which allowed to introduce the concept of using different photopolymer resins simultaneously (Curti, Kirby and Russell, 2021). More precisely, the novel SLA apparatus that was developed allowed to operate with up to twelve different photopolymer resins within the same printing cycle, while sample amount required for 3D printing was reduced from 200 mL to 10 mL, thus enabling high cost-effectiveness and a more sustainable process. Moreover, the investigation of waste generation caused by the use of printing supports concluded that the manufacturing of supported 3D printed tablets would result in about 50% of the photopolymer material being wasted.

Ultimately, the remarkable features of the novel SLA apparatus made it the ideal tool to carry out a high-throughput screening of photopolymer formulations, as described in Chapter III of this Thesis.

## **- Chapter III -**

PRINTABILITY SCREENING OF PHOTOPOLYMER RESIN  
FORMULATIONS FOR STEREOLITHOGRAPHY 3D PRINTING OF SOLID  
ORAL DOSAGE FORMS

---

### **Publications arising from the work in this chapter:**

Curti, C., Kirby, D.J. & Russell, C.A., 2021. Stereolithography Apparatus Evolution: Enhancing Throughput and Efficiency of Pharmaceutical Formulation Development. *Pharmaceutics*, 13(5), p.616.

### 3.1 Introduction

The working principle of stereolithography (SLA) three-dimensional printing (3DP) is based on photopolymerisation, a process in which a liquid prepolymer is turned into a solidified part, more specifically into a thermoset (Horie *et al.*, 2004; Voet, Guit and Loos, 2021). The prepolymer is generally a blend of reactive monomers and oligomers, mixed with a photoinitiator (PI) system to make up the resin feedstock material; other additives, such as light absorbing pigments or dyes, can be added for specialty applications (Jacobs, 1996; Ligon *et al.*, 2017).

The term photopolymerisation is based on the Greek word φῶς (phos), meaning ‘light’, because the reaction requires a certain light radiation to take place. Specifically, the interaction of light with the PI molecules dissolved in the liquid resin generates the free radicals needed to initiate polymerisation (Bagheri and Jin, 2019) as schematically shown in figure 3.1.

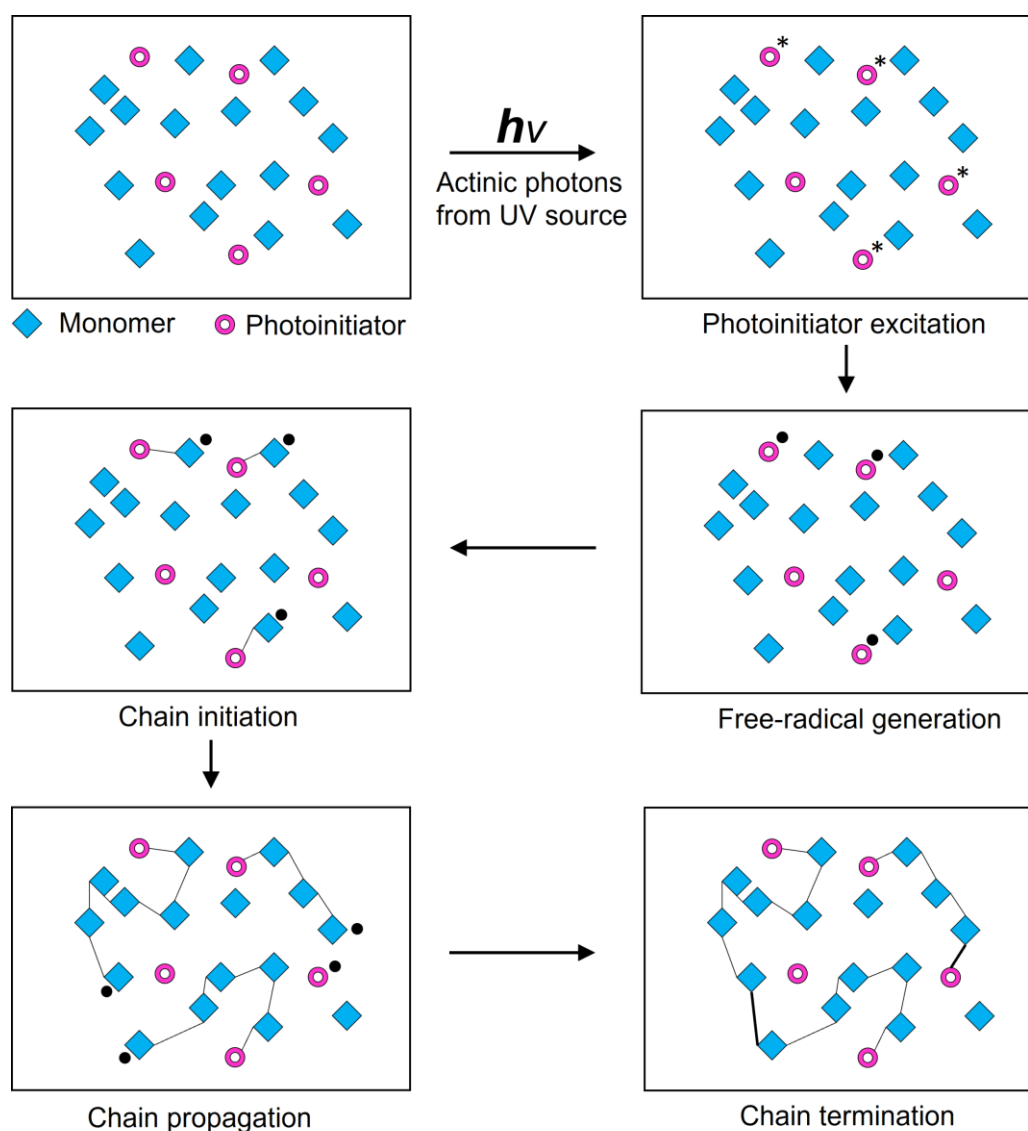


**Figure 3.1.** Example of a simplified free-radical photopolymerisation sequence. PI molecules, mixed with the reactive monomers, are exposed to a ultraviolet (UV) source of actinic photons ( $h\nu$ ). PIs absorb photons and yield an excited PI species (PI\*). Then, a fraction of PI\* is converted into free radicals (PI•) able to react with a monomer molecule (chain initiation step). The addition of other monomers allows the chain to grow (chain propagation step), until the reaction between two radical species terminates the polymerisation process (chain termination step). Figure readapted from Jacobs, 1996.

Free radical PIs are classified as Norrish type I and type II depending on the mechanism by which they generate free radicals (Ligon *et al.*, 2017). Norrish type I PIs are subjected to a photocleavage reaction generating radical fragments when exposed to light in a specific wavelength (Yao *et al.*, 2021). Norrish type II PIs are instead bi-component systems

involving a light absorbing molecule (sensitiser) and a co-initiator (synergist), reacting together upon light irradiation to generate free radicals (Ligon *et al.*, 2017).

While several free radical PIs are available for industrial applications, the recent development of SLA 3DP in the pharmaceutical field is opening the way to the introduction of novel PIs, whose primary requirements is safety for oral administration (Wang *et al.*, 2016; Martinez *et al.*, 2017). As a result, the first objective to accomplish in this Chapter was to identify free radical PIs with toxicity profiles compatible with the intended purpose, and to verify their effectiveness for SLA 3DP using a 405 nm laser.

Testing PIs efficacy required the implementation of a classification system for printability assessment. Kadry (2019) suggested a basic classification method to differentiate printability outcomes of photopolymerised tablets based on mechanical resistance and geometrical accuracy. However, a standard printability classification system is lacking, and it was of particular importance to develop one.

With at least one active PI system available, it was possible to design a large set of photopolymer formulations. Indeed, the narrow choice of photopolymers available limits the pharmaceutical application of SLA (Martinez *et al.*, 2018c; Krkobabić *et al.*, 2019; Robles Martinez *et al.*, 2019; Madžarević and Ibrić, 2021) and, as a result, lays the foundations for extensive formulation development work. Therefore, this Chapter describes the design, preparation, and screening of 156 photopolymer formulations whose printability outcomes were evaluated with the view to develop a pool of multi-purpose, drug-loadable resins that can be flexibly used to deliver safe, effective, and personalised dosage forms.

### 3.2 Chapter aim and objectives

-To conduct a high throughput printability screening aimed to identify candidate formulations for SLA 3DP of drug loaded solid oral dosage forms. The need for such a systematic screening arises from the lack of photopolymer materials commercially available for pharmaceutical SLA 3D printing, which represents a major limitation for the implementation of such technology in the pharmaceutical field; as a result, it is necessary for formulation scientists to prepare custom blends comprising monomers, oligomers, photoinitiators, and active pharmaceutical ingredients. However, the printability of such photopolymer formulations can be challenging and must be optimised through a rigorous screening and evaluation process.

Therefore, this Chapter describes the pipeline used to develop photopolymer resin formulations with a good safety profile suitable for SLA 3D printing of solid oral dosage forms.

To achieve the abovementioned aim, the work presented in this chapter was essentially carried out in three different phases characterised by the following objectives:

- Selection and preliminary printability evaluation of effective PI systems. The rationale for PIs selection at this stage was based on their safety profile, with the view to formulate printable photopolymer resins using the lowest effective PI concentration.
- Selection of photopolymers and liquid fillers to use in the design of several photopolymer resin formulations.
- Implementation of a novel classification system for printability assessment, designed to qualitatively evaluate the printability outcomes of SLA 3D printed dosage forms.
- Systematic printability screening, evaluation of formulation and process factors on printability, and identification of lead photopolymer formulations.

### **3.3 Materials and Methods**

#### ***3.3.1 Materials***

Polyethylene glycol diacrylate with molecular number ( $M_n$ ) 250, 575, and 700, N-vinylpyrrolidone, polyethylene glycol 300, propylene glycol, glycerol and the photoinitiators diphenyl (2,4,6-trimethylbenzoyl) phosphine oxide, 2-hydroxy-2-methylpropiophenone, 2-hydroxy-4-(2-hydroxy ethoxy)-2-methyl propiophenone, riboflavin, and triethanolamine were purchased from Sigma-Aldrich, UK. Acetophenone and camphorquinone were purchased from Alfa Aesar, UK.

#### ***3.3.2 Methods***

##### ***3.3.2.1 Photoinitiators selection***

The inclusion criteria to select a pool of PIs to screen were based on the respective safety profiling (according to the data available in the literature and information reported on the safety data sheet), and previously described use in solid oral dosage forms and other biocompatible applications reported in the scientific literature.

##### ***3.3.2.2 UV-visible spectrophotometry***

The wavelength of maximum absorption ( $\lambda_{max}$ ) of each PI was determined through UV-Vis spectrophotometry carried on a Genesys 10S UV/Vis Spectrophotometer (Thermo Fisher Scientific, USA) using a 50% v/v water/methanol solution as solvent. Prior to analysis, a baseline was acquired by running a blank sample. PI samples were scanned within a range of 190 to 500 nm with an interval of 1 nm.

### ***3.3.2.3 Formulation of photopolymer resins***

All photopolymer resin formulations described in this Chapter were prepared following the same procedure. Firstly, polyethylene glycol diacrylate (PEGDA) was directly weighed in 30 mL glass vials. Solid PIs were weighed separately and later transferred to the photopolymer base, while liquid PIs were accurately withdrawn and directly transferred to the PEGDA vials. Then, any other liquid component was added to the PEGDA vials, and the mixtures were stirred for 12 hours at room temperature until complete solubilisation of the PI. All operations were carried out away from light by working in dark environment and covering the glass vials with aluminum foil, in order to avoid premature photopolymerisation. Once ready, photopolymer formulations were transferred for 3D printing to the 12-vats resin tank described in Chapter II.

### ***3.3.2.4 Stereolithography 3D printing***

PIs efficacy and printability of photopolymer resin formulations were evaluated by 3DP test tablets using a Form 2 SLA 3D printer modified to have high throughput capability, described in Chapter II. Tablet CAD models used in this Chapter were based on cylindrical tablet designs shown in Chapter II ( $12 \times 4$  mm, diameter  $\times$  thickness), and were 3D printed directly on the build platform (BP), thus avoiding the use of printing supports. Formulations related to PIs efficacy screening were 3D printed setting layer thickness to 100  $\mu\text{m}$ , while the subsequent printability screening of photopolymer resins was carried out setting layer thickness to 25  $\mu\text{m}$ , 50  $\mu\text{m}$ , and 100  $\mu\text{m}$ . All formulations were 3D printed in triplicates. At the completion of the 3D printing process, tablet samples were removed from the BP and the uncured resin was blotted using paper.

### ***3.3.2.5 Printability evaluation***

To evaluate printability outcomes, a points-based scale was designed and developed (figure 3.2). A printability score (PS) from 1 to 6 was assigned to each formulation based on the

visual observation after a print was completed. An extra mark, indicated as \*, was assigned to tablets showing defined edges indicating geometrical accuracy of the 3D printed design.

Observation	Formulation remains liquid	Gel-like texture	Polymerised fragments	Incomplete or fallen object	Accurately printed object	Broadening	Defined edges
Printability Score	1	2	3	4	5	6	*
Comments	No polymerisation	Insufficient crosslinking	Partial crosslinking	Failed Print	Successful Print	Uncontrolled polymerisation	Geometrical accuracy

**Figure 3.2.** Points-based printability scale developed to evaluate printability outcomes based on visual observation of the 3D printed tablet samples.

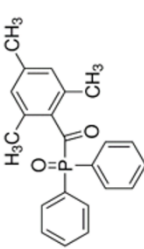
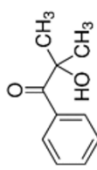
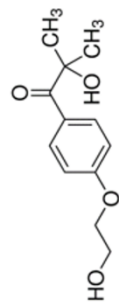
Photopolymer formulations remaining entirely liquid in the resin tank after 3DP were assigned a PS = 1, indicating that no photopolymerisation occurred. Formulations changing to a soft gel-like consistency were given a PS = 2, suggesting that photocrosslinking was too low to form solid structures, while a PS = 3 was used to classify formulations reaching partial crosslinking, as shown by the presence of polymerised debris in the resin tank at the end of the print run. A PS = 4 was used to identify a failed print, in form of a partially or inaccurately 3D printed object, or resulting from the detachment from the BP. A PS = 5 represented the experiment target, indicating a fully 3D printed object, accurately matching the 3D model designed. Photopolymer formulations showing uncontrolled and extensive polymerisation during 3DP, a multiple causes phenomenon significantly compromising the geometrical accuracy of the design, were given a PS = 6.

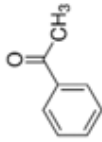
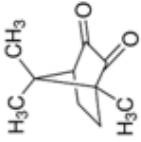
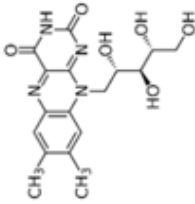
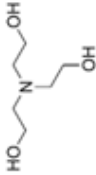
## 3.4 Results and Discussion

### 3.4.1 Photoinitiator selection

The PIs shortlisted to be used for a preliminary screening to evaluate their efficacy in SLA 3DP using a 405 nm laser, are reported in table 3.1. Abbreviations used to simplify the reference to PIs in the following paragraphs are also shown in table 3.1.

**Table 3.1.** List of PI systems selected for a preliminary printability screening. Triethanolamine was used as a synergist with both camphorquinone and riboflavin (Norrish type II PIs).

Photoinitiator	Abbreviation	Norrish Type Photoinitiator	Acute toxicity LD50 Oral (rat)	Health risks	Published examples of application
Diphenyl (2,4,6-trimethylbenzoyl) phosphine oxide 	PIa	Type I	>5000 mg/kg (SIGMA-ALDRICH, 2018d)	Infertility, damages to the fetus	(Wang <i>et al.</i> , 2016), (Voet <i>et al.</i> , 2018)
2-Hydroxy-2-methylpropiophenone 	PIb	Type I	1694 mg/kg (SIGMA-ALDRICH, 2018a)	Harmful if swallowed	(Kochhar <i>et al.</i> , 2012)
2-Hydroxy-4-(2-hydroxyethoxy)-2-methylpropiophenone 	PIc	Type I	4082 mg/kg (SIGMA-ALDRICH, 2018b)	*	(Williams <i>et al.</i> , 2005)

Acetophenone		PI <sub>d</sub>	Type I	815 mg/kg (AlfaAesar, 2015)	Harmful if swallowed, eye irritation	(Robles Martinez, Basit and Gaisford, 2018)
Camphorquinone		PI <sub>e</sub>	Type II	*	*	(Fouassier, Allonas and Burget, 2003)
Riboflavin		PI <sub>f</sub>	Type II	>10000 mg/kg (SIGMA-ALDRICH, 2018c)	*	(Bertolotti <i>et al.</i> , 1999), (Martinez <i>et al.</i> , 2017)
Triethanolamine		TEOA	Type II (synergist)	7390 mg/kg (SIGMA-ALDRICH, 2015)	Allergic reactions	(Bertolotti <i>et al.</i> , 1999), (Martinez <i>et al.</i> , 2017)

\*Not a hazardous substance or mixture according to Regulation (EC) No 1272/2008.

Spectrophotometric analysis was carried out on each PI to measure the respective  $\lambda$  max, with the view to obtain predictive information on which PI would be compatible with an SLA apparatus equipped with a 405 nm laser. Measured  $\lambda$  max values of each PI are reported in table 3.2.

**Table 3.2.** Measured  $\lambda$  max values of the photoinitiators selected for efficacy screening.

<b>Photoinitiator</b>	<b><math>\lambda</math> max</b>
Diphenyl-(2,4,6-trimethyl benzoyl)-phosphine oxide	380.5 nm
2-Hydroxy-2-methyl propiophenone	243.5 nm
2-Hydroxy-4-(2-hydroxyethoxy)-2-methylpropiophenone	273.5 nm
Acetophenone	239.5 nm
Camphorquinone	468.0 nm
Riboflavin	463.0 nm

Of the 6 PIs analysed, diphenyl-(2,4,6-trimethyl benzoyl)-phosphine oxide (PIa) showed maximum absorption at 380.5 nm, making it the PI most closely matching the target wavelength of 405 nm emitted by the Form 2 3D printer laser. Therefore, PIa was found to be the most promising candidate for SLA 3DP, and its efficacy was tested through subsequent formulation development phases described in this Chapter.

#### ***3.4.2 Design of photopolymer formulations for photoinitiator screening***

To investigate the efficacy of selected PIs in SLA 3DP, 12 photopolymer formulations were prepared. The exact % w/w composition of the 12 formulations is given in table 3.3. PEGDA 700 was used as photopolymer base for all formulations, due to its widely reported use in SLA 3DP of solid oral dosage forms (Wang *et al.*, 2016; Martinez *et al.*, 2018; Robles Martinez *et al.*, 2019). Each PI was used at a concentration of 1% w/w and 0.1% w/w; 3% w/w triethanolamine (TEOA) was used as synergist in combination with

riboflavin and camphorquinone, both Norrish type II PIs. PIs concentrations were selected according to previous evidence of SLA 3D printed solid oral dosage forms available in the scientific literature (Wang *et al.*, 2016; Martinez *et al.*, 2017). Furthermore, while the first aim of such screening remained to identify effective PIs, a second goal was to verify the efficacy of reduced PI amounts required for a successful 3D print.

**Table 3.3.** % w/w composition of 12 photopolymer resin formulations designed to evaluate the efficacy of 6 photoinitiator systems (PIa - PI<sub>f</sub>).

Formulation	PEGDA 700	PIa	PIb	PIc	PI <sub>d</sub>	PI <sub>e</sub>	PI <sub>f</sub>
PIsF1	99.9	0.1	-	-	-	-	-
PIsF2	99.9	-	0.1	-	-	-	-
PIsF3	99.9	-	-	0.1	-	-	-
PIsF4	99.9	-	-	-	0.1	-	-
PIsF5	99.9	-	-	-	-	0.1	-
PIsF6	99.9	-	-	-	-	-	0.1
PIsF7	99.0	1.0	-	-	-	-	-
PIsF8	99.0	-	1.0	-	-	-	-
PIsF9	99.0	-	-	1.0	-	-	-
PIsF10	99.0	-	-	-	1.0	-	-
PIsF11	99.0	-	-	-	-	1.0	-
PIsF12	99.0	-	-	-	-	-	1.0

### 3.4.3 Photoinitiator suitability for stereolithography 3D printing

PI efficacy was evaluated by assigning to the 12 formulations previously described a printability score based on the printability scale shown in figure 3.2. Printability outcomes of the 12 formulations tested are summarised in table 3.4.

**Table 3.4.** Printability score (PS) assigned to photopolymer formulations used for photoinitiator screening.

Formulation	PS	Formulation	PS
PIsF1	5*	PIsF7	6
PIsF2	1	PIsF8	1
PIsF3	1	PIsF9	1
PIsF4	1	PIsF10	1
PIsF5	3	PIsF11	4
PIsF6	1	PIsF12	3

0.1% w/w PIa (formulation PIsF1) was assigned a PS = 5\* indicating its efficacy to 3D print accurately shaped tablets (figure 3.3A). However, increasing its concentration to 1% w/w (formulation PIsF7) caused high broadening (PS = 6), resulting in a 3D printed tablet whose bottom side had undergone uncontrolled polymerisation (figure 3.3B). Interestingly, the use of 1% w/w PIa was already reported in the fabrication of SLA 3D printed dosage forms, with no reports of broadening (Wang *et al.*, 2016). Factors including high extinction coefficients at the irradiation wavelength (resulting in  $n-\pi^*$  excitation), high dissociation quantum yields, and excellent reactivity of the primary radicals towards the monomer, suggest that the reactivity of PIa is particularly high (Eibel, Fast and Gescheidt, 2018), and an increase of its concentration will result in high radical generation and polymerisation rate (Meereis *et al.*, 2014), potentially leading to the loss of geometrical control during photopolymerisation. A further explanation could be attributed to the scattering of the light emitted by the laser beam. In fact, when the incident light is scattered, more radiation is delivered to the sideways directions thus increasing the  $C_w$ , eventually resulting in a reduced printing accuracy (Zakeri, Vippola and Levänen, 2020).

Formulations containing PIb, PIc, and PId, in concentrations of both 0.1% and 1% w/w, were given a PS = 1 because no changes were observed in the photopolymer resin at the end of the print, indicating their inefficacy in initiating photopolymerisation at the used wavelength. Based on the spectrophotometric analysis previously carried out on the PIs, these results were expectable as their  $\lambda_{max}$  was found to be in a range of 239.5 nm to

273.5 nm, while the laser in the SLA apparatus emits light radiation with a wavelength of 405 nm.

Formulations containing PIe/TEOA at concentrations of 0.1% and 1% w/w were respectively assigned a PS of 3 and 4. Since a PS = 4 indicates a failed print featuring inaccurate or missing details of the 3D printed tablet (figure 3.3C), PIe will not be further investigated at this stage, although it could be considered for future studies due to its good biocompatibility (Kamoun *et al.*, 2016).

PIf/TEOA was not found to initiate polymerisation when used at 0.1% w/w (PS = 1), while its increase to 1% w/w allowed the formation of partially crosslinked structures (PS = 3) (figure 3.3D). Surprisingly, these results are in contrast with those found by Martinez (2017). However, it should be considered that in this work PIf was not solubilised in water to eventually formulate hydrogels (Martinez *et al.*, 2017), but rather it was mixed with pure PEGDA 700 where it was seen to be slightly soluble.

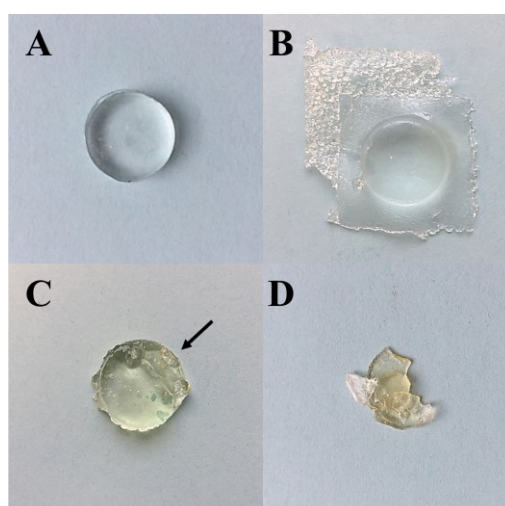


**Figure 3.3.** Test tablets 3D printed with (A) 0.1% w/w and (B) 1% w/w PIa. (B) Tablet on the top right shows extended and uncontrolled polymerisation resulting in poor geometrical accuracy. (C) Failed print of a test tablet made using 0.1% w/w PIe/TEOA: inaccuracies are visible on the tablet sides, while the arrow indicates a partially printed edge. (D) Polymerised fragments originated from formulation PIsF12, containing 1% w/w PIf/TEOA.

To summarise, 0.1% w/w PIa demonstrated to be effective in initiating photopolymerisation of PEGDA based photopolymer formulations, thus allowing for the successful fabrication through SLA 3D printing of non-drug loaded test tablets. As a result, PIa represented the photoinitiator selected to be furtherly investigated in this Thesis.

#### 3.4.4 Systematic printability screening of photopolymer formulations

##### 3.4.4.1 Materials selection and formulation design

Having identified PIa, hereinafter abbreviated as TPO, as an effective PI for SLA 3DP, the next step consisted in conducting a systematic printability screening of photopolymer formulations to identify the best candidates for subsequent drug loading studies. A representation of TPO photolysis reaction is shown in figure 3.4 (Sluggett *et al.*, 1995).

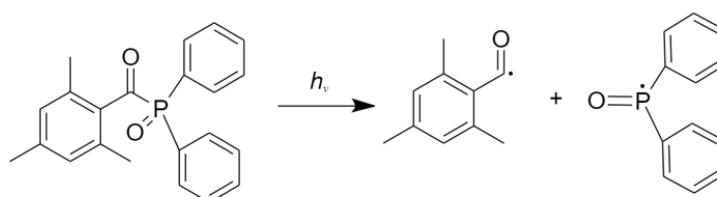


**Figure 3.4.** Generation of radical fragments resulting from TPO photolysis

The first compound to be included in the pool of materials used to assemble photopolymer formulations was PEGDA, selected in the average  $M_n$  of 250, 575, and 700. Several applications of PEGDA 700 regarding the preparation of solid oral dosage forms have been described in the scientific literature, while less evidence is available for PEGDA 250 (Acosta-Vélez *et al.*, 2018) and 575 (Robles Martinez *et al.*, 2019). PEGDA is a linear homobifunctional polymer, featuring a polyethylene glycol backbone terminating with acrylate groups allowing it to form crosslinked networks via free-radical photopolymerisation. The chain initiation mechanism is represented in figure 3.5, where the radical fragments  $R_1$  and  $R_2$ , generated from the photocleavage of the PI, are involved

in an addition reaction with the C=C double bond of the acrylate moieties in PEGDA. The resulting formation of 2 new radicals in the PEGDA molecule allows the reaction to propagate and to form a highly crosslinked polymer (figure 3.6).

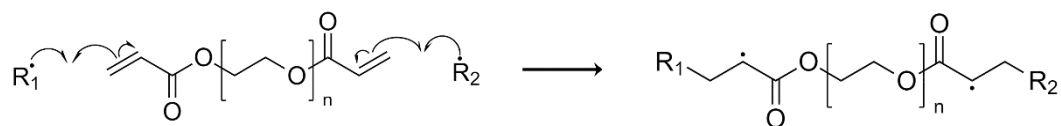


**Figure 3.5.** Chain initiation reaction between radical fragments ( $R_1$  and  $R_2$ ) produced following PI photocleavage and C=C double bonds of PEGDA.

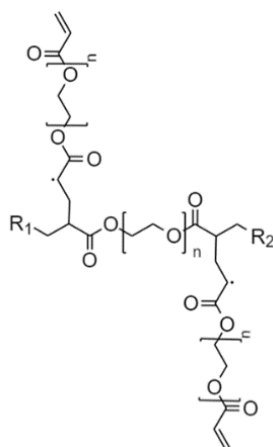


**Figure 3.6.** Partial representation of a chain propagation reaction involving the radical PEGDA molecule showed in figure 3.5, and 2 unreacted PEGDA molecules. The reaction can then propagate further.

A second component included in the photopolymer formulation screening was N-vinyl-2-pyrrolidone (N-VP). Due to its low viscosity (2.1 cP at 20 °C) and its inability to crosslink, N-VP was investigated by mixing it in different ratios with PEGDA in different  $M_n$ , to potentially obtain a form of crosslinked polyvinyl pyrrolidone (PVP) (figure 3.7), whose pharmaceutical applications are well renowned. Nevertheless, it should be considered that any speculation conducted at this point on the structural nature of co-photopolymerised N-

VP and PEGDA remains to be confirmed by appropriate means and it was not among the aims of this Thesis.

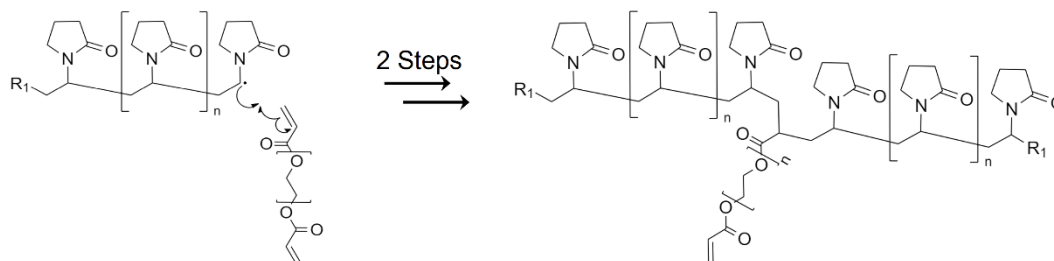


**Figure 3.7.** Simplified representation of the addition of a radical linear chain of PVP to a PEGDA molecule, resulting in the formation of a growing network of crosslinked PVP. R<sub>1</sub> represents the radical fragment originally provided by the PI.

Polyethylene glycol (PEG) 300, propylene glycol (PG), and glycerol, were selected as liquid fillers (figure 3.8). Since they cannot take part in the photopolymerisation process, their inclusion is expected to increase molecular mobility within the crosslinked matrix, aiding the release of drug molecules eventually present. Moreover, the hydrophilicity of these compounds could increase the recall of water inside the tablet thanks to the formation of hydrogen bonds, which in turn could contribute to an increase in the extent of drug release.

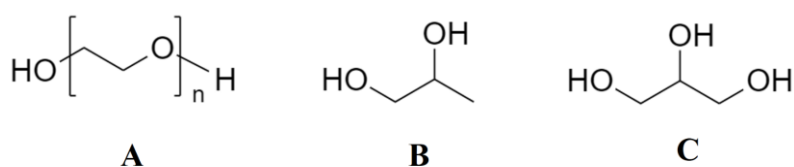


**Figure 3.8.** Structures of (A) polyethylene glycol, (B) propylene glycol, and (C) glycerol.

The components described above were used to design and prepare a total of 156 photopolymer formulations, whose exact compositions are reported in table 3.5.

**Table 3.5.** % w/w composition of the 156 photopolymer formulations designed and prepared to carry out a systematic printability screening.

	PEGDA 250	PEGDA 575	PEGDA 700	PEG 300	Propylene Glycol	Glycerol	N-Vinyl Pyrrolidone	TPO
<b>F1</b>	99.00	-	-	-	-	-	-	1.00
<b>F2</b>	99.50	-	-	-	-	-	-	0.50
<b>F3</b>	99.90	-	-	-	-	-	-	0.10
<b>F4</b>	99.95	-	-	-	-	-	-	0.05
<b>F5</b>	-	99.00	-	-	-	-	-	1.00
<b>F6</b>	-	99.50	-	-	-	-	-	0.50
<b>F7</b>	-	99.90	-	-	-	-	-	0.10
<b>F8</b>	-	99.95	-	-	-	-	-	0.05
<b>F9</b>	-	-	99.00	-	-	-	-	1.00
<b>F10</b>	-	-	99.50	-	-	-	-	0.50
<b>F11</b>	-	-	99.90	-	-	-	-	0.10
<b>F12</b>	-	-	99.95	-	-	-	-	0.05
<b>F13</b>	86.50	-	-	12.50	-	-	-	1.00
<b>F14</b>	74.00	-	-	25.00	-	-	-	1.00
<b>F15</b>	49.00	-	-	50.00	-	-	-	1.00
<b>F16</b>	87.00	-	-	12.50	-	-	-	0.50
<b>F17</b>	74.50	-	-	25.00	-	-	-	0.50
<b>F18</b>	49.50	-	-	50.00	-	-	-	0.50
<b>F19</b>	87.40	-	-	12.50	-	-	-	0.10
<b>F20</b>	74.90	-	-	25.00	-	-	-	0.10
<b>F21</b>	49.90	-	-	50.00	-	-	-	0.10
<b>F22</b>	87.45	-	-	12.50	-	-	-	0.05
<b>F23</b>	74.95	-	-	25.00	-	-	-	0.05
<b>F24</b>	49.95	-	-	50.00	-	-	-	0.05
<b>F25</b>	-	86.50	-	12.50	-	-	-	1.00
<b>F26</b>	-	74.00	-	25.00	-	-	-	1.00
<b>F27</b>	-	49.00	-	50.00	-	-	-	1.00
<b>F28</b>	-	87.00	-	12.50	-	-	-	0.50
<b>F29</b>	-	74.50	-	25.00	-	-	-	0.50
<b>F30</b>	-	49.50	-	50.00	-	-	-	0.50
<b>F31</b>	-	87.40	-	12.50	-	-	-	0.10
<b>F32</b>	-	74.90	-	25.00	-	-	-	0.10
<b>F33</b>	-	49.90	-	50.00	-	-	-	0.10

<b>F34</b>	-	87.45	-	12.50	-	-	-	0.05
<b>F35</b>	-	74.95	-	25.00	-	-	-	0.05
<b>F36</b>	-	49.95	-	50.00	-	-	-	0.05
<b>F37</b>	-	-	86.50	12.50	-	-	-	1.00
<b>F38</b>	-	-	74.00	25.00	-	-	-	1.00
<b>F39</b>	-	-	49.00	50.00	-	-	-	1.00
<b>F40</b>	-	-	87.00	12.50	-	-	-	0.50
<b>F41</b>	-	-	74.50	25.00	-	-	-	0.50
<b>F42</b>	-	-	49.50	50.00	-	-	-	0.50
<b>F43</b>	-	-	87.40	12.50	-	-	-	0.10
<b>F44</b>	-	-	74.90	25.00	-	-	-	0.10
<b>F45</b>	-	-	49.90	50.00	-	-	-	0.10
<b>F46</b>	-	-	87.45	12.50	-	-	-	0.05
<b>F47</b>	-	-	74.95	25.00	-	-	-	0.05
<b>F48</b>	-	-	49.95	50.00	-	-	-	0.05
<b>F49</b>	-	86.50	-	-	12.50	-	-	1.00
<b>F50</b>	-	74.00	-	-	25.00	-	-	1.00
<b>F51</b>	-	49.00	-	-	50.00	-	-	1.00
<b>F52</b>	-	87.00	-	-	12.50	-	-	0.50
<b>F53</b>	-	74.50	-	-	25.00	-	-	0.50
<b>F54</b>	-	49.50	-	-	50.00	-	-	0.50
<b>F55</b>	-	87.40	-	-	12.50	-	-	0.10
<b>F56</b>	-	74.90	-	-	25.00	-	-	0.10
<b>F57</b>	-	49.90	-	-	50.00	-	-	0.10
<b>F58</b>	-	87.45	-	-	12.50	-	-	0.05
<b>F59</b>	-	74.95	-	-	25.00	-	-	0.05
<b>F60</b>	-	49.95	-	-	50.00	-	-	0.05
<b>F61</b>	-	-	86.50	-	12.50	-	-	1.00
<b>F62</b>	-	-	74.00	-	25.00	-	-	1.00
<b>F63</b>	-	-	49.00	-	50.00	-	-	1.00
<b>F64</b>	-	-	87.00	-	12.50	-	-	0.50
<b>F65</b>	-	-	74.50	-	25.00	-	-	0.50
<b>F66</b>	-	-	49.50	-	50.00	-	-	0.50
<b>F67</b>	-	-	87.40	-	12.50	-	-	0.10
<b>F68</b>	-	-	74.90	-	25.00	-	-	0.10
<b>F69</b>	-	-	49.90	-	50.00	-	-	0.10

<b>F70</b>	-	-	87.45	-	12.50	-	-	0.05
<b>F71</b>	-	-	74.95	-	25.00	-	-	0.05
<b>F72</b>	-	-	49.95	-	50.00	-	-	0.05
<b>F73</b>	-	86.50	-	-	-	12.50	-	1.00
<b>F74</b>	-	74.00	-	-	-	25.00	-	1.00
<b>F75</b>	-	49.00	-	-	-	50.00	-	1.00
<b>F76</b>	-	87.00	-	-	-	12.50	-	0.50
<b>F77</b>	-	74.50	-	-	-	25.00	-	0.50
<b>F78</b>	-	49.50	-	-	-	50.00	-	0.50
<b>F79</b>	-	87.40	-	-	-	12.50	-	0.10
<b>F80</b>	-	74.90	-	-	-	25.00	-	0.10
<b>F81</b>	-	49.90	-	-	-	50.00	-	0.10
<b>F82</b>	-	87.45	-	-	-	12.50	-	0.05
<b>F83</b>	-	74.95	-	-	-	25.00	-	0.05
<b>F84</b>	-	49.95	-	-	-	50.00	-	0.05
<b>F85</b>	-	-	86.50	-	-	12.50	-	1.00
<b>F86</b>	-	-	74.00	-	-	25.00	-	1.00
<b>F87</b>	-	-	49.00	-	-	50.00	-	1.00
<b>F88</b>	-	-	87.00	-	-	12.50	-	0.50
<b>F89</b>	-	-	74.50	-	-	25.00	-	0.50
<b>F90</b>	-	-	49.50	-	-	50.00	-	0.50
<b>F91</b>	-	-	87.40	-	-	12.50	-	0.10
<b>F92</b>	-	-	74.90	-	-	25.00	-	0.10
<b>F93</b>	-	-	49.90	-	-	50.00	-	0.10
<b>F94</b>	-	-	87.45	-	-	12.50	-	0.05
<b>F95</b>	-	-	74.95	-	-	25.00	-	0.05
<b>F96</b>	-	-	49.95	-	-	50.00	-	0.05
<b>F97</b>	-	-	94.00	-	-	-	5.00	1.00
<b>F98</b>	-	-	89.00	-	-	-	10.00	1.00
<b>F99</b>	-	-	79.00	-	-	-	20.00	1.00
<b>F100</b>	-	-	94.50	-	-	-	5.00	0.50
<b>F101</b>	-	-	89.50	-	-	-	10.00	0.50
<b>F102</b>	-	-	79.50	-	-	-	20.00	0.50
<b>F103</b>	-	-	94.90	-	-	-	5.00	0.10
<b>F104</b>	-	-	89.90	-	-	-	10.00	0.10
<b>F105</b>	-	-	79.90	-	-	-	20.00	0.10

<b>F106</b>	-	-	94.95	-	-	-	5.00	0.05
<b>F107</b>	-	-	89.95	-	-	-	10.00	0.05
<b>F108</b>	-	-	79.95	-	-	-	20.00	0.05
<b>F109</b>	-	94.00	-	-	-	-	5.00	1.00
<b>F110</b>	-	89.00	-	-	-	-	10.00	1.00
<b>F111</b>	-	79.00	-	-	-	-	20.00	1.00
<b>F112</b>	-	94.50	-	-	-	-	5.00	0.50
<b>F113</b>	-	89.50	-	-	-	-	10.00	0.50
<b>F114</b>	-	79.50	-	-	-	-	20.00	0.50
<b>F115</b>	-	94.90	-	-	-	-	5.00	0.10
<b>F116</b>	-	89.90	-	-	-	-	10.00	0.10
<b>F117</b>	-	79.90	-	-	-	-	20.00	0.10
<b>F118</b>	-	94.95	-	-	-	-	5.00	0.05
<b>F119</b>	-	89.95	-	-	-	-	10.00	0.05
<b>F120</b>	-	79.95	-	-	-	-	20.00	0.05
<b>F121</b>	94.00	-	-	-	-	-	5.00	1.00
<b>F122</b>	89.00	-	-	-	-	-	10.00	1.00
<b>F123</b>	79.00	-	-	-	-	-	20.00	1.00
<b>F124</b>	94.50	-	-	-	-	-	5.00	0.50
<b>F125</b>	89.50	-	-	-	-	-	10.00	0.50
<b>F126</b>	79.50	-	-	-	-	-	20.00	0.50
<b>F127</b>	94.90	-	-	-	-	-	5.00	0.10
<b>F128</b>	89.90	-	-	-	-	-	10.00	0.10
<b>F129</b>	79.90	-	-	-	-	-	20.00	0.10
<b>F130</b>	94.95	-	-	-	-	-	5.00	0.05
<b>F131</b>	89.95	-	-	-	-	-	10.00	0.05
<b>F132</b>	79.95	-	-	-	-	-	20.00	0.05
<b>F133</b>	86.50	-	-	-	-	12.50	-	1.00
<b>F134</b>	74.00	-	-	-	-	25.00	-	1.00
<b>F135</b>	49.00	-	-	-	-	50.00	-	1.00
<b>F136</b>	87.00	-	-	-	-	12.50	-	0.50
<b>F137</b>	74.50	-	-	-	-	25.00	-	0.50
<b>F138</b>	49.50	-	-	-	-	50.00	-	0.50
<b>F139</b>	87.40	-	-	-	-	12.50	-	0.10
<b>F140</b>	74.90	-	-	-	-	25.00	-	0.10
<b>F141</b>	49.90	-	-	-	-	50.00	-	0.10

<b>F142</b>	87.45	-	-	-	-	12.50	-	0.05
<b>F143</b>	74.95	-	-	-	-	25.00	-	0.05
<b>F144</b>	49.95	-	-	-	-	50.00	-	0.05
<b>F145</b>	86.50	-	-	-	12.50	-	-	1.00
<b>F146</b>	74.00	-	-	-	25.00	-	-	1.00
<b>F147</b>	49.00	-	-	-	50.00	-	-	1.00
<b>F148</b>	87.00	-	-	-	12.50	-	-	0.50
<b>F149</b>	74.50	-	-	-	25.00	-	-	0.50
<b>F150</b>	49.50	-	-	-	50.00	-	-	0.50
<b>F151</b>	87.40	-	-	-	12.50	-	-	0.10
<b>F152</b>	74.90	-	-	-	25.00	-	-	0.10
<b>F153</b>	49.90	-	-	-	50.00	-	-	0.10
<b>F154</b>	87.45	-	-	-	12.50	-	-	0.05
<b>F155</b>	74.95	-	-	-	25.00	-	-	0.05
<b>F156</b>	49.95	-	-	-	50.00	-	-	0.05

#### ***3.4.4.2 Stereolithography 3D printing and printability evaluation***

The 156 photopolymer formulations were screened via SLA 3DP using a modified SLA apparatus previously described in Chapter II, allowing to simultaneously 3D print up to 12 different resins (Curti, Kirby and Russell, 2021). Each formulation was 3D printed setting the layer thickness to 25  $\mu\text{m}$ , 50  $\mu\text{m}$ , and 100  $\mu\text{m}$ , therefore the whole screening process required only 39 print cycles to be completed, instead of 468, with substantial implications in terms of time and cost saving (Curti, Kirby and Russell, 2021).

Pictures of the 3D printed test tablets are shown in figures 3.9-3.21, while the PS for each formulation at any layer thickness is given in table 3.6.

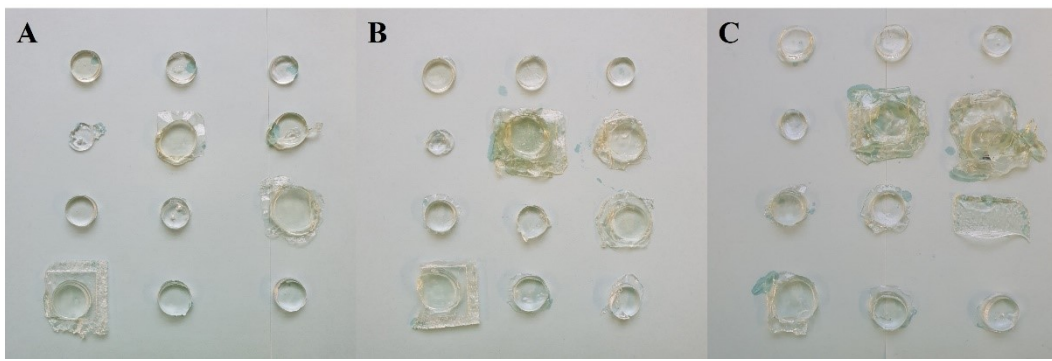


**Figure 3.9.** From top left to bottom right: formulations F1-F12, 3D printed setting the layer thickness to (A) 25  $\mu\text{m}$ , (B) 50  $\mu\text{m}$ , and (C) 100  $\mu\text{m}$ .

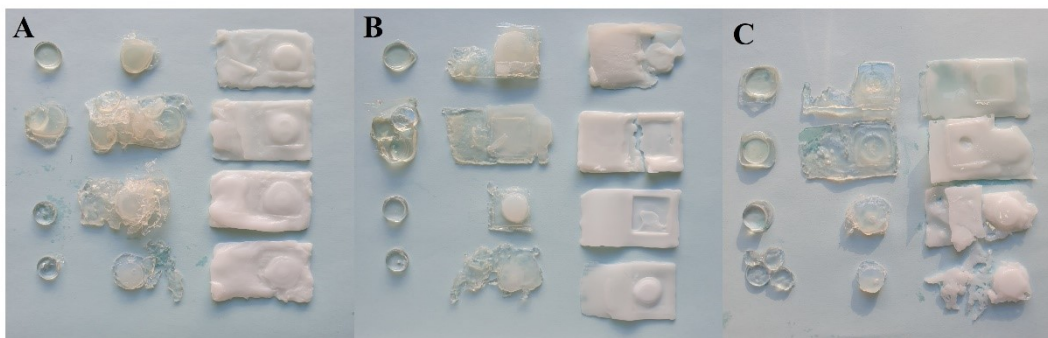


**Figure 3.10.** From top left to bottom right: formulations F13-F24, 3D printed setting the layer thickness to (A) 25  $\mu\text{m}$ , (B) 50  $\mu\text{m}$ , and (C) 100  $\mu\text{m}$ .



**Figure 3.11.** From top left to bottom right: formulations F25-F36, 3D printed setting the layer thickness to (A) 25  $\mu\text{m}$ , (B) 50  $\mu\text{m}$ , and (C) 100  $\mu\text{m}$ .

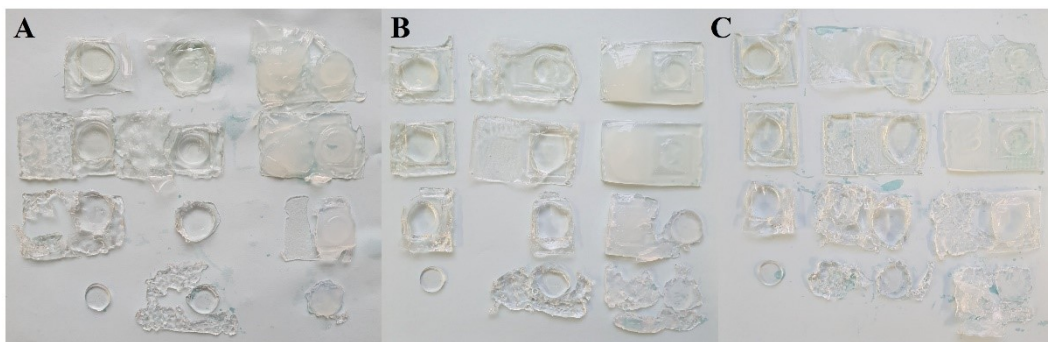


**Figure 3.12.** From top left to bottom right: formulations F37-F48, 3D printed setting the layer thickness to (A) 25 µm, (B) 50 µm, and (C) 100 µm.

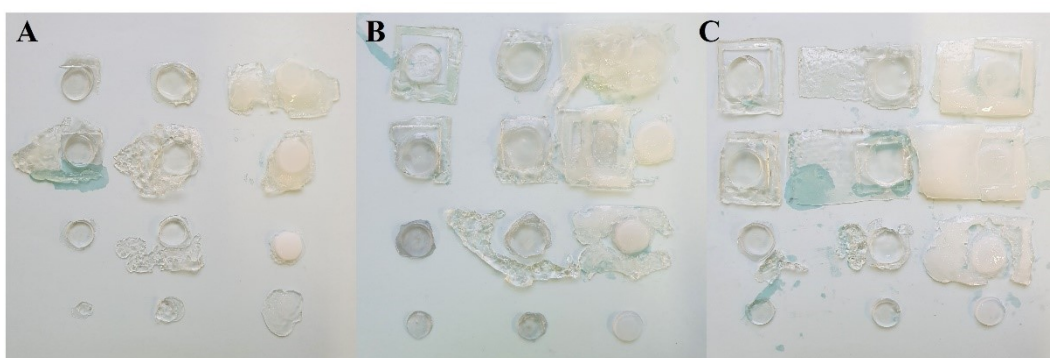


**Figure 3.13.** From top left to bottom right: formulations F49-F60, 3D printed setting the layer thickness to (A) 25 µm, (B) 50 µm, and (C) 100 µm.

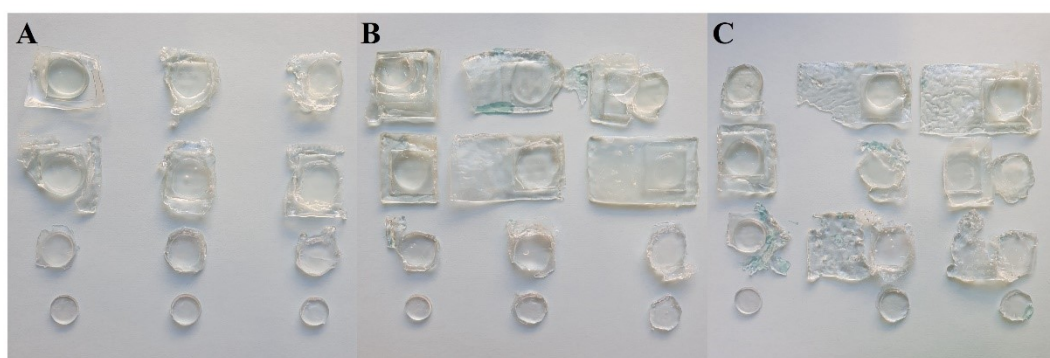


**Figure 3.14.** From top left to bottom right: formulations F61-F72, 3D printed setting the layer thickness to (A) 25 µm, (B) 50 µm, and (C) 100 µm.

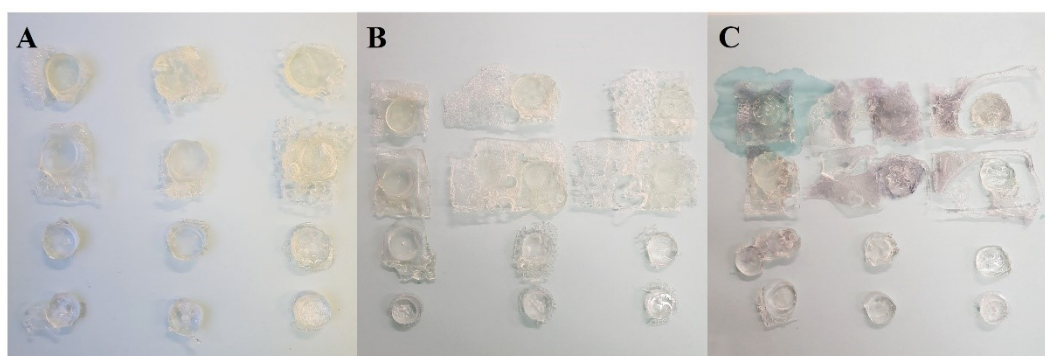


**Figure 3.15.** From top left to bottom right: formulations F73-F84, 3D printed setting the layer thickness to (A) 25 μm, (B) 50 μm, and (C) 100 μm.

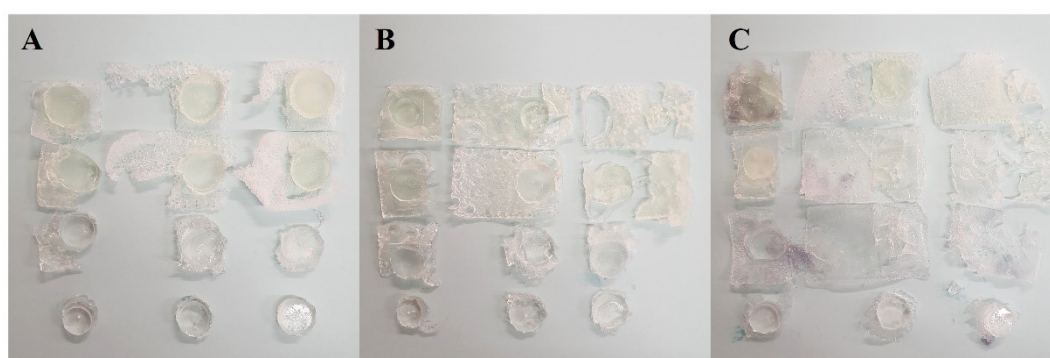


**Figure 3.16.** From top left to bottom right: formulations F85-F96, 3D printed setting the layer thickness to (A) 25 μm, (B) 50 μm, and (C) 100 μm.

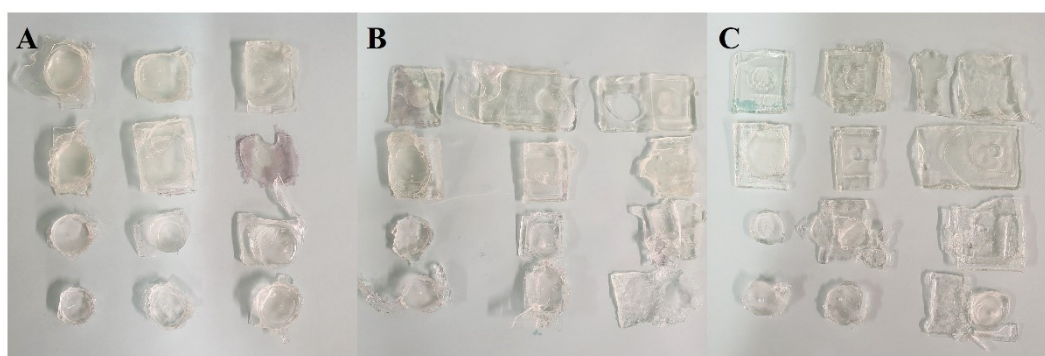


**Figure 3.17.** From top left to bottom right: formulations F97-F108, 3D printed setting the layer thickness to (A) 25 μm, (B) 50 μm, and (C) 100 μm.

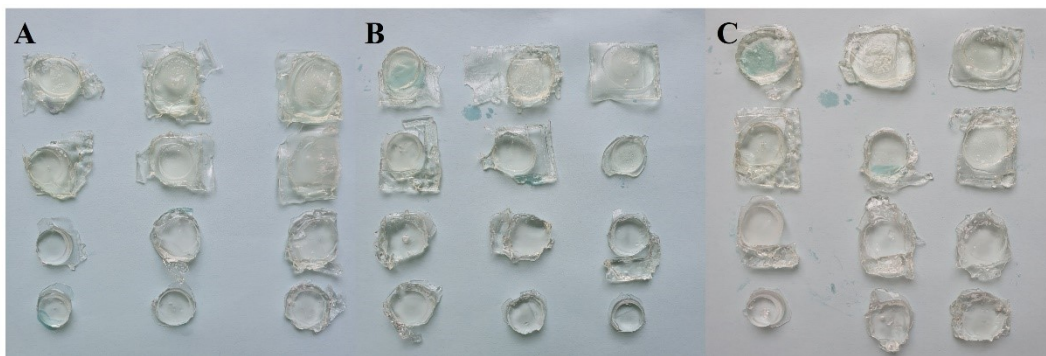


**Figure 3.18.** From top left to bottom right: formulations F109-F120, 3D printed setting the layer thickness to (A) 25  $\mu\text{m}$ , (B) 50  $\mu\text{m}$ , and (C) 100  $\mu\text{m}$ .

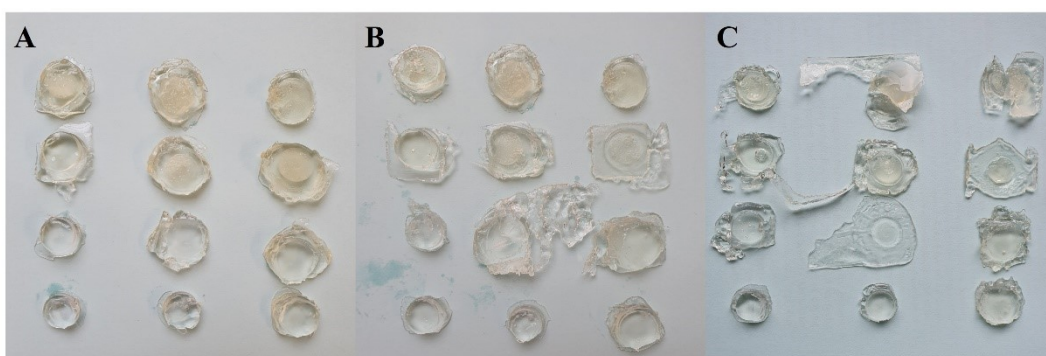


**Figure 3.19.** From top left to bottom right: formulations F121-F132, 3D printed setting the layer thickness to (A) 25  $\mu\text{m}$ , (B) 50  $\mu\text{m}$ , and (C) 100  $\mu\text{m}$ .

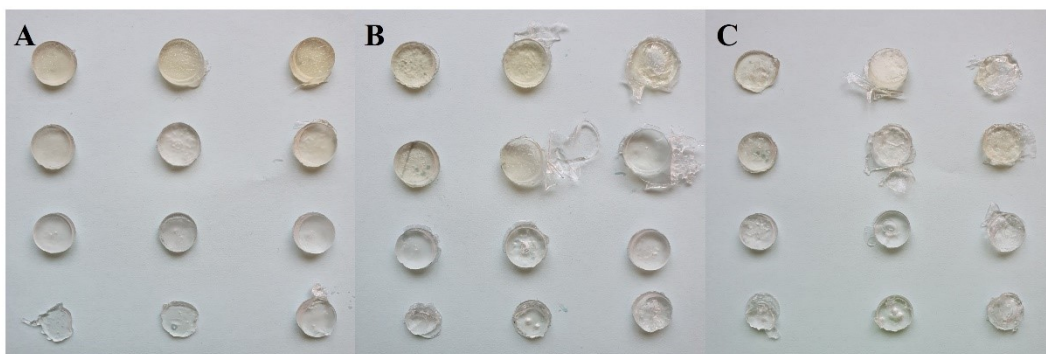


**Figure 3.20.** From top left to bottom right: formulations F133-F144, 3D printed setting the layer thickness to (A) 25  $\mu\text{m}$ , (B) 50  $\mu\text{m}$ , and (C) 100  $\mu\text{m}$ .

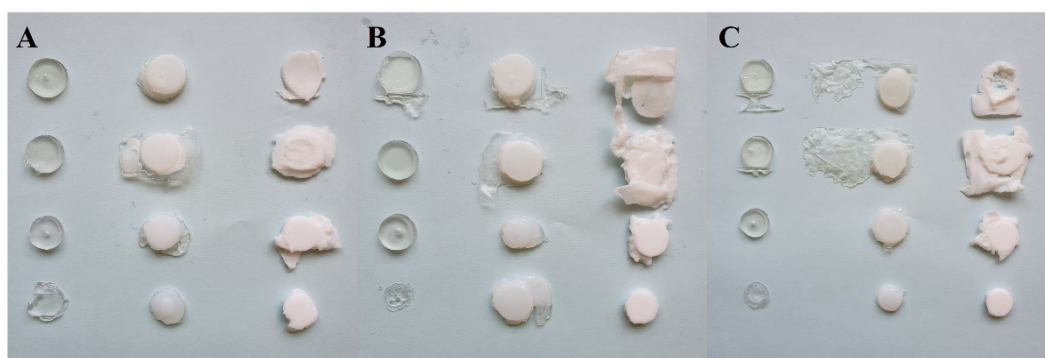


**Figure 3.21.** From top left to bottom right: formulations F145-F156, 3D printed setting the layer thickness to (A) 25 µm, (B) 50 µm, and (C) 100 µm.

**Table 3.6.** Printability score (PS) and classification group assigned to each photopolymer formulation screened. Group A indicates formulations with PS  $\neq$  5 (n = 96); group B reports formulations with a PS = 5 or PS = \* at least at one printing resolution (n = 60); groups B1 (n = 35) and B2 (n = 5) list formulations with a PS = 5\* at least at one or at each printing resolution used, respectively.

Formulation	PS - 25 $\mu\text{m}$	PS - 50 $\mu\text{m}$	PS - 100 $\mu\text{m}$	Group assigned
F1	5*	5*	6	B1
F2	5*	5*	6	B1
F3	4	5	5*	B1
F4	4	4	4	A
F5	6	6	6	A
F6	6	6	6	A
F7	5*	6*	6*	B1
F8	4	6	6	A
F9	6	6	6	A
F10	6	6	6	A
F11	5*	6*	6	B1
F12	5*	6*	5*	B1
F13	5*	6	6	B1
F14	6	6	6	A
F15	6	6	6	A
F16	6	6	6	A
F17	6	6	6	A
F18	6	6	6	A
F19	5	5*	5*	B1
F20	6	6	6	A
F21	6	6	6	A
F22	4	4	4	A
F23	6	6	6*	B
F24	6	6	6	A
F25	6	6	6*	B
F26	6	6	6	A
F27	6	6	6	A
F28	6	6	6	A
F29	6	6*	6	B
F30	6	6	6	A
F31	6*	6	6*	B
F32	6	6	6	A
F33	6	6	6	A
F34	5	5*	5*	B1
F35	5*	6	5*	B1

F36	6	6	6	A
F37	6	6	6	A
F38	6	6	6	A
F39	6	6	6	A
F40	6	6	6	A
F41	6	6	6	A
F42	6	6	6	A
F43	6	6	6	A
F44	6	6	6	A
F45	6	6	6	A
F46	5*	5*	5*	B2
F47	6	6	6	A
F48	6	6	6	A
F49	6	6	6	A
F50	6	6	6	A
F51	6	6	6	A
F52	6	6	6	A
F53	6	6	6	A
F54	6	6	6	A
F55	6*	6*	6*	B
F56	6*	6	6	B
F57	6*	6	6	B
F58	4	4	5*	B1
F59	4	4	5*	B1
F60	4	5	5*	B1
F61	6	6	6	A
F62	6	6	6	A
F63	6	6	6	A
F64	6	6	6	A
F65	6	6	6	A
F66	6	6	6	A
F67	6*	6	6	B
F68	6	6	6	A
F69	6	6	6	A
F70	5*	5*	5*	B2
F71	5*	5	5	B1
F72	5*	5	5	B1
F73	6	6	6	A
F74	6	6	6	A
F75	6	6	6	A
F76	6*	6	6	B
F77	6	6	6	A

F78	6	6	6	A
F79	5*	6	4	B1
F80	6*	6	6	B
F81	6*	6*	6	B
F82	4	5*	6	B1
F83	4	5*	5*	B1
F84	5*	5*	5*	B2
F85	6	6	6	A
F86	6	6	6	A
F87	6	6	6	A
F88	6	6	6	A
F89	6	6	6	A
F90	6	6	6	A
F91	6*	6	6	B
F92	6	6	6	A
F93	6	6	6	A
F94	5*	6	6	B1
F95	5*	6	6	B1
F96	6	6	6	A
F97	6	6	6	A
F98	6	6	6	A
F99	6	6	6	A
F100	6	6	6	A
F101	6	6	6	A
F102	6	6	6	A
F103	6	6	6	A
F104	6	6	6	A
F105	6	6	6	A
F106	6	6	6	A
F107	6	6	6	A
F108	6	6	6	A
F109	6	6	6	A
F110	6	6	6	A
F111	6	6	6	A
F112	6	6	6	A
F113	6	6	6	A
F114	6	6*	6	B
F115	5*	6	6	B1
F116	6	6	6	A
F117	6	6	6	A
F118	5*	6	5*	B1
F119	6*	6	6	B

F120	6	5*	6	B1
F121	6	6	6	A
F122	6	6	6	A
F123	6	6	6	A
F124	6*	6*	6	B
F125	6	6	6	A
F126	6	6	6	A
F127	5*	5	6*	B1
F128	6	6	6	A
F129	6	6	6	A
F130	4	5*	5*	B1
F131	4	4	5*	B1
F132	6	6	6	A
F133	5*	5*	4	B1
F134	6*	6*	6*	B
F135	6*	4	4	B
F136	5*	5*	5*	B2
F137	5*	6*	6	B1
F138	5*	6*	6	B1
F139	5*	5*	5*	B2
F140	4	5*	5*	B1
F141	5*	5*	6*	B1
F142	4	4	4	A
F143	4	4	5	B
F144	4	5	4	B
F145	5*	6*	6*	B1
F146	6	6	6	A
F147	4	6	4	A
F148	5*	5*	6*	B1
F149	6	6	6	A
F150	6	6	6	A
F151	5	5*	5*	B1
F152	6*	4	6	B
F153	6	6	6	A
F154	4	4	4	A
F155	4	6	4	A
F156	4	5	5*	B1

---

Based on the inclusion criteria, the whole set of photopolymer formulations screened was classified in four groups (figure 3.22). Out of the 156 formulations tested, 96 provided a PS  $\neq$  5 indicating poor printability outcomes (figure 3.22, group A), while the remaining

60 formulations met the eligibility criteria by reaching a PS = 5 or showing defined edges (\*) at least at one printing resolution, making up a pool labelled as printable formulations (PF, n = 60) (figure 3.22, group B).

Formulations included in group B were then subclassified into groups B1 (n = 35; formulations reaching PS = 5\* at least for one printing resolution) and B2 (n = 5; formulations reaching PS = 5\* at each printing resolution). Formulations belonging to groups B1 and B2 were jointly labelled as best formulations (BF, n = 40).

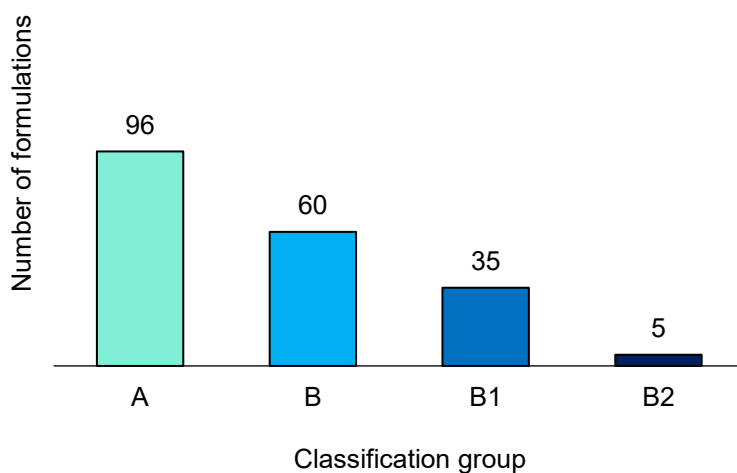


**Figure 3.22.** Group classification of photopolymer formulations screened. Group A indicates formulations with PS  $\neq$  5 (n = 96); group B reports formulations with a PS = 5 or PS = \* at least at one printing resolution (n = 60); groups B1 (n = 35) and B2 (n = 5) list formulations with a PS = 5\* at least at one or at each printing resolution used, respectively.

#### 3.4.4.3 Polyethylene glycol diacrylate influence on printability

The role of PEGDA  $M_n$  on printability outcomes was investigated. The graph in figure 3.23 displays the number of PFs and BFs containing PEGDA 250, 575, and 700, respectively.

According to the results, PEGDA 250 was the most frequently effective polymer both among PFs (26) and BFs (19). PEGDA 575 was present in 24 PFs and 13 BFs, while PEGDA 700 in 10 PFs and 8 BFs. However, PEGDA 700 showed the highest BF/PFs ratio (0.80) in comparison to PEGDA 250 (0.73) and PEGDA 575 (0.54), suggesting that

its use is more likely to provide tablets 3D printed in accurate size and shape. As a result, PEGDA 700 was selected as the main photocrosslinkable polymer for the subsequent stages of this research, involving the formulation of drug loaded photopolymer resins.

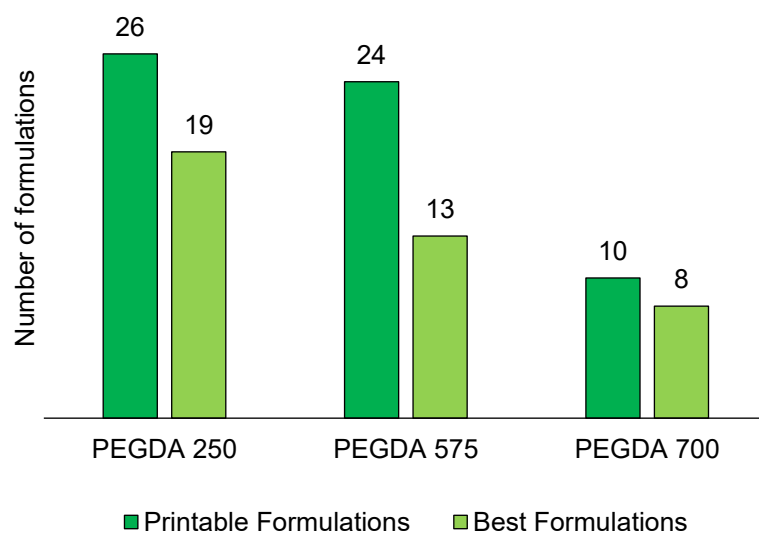


**Figure 3.23.** Number of formulations containing PEGDA 250, 575, and 700 classified as PFs and BFs.

#### ***3.4.4.4 Liquid fillers influence on printability***

PEG 300, PG, and glycerol were individually used as liquid fillers combined in different concentrations with PEGDA. Liquid fillers can act as co-solvents to enhance drug solubility in the liquid photopolymer or as release-tuning agents, and their incorporation into SLA printable formulations represents a standard strategy to overcome such issues.

The data in figures 3.24-3.26 show the number of formulations containing PEG 300, PG, or glycerol, in different concentrations, that were classified as PFs and BFs.

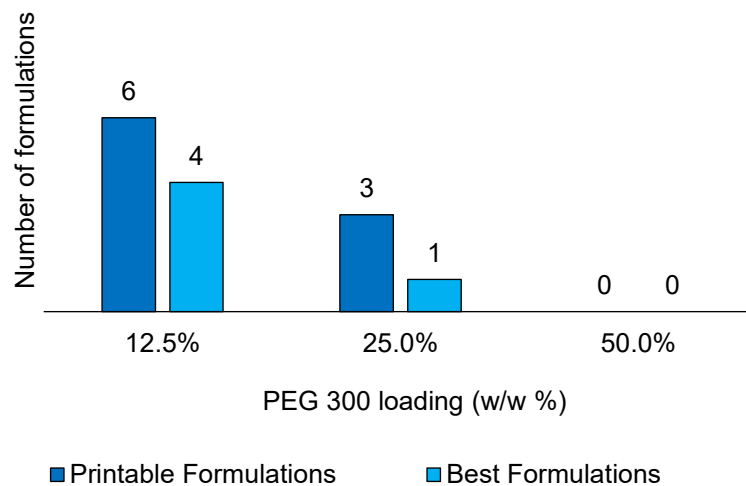


**Figure 3.24.** Number of formulations containing PEG 300 classified as PFs and BFs.

When PEG 300 was used in a concentration of 12.5% w/w, a total of 6 PFs and 4 BFs were obtained (figure 3.24). Doubling PEG 300 concentration to 25% w/w led to the classification of 3 PFs and 1 BF, while a further PEG 300 increase to 50% w/w did not allow to identify any PFs and BFs. Therefore, the inclusion of PEG 300 in a concentration of 12.5% w/w was most effective in ensuring good printability, as also indicated by the high BFs/PFs ratio (0.67).

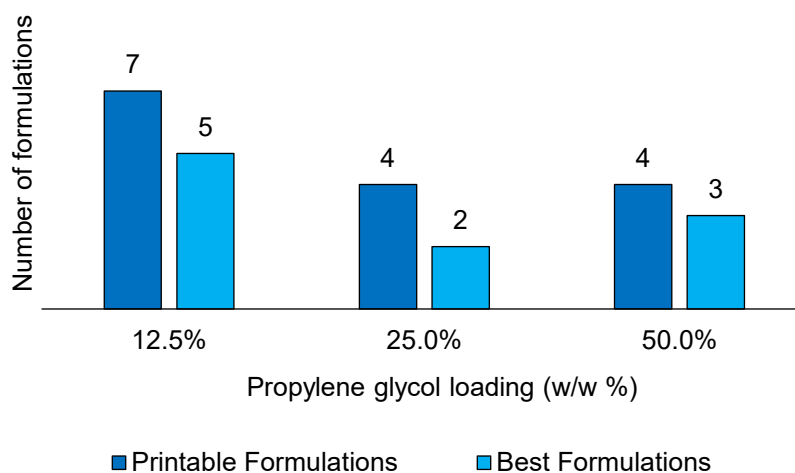


**Figure 3.25.** Number of formulations containing propylene glycol classified as PFs and BFs.

PG provided better results when loaded at higher concentrations, in comparison to PEG 300 (figure 3.25). Again, it was found to be most effective when used at 12.5% w/w, resulting in 7 PFs and 5 BFs. An increase of PG to 25% w/w led to the identification of 4 PFs and 2 BFs, while a further increase to 50% resulted in 4 PFs and 3 BFs. Interestingly, the highest BFs/PFs ratio (0.75) was observed when the maximum concentration of propylene glycol was used. Based on these observations, PG was selected as the main liquid filler to be included in the next-phase studies on drug loaded photopolymer formulations.

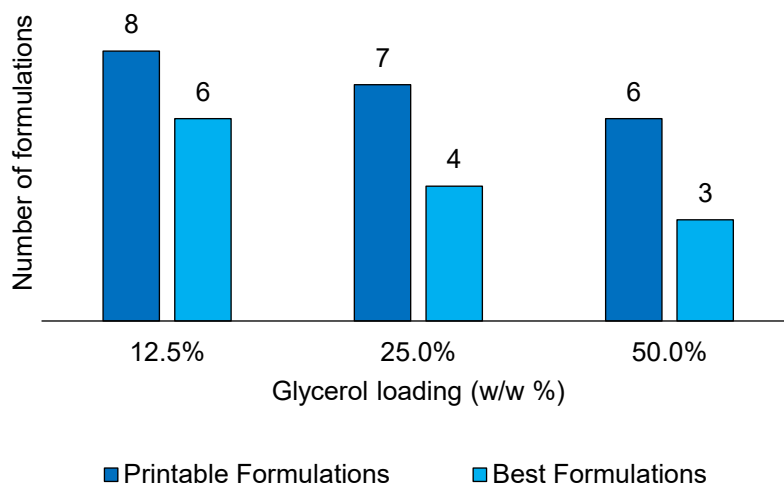


**Figure 3.26.** Number of formulations containing glycerol classified as PFs and BFs.

Glycerol was found to be unmixable with PEGDA of any  $M_n$ . Indeed, when added to PEGDA, it caused a well distinguishable phase separation of the photopolymer mixture and, as a result, poor printability outcomes were observed. Nevertheless, several formulations containing glycerol showed good printability outcomes (figure 3.26). However, it should be noted that this could be due to a bias caused by the phase separation between glycerol and PEGDA in the resin tank, leading to photopolymerisation occurring in the pure PEGDA. Undoubtedly, the incompatibility between PEGDA and glycerol makes the latter unsuitable for the formulation of a photopolymer resin to be used in SLA 3D printing, therefore it will not be furtherly investigated.

#### 3.4.4.5 *N*-vinyl pyrrolidone influence on printability

N-VP was included as a reactive monomer with the view to improve geometrical accuracy of the 3D printed tablets, and to investigate its potential drug release tuning properties. It was used in combination with PEGDA at a concentration of 5%, 10% and 20% w/w. The use of 5% N-VP allowed to identify 5 PFs and 4 BFs, with a BFs/PFs ratio of 0.80 (figure 3.27). When N-VP concentration was increased to 10% and 20% w/w, printability results worsened showing comparable results.

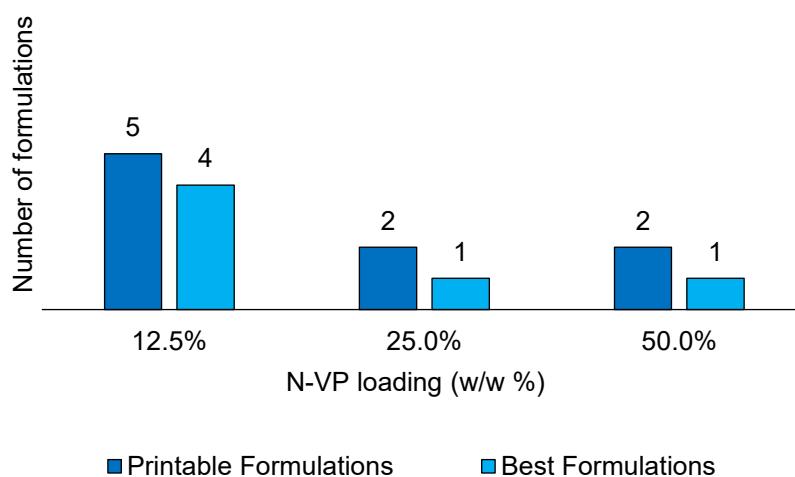


**Figure 3.27** Number of formulations containing N-VP classified as PFs and BFs.

Most importantly, it was noticed that the inclusion on N-VP in the photopolymer resins, led to hardening of the 3D printed tablets, which became visibly tough and difficult to remove from the build platform. Furthermore, even after 3DP and removal of the uncured resin, 3D printed dosage forms were characterised by a strong N-VP smell, possibly indicating the presence of uncured residues and likely a negative factor for patient compliance.

For this reason, N-VP was not furtherly investigated, despite the interest for its use to generate crosslinked PVP in situ through SLA 3DP remains.

#### 3.4.4.6 Evaluation of photoinitiator concentration on printability

TPO was used at concentrations of 1%, 0.5%, 0.1%, and 0.05% w/w. As it can be seen in figure 3.28, the number of formulations classified as PFs and BFs increases with the decrease of TPO concentration. Indeed, only 7 PFs and 4 BF were related to the use of 1% TPO. On the contrary, 0.05% TPO allowed to identify 24 PFs and 20 BF. This is furtherly evidenced by the high BF/PFs ratio related to 0.05% w/w TPO (0.83).

This demonstrates that TPO is not only effective at low concentrations in presence of liquid fillers, but it also provides better printability outcomes. Among the advantages of using a low amount of PI, a key role is held by the reduced toxicity concerns, as well as the potential to increase drug loading and reducing costs.

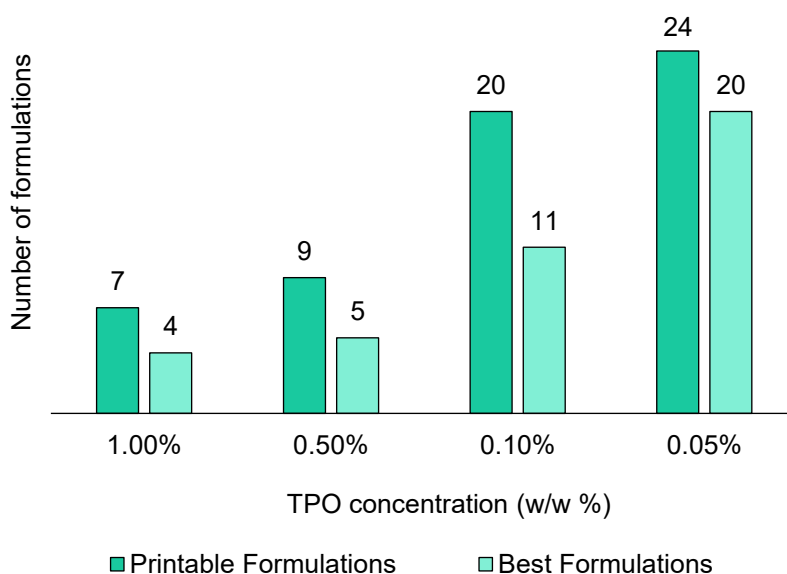


**Figure 3.28.** Number of formulations containing 1%, 0.5%, 0.1% and 0.05% w/w TPO classified as PFs and BF.

#### 3.4.4.7 Evaluation of printing resolution on printability outcomes

The effect of 3DP resolution on printability outcomes was also investigated (figure 3.29).

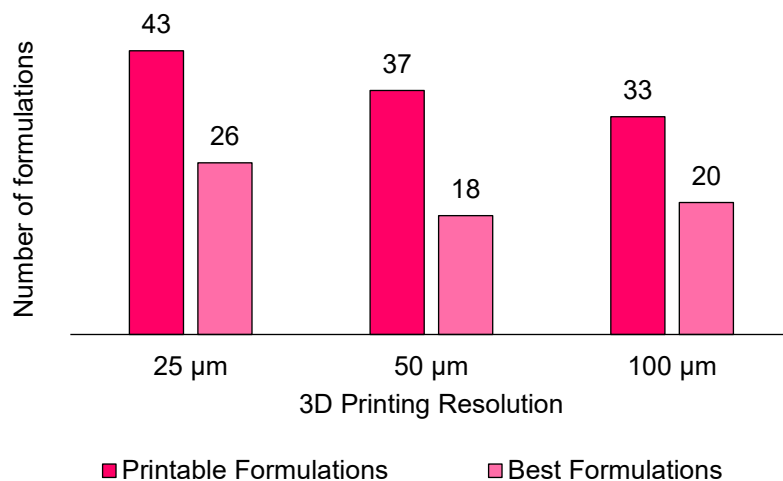


**Figure 3.29.** Number of formulations classified among PFs and BFs for each 3D printing resolution used.

When a 3DP resolution of 25 µm was used, 43 PFs and 26 BFs were obtained. Lowering the resolution to 50 µm resulted instead in 37 PFs and 18 BFs, while a further decrease to 100 µm allowed to identify 33 PFs and 20 BFs. These results point out that a higher printing resolution (25 µm) leads to better printability outcomes. It is also interesting to notice that the BFs/PFs ratio is higher when the lowest resolution (100 µm) was used.

However, it should be considered that 3DP with a resolution of 25 µm increases manufacturing time by 55.38% and 74.83% compared to using a resolution of 50 µm and 100 µm, respectively. Despite the better results observed using higher resolution, the increase in production time should not be underestimated. The implementation of SLA 3DP in clinical settings to produce personalised dosage forms will in fact be possible if the overall efficiency of the process is optimised, reducing costs and production times, and ensuring safety and efficacy of the printed medicines (Awad, Sarah J. Trenfield, *et al.*, 2018; Rautamo *et al.*, 2020). It is therefore essential to identify novel formulations, designed to provide best printability even at low resolution.

For such reason, a printing resolution of 100  $\mu\text{m}$  was selected to 3D print the drug loaded photopolymer formulations described in the next Chapter.

### **3.5 Conclusion**

In summary, in this Chapter was described the high-throughput printability screening conducted on 156 photopolymer formulations designed to develop safe SLA 3D printed solid oral dosage forms. This followed the preliminary identification of TPO as a suitable PI for SLA 3DP at 405 nm and the implementation of a points-based classification system to assess printability outcomes.

The printability assessment allowed to identify PEGDA 700 as the main photopolymer and PG as the best liquid filler, with best results when loaded as 12.5% in the photopolymer resin. TPO was found to be most effective when used at lowest concentration (0.05% w/w).

The effect on printability outcomes of the 3D printing resolution selected was also investigated, and it was found that better results are obtained when the highest resolution (corresponding to a layer thickness of 25  $\mu\text{m}$ ) is used. However, a printing resolution of 100  $\mu\text{m}$  was selected for the subsequent work described herein in this Thesis, due to the substantial decrease in manufacturing time compared to using higher resolutions.

Finally, from the 156 formulations screened, 5 were identified as lead formulations and were therefore selected to assemble drug-loaded photopolymer resins used to 3D print solid oral dosage forms, as it will be described in Chapter IV.

## **- Chapter IV -**

### **STEREOLITHOGRAPHY 3D PRINTING OF SOLID ORAL DOSAGE FORMS**

---

## 4.1 Introduction

Stereolithography (SLA) three-dimensional printing (3DP) offers unique features making it particularly suitable for the fabrication of solid oral dosage forms (Curti, Kirby and Russell, 2020). Indeed, its unrivalled advantages in terms of printing accuracy and resolution have promoted the progress of this technology in the manufacture of personalised dosage forms (Xu *et al.*, 2021). However, limitations caused by the lack of photopolymers available, and poor cost-effectiveness of the process, led to the underdevelopment of SLA in comparison to other 3DP technologies (Curti, Kirby and Russell, 2021).

In the previous Chapters of this Thesis, the development of a highly cost-effective SLA apparatus, and the systematic printability screening of a large number of photopolymer formulations have aimed to address the aforementioned limitations. In particular, the identification of formulations with optimal printability allowed to move to the next and last objective of this research: the fabrication of SLA 3D printed drug loaded tablets.

The work herein described aims to demonstrate the suitability of photopolymer resins with low photoinitiator (PI) concentration, shortlisted from the systematic screening reported in Chapter III, to produce SLA 3D printed solid oral dosage forms containing clinically relevant dosages of active pharmaceutical ingredient(s) (API). Most of the research conducted on SLA 3DP of solid oral dosage forms describes in fact the inclusion of PIs in concentrations of 1% w/w (Wang *et al.*, 2016; Robles Martinez *et al.*, 2019; Xu *et al.*, 2020). In an attempt to reduce toxicity concerns related to photopolymer resins, this work reported for the first time the fabrication of drug loaded tablets using a PI concentration as low as 0.05% w/w. Furthermore, this research intends to shed light on the physical properties of SLA 3D printed dosage forms, mainly hardness and friability, so far limitedly investigated (Healy *et al.*, 2019).

With regards to the selection of model compounds to use in this study, the focus was on narrow therapeutic index (NTI) drugs as these represent the first choice in the formulation

of 3D printed personalised medicines (Curti, Kirby and Russell, 2020). Indeed, the personalisation of pharmacotherapies shows higher importance when NTI drugs are used. In this context, oral anticoagulants undoubtedly meet the criteria for rational drug selection (Wadelius *et al.*, 2005; Epstein *et al.*, 2010; Arafat, Qinna, *et al.*, 2018). For example, coumarin-based regimens are known to be difficult to manage because of the many interactions with food and other drugs, requiring the continuous INR (International Normalised Ratio) profile monitoring and dose titration (Holbrook *et al.*, 2005). Therefore, the oral anticoagulant drug warfarin was selected for this research as a model compound to be included in clinically relevant dosages in SLA 3D printed tables. Another NTI drug, theophylline, was also selected for the investigation of potential drug loading limitations of the photopolymer resins.

Finally, 3D printed dosage forms were thoroughly characterised, with the view to inform on the opportunities and remaining challenges of SLA 3DP in the pharmaceutical field.

## 4.2 Chapter aim and objectives

The primary aim of this chapter was to develop a wide set of drug loaded solid oral dosage forms using SLA 3D printing. Following the work described in the previous chapters, it was indeed possible to use a SLA 3DP apparatus with enhanced efficiency and productivity, while having available a set of photopolymer resin formulations with optimised printability. This allowed us to substantially reduce both cost and time of the final phase of this research project.

To achieve the abovementioned aim, the work presented in this chapter was essentially carried out in three different phases characterised by the following objectives:

- Rational selection of APIs. Ideal drug candidates for 3D printing would be those having a narrow therapeutic index and for which the continuous dose titration based on individual patients' characteristics is usually needed, even on a daily basis.
- Design of printable photopolymer formulations loaded with clinically relevant dosages of APIs. This would indeed demonstrate that 3D printing can represent a valid manufacturing technology for solid oral dosage forms, in parallel with conventional production processes.
- Characterisation of drug loaded SLA 3D printed solid oral dosage forms by the application of analytical methods and physical characterisation tools. Such step would allow to acquire a thorough understanding of the advantages and limitations characterising SLA 3D printing in the pharmaceutical field, with the view to inform formulation scientists on the main features of such novel drug delivery devices.

## 4.3 Materials and methods

### 4.3.1 Materials

Diphenyl-(2,4,6-trimethylbenzoyl)-phosphine oxide (TPO), polyethylene glycol diacrylate (PEGDA) 700, triglycerol diacrylate (TGDA), polyethylene glycol (PEG) 300, propylene glycol (PG), polyethylene glycol dimethyl ether (PEGDME), sodium chloride, potassium bicarbonate, theophylline and warfarin were purchased from Sigma-Aldrich, UK. Warfarin sodium was acquired from Glentham Life Sciences Ltd, UK. Fasted state simulated gastric fluid (FaSSGF) and fasted state simulated intestinal fluid (FaSSIF) dissolution media were prepared from FaSSIF/FeSSIF/FaSSGF powder (Biorelevant Ltd, UK). High performance liquid chromatography (HPLC) grade methanol and acetonitrile were purchased from Fisher Scientific. HPLC grade phosphoric acid was obtained from Sigma-Aldrich. Clear resin V4.0 photopolymer was acquired from Formlabs Inc, USA.

### 4.3.2 Development and validation of a HPLC method for theophylline detection

A HPLC method for theophylline detection was developed using an Agilent 1200 HPLC system (Agilent Technologies, Inc. USA) equipped with a G1312A binary pump coupled to a G1314D Variable Wavelength Detector (VWD) and a G1329A auto sampler. A Phenomenex HyperClone Octadecyl-silica (ODS) C18 reverse phase HPLC column (150mm x 4.6mm; 5µm Particle Size) was used as stationary phase. The mobile phase was filtered and vacuum degassed prior to use using a Pall SolVac filter holder equipped with GH Polypro 47mm 0.45µm hydrophilic polypropylene membrane filters. The ultraviolet (UV) detector was set at a wavelength of 271 nm. The injection volume was 20 µL and run time was 10 minutes. A column oven set at 25 °C was used to keep the column temperature stable. A 1.0 mg/mL stock solution was prepared by solubilising 200.00 mg of theophylline accurately weighted in 200.00 mL of mobile phase in a volumetric flask; standards were then produced via serial dilution in mobile phase. Six calibration standards at 500, 250,

125, 62.5, 31.25 and 15.625 µg/mL were produced via serial dilution in mobile phase. Method validation was carried out following ICH Guidelines Q2(R1).

#### ***4.3.3 Development and validation of a HPLC method for warfarin detection***

A HPLC method for warfarin detection was developed using an Agilent 1200 HPLC system equipped with a G1312A binary pump coupled to a G1314D VWD and a G1329A auto sampler. A Phenomenex HyperClone ODS C18 reverse phase HPLC column (150mm x 4.6mm; 5µm particle size) was used as stationary phase. The mobile phase consisted of a mixture of 20 mM phosphoric acid (pH 2.0) and methanol in a ratio of 30:70, respectively. The mobile phase was filtered and vacuum degassed prior use using a Pall SolVac filter holder equipped with GH Polypro 47mm 0.45 µm hydrophilic polypropylene membrane filters. The UV detector was set at a wavelength of 280 nm. The injection volume was 20 µL and run time was 10 minutes. A column oven set at 20 °C was used to keep the column temperature stable. A 500 µg/mL stock solution was prepared by solubilising 25.00 mg of accurately weighted warfarin in mobile phase using a 50 mL volumetric flask; standards were then produced via serial dilution in mobile phase. Method validation was carried out following ICH Guidelines Q2(R1) (ICH, 2005).

#### ***4.3.4 Size reduction of solid fillers***

Sodium chloride and potassium bicarbonate were reduced to fine particles by grinding in a Fritsch Pulverisette 7 ball mill (FRITSCH GmbH, Germany). Powders were individually loaded into agate bowls containing agate balls. The mill was set at a rotational speed of 500 revolutions per minute (rpm). All powders were milled for 5 minutes.

#### ***4.3.5 Particle size distribution analysis of solid fillers***

Particle size and particle size distribution of both unprocessed and milled sodium chloride and potassium bicarbonate were analysed using a Sympatec Helos laser diffraction system (Sympatec GmbH, Germany) equipped with a Rodos disperser and a Vibri feeder. A measuring range R5 (0.5/4.50  $\mu\text{m}$  – 875.00  $\mu\text{m}$ ) was selected. Circa 1 g of powder was used for each experimental run. Particle size was reported as volume mean diameter (VMD). Data were visualised and analysed using Sympatec PAQXOS V5.0.

#### ***4.3.6 Preparation of drug loaded photopolymer resins***

Drug loaded photopolymer resins were prepared by firstly dissolving the PI in the polymer mixture; any liquid or solid fillers were added at the same stage, thus preparing a photopolymer reservoir. Then, the required amount of photopolymer solution or suspension was transferred to a volumetric flask containing an accurately weighed amount of API. All drug loaded photopolymer resins were stirred at room temperature until complete solubilisation of the API. Then, each formulation was vacuum degassed for 5 min to eliminate dissolved air that could cause oxygen-mediated polymerisation inhibition (Ligon *et al.*, 2017). All steps were carried out away from light to avoid polymerisation to occur.

#### ***4.3.7 Determination of drug solubility in polyethylene glycol diacrylate***

Saturated solutions of theophylline, warfarin, and warfarin sodium in PEGDA 700 were prepared by adding drug to the polymer solution until no complete solubilisation was observed after 24 hours under vigorous electromagnetic stirring. Subsequently, the saturated solutions were passed through a 0.45  $\mu\text{m}$  membrane filter and 100  $\mu\text{L}$  aliquots were diluted 1:1000 with mobile phase prior HPLC analysis.

#### ***4.3.8 Determination of drug concentration in photopolymer resin***

100 µL aliquots of drug loaded photopolymer formulations were collected immediately after preparing each formulation. Resin samples were then diluted 1:100 with mobile phase and analysed in HPLC.

#### ***4.3.9 Computer-aided design of solid oral dosage forms***

3D models of solid oral dosage forms were generated using the computer-aided design (CAD) software TinkerCAD (Autodesk Inc, USA). Cylindrical theophylline and warfarin dosage forms were designed in different sizes based on the volume determined using the following equation:

$$V = \pi \times r^2 \times h$$

Where  $r$  is the radius of the cylinder and  $h$  is the height. Dosage forms' 3D models were saved as stereolithography files (.stl) to be exported for 3D printing.

#### ***4.3.10 Stereolithography 3D printing of solid oral dosage forms***

Drug loaded photopolymer resins were transferred to a modified resin tank specifically designed to contain up to 12 different formulations (Curti, Kirby and Russell, 2021). The resin tank was then connected to a Form 2 SLA 3D printer (FormLabs Inc, USA) equipped with a modified build platform (BP) (Curti, Kirby and Russell, 2021). A layer thickness of 100 µm was used for the 3D printing process. Dosage forms were printed directly on the BP, hence no printing supports were used. Once printed, dosage forms were removed from the BP and any uncured resin on their surface was accurately blotted with paper. 3D printed tablets were then assigned a printability score (PS) for printability assessment and stored in the fridge. The PS was based on the printability scale previously described in Chapter III (figure 3.2).

#### ***4.3.11 Determination of drug concentration in 3D printed dosage forms***

Ten 3D printed dosage forms per formulation were crushed using a mortar and pestle, then the finely divided material was transferred to a 100 mL volumetric flask. Acetonitrile was used to extract theophylline and warfarin, while a 50:50 mixture of acetonitrile and deionised water was used to extract warfarin sodium. Samples were kept away from light and continuously stirred for 24 hours. Then, aliquots were collected from each flask and filtered using a 0.45 µm membrane filter prior to HPLC analysis.

#### ***4.3.12 Tablet weight uniformity***

For each successfully 3D printed formulation, ten dosage forms were randomly picked and weighed using a semi-micro balance (Sartorius AG, Germany) with a scale interval of 0.01 mg.

#### ***4.3.13 Tablet friability testing***

Dosage forms friability was established using a Sotax F2 USP Friabilator (Sotax AG, Switzerland). Drum rotation was set at 25 rpm and a total of 100 revolutions were performed. Ten 3D printed dosage forms per each formulation were randomly picked, weighed, and loaded in the drum. At the end of the run, tablets were collected, any residues brushed, and weighed again. Friability data were determined according to the British Pharmacopoeia standards ('British Pharmacopoeia, Appendix XVII G; Friability of Uncoated Tablets; Ph. Eur. method (2.9.7)', 2011).

#### ***4.3.14 Tablet hardness testing***

Dosage forms breaking force was determined using a Copley tablet hardness tester model TBF 1000 (Copley Scientific, Ltd., UK) and a Brookfield CT3 texture analyser (AMETEK Inc., USA) equipped with a 6 mm Magness-Taylor probe. Data from the texture analyser

were collected using Texture Pro CT V1.9 Build 35 (AMETEK Inc., USA). Six 3D printed dosage forms from each formulation were randomly picked and analysed. A 3D printed shield was specifically designed to fit in the texture analyser and fabricated to protect the operator from potential high speed fragments originating from the tested samples (figure 4.1).

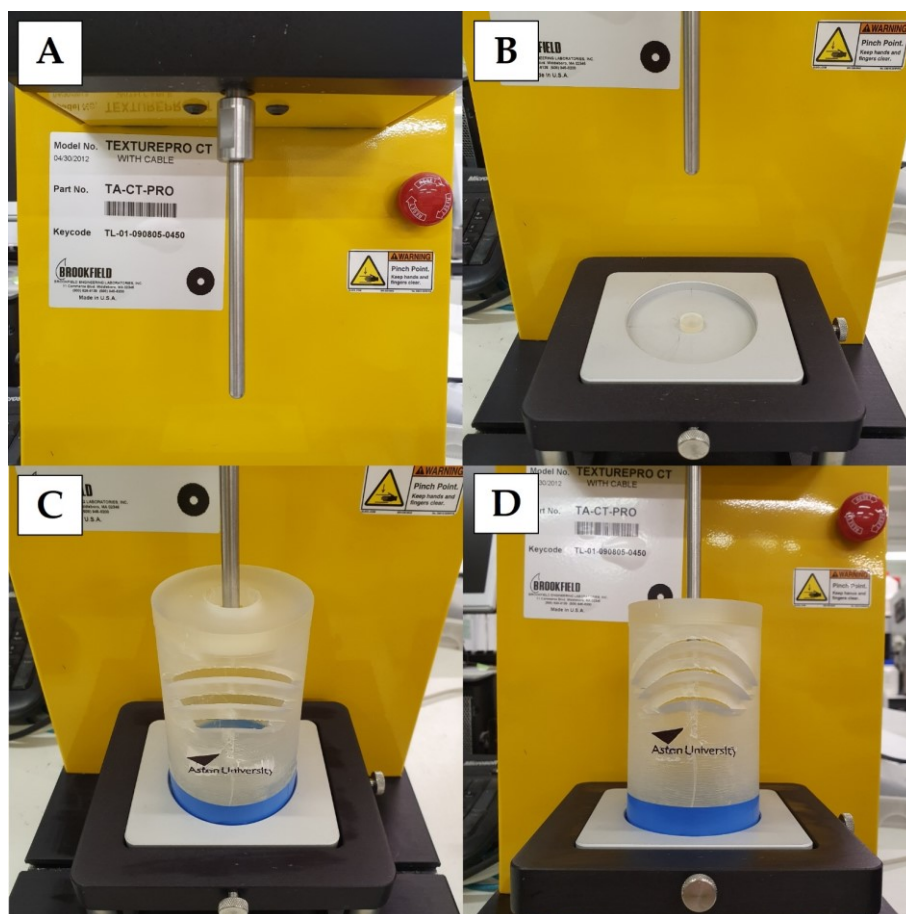


**Figure 4.1.** (A) 6 mm Magness-Taylor probe mounted on a Brookfield CT3 texture analyser; (B) 3D printed tablet placed on the testing plate; (C-D) 3D printed shield designed to fit on the testing plate and protect the operator from any fragments.

#### ***4.3.15 Dissolution testing of 3D printed dosage forms***

Dissolution profiles data were obtained using a USP type I -II dissolution testing apparatus (Erweka GmbH, Germany). For theophylline, the USP protocol for dissolution testing of extended-release capsules was followed. The protocol involved the use of 900 mL of two

different media, pH 1.2 simulated gastric fluid for the first hour and pH 6.0 phosphate buffer for the remaining 7 hours. A USP type-II apparatus equipped with paddles set at a speed of 50 rpm was used. Dissolution media were prepared based on the USP recommendations in the section 'Reagents, indicators, solutions' (U.S. Pharmacopoeial Convention, 2011). Dissolution apparatus operated at  $37 \pm 0.5$  °C and samples were collected every hour using 5 mL Luer tip glass syringes.

For warfarin and warfarin sodium formulations, two different dissolution conditions were investigated. First, the USP monograph for warfarin sodium was followed and 450 mL of purified water were used as dissolution medium. A USP type-II apparatus equipped with paddles set at a speed of 50 rpm was used. A second investigation consisted of a novel protocol based on the use of a biorelevant dissolution media, with dosage forms being placed in type-I apparatus baskets, set at 100 rpm. Dissolution data were collected in FaSSGF for the first 3 hours and in FaSSIF for the subsequent 5 hours, for a total of 8 hours. Dissolution apparatus operated at  $37 \pm 0.5$  °C. Dissolution profiles for raw warfarin and warfarin sodium were also obtained as a comparison with the 3D printed dosage forms.

Samples were collected every hour using 5 mL Luer tip glass syringes; for 24 hours dissolution studies, extra data point were acquired at 12 and 24 hours. 5 mL samples were withdrawn at each time point and replaced with pre-warmed dissolution medium to keep sink conditions.

#### ***4.3.16 Swelling ratio and sol-fraction determination***

To determinate swelling ratio, 3D printed drug loaded dosage forms were weighed before and immediately following dissolution testing after wiping off the excess of dissolution medium with paper. Swelling ratio was calculated according to the following equation:

$$\% \text{ Swelling Ratio} = \frac{(W_s - W_i)}{W_i} \times 100$$

Where  $W_s$  is the weight of the swollen sample after dissolution testing, and  $W_i$  is the initial weight of the dosage form.

Sol-fraction was calculated according to the following equation:

$$\% \text{ Sol fraction} = \frac{(W_i - W_d)}{W_i} \times 100$$

Where  $W_i$  is the initial weight of the dosage form, and  $W_d$  is the weight of the dry sample recorded 24 hours after the dissolution testing was completed. The drying process was carried out at room conditions.

#### ***4.3.17 Determination of liquid fillers leakage***

Formulations containing PG and PEG 300 as liquid fillers were investigated to evaluate any potential leak of the liquid, unreacted filler over time. A total of seven 3D printed formulations were tested. Three dosage forms per each formulation were weighed and their diameter and height measured by using a digital calliper. Then, each sample was individually placed onto a 55 mm filter paper disk (VWR International, USA) situated into a 100 mL diamond weighing boat (VWR International, USA) as shown in figure 4.2.



**Figure 4.2.** 3D printed dosage form placed on filter paper to investigate potential leakage of the liquid fillers from the crosslinked structure.

The samples were then left at room condition protected from light for one week. Afterwards, dosage forms were weighed, and their size measured again to be compared to the initial values. The drug loss resulted from a potential leak of liquid filler was determined via HPLC. Each filter paper disk was placed into 25 mL volumetric flask and extracted in mobile phase (20 mM phosphoric acid at pH 2.0 and methanol, 30:70) for 12 hours under vigorous electromagnetic stirring.

#### ***4.3.18 Weight uniformity determination of manually split tablets***

Conventional commercially available 1 mg and 5 mg warfarin sodium tablets were obtained from Crescent Pharma Ltd, UK. Ten tablets of each strength were individually weighed. Then, each tablet was manually split through its groove to obtain a total of 20 halves per strength. Each half tablet was weighed separately. Then, 10 tablet halves for each strength were split to obtain a total of 20 quarters, and each quarter was weighed separately. The percentage dose loss due to splitting was calculated from the weight of the resulting two tablet halves and four tablet quarters by comparing their sum against the original whole tablet weight. Dosage accuracy of tablet halves and quarters was calculated by estimating the theoretical drug content in the tablet fragment mass, according to the manufacturer label claim. Then, the number of tablet halves and quarters outside the 85% to 115% range and 75 to 125% was counted (Teng *et al.*, 2002).

#### ***4.3.19 Optical microscopy imaging***

A Zeiss Axio Vert.A1 microscope equipped with a AxioCam MR monochrome camera was used to take images of various sample types. All images were acquired using a magnification of  $\times 10$ .

#### ***4.3.20 Fourier-transform infrared spectroscopy***

Fourier-transform infrared spectroscopy (FTIR) was used to determine the presence of any acrylate residues in the 3D printed dosage forms. Samples were taken from the surface and at the core of the tablet and pulverised using a mortar and pestle. Circa 5 mg of each sample were analysed using a Nicolet™ iS™ 5 FTIR Spectrometer (Thermo Fisher Scientific Inc, USA) equipped with an iD5 monolithic diamond Attenuated Total Reflectance (ATR) crystal. FTIR spectra were visualised and processed using software OMNIC V9.0 software (Thermo Fisher Scientific Inc, USA). Liquid PEGDA 700 was used to identify a reference spectrum featuring the acrylate group.

#### ***4.3.21 Differential scanning calorimetry***

Thermal analysis of SLA 3D printed drug loaded dosage forms was carried out by Differential scanning calorimetry (DSC) using a TA Q200 (TA instruments - Waters, USA). 3D printed tablets were pulverised using a mortar and pestle, then an accurately weighed sample amount (5 mg) was transferred into TA Tzero low-mass aluminium pan (sensitivity for a minimum sample size of 0.5 mg). Samples were heated in the range of 50–300 °C at a scanning rate of 10 °C/min under nitrogen airflow of 50 mL/min. TA universal analysis 2000 software (version 4.5) was used to analyse the resulting DSC thermograms.

#### ***4.3.22 X-ray powder diffractometry***

The X-ray powder diffraction (XRPD) patterns were collected using an Empyrean diffractometer (Malvern Panalytical Ltd, UK) with Cu K $\alpha_1$  and K $\alpha_2$  radiation ( $\lambda = 1.5406$  Å and 1.5444 Å) over the  $2\theta$  range 5–70°, using a step size of 0.026° and a scan speed of 0.040° s<sup>-1</sup>. Selected 3D printed dosage forms were pulverised using a mortar and pestle and circa 20 mg of powdered material per sample were analysed, together with the raw APIs, the PI, and a non-drug loaded SLA 3D printed tablet.

#### ***4.3.23 Scanning electron microscopy imaging***

Scanning electron microscopy (SEM) images of the surface and cross-section images of selected 3D printed dosage forms were captured with a TESCAN Vega3 (TESCAN UK, Ltd) to evaluate the microstructure of the devices. The voltage and working distance were set at 10.0 kV and 18 mm, respectively. Seven images were collected from each sample. A magnification of  $\times 40$  and  $\times 200$  was used for the images taken at the surface while for images of the internal structure it was set at  $\times 40$ ,  $\times 100$ ,  $\times 200$ ,  $\times 1000$  and  $\times 5000$ .

#### ***4.3.24 Raman spectroscopy imaging***

A RA802 Pharmaceutical Analyser was used for Raman analysis (Renishaw Plc, UK). StreamLine™ and LiveTrack™ technologies were used to acquire Raman images of 3D printed dosage forms. StreamLine™ image acquisition configuration included laser wavelength set to 785 nm, grating set at 1500 lines per mm, and a spectral range of  $600\text{ cm}^{-1}$  to  $1885\text{ cm}^{-1}$ . Step size was set to  $5\text{ }\mu\text{m}$  and a total of circa 50,000 spectra were collected for each map. For surface mapping, the tablet was put straight onto the sample holder. For core mapping, a sharp scalpel was used to cut the tablet and expose the core; the sample was then placed onto the sample holder. Raman maps of tablet core and surface were also collected after dissolution testing in deionised water ( $T = 37^\circ\text{C}$ ) for 24 hours at 50 rpm. Non-Negative Least Squares (NNLS) component analysis was used to generate Raman images using reference spectra of the materials within the sample. Images are based on NNLS scores, which indicate the correlation between each map spectrum and each reference spectrum.

Using NNLS component analysis with “no normalization” allowed for quantitative data collection in the form of concentration estimates. Concentration estimates are defined as percentage values derived from the least squares fitting of multiple reference spectra at all points in the analysed area. The values are related to the concentration of species relative to each other, dependent on the particle shapes, sizes, and depths.

## 4.4 Results and Discussion

### 4.4.1 Development and validation of a HPLC method for theophylline detection

A HPLC method for theophylline detection was developed and validated based on the method previously described by Kanakal and co-workers (Kanakal *et al.*, 2014). The original method involved a reverse phase ODS (C18) column (150 × 4.6mm; 5µm particle size) as stationary phase and a mobile phase consisting in water, acetonitrile, and methanol at the ratio of 90:03:07, respectively. This method was selected by virtue of the mobile phase used; in fact, salts and acids used in buffer solutions might dramatically affect HPLC columns lifespan and therefore a buffer-free mobile phase results in an advantageous approach to preserve columns (Phenomenex, 2010). Furthermore, the high percentage of water over organic solvents in the mobile phase allows economical and environmentally friendly analyses.

Following the method described by Kanakal, a sample containing 0.500 mg/mL of theophylline dissolved in mobile phase was ran in HPLC and the chromatogram produced showed a retention time (RT) of 9.208 min (figure 4.3).

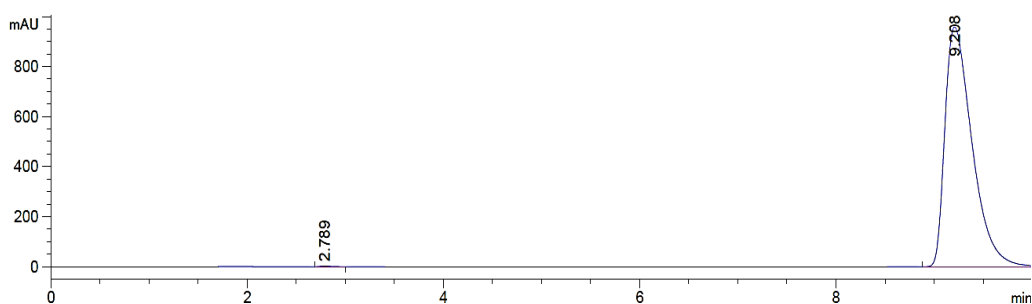


**Figure 4.3.** HPLC chromatogram of 0.500 mg/mL theophylline in mobile phase showing a retention time of 9.208 minutes produced following the method described by Kanakal (2014) using a mobile phase consisting in a mixture of water, acetonitrile, and methanol (90:03:07).

Although the signal produced was clear and no noise was observed, the resulting peak was slightly broad, and a modest tailing was observed. Also, the RT was considerably longer

than the value reported in literature (Kanakal *et al.*, 2014). With the aim to speed up the analysis and improve peak's shape, the mobile phase composition was changed to a mixture of water, acetonitrile, and methanol at a ratio of 80:06:14 and the flow rate was set at 1.5 mL/min. Decreasing the water percentage would result in a decreased polarity of the mobile phase and a faster elution of theophylline. Six calibration standards were produced via serial dilution of a 1.00 mg/mL stock solution and were ran in triplicates to produce a calibration curve (figure 4.4).

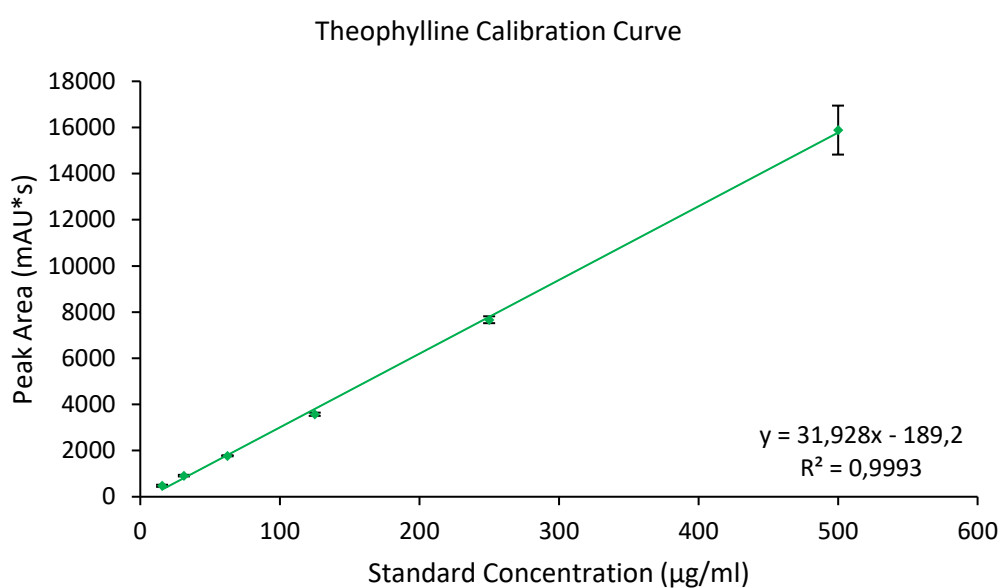


**Figure 4.4.** Calibration curve produced modifying the method reported by Kanakal running six calibration standards. The mobile phase used consisted in a mixture of water, acetonitrile, and methanol (80:06:14); flow rate was set at 1.5 mL/min. The calibration range was 15.625-500 µg/mL. Results were generated from triplicates (n=3). Error bars indicate standard deviation.

Although the resulting calibration curve showed a good linearity with a  $R^2$  value of 0,9993 (figure 4.4), there was no consistency in the retention time (figure 4.5). This was accounted to the column age and the resulting increase and instability in pressure.

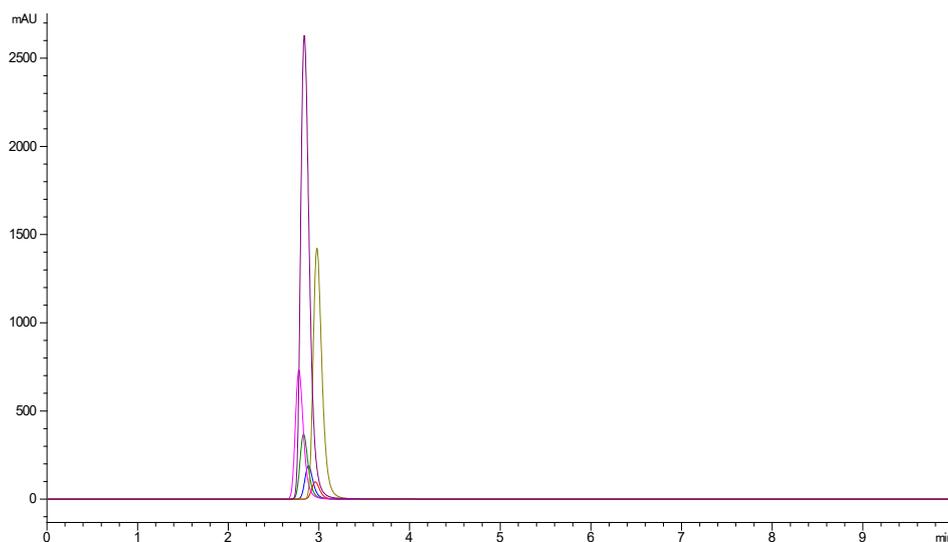


**Figure 4.5.** Chromatogram of six calibrations standards produced modifying the method reported by Kanakal. The mobile phase used consisted in a mixture of water, acetonitrile, and methanol (80:06:14); flow rate was set at 1.5 mL/min. Overlaid peaks highlight inconsistency in retention time.

In order to achieve consistent and reliable analyses, a brand new Phenomenex HyperClone ODS (C18) reverse phase HPLC column (150 × 4.6mm; 5µm particle size) was used to run six calibration standards again. The mobile phase was a mixture of water, acetonitrile, and methanol (80:06:14) and the flow rate was set at 1.5 mL/min. Retention time was found to be consistent (figure 4.6); however, a RT of 2.3 min was considered as potentially too short to achieve efficient separation when detecting theophylline from dosage forms containing different excipients.

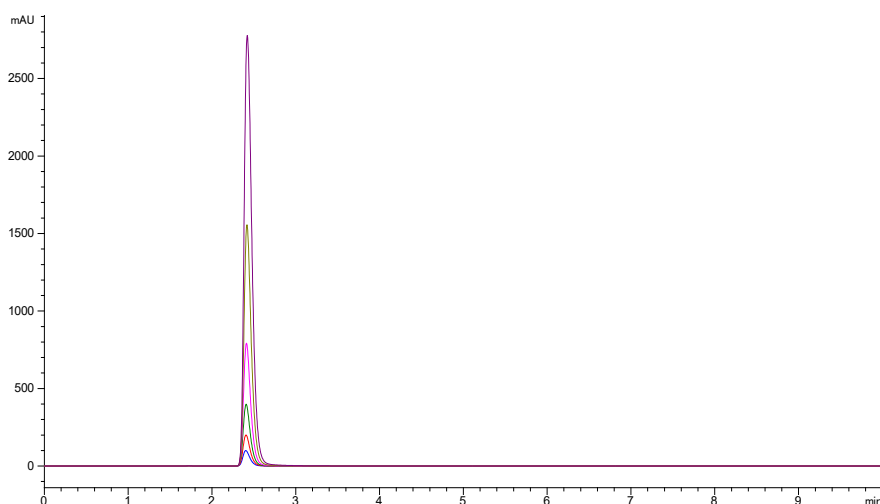


**Figure 4.6.** Chromatogram of six calibrations standards produced modifying the method reported by Kanakal (2014) and using a brand new Phenomenex reverse phase C18 HPLC column. The mobile phase used was a mixture of water, acetonitrile, and methanol (80:06:14); flow rate was set at 1.5mL/min. Consistency in retention time was observed.

In order to increase the retention time, the mobile phase polarity was slightly increased using a mixture of water, acetonitrile, and methanol (90:03:07). Six calibration samples were ran at a flow rate of 1.5 mL/min. A consistent retention time of 5.665 min was achieved (figure 4.7).

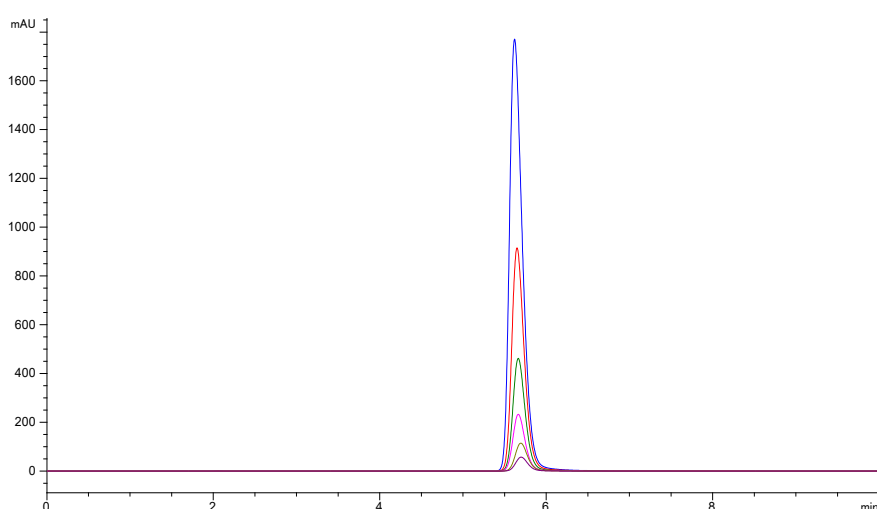


**Figure 4.7.** Chromatogram of six calibrations standards produced using a mobile phase of water, acetonitrile, and methanol (90:03:07) as described by Kanakal (2014), and a flow rate of 1.5mL/min. The chromatogram shows a consistent retention time of 5.665 min.

Having identified suitable conditions to detect theophylline, a new calibration curve was produced using six calibration standards produced via serial dilution of a 1.00 mg/mL stock solution. The calibration curve (figure 4.8) showed excellent linearity with a  $R^2$  value of 1.

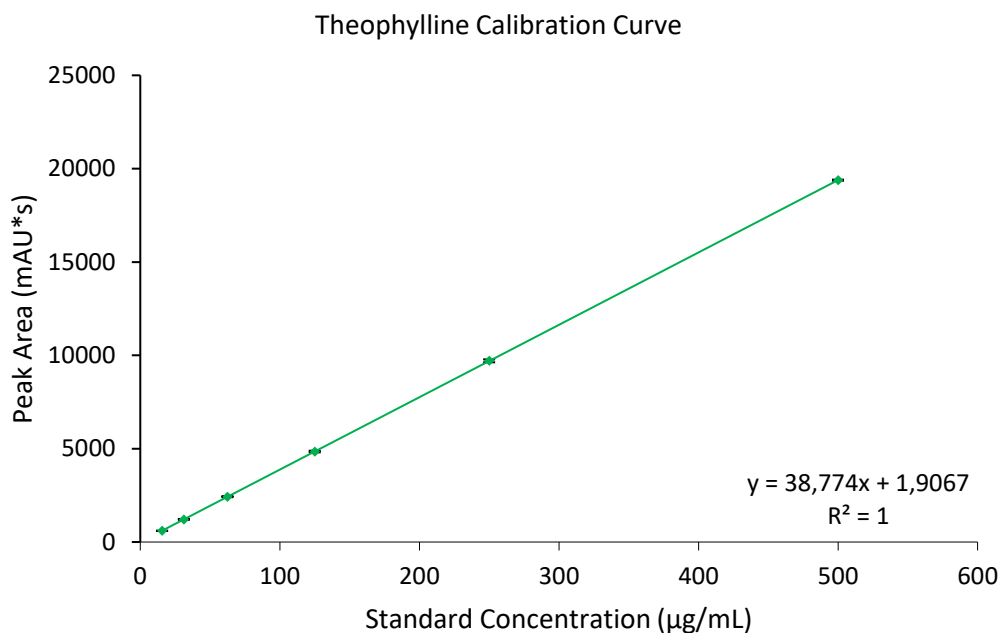


**Figure 4.8.** Calibration curve for HPLC detection of theophylline produced using a mobile phase consisting in a mixture of water, acetonitrile, and methanol (90:03:07) and a flow rate set at 1.5 mL/min. Results were generated from triplicates ( $n=3$ ). Error bars indicate standard deviation.

Regression residuals were determined (figure 4.9) and used to calculate uncertainty of the regression line. Data analysis was carried out considering the calibration curve in figure 4.8. Results are indicated in table 4.1.

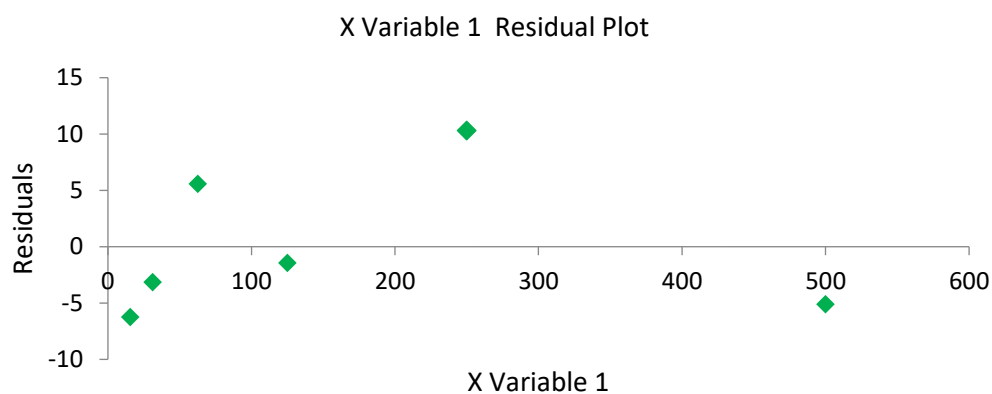


**Figure 4.9.** Regression residuals from calibration curve in figure 4.8. Regression residuals were used to determinate the uncertainty of the regression line.

**Table 4.1.** Linear regression analysis results of the calibration curve reported in figure 4.8.

Slope $b$	38.77404295	Intercept $a$	1.906667562
Standard error of the slope $sb$	0.017635741	Standard error of the intercept $sa$	4.156276596
Correlation coefficient $R^2$	0.999999173	Standard error of the regression $S_{y/x}$	7.30879519
Fisher's $F$	4833867.519	Degrees of freedom $\nu$	4
Sum of the squares of the regression	258217889.9	Sum of the squares of the residuals	213.6739485

Having developed a suitable calibration curve, the method was tested for its ability to recover theophylline from formulations consisting of solutions containing the PI TPO in order to exclude any interferences. Formulations containing 25  $\mu\text{g/mL}$  and 100  $\mu\text{g/mL}$  of theophylline and 0.1% w/v of TPO were produced in mobile phase and analysed. No peaks related to TPO were seen; recovery results are reported in table 4.2.

**Table 4.2.** Theophylline formulations spiked with TPO tested for recovery accuracy. All the formulations were prepared using mobile phase.

Theophylline Sample Concentration	Photoinitiator concentration	Mean Recovery
25.00 $\mu\text{g/mL}$	TPO (0.1% w/w)	103.54 %
100.00 $\mu\text{g/mL}$	TPO (0.1% w/w)	99.78 %

Having established its suitability for theophylline detection, the method was validated according to the ICH Guidelines Q2 (R1) (ICH, 2005).

Method's specificity was investigated by running blank mobile phase and a theophylline spiked sample. The relative chromatograms were compared to exclude presence of peaks overlaying theophylline's peak (figure 4.10).

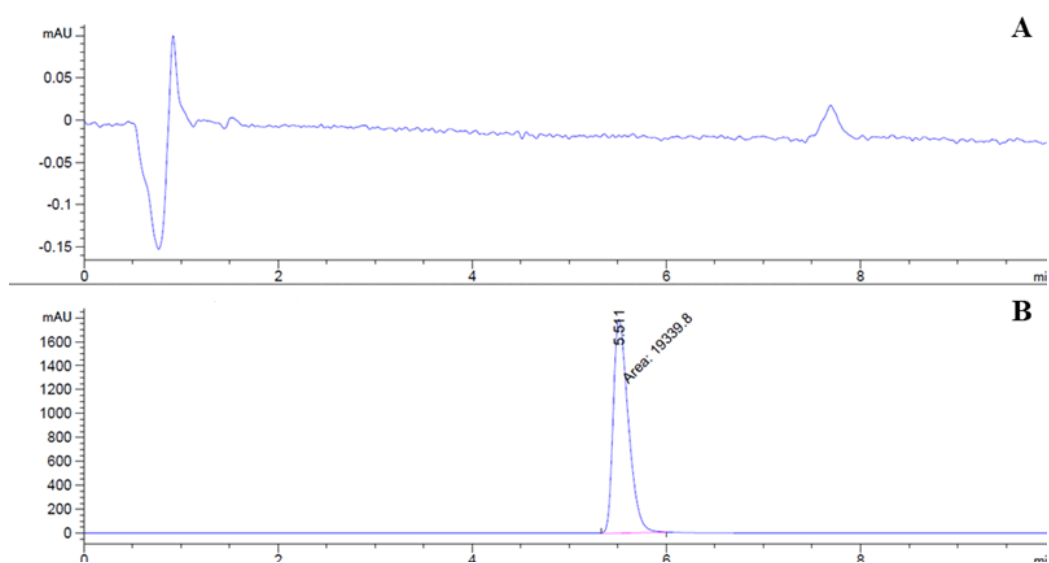


**Figure 4.10.** Comparison of the chromatograms produced by running blank mobile phase (A) and 0.500 mg/mL theophylline in mobile phase (B).

Accuracy of the method was assessed by analysing three theophylline samples having a known concentration of 50.00  $\mu\text{g/mL}$ , 100.00  $\mu\text{g/mL}$ , and 250.00  $\mu\text{g/mL}$ . Each sample was analysed in triplicates. Samples' concentration was within the calibration range and theophylline recovery was calculated based on the calibration curve previously produced (figure 4.8). Accuracy results are reported in table 4.3.

**Table 4.3.** Theophylline HPLC method accuracy data. Accuracy was assessed using nine determinations over three concentration levels. Results are reported as percent recovery in accordance with the ICH Q2(R1) guidelines.

Theophylline standard concentration	Mean Recovery (n=3)
50.00 µg/mL	97.12 %
100.00 µg/mL	97.71 %
250.00 µg/mL	99.70 %

An investigation of the precision of the method was carried out by assessing repeatability. Nine determinations (three theophylline concentrations, analysed in triplicates) were used in accordance with the ICH Q2(R1) guidelines. Precision results are reported in table 4.4.

**Table 4.4.** Theophylline HPLC method precision assessment. Results are expressed as analyte concentration found, standard deviation (SD), relative standard deviation (RSD), and confidence interval. Concentrations values are expressed as µg/mL.

Theophylline standard concentration	Concentration found (Mean ± SD)	RSD	Confidence interval
50.00 µg/mL	50.03 ± 0.72	1.44 %	± 0.82
100.00 µg/mL	99.10 ± 1.38	1.39 %	± 1.56
250.00 µg/mL	248.21 ± 4.06	1.63 %	± 4.59

The detection limit (DL) of the method was determined based on the standard deviation of the y-intercept and the slope. DL indicates the minimum analyte concentration that can be detected as a distinguished signal from the background noise. According to the ICH Guidelines Q2 (R1), the DL can be determined as:

$$DL = \frac{3.3 \sigma}{S}$$

where  $\sigma$  is the standard deviation of the y-intercept and S is the slope of the calibration curve (figure 4.8).

According to this, the theophylline detection limit for the method was found to be 0.35  $\mu\text{g/mL}$ .

The quantification limit (QL) of the method was determined based on the standard deviation of the y-intercept and the slope. Quantification limit is the minimum analyte concentration that can be accurately determined from a sample. QL is calculated as:

$$\text{QL} = \frac{10 \sigma}{S}$$

where  $\sigma$  is the standard deviation of the y-intercept and S is the slope of the calibration curve (figure 4.8).

According to this, the theophylline quantification limit for the method was found to be 1.07  $\mu\text{g/mL}$ .

To summarise, a specific, accurate, and precise method for theophylline detection and quantification in SLA resin formulations and final 3D printed dosage forms has been developed and validated according to the ICH Q2(R1) guidelines (table 4.5). Having available an analytical method suitable for the intended purpose, the next step is the development of theophylline loaded photopolymer resins for SLA 3D printing.

**Table 4.5.** Theophylline method validation procedure.

<b>Specificity</b>	Blank mobile phase samples and theophylline spiked samples were ran to exclude presence of peaks overlaying analyte's peak (figure 4.10).
<b>Accuracy</b>	Recovery from 50.00 µg/mL, 100.00 µg/mL and 250.00 µg/mL theophylline samples was found to be 97.12%, 97.71% and 99.70%, respectively.
<b>Linearity</b>	A calibration curve covering a range from 15.625 µg/mL to 500 µg/mL was produced. Response for the detector was found to be linear over the calibration range. $R^2 = 1$ . $Sy/x = 7.31$ .
<b>Precision</b>	Precision of the method was assessed in terms of repeatability. Results reported in table 4.4.
<b>Detection Limit</b>	0.35 µg/mL.
<b>Quantification Limit</b>	1.07 µg/mL.

#### ***4.4.2 Development and validation of a HPLC method for warfarin detection***

A HPLC method for warfarin detection was developed based on the API manufacturer suggestion for analysis (SIGMA-ALDRICH, 2020). Such method involved the use of a C18 column measuring 150 mm (length) × 4.6 mm (internal diameter) with a particle size of 5 µm as stationary phase; the column was kept at a temperature of 35°C. The mobile phase used was a mixture of 20 mM phosphoric acid (pH 2.0) and methanol (30:70).

The method described above was used to analyse a 500 µg/mL warfarin sample dissolved in mobile phase and ran into HPLC. The chromatogram obtained showed a neat peak with a RT of 2.543 min (figure 4.11).

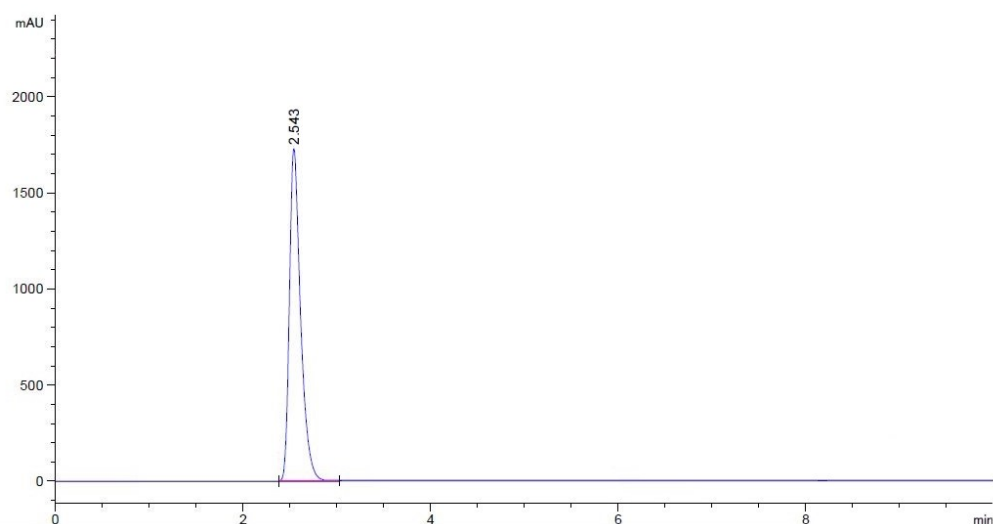


**Figure 4.11.** HPLC chromatogram of 500 µg/mL warfarin in mobile phase (20 mM phosphoric acid and methanol, 30:70) showing a retention time of 2.543 minutes.

Although the method used allowed to obtain a good peak shape, the analyte elution at 2.543 min was considered too rapid and a potential source of poor separation in multicomponent samples.

As a result, a first line of intervention consisted in lowering the column temperature to 20°C with the view to increase the RT without changing the composition of the mobile phase (figure 4.12).

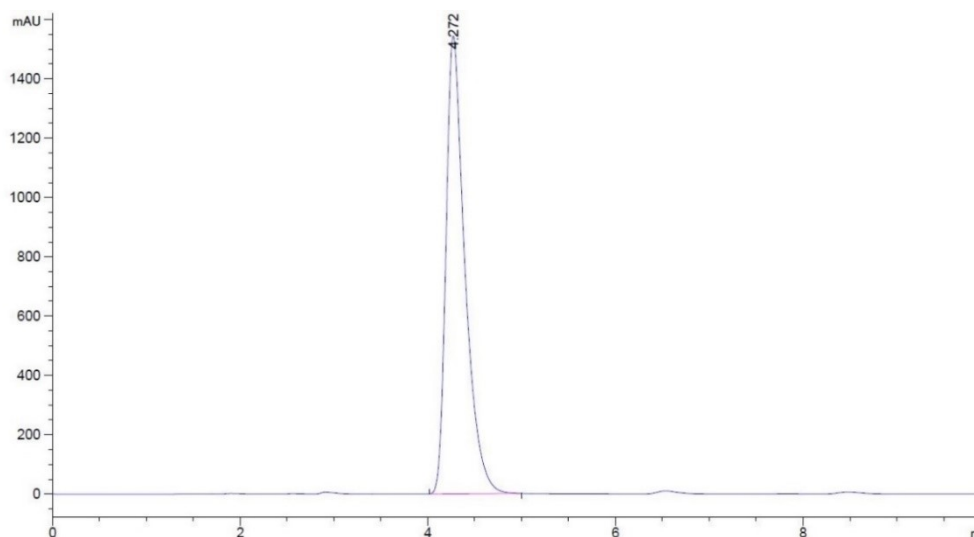


**Figure 4.12.** HPLC chromatogram of 500 µg/mL warfarin in mobile phase (20 mM phosphoric acid and methanol, 30:70) showing a retention time of 4.272 minutes. This was obtained by lowering column temperature to 20°C.

The change in column temperature allowed to obtain a neat warfarin peak, this time with a RT of 4.272 min. Consistency in the RT was also observed, an indicator of the good operative conditions of the HPLC system under the method parameters used.

Having obtained a clear signal and a good peak shape, the next step consisted in running into HPLC a series of six calibration standards with the aim to produce a calibration curve (figure 4.13). The calibration standards were produced via serial dilution in mobile phase and had a concentration of 250, 125, 50, 5, 0.50 and 0.25 µg/mL. The resulting calibration curve showed excellent linearity as indicated by a  $R^2$  value of 1 (figure 4.13).

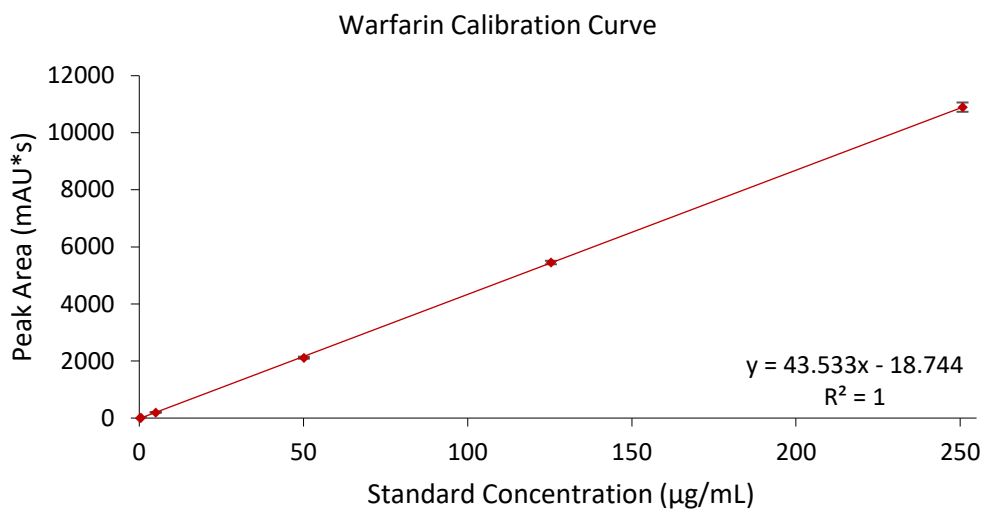


**Figure 4.13.** Calibration curve from warfarin standards analysis. Results were generated from triplicates (n=3). Error bars indicate standard deviation.

Regression residuals were determined (figure 4.14) and used to calculate uncertainty of the regression line. Data analysis was carried out considering the calibration curve in figure 4.13. Results are indicated in table 4.6.

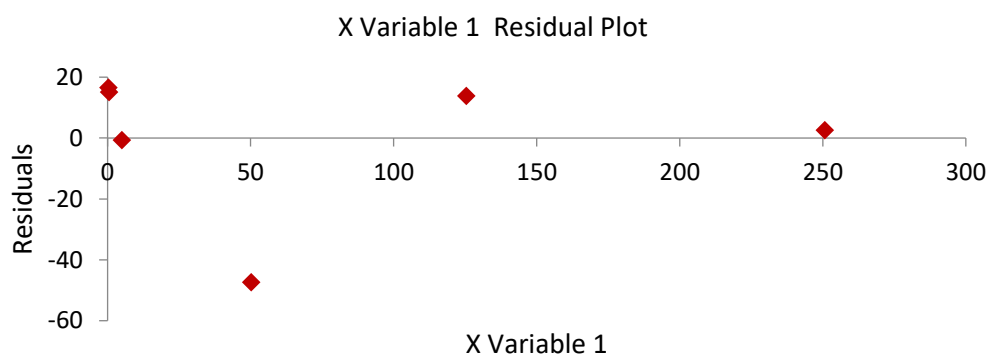


**Figure 4.14.** Regression residuals from calibration curve in figure 4.13. Regression residuals were used to determinate the uncertainty of the regression line.

**Table 4.6.** Linear regression analysis results of the calibration curve reported in figure 4.13.

Slope $b$	43.5331	Intercept $a$	-18.7441
Standard error of the slope $sb$	0.1214	Standard error of the intercept $sa$	14.11483
Correlation coefficient $R^2$	1.0000	Standard error of the regression $Sy/x$	27.14816
Fisher's $F$	128596.64	Degrees of freedom $v$	4
Sum of the squares of the regression	94778608	Sum of the squares of the residuals	2948.09

Having developed a suitable calibration curve, the method was tested for its ability to recover warfarin from formulations containing the PI TPO in order to exclude any interferences that could arise in samples of 3D printed dosage forms. Two formulations containing 5.0  $\mu\text{g/mL}$  and 50.0  $\mu\text{g/mL}$  of warfarin, respectively, and 0.05% w/w TPO were produced in mobile phase and ran into HPLC. No peaks related to TPO were seen; warfarin recovery is shown in table 4.7.

**Table 4.7.** Warfarin recovery from formulations containing 0.05% TPO w/w. Recovery results excluded interferences due to the presence of the PI.

<b>Warfarin Samples Concentration</b>	<b>Photoinitiator concentration</b>	<b>Mean Recovery</b>
5.0 $\mu\text{g/mL}$	TPO (0.05% w/v)	100.04 %
50.0 $\mu\text{g/mL}$	TPO (0.05% w/v)	99.46 %

Having established its suitability for warfarin detection, the method was validated according to the ICH Guidelines Q2 (R1).

Method's specificity was investigated by running blank mobile phase and a warfarin spiked sample. The relative chromatograms were compared to exclude presence of peaks overlaying warfarin peak (figure 4.15).

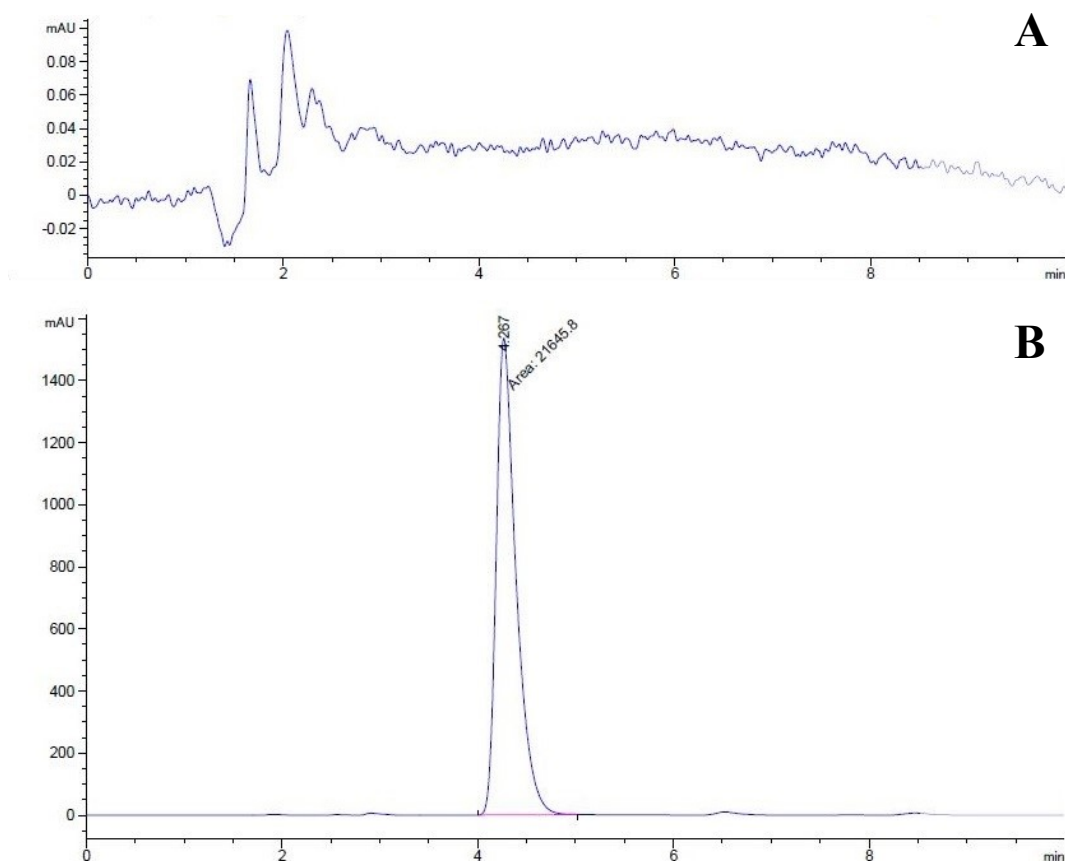


**Figure 4.15.** Comparison of the chromatograms produced by running blank mobile phase (A) and 0.500 mg/mL warfarin in mobile phase (B).

Accuracy of the method was assessed by analysing three warfarin samples with a known concentration of 5.00 µg/mL, 25.00 µg/mL, and 50.00 µg/mL. Each sample was analysed in triplicates. Samples' concentration was within the calibration range and warfarin recovery was calculated based on the calibration curve previously produced (figure 4.13). Accuracy results are reported in table 4.8.

**Table 4.8.** Warfarin HPLC method accuracy data. Accuracy was assessed using nine determinations over three concentration levels. Results are reported as percent recovery in accordance with the ICH Q2(R1) guidelines.

Warfarin standard concentration	Mean Recovery (n=3)
5.00 µg/mL	96.99 %
25.00 µg/mL	100.54 %
50.00 µg/mL	101.22 %

An investigation of the precision of the method was carried out by assessing repeatability. A total of nine determinations covering a range of three warfarin concentrations were used; precision results are reported in table 4.9. Greater variability was observed for the 5 µg/mL warfarin sample, as explained by the closeness to the QL value (3.24 µg/mL).

**Table 4.9.** Warfarin HPLC method precision assessment. Results are expressed as analyte concentration found, standard deviation, relative standard deviation, and confidence interval. Concentrations values are expressed as µg/mL.

Warfarin standard concentration	Concentration found (Mean ± SD)	RSD	Confidence interval
5.00 µg/mL	4.85 ± 0.11	2.19 %	± 0.12
25.00 µg/mL	25.11 ± 0.46	1.85 %	± 0.52
50.00 µg/mL	50.60 ± 0.99	1.95 %	± 1.12

DL of the method was determined based on the standard deviation of the y-intercept and the slope. DL indicates the minimum analyte concentration that can be detected as a distinguished signal from the background noise. According to the ICH Guidelines Q2(R1), the DL can be determined as:

$$DL = \frac{3.3 \sigma}{S}$$

where  $\sigma$  is the standard deviation of the y-intercept and S is the slope of the calibration curve (figure 4.13). Detection limit of warfarin for the method developed was 1.07 µg/mL.

QL of the method was determined based on the standard deviation of the y-intercept and the slope. Quantification limit is the minimum analyte concentration that can be accurately determined from a sample. QL is calculated as:

$$QL = \frac{10 \sigma}{S}$$

where  $\sigma$  is the standard deviation of the y-intercept and S is the slope of the calibration curve (figure 4.13). Quantification limit of warfarin for the method developed was 3.24 µg/mL.

In summary, a specific, accurate and precise method for warfarin detection in SLA resin formulations and 3D printed dosage forms has been developed and validated according to the ICH guidelines (table 4.10).

**Table 4.10.** Warfarin method validation procedure.

<b>Specificity</b>	Blank mobile phase samples and warfarin spiked samples were run to exclude presence of peaks overlaying analyte's peak (figure 4.15).
<b>Accuracy</b>	Recovery from 5.00 µg/mL, 25.00 µg/mL, and 50.00 µg/mL warfarin samples was found to be 96.99%, 100.54% and 101.22% respectively.
<b>Linearity</b>	A calibration curve covering a range from 0.25 µg/mL to 250.00 µg/mL was produced. Response for the detector was found to be linear over the calibration range. $R^2 = 1$ . $Sy/x = 27.14816$ .
<b>Precision</b>	Precision of the method was assessed in terms of repeatability. Results reported in table 4.9.
<b>Detection Limit</b>	1.07 µg/mL.
<b>Quantification Limit</b>	3.24 µg/mL.

#### **4.4.3 Particle size reduction and distribution analysis of solid fillers**

Sodium chloride and potassium bicarbonate were used as solid fillers for SLA 3D printed dosage forms. In order to evaluate their potential to affect drug release, they were loaded into the photopolymer resin either as received or milled. A ball mill was used for the size reduction operation and all powdered samples were then analysed through a laser-diffraction particle sizer to better characterise the size distribution of the material (figures 4.16-4.17).

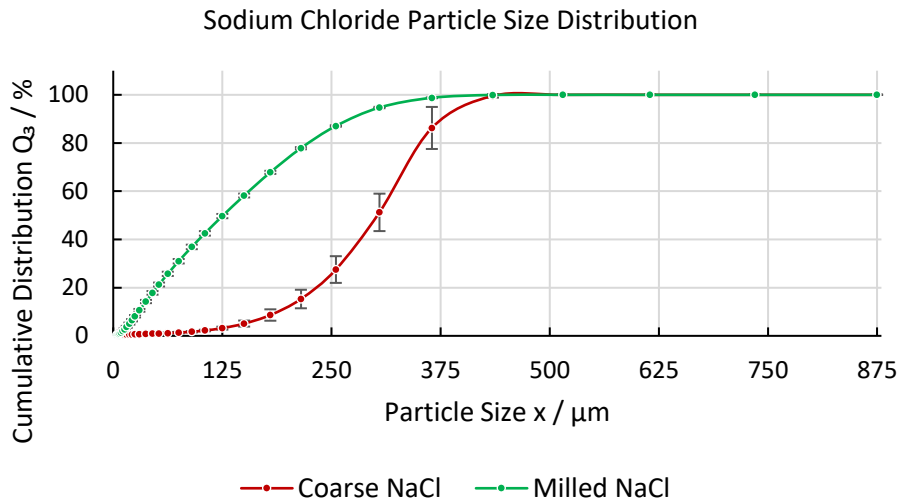


**Figure 4.16.** Particle size distribution analysis of coarse NaCl (VMD = 291.72 μm) and ball milled NaCl (VMD = 140.12 μm). Error bars indicate standard deviation of the measurement (n=3).

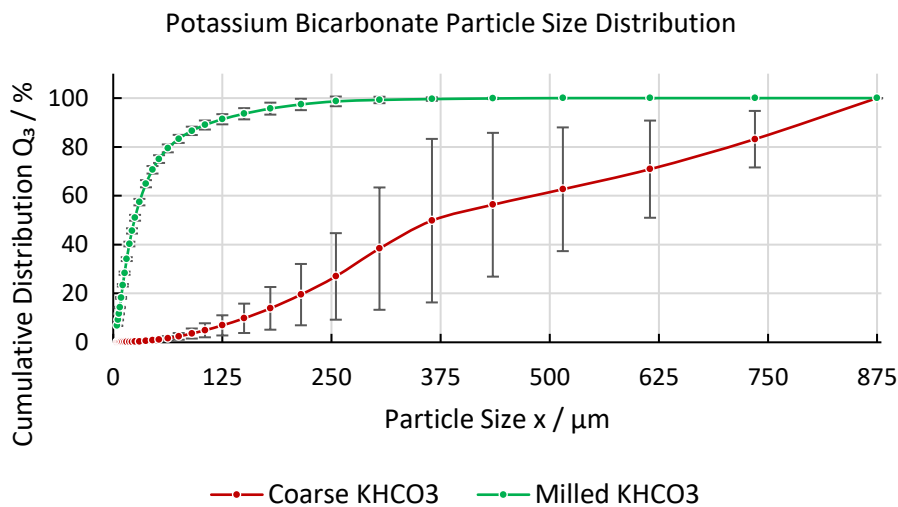


**Figure 4.17.** Particle size distribution analysis of coarse KHCO<sub>3</sub> (VMD = 436.91 μm) and ball milled KHCO<sub>3</sub> (VMD = 45.44 μm). Error bars indicate standard deviation of the measurement (n=3).

Images of sodium chloride and potassium bicarbonate particles were taken using a light microscope before carrying out any size reduction operation in an attempt to visualise sample homogeneity. Sodium chloride crystal size appeared to be more uniform as also indicated by the SD of particle size distribution (figures 4.16, 4.18). On the contrary,

potassium bicarbonate was characterised by a much larger particle size distribution range, as readily seen from the microscopy analysis (figure 4.19) and the high SD obtained in the particle size measurement (figure 4.17).

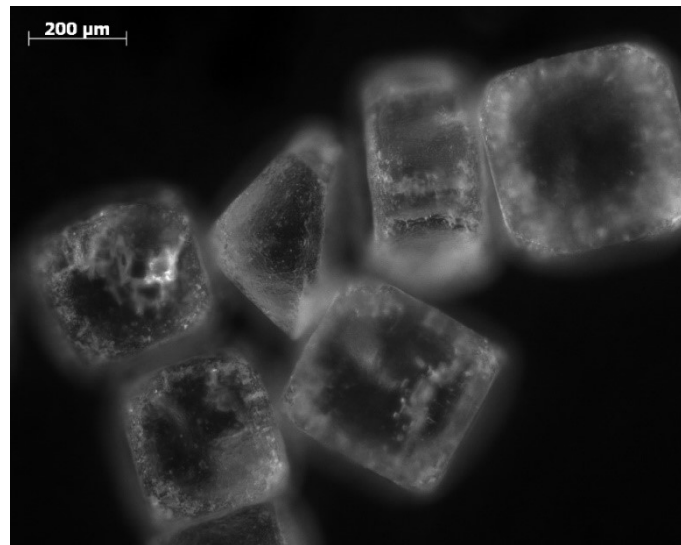


**Figure 4.18.** Light microscope image of coarse sodium chloride. Particle size within the sample was observed to be generally homogeneous.

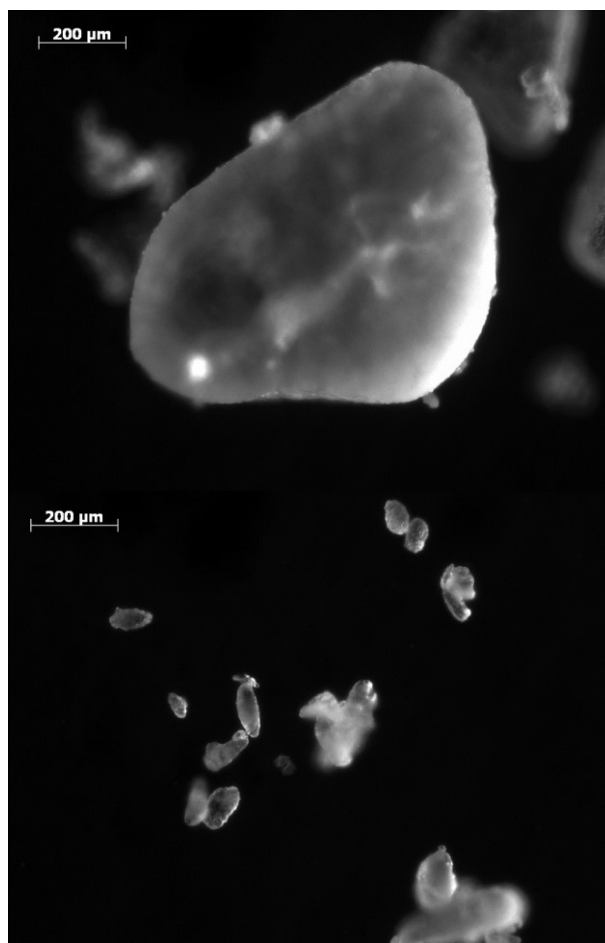


**Figure 4.19.** Light microscope image of coarse potassium bicarbonate. Particle size within the sample was observed to be heterogeneous, with large particles (top image) found together with small fragments (bottom image).

As a result of ball milling, data in figures 4.16-4.17 show a reduction of the VMD from 291.72 µm to 140.12 µm for sodium chloride, and from 436.91 µm to 45.44 µm for potassium bicarbonate. It is clear that the same operating conditions used for milling both sodium chloride and potassium bicarbonate did not bring to the formation of finer particle populations with comparable size.

It is worth noticing that both coarse sodium chloride and potassium bicarbonate particles had a VMD larger than the laser spot size of the Form 2 SLA 3D printer (140 µm - full width at half maximum) used in this work (FormLabs, 2021). On the contrary, milled sodium chloride showed a VMD (140.12 µm) of just the size of the laser beam, while milled potassium bicarbonate had a lower VMD (45.44 µm). However, all powdered materials

were characterised by a larger particle size than the recommended range suggested for loading fine powder particles (0.05  $\mu\text{m}$  to 10  $\mu\text{m}$ ) (Zakeri, Vippola and Levänen, 2020).

The use of powdered material is in fact typical of ceramic stereolithography, while conventional resins for SLA 3DP generally do not contain suspended fine particles. However, pharmaceutical applications of SLA 3DP may require the formulation of photopolymer resins suspensions loaded with APIs and/or excipients' particles. Therefore, it is important to understand the factors that can affect printability when powdered material is suspended into a photopolymer resin thus generating a heterogeneous system (de Hazan and Penner, 2017). Among these, particle size and the number of particles loaded play a crucial role as a cause of light scattering; more specifically, a smaller particle size and a high particle concentration increase the scattering effect (Tomeckova and Halloran, 2010; Zakeri, Vippola and Levänen, 2020; Qian *et al.*, 2021). Scattering of the incident laser beam causes a reduction in curing depth ( $C_d$ ) and an enlargement of curing width ( $C_w$ ). Both  $C_d$  and  $C_w$  are essential parameters to control for printing objects with high accuracy (Zakeri, Vippola and Levänen, 2020).

Hence, the inclusion of solid fillers in pharmaceutical photopolymer resins should be cautious of the potential effect of particle properties on the quality of the 3D printed dosage form.

In this piece of work, both particle size and particle concentration in the photopolymer suspension were carefully considered prior to formulating drug loaded photopolymer resin for SLA 3D printing.

#### ***4.4.4 Preparation of drug loaded photopolymer resins***

A total of 43 drug loaded photopolymer resin formulations comprising different APIs, liquid and solid fillers, and photopolymers were designed and prepared. All formulations contained TPO as a PI. TPO concentration was 0.10 % w/w in theophylline formulations

(T1-T3) and 0.05 % w/w in warfarin and warfarin sodium formulations (W1-W40). A detailed list of all the formulations prepared is described in table 4.11.

Table 4.11.1. Composition of drug-loaded photopolymer resins formulated for 3D printing.

Formulation	PEGDA (w/w %)	TPO (w/w %)	Theophylline (w/v %)	Wa FA (w/v %)	Wa Na (w/v %)	PG (w/w %)	TGDA (w/w %)	PEG (w/w %)	PEG DME (w/w %)	Milled KHCO <sub>3</sub> (w/w %)	Raw KHCO <sub>3</sub> (w/w %)	Milled NaCl (w/w %)	Raw NaCl (w/w %)
TF1	99.90	0.10	0.5										
TF2	99.90	0.10	5.0										
TF3	99.90	0.10	50.0										
WF1	99.95	0.05	0.5										
WF2	99.95	0.05	2.5										
WF3	99.95	0.05	5.0										
WF4	99.95	0.05		0.5									
WF5	99.95	0.05		2.5									
WF6	99.95	0.05		5.0									
WF7	87.45	0.05		0.5	12.5								
WF8	87.45	0.05		2.5	12.5								
WF9	87.45	0.05		5.0	12.5								
WF10	74.95	0.05		0.5	25.0								
WF11	74.95	0.05		2.5	25.0								
WF12	74.95	0.05		5.0	25.0								
WF13	49.95	0.05		0.5	50.0								
WF14	49.95	0.05		2.5	50.0								
WF15	49.95	0.05		5.0	50.0								
WF16		0.05		5.0		99.95							
WF17	49.95	0.05		5.0		50.0							
WF18	74.95	0.05		5.0		25.0							
WF19	24.95	0.05		5.0		75.0							
WF20	87.45	0.05		5.0				12.5					
WF21	74.95	0.05		5.0				25.0					
WF22	49.95	0.05		5.0				50.0					
WF23	98.95	0.05		5.0						1.0			
WF24	98.95	0.05		5.0						1.0			
WF25	97.95	0.05		5.0							2.0		

Formulation	PEGDA (w/w %)	TPO (w/v %)	Theophylline (w/v %)	Wa FA (w/v %)	Wa Na (w/v %)	PG (w/w %)	TGDA (w/w %)	PEG (w/w %)	PEG-DME (w/w %)	Milled KHCO <sub>3</sub> (w/w %)	Raw KHCO <sub>3</sub> (w/w %)	Milled NaCl (w/w %)	Raw NaCl (w/w %)
WF26	97.95	0.05			5.0					2.0			
WF27	95.95	0.05			5.0						4.0		
WF28	95.95	0.05			5.0					4.0			
WF29	98.95	0.05			5.0								1.0
WF30	98.95	0.05			5.0							1.0	
WF31	97.95	0.05			5.0								2.0
WF32	97.95	0.05			5.0							2.0	
WF33	95.95	0.05			5.0								4.0
WF34	95.95	0.05			5.0							4.0	
WF35	87.45	0.05			5.0			12.5					
WF36	74.95	0.05			5.0			25.0					
WF37	49.95	0.05			5.0			50.0					
WF38		0.05			5.0	12.5	87.45						
WF39		0.05			5.0	25.0	74.95						
WF40		0.05			5.0	50.0	49.95						

#### 4.4.5 Determination of drug solubility in polyethylene glycol diacrylate

Dimensional and geometrical accuracy of SLA 3D printed objects, including solid oral dosage forms, is generally higher when the photopolymer formulation used is in form of a solution. On the contrary, printing quality can decrease when photopolymer resins with suspended particles are used (Zakeri, Vippola and Levänen, 2020).

As a result, it would be ideal to fully solubilise the drug into the photopolymer mixture before 3DP. However, this is not always possible because the drug mass required to prepare a clinically relevant drug loaded formulation could be insoluble into the liquid photopolymer. Therefore, in order to predict the feasibility of producing clinically relevant drug loaded photopolymer solutions, the solubility of theophylline, warfarin and warfarin sodium in PEGDA 700 was determined (table 4.12).

**Table 4.12.** Theophylline, warfarin, and warfarin sodium solubility in PEGDA 700 at 20°C. Results are expressed as solubility  $\pm$  SD.

Drug	Solubility (mg/mL)	Maximum drug loading (% w/v)
Theophylline	5.475 $\pm$ 0.075	0.547 %
Warfarin	28.927 $\pm$ 0.018	2.893 %
Warfarin sodium	326.787 $\pm$ 0.206	32.679 %

Solubility data of theophylline, warfarin and warfarin sodium in PEGDA 700 offer an insight on the drug loading limitations to prepare a drug solution in the liquid photopolymer. Naturally, a higher drug loading can be obtained by creating a suspension of the drug in the photopolymer mixture.

Among the three APIs tested, theophylline had the lowest solubility (5.475 mg/mL) and drug loading capacity (0.547% w/v), while warfarin sodium salt was found to be 91.15% more soluble than warfarin, hence it can be used to prepare photopolymer resin solutions with drug loading of up to 32.679% w/v. On the other hand, warfarin can be used to produce clear photopolymer solutions only when loaded up to 2.893% w/v, while increasing its

concentration would result in the formulation of a suspension of the drug in the photopolymer blend.

The results obtained from this experiment were confirmed by the preparation of drug loaded photopolymer formulations as described in table 4.11.

A theophylline loading of 0.5% w/v (formulation T1) allowed full solubilisation of the API into the photopolymer mixture, while increasing the drug amount to 5.0% w/v resulted insoluble. Similarly, a warfarin loading up to 2.5% w/v resulted completely soluble, in line with the experimental data (2.893% w/v). Warfarin sodium allowed the preparation of drug solutions in the photopolymer blend at all levels of drug loading employed (0.5%, 2.5%, 5.0% w/v), in agreement with the solubility data obtained (32.679% w/v). This is particularly encouraging as it allows the formulation of high drug loaded photopolymer resins for SLA 3DP, reducing printing accuracy issues while making it possible to fabricate dosage forms with clinically relevant drug amounts (1-10 mg). The usual warfarin sodium dose is indeed 10 mg a day for the first 2 days, then it is reduced to 3-9 mg a day, and it is subject to continuous adjustments (NHS, 2020).

#### ***4.4.6 Determination of drug concentration in photopolymer resin***

Drug loading accuracy in photopolymer resins was determined on freshly prepared formulations after completed dissolution of the API, or within 12 hours of preparation if the API could not be fully dissolved. Results are reported in table 4.13.

**Table 4.13.** Drug recovery in photopolymer resin. Measurements were taken on freshly prepared samples (n=3). Drug loading percentages are expressed as w/v %.

<b>Formulation</b>	<b>% Recovery <math>\pm</math> SD</b>	<b>Formulation</b>	<b>% Recovery <math>\pm</math> SD</b>
TF1	101.06 $\pm$ 0.47	WF21	99.20 $\pm$ 1.41
TF2	120.85 $\pm$ 9.37	WF22	98.47 $\pm$ 1.90
TF3	116.65 $\pm$ 10.91	WF23	101.50 $\pm$ 1.04
WF1	103.76 $\pm$ 0.56	WF24	99.01 $\pm$ 1.08
WF2	99.03 $\pm$ 0.96	WF25	99.08 $\pm$ 1.67
WF3	96.42 $\pm$ 0.43	WF36	99.58 $\pm$ 1.30
WF4	99.55 $\pm$ 0.05	WF27	98.68 $\pm$ 1.90
WF5	97.53 $\pm$ 0.05	WF28	100.70 $\pm$ 2.16
WF6	95.21 $\pm$ 0.05	WF29	99.15 $\pm$ 1.19
WF7	103.37 $\pm$ 2.44	WF30	99.37 $\pm$ 2.48
WF8	100.21 $\pm$ 1.52	WF31	97.53 $\pm$ 2.72
WF9	100.17 $\pm$ 0.65	WF32	99.29 $\pm$ 1.03
WF10	101.87 $\pm$ 0.04	WF33	99.64 $\pm$ 2.37
WF11	100.82 $\pm$ 0.06	WF34	98.32 $\pm$ 0.94
WF12	100.56 $\pm$ 0.12	WF35	99.56 $\pm$ 1.61
WF13	99.09 $\pm$ 0.05	WF36	96.94 $\pm$ 0.87
WF14	100.74 $\pm$ 1.71	WF37	99.57 $\pm$ 1.16
WF15	98.47 $\pm$ 2.12	WF38	77.91 $\pm$ 3.69
WF16	73.52 $\pm$ 9.14	WF39	96.09 $\pm$ 0.50
WF17	95.96 $\pm$ 3.41	WF40	96.89 $\pm$ 0.37
WF18	98.47 $\pm$ 2.94	-	-
WF19	76.03 $\pm$ 5.37	-	-
WF20	98.90 $\pm$ 1.85	-	-

Drug recovery from most photopolymer formulations was well within the 85% to 115% range (Teng *et al.*, 2002). However, drug recovery from formulations TF2, TF3, WF16, WF19 and WF38 fell outside the 85% to 115% range. This was probably due to the presence of large amounts of suspended theophylline particles in TF2 and TF3, making accurate sampling complex. Formulations WF16, WF19 and WF38 contained high mass fractions of TGDA, which caused the photopolymer resin to be highly viscous (Uguzdogan,

2013). Such high viscosity led to electromagnetic stirring issues, resulted in only partial solubilisation of the API which formed hardly dissolvable clusters.

#### 4.4.7 Computer-aided design of solid oral dosage forms

Cylindrical solid oral dosage forms 3D models were designed using TinkerCAD. Theophylline tablets' models (figure 4.20) were based on the same design measuring 12 mm (d) × 4 mm (h) which was previously used in Chapters II-III as a proof-of-concept to evaluate formulations' printability and potential drug loading-related limitations. Tablet volume was 0.452 mL, therefore allowing a theoretical theophylline dosage for formulations TF1, TF2 and TF3 of 2.26 mg, 22.62 mg, and 226.19 mg, respectively

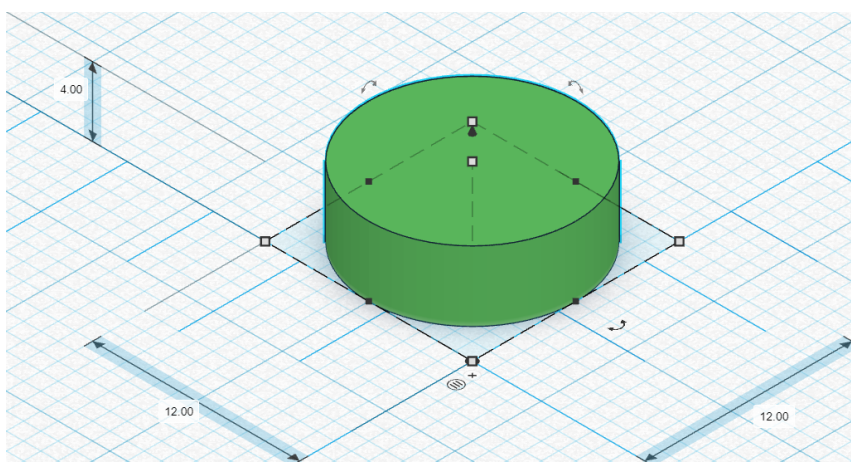


**Figure 4.20.** CAD model used for 3D printing theophylline dosage forms.

Warfarin dosage forms were designed with the aim to achieve clinically relevant dosages. Tablet volume was set at 0.200 mL using a cylindrical geometry measuring 8 mm (d) × 4 mm (h), respectively (figure 4.21). As a result, formulations loaded with 0.5% w/v, 2.5% w/v and 5.0% w/v of warfarin and warfarin sodium allowed a theoretical drug dosage of 1 mg, 5 mg, and 10 mg, respectively.

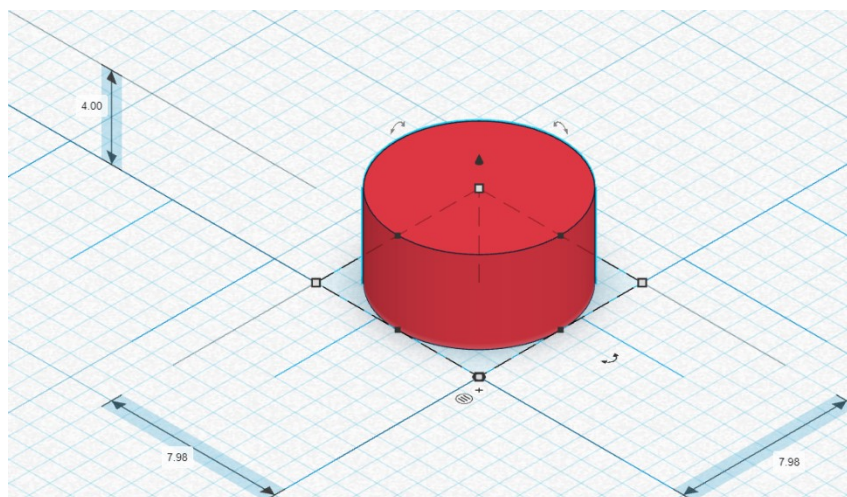


**Figure 4.21.** CAD model used for 3D printing warfarin and warfarin sodium dosage forms.

#### ***4.4.8 Stereolithography 3D printing of solid oral dosage forms***

Having developed a wide set of drug loaded photopolymer formulations and suitable 3D models, the following phase consisted in the production of solid oral dosage forms through SLA 3DP. 10 mL of each photopolymer resin were individually loaded in the compartments of a modified resin tray redesigned to accommodate 12 different formulations and already described in Chapter II.

The use of the modified SLA apparatus allowed a major reduction in the amount of formulation needed. An estimate of the cost-saving resulting from the use of the modified SLA system was determined by considering 200 g as the amount of formulation needed when using the original SLA apparatus, and 10 g as the formulation amount required in the modified SLA apparatus. Results are reported in table 4.14.

**Table 4.14.** Individual cost of drug loaded photopolymer formulations. Results are expressed in GBP for 200 g (formulation amount required in the original Form 2 3D printer) and 10 g (formulation amount required in the modified SLA apparatus).

<b>Formulation</b>	<b>Cost (GBP/200 g)</b>	<b>Cost (GBP/10 g)</b>
TF1	43.11	2.16
TF2	43.45	2.17
TF3	46.84	2.34
WF1	51.09	2.55
WF2	84.92	4.25
WF3	127.21	6.36
WF4	44.94	2.25
WF5	54.17	2.71
WF6	65.71	3.29
WF7	40.72	2.04
WF8	50.03	2.50
WF9	61.67	3.08
WF10	36.49	1.82
WF11	45.89	2.29
WF12	57.64	2.88
WF13	28.04	1.40
WF14	37.61	1.88
WF15	49.57	2.48
WF16	76.53	3.83
WF17	71.12	3.56
WF18	68.41	3.42
WF19	73.83	3.69
WF20	78.82	3.94
WF21	91.93	4.60
WF22	118.15	5.91
WF23	65.46	3.27
WF24	65.46	3.27
WF25	65.21	3.26
WF26	65.21	3.26
WF27	64.72	3.24
WF28	64.72	3.24
WF29	65.41	3.27
WF30	66.75	3.34
WF31	65.11	3.26
WF32	65.11	3.26
WF33	64.52	3.23
WF34	64.52	3.23
WF35	62.30	3.12
WF36	58.89	2.94
WF37	52.08	2.60
WF38	71.14	3.56
WF39	65.75	3.29
WF40	54.98	2.75
<b>Total</b>	<b>2695.24</b>	<b>134.76</b>

As reported above, the use of the original Form 2 SLA apparatus would have led to a total materials cost of 2695.24 GBP resulting from the large amount of drug loaded photopolymer formulation samples needed. On the contrary, the modified SLA apparatus, able to operate using small formulation samples volume, allowed to contain the total cost to 134.76 GBP, resulting in 2000.03% saving than the original Form 2 SLA system.

Once the resin tray containing the drug loaded photopolymer formulations was connected to the 3D printer, 3D models of theophylline, warfarin and warfarin sodium dosage forms opened in PreForm software to set the print area. A total of 30 tablets per formulation were 3D printed. One dosage form for each formulation was fabricated in a single printing run.

Theophylline formulations TF1-TF3 were set to be 3D printed simultaneously (figure 4.22). The time required to complete a single printing cycle was 56 min, hence 28 hours were necessary to 3D print 30 tablets per formulation.

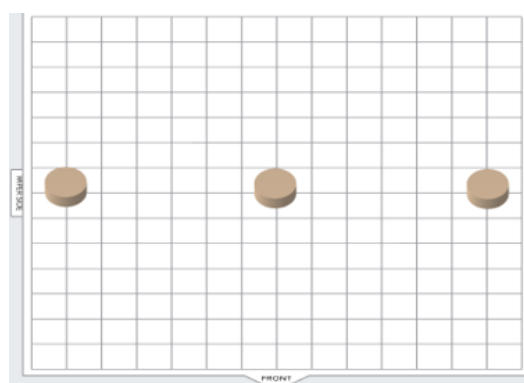


**Figure 4.22.** FormLabs PreForm view of theophylline 3D models used for 3D printing solid oral dosage forms. One tablet was fabricated for each formulation in a single printing cycle. Each printing cycle required 56 min to be completed. Layer thickness was set at 100  $\mu\text{m}$ .

Similarly, warfarin and warfarin sodium formulations WF1-WF12, WF13-WF24, and WF25-WF36 were loaded in the same resin tray to be 3D printed simultaneously (figure 4.23). As a result, a single printing cycle of 1 hour allowed to 3D print one tablet from 12 different formulations. 30 hours were necessary to 3D print 30 dosage forms per each

formulation. 3D printing of formulations WF37-WF40 (figure 4.23) took 55 min for a single print run, and 27.5 hours to produce 30 dosage units.

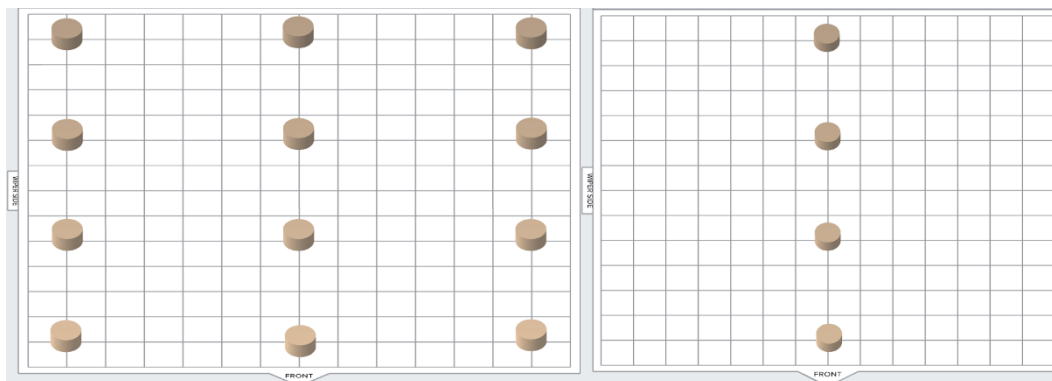


**Figure 4.23.** Formlabs PreForm view of warfarin and warfarin sodium 3D models used for 3D printing solid oral dosage forms. One tablet was fabricated for each formulation in a single printing cycle. To be completed, each printing cycle required 1 hour when 12 different formulations were used simultaneously (**left**), and 55 min when 4 different formulations were used simultaneously (**right**). Layer thickness was set at 100  $\mu\text{m}$ .

According to the figures reported above (4.22-4.23), the total amount of time required for 3D printing 30 dosage forms from 43 drug loaded photopolymer formulations using the modified SLA apparatus was 145.5 hours. In contrast, the use of the original Form 2 SLA apparatus would have allowed a different arrangement of the printing area (figure 4.24), making it possible to 3D print 30 dosage units from the same formulation in a single printing run. In this way, 3D printing time for formulations TF1-TF3 and WF1-WF40 would be 1.45 hours and 1.15 hours each, respectively.

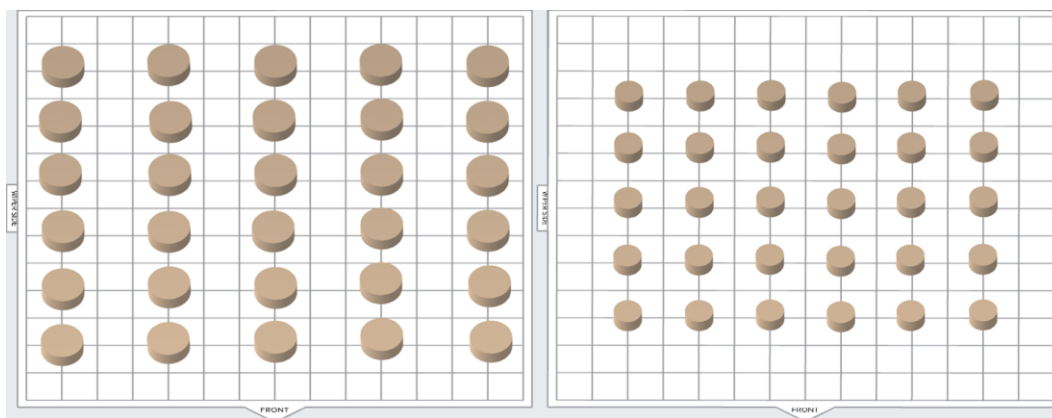


**Figure 4.24.** FormLabs PreForm view of 3D models used for formulations TF1-TF3 (**left**) and WF1-WF40 (**right**). To be completed, each printing cycle would have required 1.45 hours for formulations TF1-TF3, and 1.15 hours for formulations WF1-WF40.

As a result, the use of the original SLA apparatus would have allowed to decrease the total 3DP time from 145.5 hours to 50.35 hours. However, it should be considered that although with the original SLA apparatus the manufacturing time could have been reduced to 34.60 %, materials cost due to the larger formulation samples amount needed would have skyrocketed to 2000.03 %.

Interestingly, these results partially confirmed our previous findings on the cost-effectiveness related to the use of a modified SLA apparatus for pharmaceutical formulation development (Curti, Kirby and Russell, 2021). In fact, in the previous work described in Chapter III, it was found that the application of the original SLA apparatus would have resulted in a 2000.00 % higher cost for the materials, in line with the figures related to the 3DP of drug loaded photopolymer formulations (2000.03 %). However, our previous findings also indicated a 3DP time 1199.96 % higher when the original SLA apparatus was used, while 3DP drug loaded photopolymer formulations using the same apparatus would have taken just 34.60 % of the time required with the modified apparatus. Such difference can be explained by the fact that when the modified SLA apparatus was used to carry out a high-throughput printability screening on 156 photopolymer formulations, only 1 tablet was 3D printed for each formulation in a single printing cycle, both using the original and the modified SLA apparatus; in this way, the capability of the

modified SLA apparatus to simultaneously 3D print 12 different formulations had a major role to cut considerably the total manufacturing time. On the contrary, when the two apparatuses were compared for the fabrication of dosage forms from drug loaded formulations, it was clear that the greater printing output of the original SLA apparatus, able to produce 30 tablets in a single printing cycle, resulted in a more time effective process.

Following the 3DP process, dosage units produced from each formulation were visually observed to evaluate printability outcomes by using the printability scale previously described in Chapter III. A printability score (PS) was assigned to each formulation as reported in table 4.15.

**Table 4.15.** Printability evaluation of drug loaded photopolymer formulations.

<b>Formulation</b>	<b>PS</b>	<b>Formulation</b>	<b>PS</b>
TF1	5*	WF21	5*
TF2	6	WF22	4
TF3	6	WF23	5*
WF1	5*	WF24	5*
WF2	5*	WF25	5*
WF3	6*	WF26	5*
WF4	5*	WF27	5*
WF5	5*	WF28	5*
WF6	5*	WF29	5*
WF7	5*	WF30	5*
WF8	5*	WF31	5*
WF9	5*	WF32	5*
WF10	5*	WF33	5*
WF11	5*	WF34	5*
WF12	5*	WF35	5*
WF13	5*	WF36	5*
WF14	5*	WF37	6*
WF15	5*	WF38	4
WF16	4	WF39	5*
WF17	5*	WF40	5*
WF18	5*		
WF19	4		
WF20	5*		

Among the theophylline loaded formulations, TF1 showed good printability and was assigned a PS = 5\*, indicating that tablets were successfully and accurately printed figure 4.25.



**Figure 4.25.** Top view of a dosage form 3D printed using TF1 resin (drug loading = 0.5 % w/v). Tablet geometry resulted accurate to the 3D model designed.

3D printed dosage forms fabricated from formulations TF2 and TF3 had a white opaque appearance resulting from the suspension nature of the drug loaded photopolymer resin and were assigned a PS = 6 due to the significant broadening that was observed (figures 4.26-4.27), making it impossible to distinguish the cylindrical geometry designed. In addition, following the 3DP process of formulation TF3, theophylline crystals could be distinctly observed on the printed surface (figure 4.27B), which resulted in mild friability upon hand contact.



**Figure 4.26.** Top view of three dosage forms 3D printed using TF2 resin (drug loading = 5% w/v). Geometrical accuracy was lost due to high broadening effect.



**Figure 4.27.** (A) Top view of three dosage forms 3D printed using TF3 resin (drug loading = 50% w/v) and (B) detail of theophylline crystals on the 3D printed surface. Geometrical accuracy was lost due to substantial broadening effect.

It can be hypothesised that formulations TF2-TF3 were not printable as a consequence of the high amount of crystalline theophylline particles suspended in the photopolymer resin. Straight after preparation, formulation TF2 appeared as a white opalescent liquid with an evident presence of dispersed particles to the naked eye. Optical microscopy analysis allowed observation of the heterogeneous presence of crystals in different sizes and characteristic of theophylline in their morphology, occasionally forming aggregates (figures 4.28-4.29).

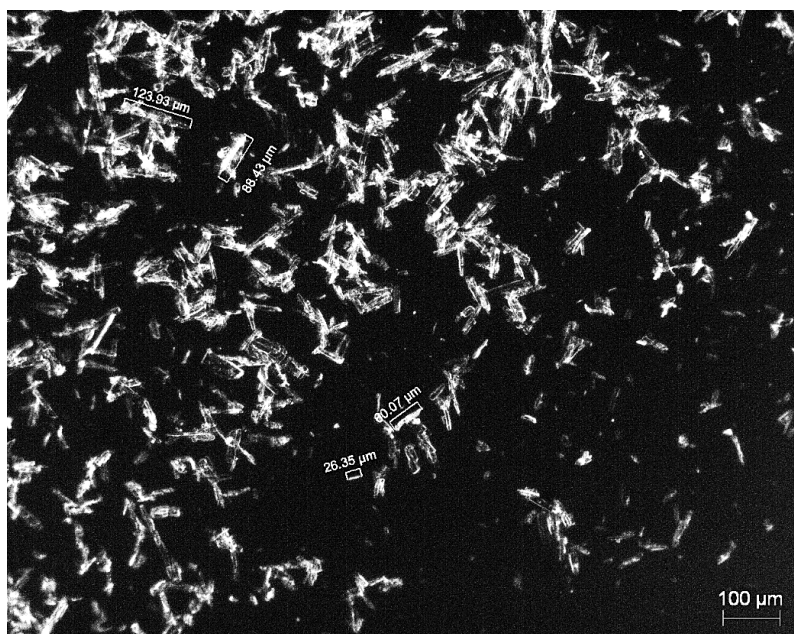


**Figure 4.28.** Optical microscope image of formulation TF2. Theophylline crystals in a size range between 26.35 µm and 123.93 µm were observed. Magnification was set at  $\times 10$ .

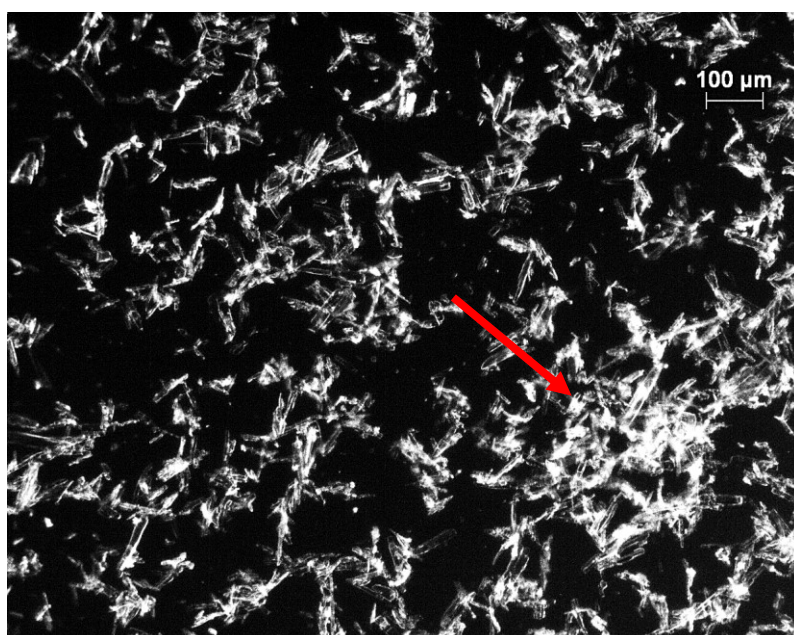


**Figure 4.29.** Optical microscope image of formulation TF2. Red arrow indicates an aggregate of theophylline crystals. Magnification was set at  $\times 10$ .

Formulation TF3 appeared instead as a semisolid paste, containing 50% w/v theophylline. Optical microscopy observation allowed to appreciate the high density of drug crystals (figure 4.30).

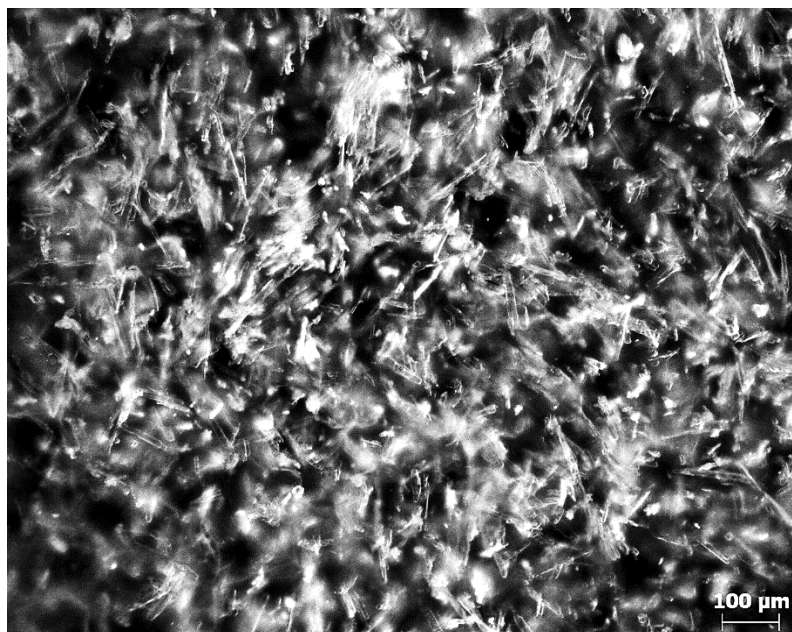


**Figure 4.30.** Optical microscope image of formulation TF3. It is visible the high density of theophylline crystals within the liquid photopolymer matrix. Magnification was set at  $\times 10$ .

For both formulations TF2 and TF3, it is very likely that the high number of particles suspended, as well as their heterogeneity, caused a substantial scattering of the incident laser beam during the 3D printing process. As a result, photopolymerisation occurred in an uncontrolled way, broadening the curing area far beyond the designated perimeter. This was particularly evident in formulation TF3 where the laser light, scattered by the large number of theophylline crystals, initiated polymerisation of all the resin contained in the tank, as it can be seen by the squared edges of 3D printed samples in figure 4.27. It is indeed known that more scattering events would occur when the number of particles suspended in the photopolymer resin is increased (Zakeri, Vippola and Levänen, 2020).

As a result, such an issue was found to be a substantial limitation in the application of theophylline for developing SLA 3D printable formulations. In fact, the typical theophylline dose in adults, administered through modified-release tablets, is between 200 and 400 mg every 12 hours (Joint Formulary Committee, 2020). Theophylline formulations are therefore commercially available in dosages of 200 mg, 300 mg, and 400 mg. According to this and based on the same 3D cylindrical tablet model (figure 4.20) with a volume of 0.452 mL, theophylline drug loading in a photopolymer formulation should be between 44.25% w/v and 88.50% w/v to achieve a clinically relevant dosage. However, a drug loading of just 5% w/v (TF2) did not result in good printability, hence limiting the further development of theophylline 3D printed solid oral dosage forms.

Among the 40 warfarin and warfarin sodium formulations, 33 were assigned a PS = 5\*. Formulations containing solely PEGDA 700 as photopolymer (WF1-WF6) showed very good printability, with only WF3 (5% w/v warfarin) being classified with a PS = 6 due to a mild broadening observed (figure 4.31). This can be explained by the fact that such a concentration of warfarin in PEGDA 700 would not be fully soluble (solubility = 28.93 mg/mL, table 4.12), hence generating a suspension of the drug in the liquid polymer. Though, it is worth noticing that due to the higher solubility in PEGDA 700 of warfarin (maximum drug loading = 2.893% w/v) than theophylline (maximum drug loading = 0.547% w/v), it is likely that the number of suspended drug particles in formulation WF3 is lower than in TF2, thus the minor entity of the light scattering induced broadening. 3D printed dosage forms produced from formulation WF3 were the only ones featuring a pale yellow opaque appearance resulting from the suspended warfarin particles in PEGDA 700 (figure 4.31). On the contrary, the more soluble warfarin sodium allowed production of tablets where the API was fully solubilised in the liquid polymer at all concentrations used, thus making 3D printed tablets looking transparent (figure 4.31).

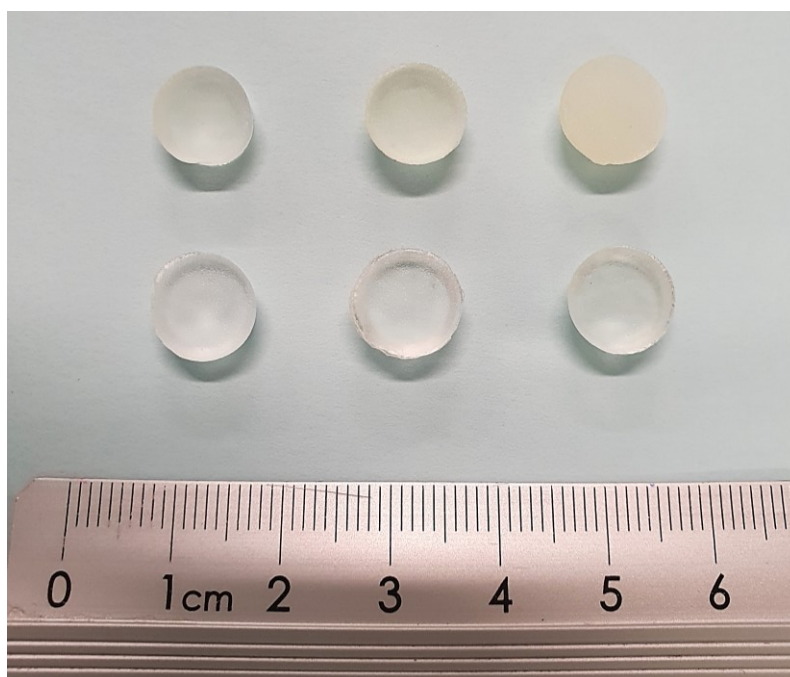


**Figure 4.31.** From top left to bottom right: SLA 3D printed dosage forms from formulations WF1, WF2, WF3, WF4, WF5, and WF6.

The inclusion of PG as a liquid filler allowed the fabrication of dosage forms with satisfactory printability at all three the concentrations used (12.5%, 25%, 50% w/w), so formulations WF7-WF15 all reached a  $PS = 5^*$  (figures 4.32-4.33).

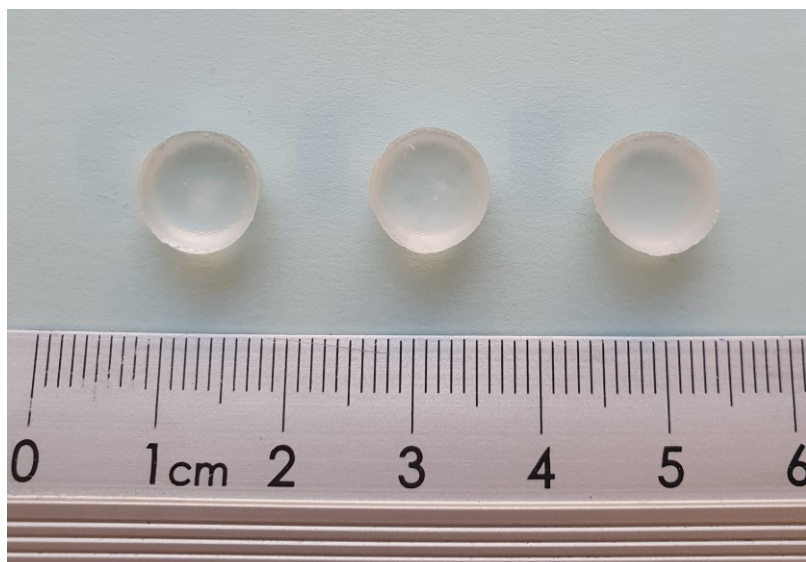


**Figure 4.32.** From left to right: SLA 3D printed dosage forms from formulations WF7, WF8, and WF9.

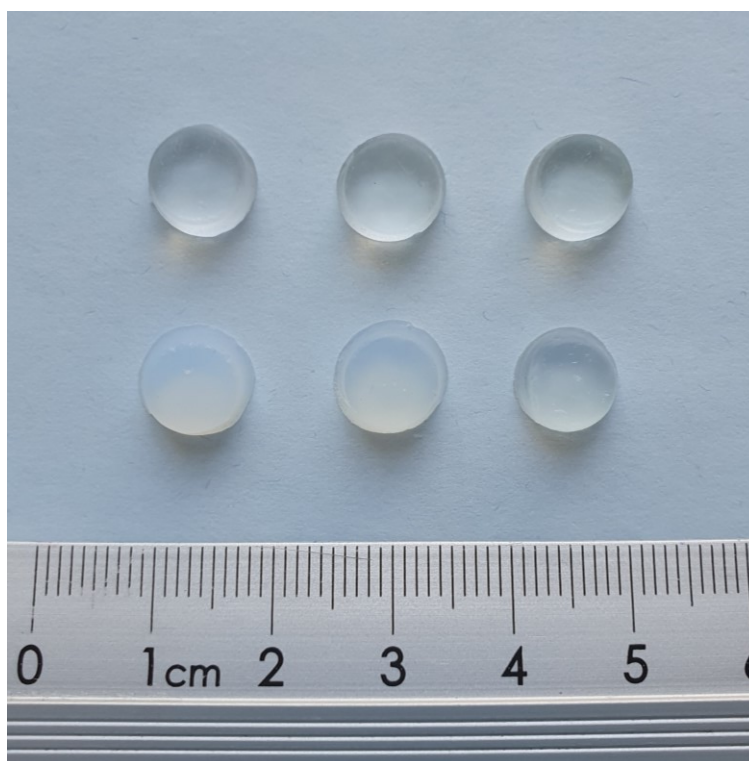


**Figure 4.33.** From top left to bottom right: SLA 3D printed dosage forms from formulations WF10, WF11, WF12, WF13, WF14, and WF15.

The evaluation of liquid fillers also included PEGDME and PEG 300 in formulations WF20-WF22 and WF35-WF37, respectively. Formulations WF20-WF21 were successfully 3D printed hence were assigned a PS = 5\* (figure 4.35), while WF22 resulted in a failed print (PS = 4) due to the dosage form falling from the BP while printing. This issue led to an incorrect alignment of the different layers making up the 3D model, which appeared sliding on each other (figure 4.34).



**Figure 4.34.** Failed print of formulation WF22. The layers sliding on each other are distinctly visible.

Such a printability issue was likely caused by the high PEGDME mass fraction (50% w/w) in the photopolymer formulation. In fact, PEGDME has a viscosity of just 7.43 cP at 20°C (Conesa, Shen and Coronas<sup>1</sup>, 1998), and its incorporation in large amounts in a PEGDA 700 resin will determinate a viscosity lowering in the final formulation. Although low viscosity resins are generally desirable in SLA 3D printing, it can be hypothesised that viscosity values below a certain threshold can lead to print failures linked to the detachment of the object from the build platform during the printing process.

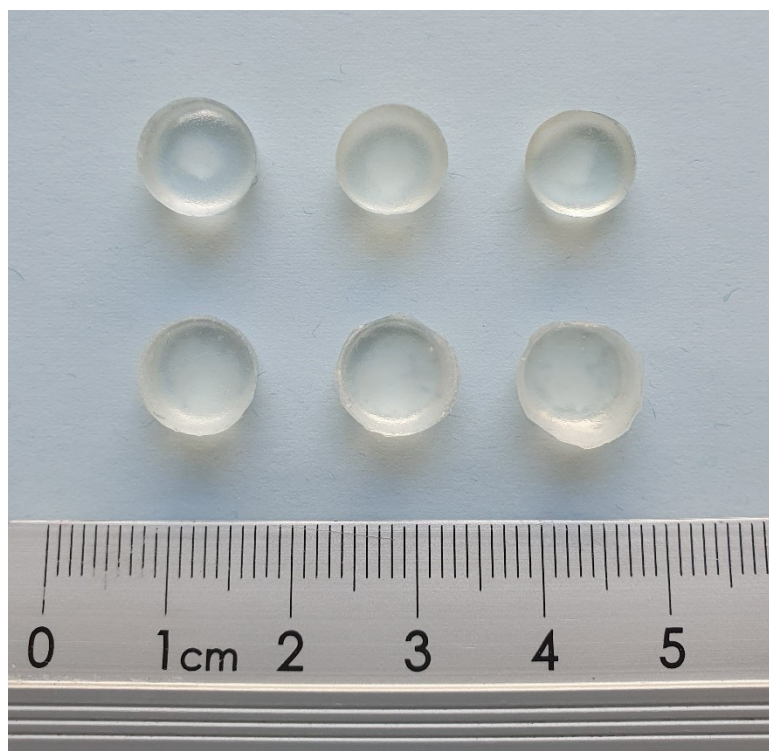


**Figure 4.35.** From top left to bottom right: SLA 3D printed dosage forms from formulations WF17, WF20, WF21, WF35, WF36, and WF37.

The inclusion of PEG 300 in formulations WF35-WF37 resulted in a satisfactory printability (PS = 5\*) when its concentration was 12.5 % and 25 % w/w. Including 50 % w/w of PEG 300 caused instead minor broadening of the model, but the cylindrical geometry could still be distinctly observed (PS = 6\*). Differently from PEGDME, PEG 300 viscosity of 84.37-106.87 cP at 20°C (Merck, 2021) is much more similar to that of PEGDA 700 (97.55 cP at 25°C), and this could explain the improved printability.

The investigation of TGDA as an alternative material to PEGDA 700 resulted in a failed print (PS = 4) when it was used as the only or majority photopolymer in formulations WF16 and WF19, respectively. More precisely, it could be seen that the initial layers were printed on the build platform, but the following ones did not stick to them, causing the tablet to remain at the bottom of the resin tank, detached from the build platform. The reasons of such printing failure were potentially to be found in the very high viscosity of TGDA,

ranging between 8000-12000 cP at 25°C (Uguzdogan, 2013). In comparison, the commercially available Clear photopolymer resin previously used in this research and PEGDA 700 have a viscosity of 850-900 cP and 97.55 cP at 25°C (Formlabs Inc., 2016; Vuksanović, Kijevčanin and Radović, 2018). The role of high resin viscosity in determining a failed print also looks confirmed by the fact that increasing the ratio of PEGDA 700 in the photopolymer mixture (WF17 and WF18) resulted in accurately printable dosage forms (figures 4.35-4.36).

Furthermore, TGDA high viscosity made formulations WF16 and WF19 workability very low, with reduced capacity to incorporate the API and large amounts of air bubbles developing and getting trapped in the viscous liquid, even after degassing. Due to the presence of drug particles' aggregates not fully solubilised, a modest broadening effect was observed in the photopolymerised material removed from the resin tank. Based on these observations, formulations WF16 and WF19 were not further characterised nor object of development in this research.

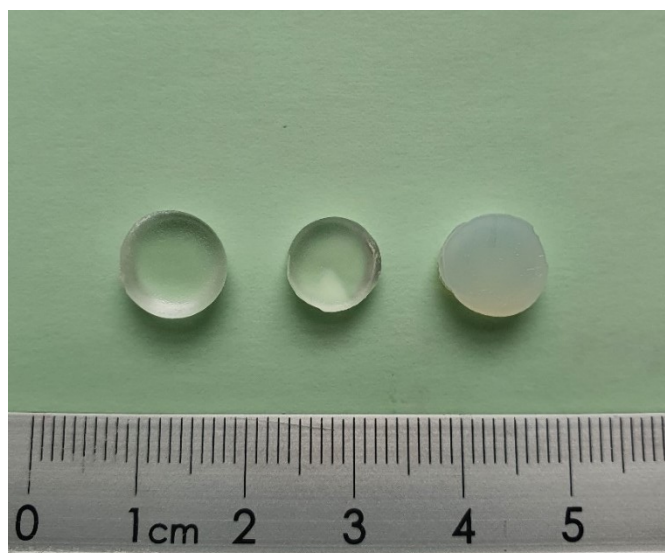


**Figure 4.36.** From left to right: SLA 3D printed dosage forms from formulations WF18, WF39, and WF40.

In another set of TGDA based photopolymer formulations (WF38-WF40), PG was included as a low viscosity (43.96 cP at 25°C Sagdeev, Fomina and Abdulagatov, 2017) liquid filler with the view to both enhance drug release and to decrease resin's viscosity, hence improving printability. Formulation WF38, containing the lowest mass fraction of PG over TGDA (12.5% w/w), was not printable (PS = 4) and the same issues previously described for formulations WF16 and WF19 were observed. Formulations WF39-WF40 provided instead good printability outcomes (PS = 5\*). Interestingly, formulation WF39 containing the same TGDA mass fraction as WF19 (75% w/w) resulted in successful prints, which is likely explainable by the viscosity difference of PEGDA 700 and PG, the latter being the less viscous.

All the photopolymer formulations containing solid fillers (WF23-WF34) achieved satisfactory printability outcomes (PS = 5\*). Dosage forms 3D printed from formulations WF23, WF25, WF27, WF29, WF31 and WF33, containing coarse potassium bicarbonate and sodium chloride, appeared as clear-opaque structures where solid particles can be distinctly observed (figure 4.37). Optical microscopy images of tablets produced from WF27 and WF33 were taken to visualise any differences in solid particles' distribution between the top and bottom surfaces of the dosage forms (figures 4.38-4.39).

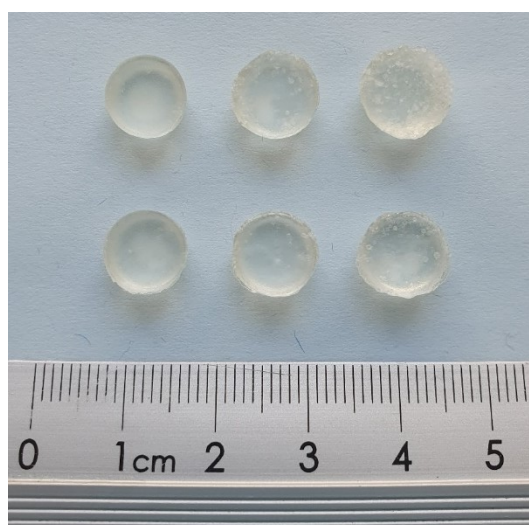


**Figure 4.37.** From top left to bottom right: SLA 3D printed dosage forms from formulations WF23, WF25, WF27, WF29, WF31, and WF33.

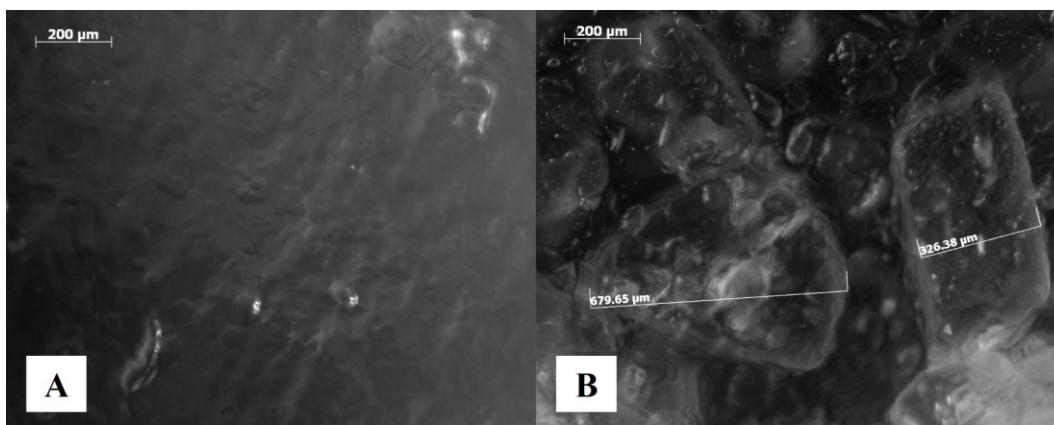


**Figure 4.38.** Optical microscope images of SLA 3D printed WF27. Tablet side facing the resin tank (A) does not allow the observation of potassium bicarbonate particles, distinctly visible at the tablet side facing the build platform (B).

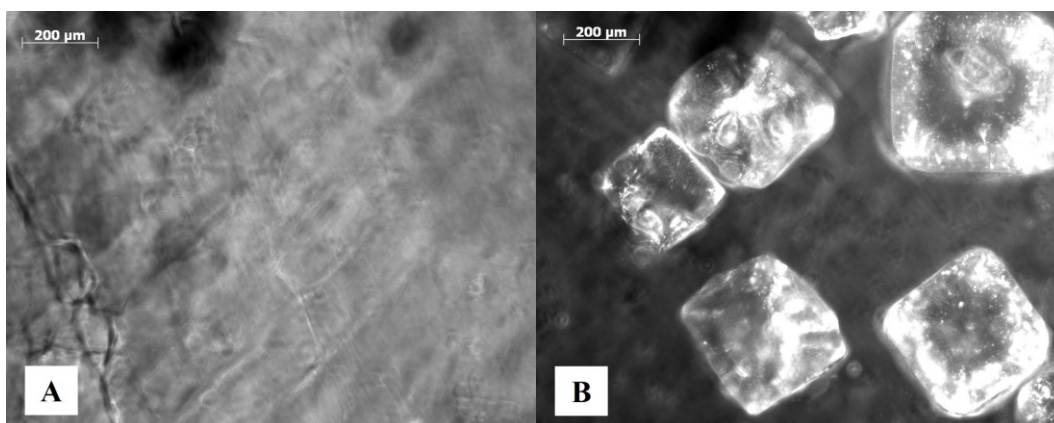


**Figure 4.39.** Optical microscope images of SLA 3D printed WF33. Tablet side facing the resin tank (A) does not allow the observation of sodium bicarbonate particles, distinctly visible at the tablet side facing the build platform (B).

As it can be seen in figures 4.38-4.39, the distribution of coarse solid fillers was not uniform across the two faces of 3D printed dosage forms. Instead, as particles tended to quickly precipitate after the photopolymer solution was poured into the resin tank, the first layers (build platform side, figures 4.38B-4.39B) resulted rich in particles, while the last layers to be built (tank side, figures 4.38A-4.39A) lacked in solid material.

Such phenomenon appeared less evident in dosage forms 3D printed from formulations WF24, WF26, WF28, WF30, WF32 and WF34, which contained milled potassium

bicarbonate and sodium chloride. As shown in figure 4.40, milled potassium bicarbonate present in WF24, WF26 and WF28 appears to be homogeneously dispersed in the polymeric matrix, giving dosage units an opaque, pale yellow aspect. Milled sodium chloride behaved instead similarly to its coarse form, grouping in particles' aggregates on one side of the tablet, especially visible when the highest concentration of sodium chloride was used.

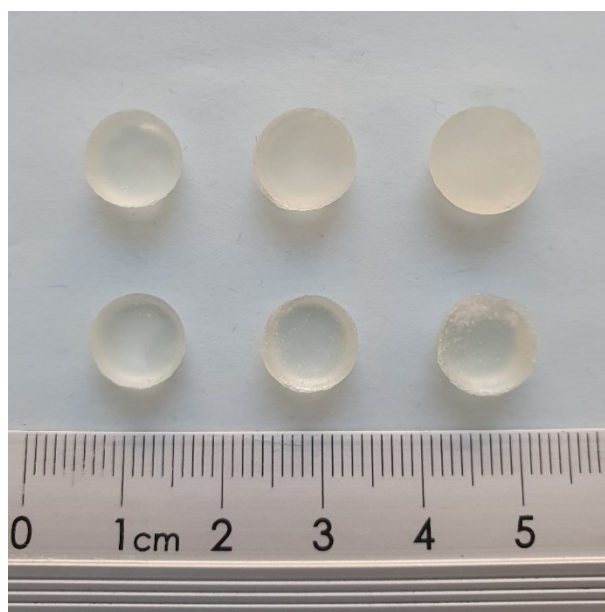


**Figure 4.40.** From top left to bottom right: SLA 3D printed dosage forms from formulations WF24, WF26, WF28, WF30, WF32, and WF34.

#### ***4.4.9 Determination of drug concentration in 3D printed dosage forms***

Successfully 3D printed dosage forms were subjected to analysis to determinate the actual API amount loaded. Due to the photocrosslinked nature of SLA 3D printed parts, whole tablets were too hard to crush by mean of a mortar and pestle, so they were firstly split in smaller sections, then these were accurately transferred into a mortar to be finely grounded. However, even this technique proved to be inadequate because the elasticity of the materials forming the tablets and the friction with the walls of the mortar caused fragments to escape at high speed with consequent sample loss. To overcome this problem, a galenic

technique known as ‘pulverisation through intermediate’ was used (figure 4.41). Sodium chloride was used as an inert substance to aid the pulverisation of 3D printed tablets avoiding the risk of escaping fragments.

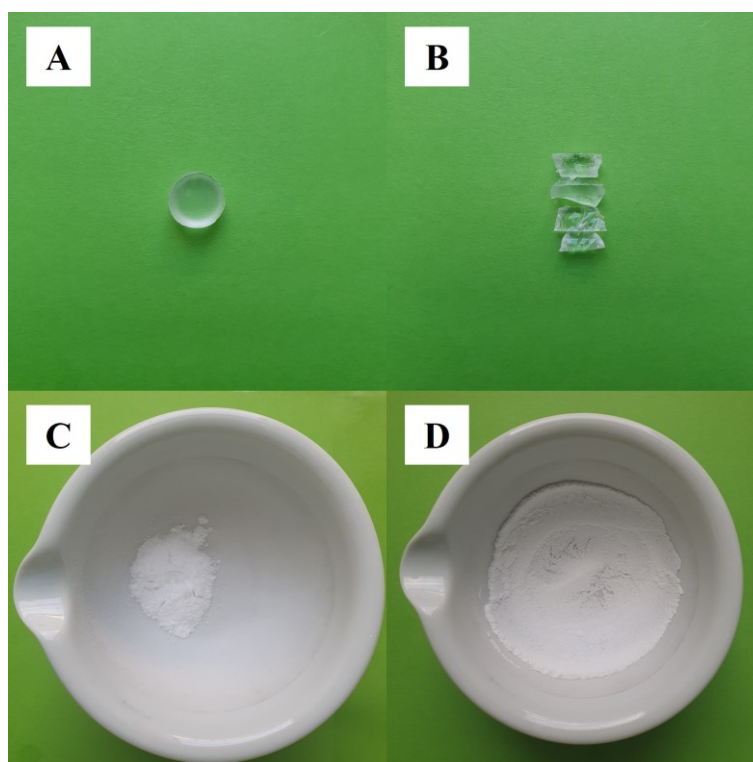


**Figure 4.41.** Protocol followed to pulverise SLA 3D printed dosage forms using a mortar and pestle. The 3DP tablet (A) is sliced into smaller fragments (B). Then, one fragment is transferred to the mortar containing grinded inert solid material (C) and finely grounded to avoid escape of fragments (D).

Following pulverisation, the powdered mixtures were extracted to be analysed in HPLC. Drug recovery from 3D printed tablets is reported in table 4.16.

Drug content uniformity was evaluated in terms of accuracy, by determining if the mean drug recovery fell outside of the 85% to 115% or the 75% to 125% range (Teng *et al.*, 2002). Content uniformity was also assessed in terms of precision by determining the relative standard deviation, considering acceptable a  $RSD \leq 6\%$  (Teng *et al.*, 2002).

Mean drug recovery from formulations WF14, WF15, WF17, WF18, WF27, WF31, WF32, WF33, WF35, WF36 and WF37 fell outside the 85% to 125% range. Drug recovery from formulations WF3, WF13, WF26, WF28 and WF34 fell outside the 75% to 125% range.

In terms of RSD, most formulations fell within the tolerable range, while WF15, WF21, WF24, WF26, WF27, WF28, WF29, WF31, WF32, WF34, WF39 exceeded a RSD of 6%.

It was interesting to note that the highest variability was observed in formulations containing solid fillers. The same trend was also observed when tablet weight uniformity was evaluated.

**Table 4.16.** Drug content uniformity evaluation of SLA 3D printed dosage forms.

<b>3DP Formulation</b>	<b>Theoretical drug content (mg)</b>	<b>% Recovery <math>\pm</math> SD</b>	<b>% RSD</b>
<b>TF1</b>	2.26	105.74 $\pm$ 3.55	3.36
<b>WF1</b>	1.00	102.70 $\pm$ 5.66	5.51
<b>WF2</b>	5.00	110.01 $\pm$ 2.21	2.01
<b>WF3</b>	10.0	129.66 $\pm$ 2.79	2.15
<b>WF4</b>	1.00	99.54 $\pm$ 0.87	0.87
<b>WF5</b>	5.00	102.07 $\pm$ 1.48	1.45
<b>WF6</b>	10.0	100.01 $\pm$ 3.38	3.38
<b>WF7</b>	1.00	103.86 $\pm$ 2.62	2.52
<b>WF8</b>	5.00	109.47 $\pm$ 2.94	2.69
<b>WF9</b>	10.0	112.43 $\pm$ 3.40	3.02
<b>WF10</b>	1.00	102.77 $\pm$ 0.67	0.65
<b>WF11</b>	5.00	113.55 $\pm$ 6.33	5.57
<b>WF12</b>	10.0	110.83 $\pm$ 3.11	2.81
<b>WF13</b>	1.00	73.51 $\pm$ 3.30	4.49
<b>WF14</b>	5.0	81.65 $\pm$ 3.46	4.24
<b>WF15</b>	10.0	84.74 $\pm$ 5.28	6.23
<b>WF17</b>	10.0	121.36 $\pm$ 3.14	2.59
<b>WF18</b>	10.0	120.28 $\pm$ 0.98	0.81
<b>WF20</b>	10.0	101.44 $\pm$ 3.67	3.62
<b>WF21</b>	10.0	93.03 $\pm$ 6.65	7.15

<b>WF23</b>	10.0	109.98 ± 3.87	3.52
<b>WF24</b>	10.0	103.68 ± 8.77	8.46
<b>WF25</b>	10.0	113.60 ± 5.74	5.05
<b>WF26</b>	10.0	134.94 ± 13.23	9.80
<b>WF27</b>	10.0	123.14 ± 8.73	7.09
<b>WF28</b>	10.0	136.55 ± 32.31	23.66
<b>WF29</b>	10.0	112.14 ± 7.19	6.41
<b>WF30</b>	10.0	113.83 ± 3.89	3.42
<b>WF31</b>	10.0	117.86 ± 7.97	6.76
<b>WF32</b>	10.0	123.53 ± 8.35	6.76
<b>WF33</b>	10.0	120.39 ± 6.76	5.62
<b>WF34</b>	10.0	138.15 ± 12.39	8.97
<b>WF35</b>	10.0	117.53 ± 3.31	2.82
<b>WF36</b>	10.0	121.69 ± 2.02	1.66
<b>WF37</b>	10.0	129.66 ± 3.80	2.93
<b>WF39</b>	10.0	90.36 ± 6.47	7.16
<b>WF40</b>	10.0	108.91 ± 5.39	4.95

#### **4.4.10 Tablet weight uniformity**

Tablet weight uniformity was evaluated in terms of relative standard deviation, considering as acceptable a  $RSD \leq 6\%$  (Teng *et al.*, 2002). Most SLA 3D printed dosage forms fell within the limits, while formulations WF14, WF15, WF21, WF24, WF26, WF27, WF28, WF29, WF31, WF32, WF34 and WF39 exceeding the acceptable RSD value (table 4.17). It is interesting to note that out of the 12 outliers, 8 were formulations containing solid fillers, indicating that higher variability may be linked to the use of such excipients.

**Table 4.17.** Weight uniformity determination of SLA 3D printed dosage forms. Results are expressed as mean  $\pm$  SD, and % RSD (n = 10).

<b>3DP Formulation</b>	<b>Mean (g) <math>\pm</math> SD</b>	<b>% RSD</b>
TF1	0.654 $\pm$ 0.014	2.141
WF1	0.266 $\pm$ 0.008	3.008
WF2	0.258 $\pm$ 0.005	1.938
WF3	0.331 $\pm$ 0.011	3.323
WF4	0.250 $\pm$ 0.001	0.400
WF5	0.277 $\pm$ 0.011	3.971
WF6	0.269 $\pm$ 0.010	3.717
WF7	0.244 $\pm$ 0.005	2.049
WF8	0.260 $\pm$ 0.007	2.692
WF9	0.268 $\pm$ 0.008	2.985
WF10	0.250 $\pm$ 0.006	2.400
WF11	0.255 $\pm$ 0.014	5.490
WF12	0.250 $\pm$ 0.013	5.200
WF13	0.270 $\pm$ 0.007	2.593
WF14	0.224 $\pm$ 0.015	6.696
WF15	0.235 $\pm$ 0.020	8.511
WF17	0.292 $\pm$ 0.008	2.740
WF18	0.285 $\pm$ 0.002	0.702
WF20	0.226 $\pm$ 0.008	3.540
WF21	0.205 $\pm$ 0.015	7.317
WF23	0.248 $\pm$ 0.009	3.629
WF24	0.235 $\pm$ 0.020	8.511
WF25	0.258 $\pm$ 0.013	5.039
WF26	0.307 $\pm$ 0.030	9.772
WF27	0.281 $\pm$ 0.020	7.117
WF28	0.400 $\pm$ 0.069	17.250
WF29	0.254 $\pm$ 0.016	6.299
WF30	0.256 $\pm$ 0.009	3.516
WF31	0.268 $\pm$ 0.018	6.716
WF32	0.281 $\pm$ 0.019	6.762
WF33	0.274 $\pm$ 0.015	5.474
WF34	0.313 $\pm$ 0.028	8.946

<b>WF35</b>	0.266 ± 0.008	3.008
<b>WF36</b>	0.276 ± 0.005	1.812
<b>WF37</b>	0.294 ± 0.009	3.061
<b>WF39</b>	0.215 ± 0.015	6.977
<b>WF40</b>	0.249 ± 0.012	4.819

#### ***4.4.11 Mechanical characterisation of stereolithographic 3D printed dosage forms***

Friability and breaking force of SLA 3D printed dosage forms were determined with the view to inform about their mechanical resistance (table 4.18).

All 3D printed formulations recorded a weight loss < 1% after being tested in a conventional tablet friabilometer, therefore complying with the USP specifications (United States Pharmacopeial Convention, 2012; Nilawar, Wankhade and Badnag, 2013).

Tablet breaking force values fell within a range of 83.92 N to 138.82 N for formulations WF1 - WF40, therefore complying with the minimum requirements (circa 40 N) (Khaled, Alexander, Irvine, *et al.*, 2018; Khaled, Alexander, Wildman, *et al.*, 2018). A higher breaking force value of 388.75 N was recorded for theophylline 3D printed dosage forms, which were designed in a larger size compared to warfarin dosage forms. However, it can be noted that tablet breaking force was not sufficiently high to target specific types of formulations such as abuse-deterrent dosage forms (Nukala, Palekar, Patki, *et al.*, 2019).

Overall, such friability and breaking force results were expected due to the robustness of SLA 3D printed structures. These results demonstrate how in a future scenario where SLA 3D printed dosage forms can be manufactured close to the patient, traditional wear issues such as chipping, capping and abrasion, typical of manufacturing, packaging and shipping processes, could become not relevant (Khaled, Alexander, Irvine, *et al.*, 2018).

**Table 4.18.** % Weight loss and tablet breaking force values of SLA 3D printed drug loaded formulations. Tablet breaking force data are reported as mean  $\pm$  SD (n = 3).

<b>Formulation</b>	<b>% Weight loss</b>	<b>Breaking force (N) <math>\pm</math> SD</b>
<b>TF1</b>	0.291	388.75 $\pm$ 82.46
<b>WF1</b>	0.039	93.77 $\pm$ 24.39
<b>WF2</b>	0.084	83.92 $\pm$ 19.79
<b>WF3</b>	0.098	91.26 $\pm$ 53.11
<b>WF4</b>	0.173	138.82 $\pm$ 38.88
<b>WF5</b>	0.123	96.18 $\pm$ 30.33
<b>WF6</b>	0.215	88.87 $\pm$ 29.67
<b>WF7</b>	0.408	126.49 $\pm$ 27.85
<b>WF8</b>	0.420	102.92 $\pm$ 19.17
<b>WF9</b>	0.232	91.34 $\pm$ 20.49
<b>WF10</b>	0.320	110.46 $\pm$ 27.36
<b>WF11</b>	0.353	118.20 $\pm$ 17.78
<b>WF12</b>	0.200	109.36 $\pm$ 20.33
<b>WF13</b>	0.445	99.52 $\pm$ 23.65
<b>WF14</b>	0.178	93.12 $\pm$ 23.28
<b>WF15</b>	0.213	99.64 $\pm$ 16.33
<b>WF17</b>	0.068	114.02 $\pm$ 27.53
<b>WF18</b>	0.105	105.78 $\pm$ 25.08
<b>WF20</b>	0.353	92.23 $\pm$ 23.83
<b>WF21</b>	0.390	85.51 $\pm$ 15.90
<b>WF23</b>	0.241	96.42 $\pm$ 14.65
<b>WF24</b>	0.212	93.97 $\pm$ 17.07
<b>WF25</b>	0.232	92.21 $\pm$ 18.18
<b>WF26</b>	0.065	102.94 $\pm$ 13.27
<b>WF27</b>	0.427	97.48 $\pm$ 25.19
<b>WF28</b>	0.176	105.15 $\pm$ 26.95
<b>WF29</b>	0.079	90.95 $\pm$ 13.66
<b>WF30</b>	0.117	94.42 $\pm$ 20.36
<b>WF31</b>	0.111	107.50 $\pm$ 25.75
<b>WF32</b>	0.142	92.89 $\pm$ 16.80
<b>WF33</b>	0.768	92.36 $\pm$ 19.05
<b>WF34</b>	0.192	94.55 $\pm$ 25.83

<b>WF35</b>	0.075	103.07 ± 14.81
<b>WF36</b>	0.072	102.84 ± 19.77
<b>WF37</b>	0.102	120.02 ± 14.99
<b>WF39</b>	0.046	107.54 ± 19.68
<b>WF40</b>	0.080	105.77 ± 17.51

#### 4.4.12 Dissolution testing of 3D printed dosage forms

The SLA 3D printed dosage forms were *in-vitro* tested to simulate the drug release in physiological conditions in the gastrointestinal tract using USP apparatus I (basket) and II (paddle) (figure 4.42).

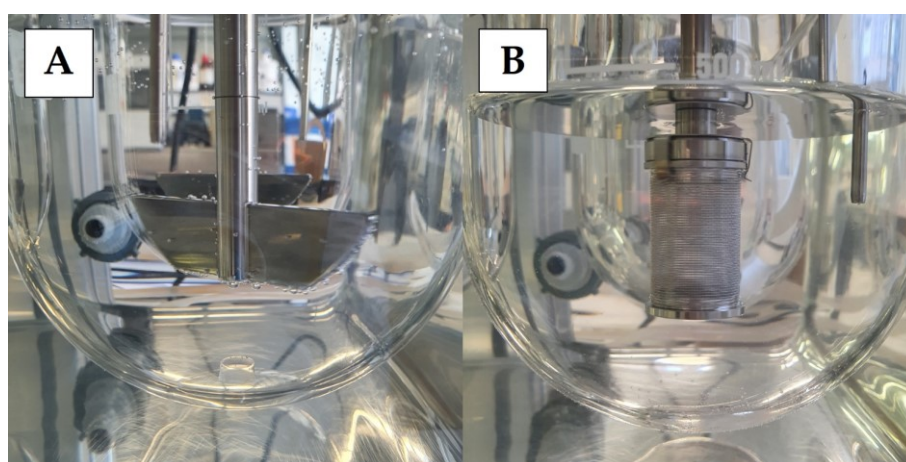


**Figure 4.42.** (A) USP apparatus II (paddle) and (B) apparatus I (basket) in operation during *in-vitro* dissolution testing.

Theophylline release from formulation TF1 was evaluated using the dissolution Test 1 described in the USP monograph of theophylline extended-release capsules. Drug release started in the simulated gastric fluid at pH 1.2 reaching 6.54% after one hour and continued in phosphate buffer (pH 6.0) eventually reaching 35.36% after 8 hours (figure 4.43). Drug release was between 3% and 15% at one hour, complying with test 1 requirements.

However, formulation TF1 did not meet test 1 specifications as drug release at 8 hours was less than 80%.

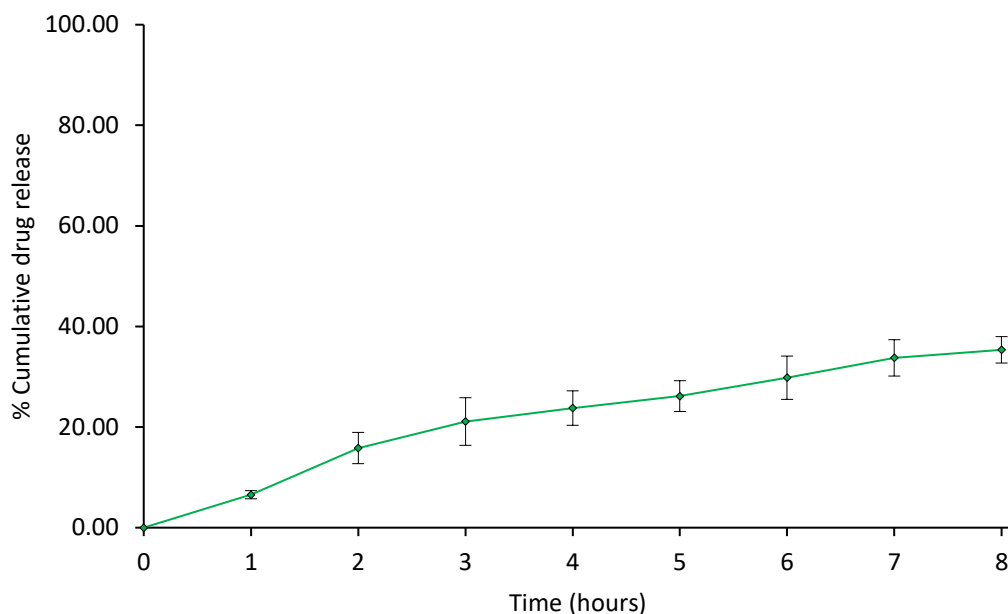


**Figure 4.43.** Theophylline release from SLA 3D printed dosage forms. Dissolution medium was simulated gastric fluid (pH 1.2) for the first hour followed by phosphate buffer (pH 6.0) for the subsequent 7 hours. Data points represent mean  $\pm$  SD (n = 3).

Warfarin and warfarin sodium release from SLA 3D printed tablets was evaluated both in water (figure 4.44), as described in the USP monograph for warfarin sodium, and in BioRelevant media (figure 4.45).

Drug release in water was evaluated over 24 hours, to gain indicative information on the extent of API release from the SLA 3D printed dosage forms after the main absorption phase (Aulton and Taylor, 2017). Due to its low water solubility (Zingone and Rubessa, 2005), 24 hours warfarin release from formulations WF1, WF2 and WF3 was 5.38% 3.92% and 1.68%, respectively. Interestingly, warfarin release from formulations WF1 and WF2 was found to be higher than the raw warfarin used as a reference (3.01%), potentially linked to the amorphous state of the API as confirmed by XRPD. On the contrary, warfarin in

formulation WF3 was found to partially maintain its crystalline state as seen from DSC and XRPD analyses.

Formulations WF4, WF5 and WF6, containing the more soluble warfarin sodium (Gao and Maurin, 2001), released respectively 20.22%, 41.01% and 46.71% of their drug content after 8 hours, and 37.85%, 67.69% and 75.13% at 24 hours. Curiously, drug release was found to be higher when warfarin sodium loading in SLA 3D printed tablets was increased.

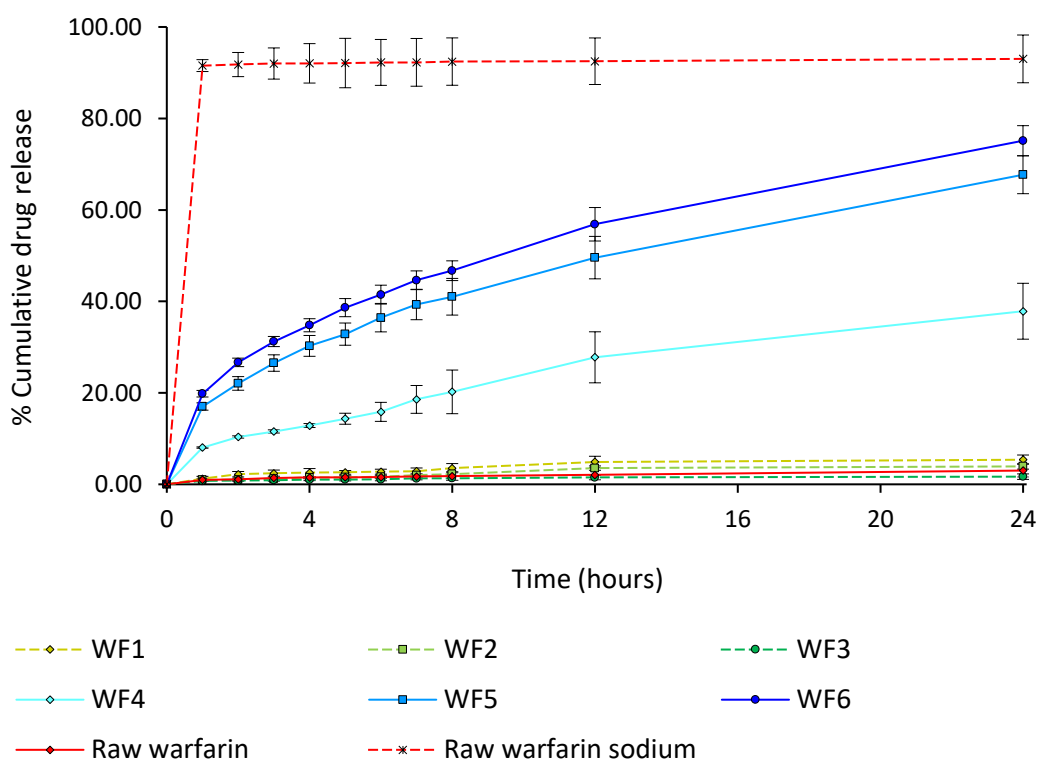


**Figure 4.44.** Warfarin and warfarin sodium release profiles in water from formulations WF1-WF6. Data points represent mean  $\pm$  SD (n = 3).

Release profiles of warfarin and warfarin sodium formulations in BioRelevant media showed a very slow dissolution rate in FaSSGF, as expected due to the acidic nature of warfarin ( $pK_a = 4.79$ ) (Zingone and Rubessa, 2005). Drug release increased substantially in FaSSIF to eventually reach a range of 12.88% to 19.57% after 8 hours.

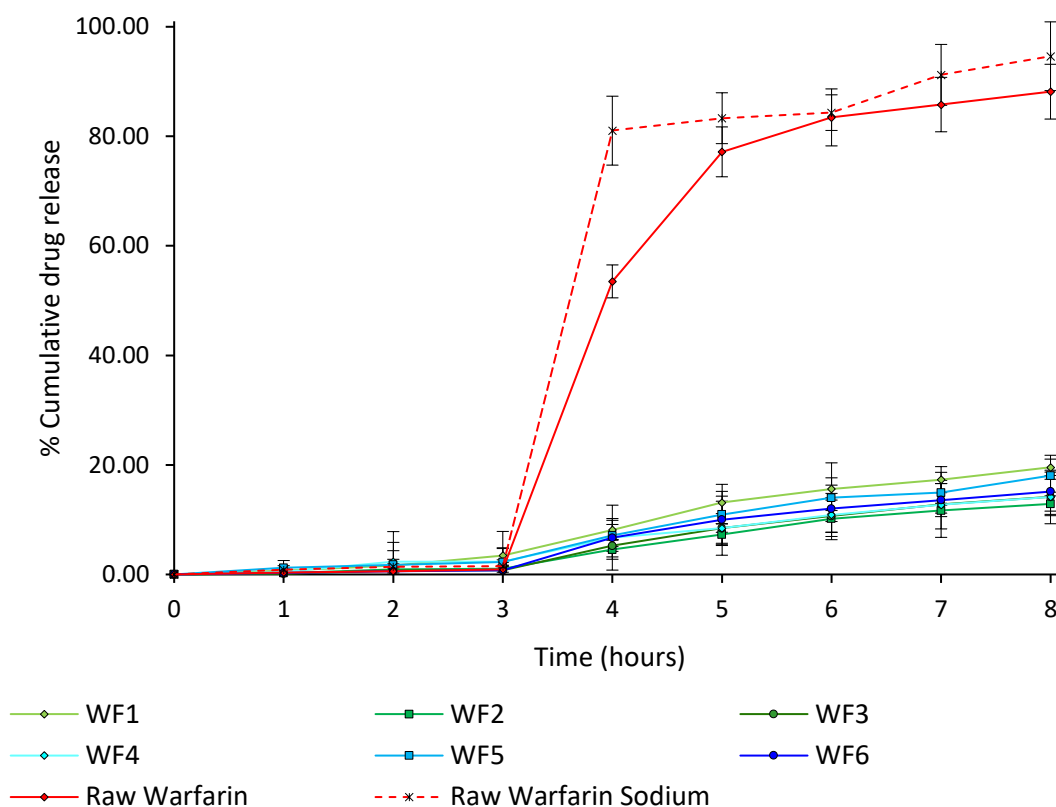


**Figure 4.45.** Warfarin and warfarin sodium release profiles in BioRelevant media from formulations WF1-WF6. Dissolution testing was carried out in FaSSGF (pH 1.6) for the first 3 hours and in FaSSIF (pH 6.5) for the subsequent 5 hours. Data points represent mean  $\pm$  SD (n = 3).

Release profiles of warfarin sodium formulations containing PG (WF7-WF15) were also determined both in water and in BioRelevant media (figures 4.46-4.47).

Dissolution profiles in water showed faster release occurring in formulations with higher loading of both API and PG, with formulation WF15 releasing 73.16% and 92.26% of its drug content at 8 and 24 hours, respectively. On the contrary, formulation WF7 showed limited drug release, reaching 22.64% and 44.42% after 8 and 24 hours, respectively.

Warfarin sodium dissolution rate from WF7-WF15 in BioRelevant media was remarkably low during the first 3 hours in FaSSGF, while it increased in FaSSIF to eventually reach a range between 13.78% (WF10) and 25.10% (WF9).

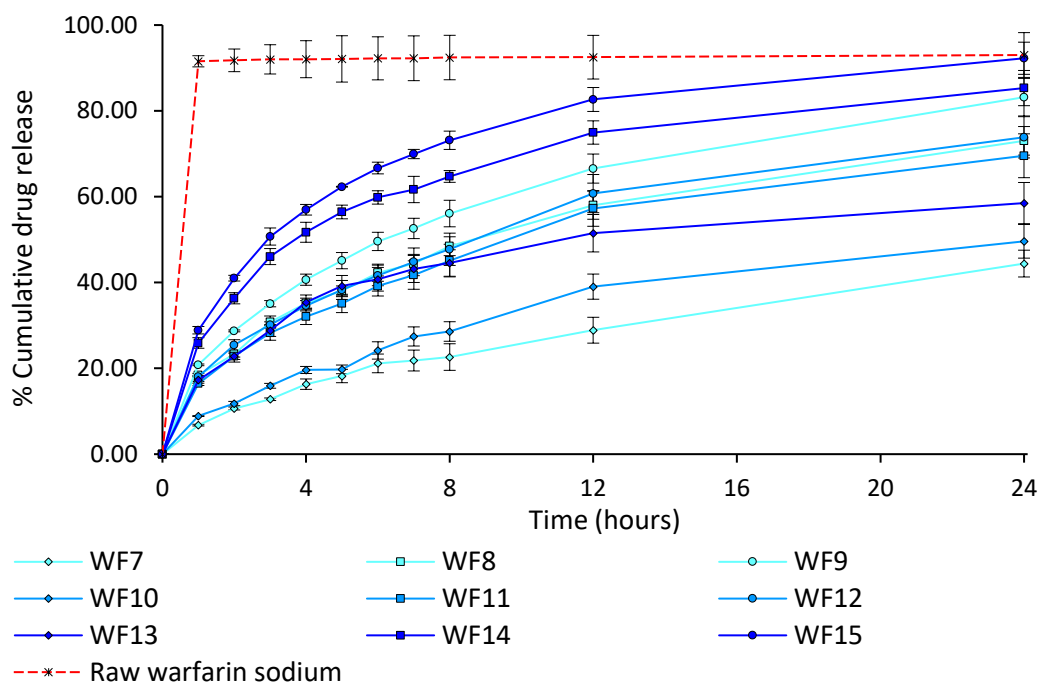


**Figure 4.46.** Warfarin sodium release profiles in water from formulations WF7-WF15. Data points represent mean  $\pm$  SD (n = 3).

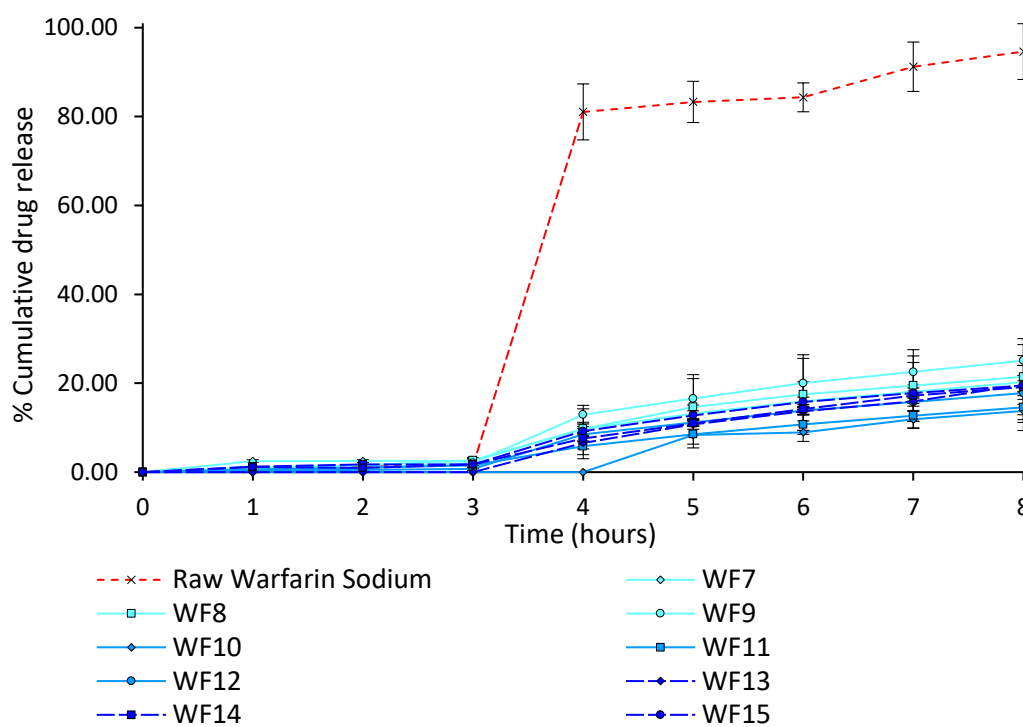


**Figure 4.47.** Warfarin sodium release profiles in BioRelevant media from formulations WF7-WF15. Dissolution testing was carried in FaSSGF (pH 1.6) for the first 3 hours and in FaSSIF (pH 6.5) for the subsequent 5 hours. Data points represent mean  $\pm$  SD (n = 3).

Dissolution profiles of SLA 3D printed warfarin sodium formulations described from herein were obtained exclusively in BioRelevant media to better simulate the GI fluids.

Formulations WF35, WF36 and WF37, containing PEG300, showed limited drug release after 8 hours (figure 4.48), ranging between 18.68% (WF36) and 20.30% (WF37).

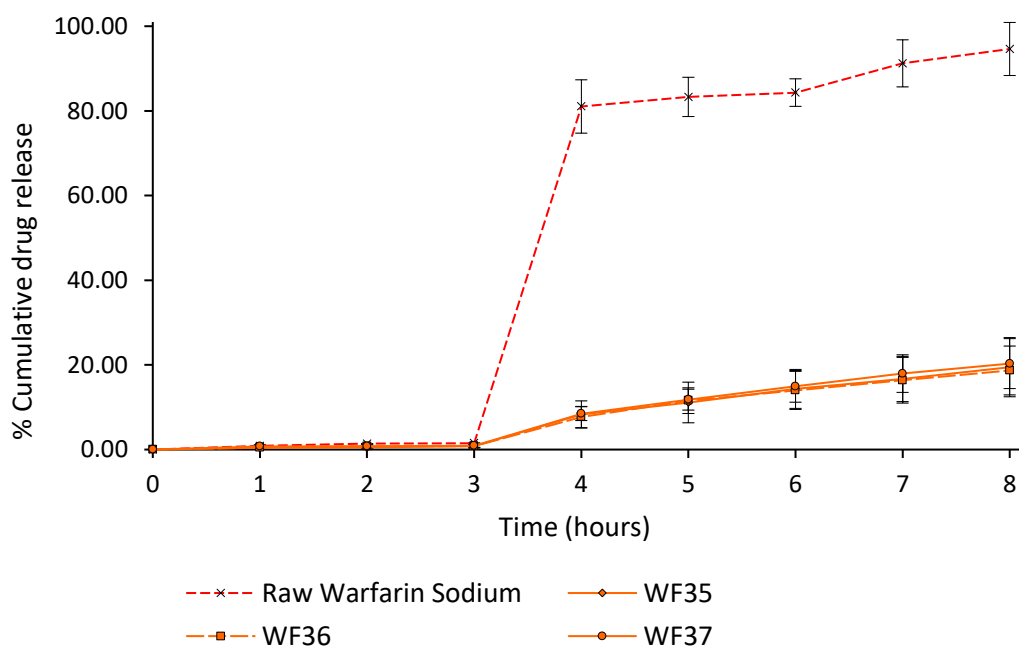


**Figure 4.48.** Warfarin sodium release profiles in BioRelevant media from formulations WF35-WF37. Dissolution testing was carried in FaSSGF (pH 1.6) for the first 3 hours and in FaSSIF (pH 6.5) for the subsequent 5 hours. Data points represent mean  $\pm$  SD (n=3).

Similarly, release profile of warfarin sodium from formulations WF20 and WF21 after 8 hours was 19.76% and 22.84% (figure 4.49).

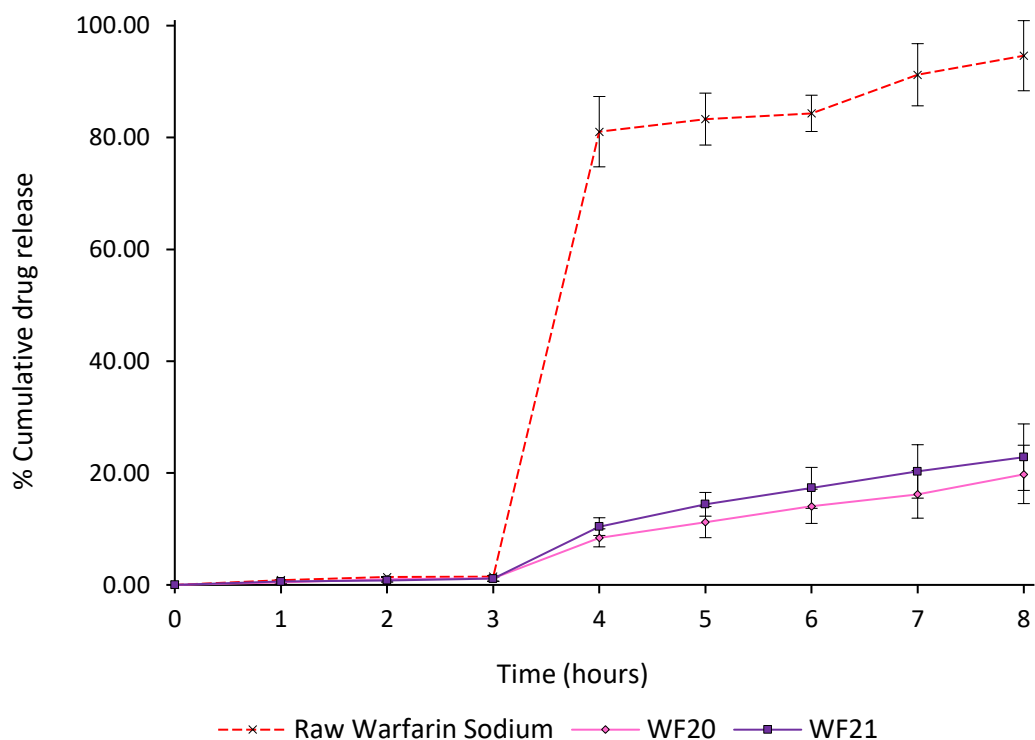


**Figure 4.49.** Warfarin sodium release profiles in BioRelevant media from formulations WF20-WF21. Dissolution testing was carried in FaSSGF (pH 1.6) for the first 3 hours and in FaSSIF (pH 6.5) for the subsequent 5 hours. Data points represent mean  $\pm$  SD (n=3).

Warfarin sodium release from SLA 3D printed dosage forms based on TGDA and PEGDA 700 was found to decrease in comparison to formulations containing liquid fillers. Drug release was also lower than formulations containing solely PEGDA 700 (WF6), suggesting that TGDA does not promote the diffusion of the API from the photocrosslinked tablet matrix. Figure 4.50 shows a drug release after 8 hours of 7.68% and 10.45% for WF17 and WF18, respectively.

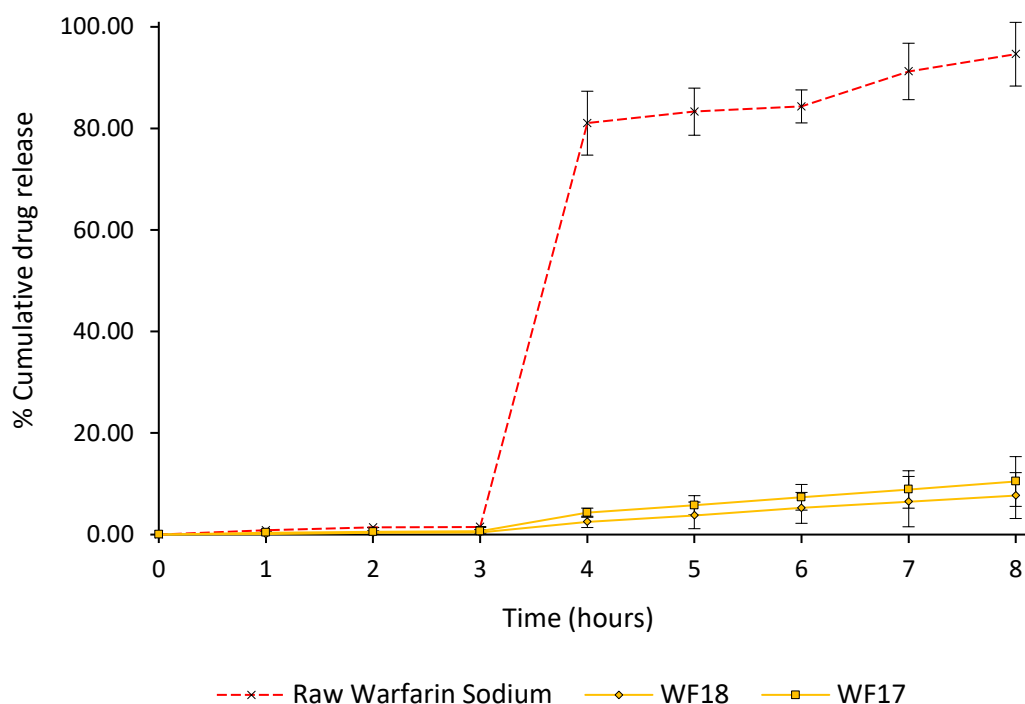


**Figure 4.50.** Warfarin sodium release profiles in BioRelevant media from formulations WF17-WF18. Dissolution testing was carried in FaSSGF (pH 1.6) for the first 3 hours and in FaSSIF (pH 6.5) for the subsequent 5 hours. Data points represent mean  $\pm$  SD (n=3).

The inclusion of PG to TGDA in formulations WF39 and WF40 did not lead to a substantial enhancement in drug release, determined after 8 hours as 10.11% and 11.82%, respectively (figure 4.51).

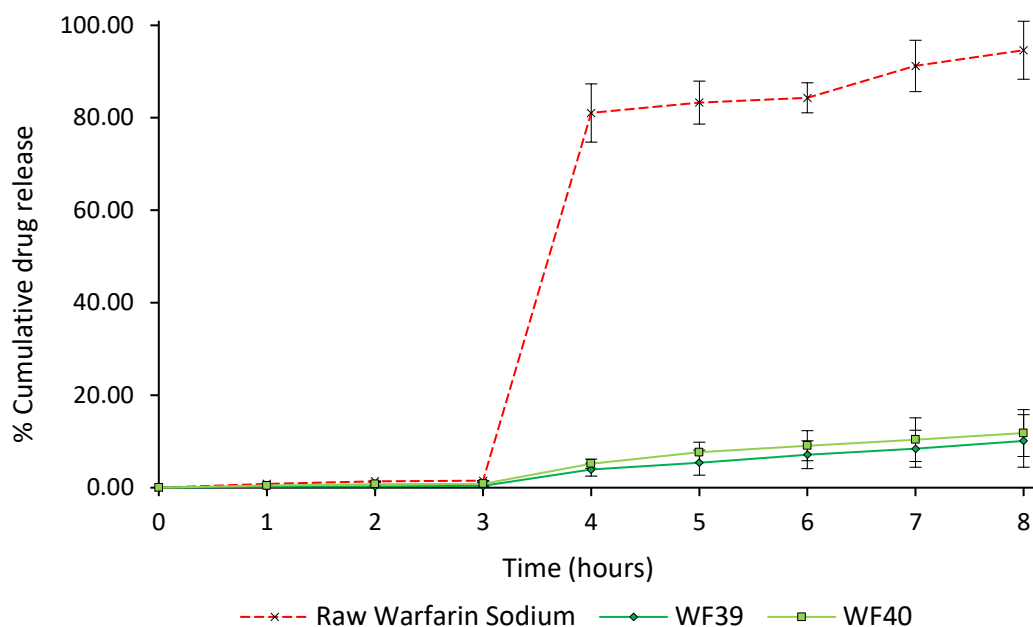


**Figure 4.51.** Warfarin sodium release profiles in BioRelevant media from formulations WF39-WF40. Dissolution testing was carried in FaSSGF (pH 1.6) for the first 3 hours and in FaSSIF (pH 6.5) for the subsequent 5 hours. Data points represent mean  $\pm$  SD (n=3).

It was observed that all formulations described above swelled during dissolution testing. Pictures were taken on swollen 3D printed tablets immediately after dissolution testing and are shown in figure 4.52.

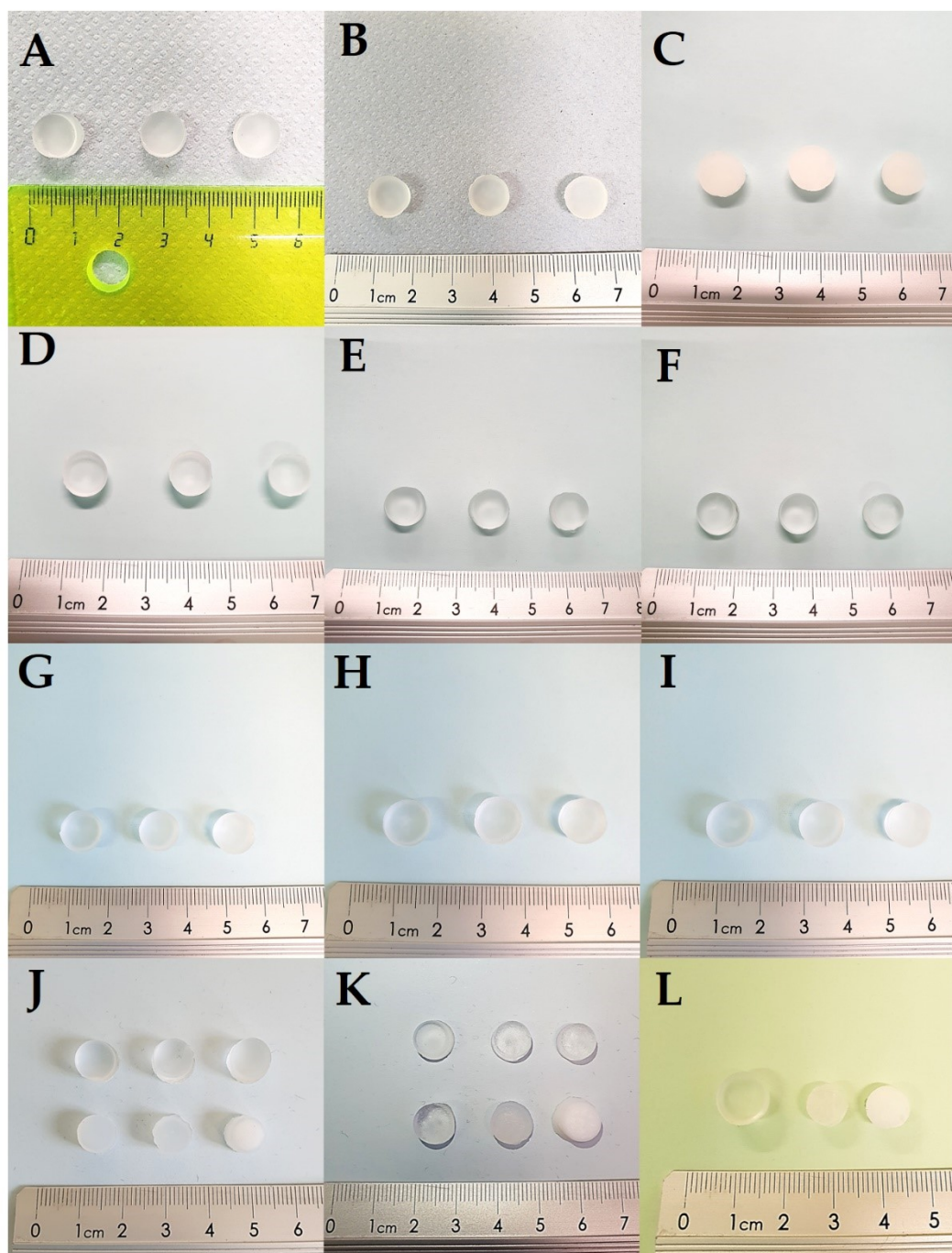


**Figure 4.52.** Images of swollen SLA 3DP dosage forms taken immediately after dissolution testing in BioRelevant media. **A:** WF1, **B:** WF2, **C:** WF3, **D:** WF4, **E:** WF5, **F:** WF6, **G:** WF7, **H:** WF8, **I:** WF9, **J:** (from top left to bottom right) WF10-WF11-WF12-WF13-WF14-WF15, **K:** (from top left to bottom right) WF17-WF20-WF21-WF35-WF36-WF37, **L:** (from left to right) WF18-WF39-WF40.

It is worth noticing that allowing the swollen SLA 3D printed dosage forms to dry at room condition for 24 hours caused them to fracture throughout their structure as shown in figure

4.53. Such phenomenon could be due to the hydration and dehydration cycle leading to swelling/shrinking-induced deformations, generating large stresses which may eventually determine fractures in the crosslinked polymer network (Rossi, Nardinocchi and Wallmersperger, 2019).

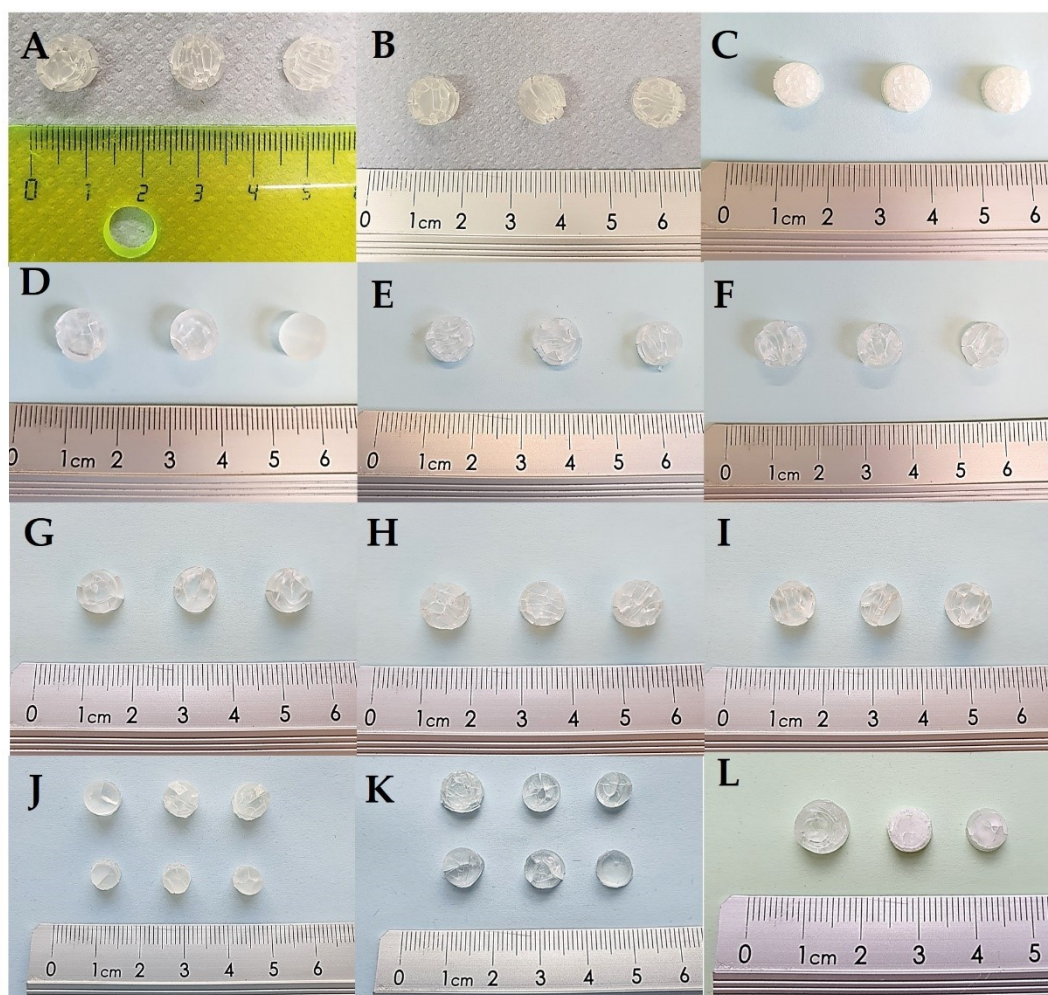


**Figure 4.53.** Images of SLA 3DP dosage forms fractured after drying at room condition for 24 hours. **A:** WF1, **B:** WF2, **C:** WF3, **D:** WF4, **E:** WF5, **F:** WF6, **G:** WF7, **H:** WF8, **I:** WF9, **J:** (from top left to bottom right) WF10-WF11-WF12-WF13-WF14-WF15, **K:** (from top left to bottom right) WF17-WF20-WF21-WF35-WF36-WF37, **L:** (from left to right) WF18-WF39-WF40.

Formulations WF23-WF25-WF27 and WF24-WF26-WF28, respectively containing coarse and milled potassium bicarbonate, showed warfarin sodium release after 8 hours between 18.16% (WF24) and 21.93% (WF28) (figure 4.54). Potassium bicarbonate was

expected to enhance drug release by effervescence in the acidic medium, thus determining the formation of pores increasing the surface area of the dosage forms, as seen from the SEM images taken after dissolution testing (figures 4.67-4.70). Release profiles of coarse and milled potassium bicarbonate formulations were comparable, and the entity of drug release was higher in comparison with formulation containing solely PEGDA 700 (WF6).

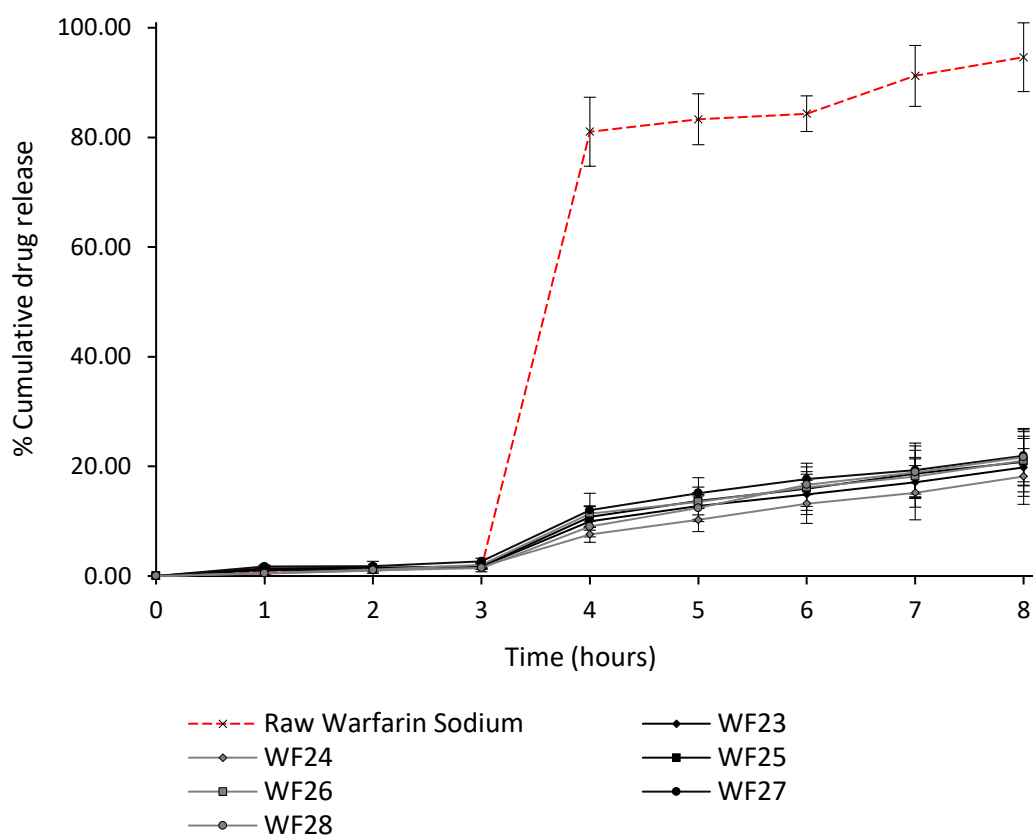


**Figure 4.54.** Warfarin sodium release profiles in BioRelevant media from formulations WF23-WF28. Dissolution testing was carried in FaSSGF (pH 1.6) for the first 3 hours and in FaSSIF (pH 6.5) for the subsequent 5 hours. Data points represent mean  $\pm$  SD (n=3).

Formulations WF29-WF31-WF33 and WF30-WF32-WF34, respectively containing coarse and milled sodium chloride, showed warfarin sodium release after 8 hours between 19.28% (WF31) and 22.41% (WF32) (figure 4.55). Sodium chloride was expected to enhance drug release by solubilising in the dissolution media, thus determining the formation of pores increasing the surface area of the dosage forms, as seen from the SEM images taken after dissolution testing (figures 4.71-4.74). Similarly to what observed for potassium bicarbonate, release profiles of coarse and milled sodium chloride formulations were comparable, and the entity of drug release was higher in comparison with formulation containing solely PEGDA 700 (WF6).

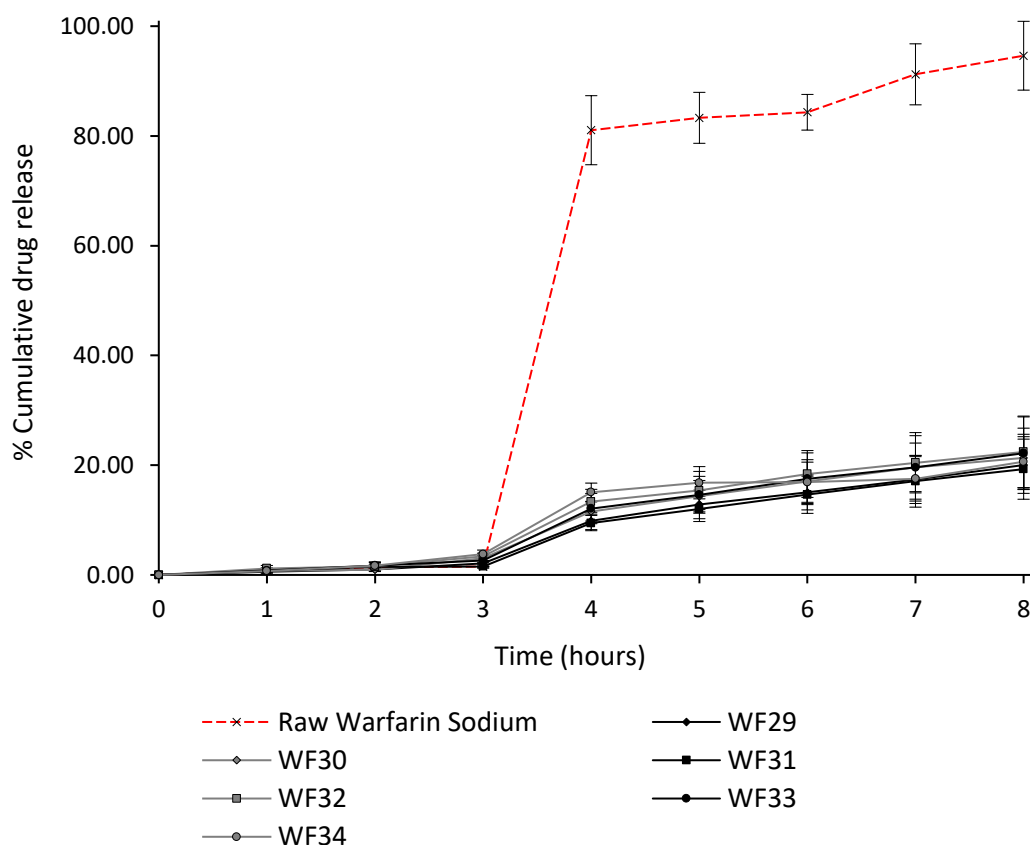


**Figure 4.55.** Warfarin sodium release profiles in BioRelevant media from formulations WF29-WF34. Dissolution testing was carried in FaSSGF (pH 1.6) for the first 3 hours and in FaSSIF (pH 6.5) for the subsequent 5 hours. Data points represent mean  $\pm$  SD (n=3).

It is very interesting to note that all 3D printed dosage forms containing solid fillers (WF23-WF34) partially broke down into fragments during dissolution testing therefore exposing a higher surface area available for drug dissolution (figures 4.56-4.57).

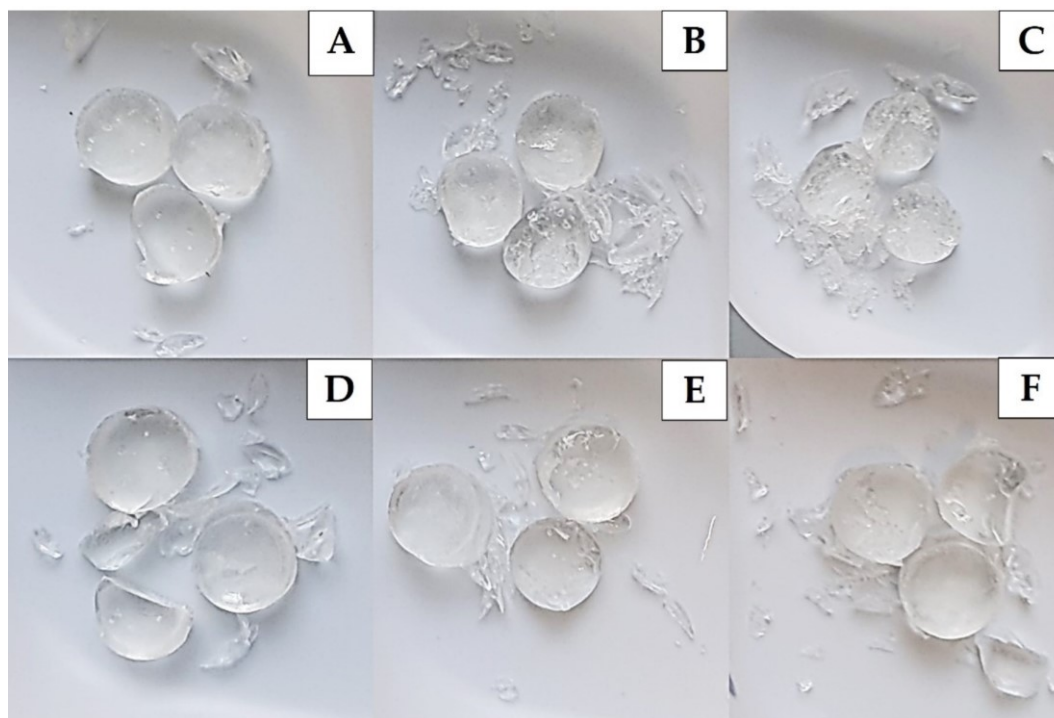


**Figure 4.56.** SLA 3D printed dosage forms produced from formulations WF23 (A), WF25 (B), WF27 (C), WF29 (D), WF31 (E), WF33 (F). Images were taken immediately after dissolution testing and show the fragments collected from the basket.

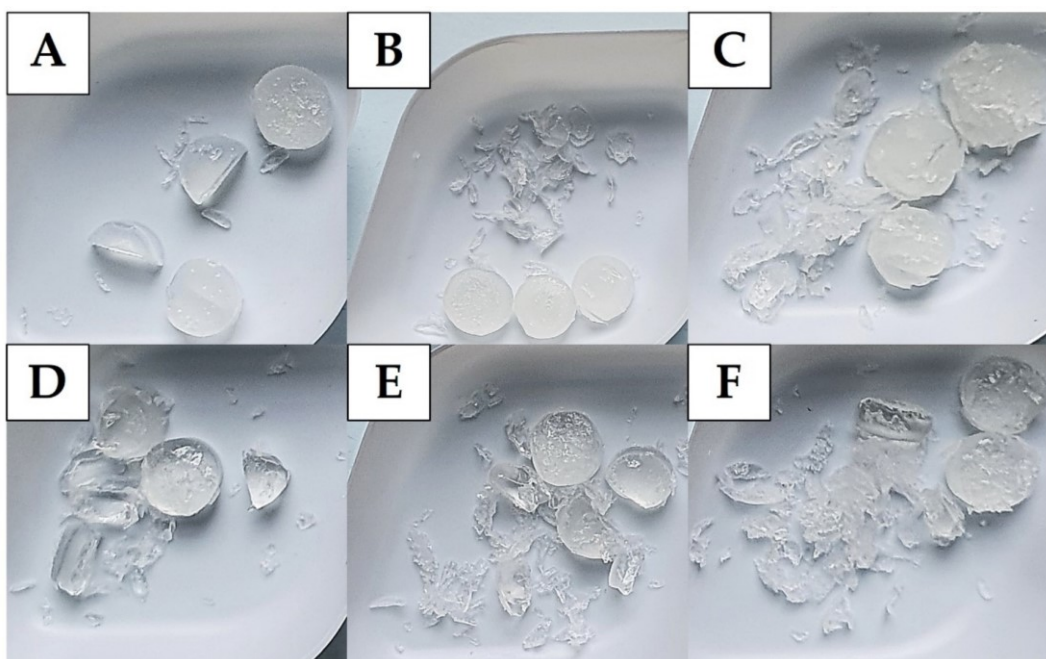


**Figure 4.57.** SLA 3D printed dosage forms produced from formulations WF24 (A), WF26 (B), WF28 (C), WF30 (D), WF32 (E), WF34 (F). Images were taken immediately after dissolution testing and show the fragments collected from the basket.

Most fragments remained in the dissolution apparatus basket where the dosage form was placed, while some could escape the basket openings measuring 0.36 mm to 0.44 mm (United States Pharmacopeial Convention, 2011). Fragments that could be found in the vessel at the end of the dissolution testing were collected and subjected to optical microscopy analysis for determining their morphology (figure 4.58).

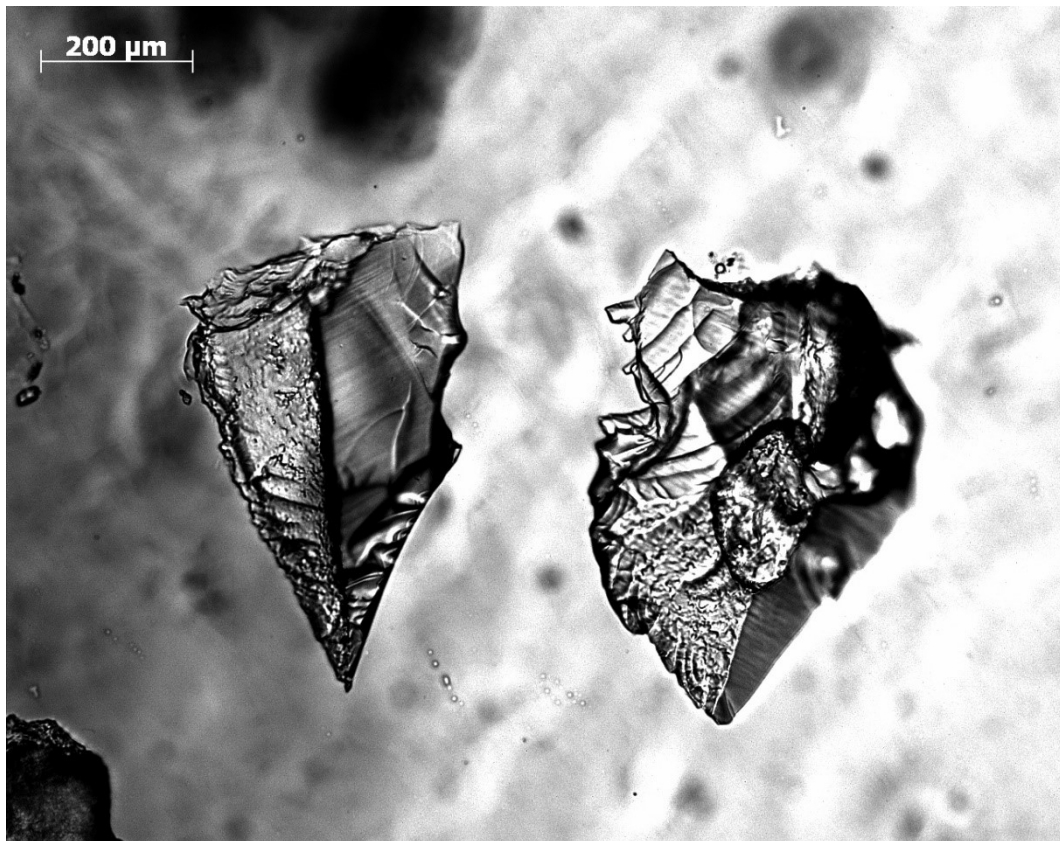


**Figure 4.58.** Optical microscope image of two fragments originating from a SLA 3D printed dosage form. Images were taken on the fragments dispersed in dissolution medium setting the magnification to  $\times 10$ .

As distinctly visible in figure 4.58, fragments of SLA 3DP dosage forms featured sharp pointy edges whose impact on the gastrointestinal mucosa is unknown. Although its good biocompatibility (Warr *et al.*, 2020), it can be hypothesised that the insoluble crosslinked PEGDA debris might behave as microplastics from a mechanical point of view. Recent research on the intestinal effects of microplastics has highlighted the risk of lesions, inflammation and gut dysbiosis (Ahrendt *et al.*, 2020; Hirt and Body-Malapel, 2020; Huang *et al.*, 2020). Therefore, it is mandatory to further investigate the safety of SLA 3D printed dosage forms fragments in contact with the gastrointestinal mucosa.

#### 4.4.13 Swelling ratio and sol-fraction determination

Determination of 3D printed dosage forms swelling ratio (SR) and sol-fraction (SF) was carried out in water (formulations TF1, WF1-WF15) and in BioRelevant media (BRm) used in dissolution testing (WF1-WF40). SR and SF data are reported in table 4.19.

**Table 4.19.** Swelling ratio and sol-fraction values of 3D printed dosage forms. Results are expressed as mean value  $\pm$  SD (n=3).

<b>Formulation</b>	<b>% SR <math>\pm</math> SD (H<sub>2</sub>O)</b>	<b>% SR <math>\pm</math> SD (BRm)</b>	<b>% SF <math>\pm</math> SD (H<sub>2</sub>O)</b>	<b>% SF <math>\pm</math> SD (BRm)</b>
<b>TF1</b>	40.98 $\pm$ 0.69	-	4.98 $\pm$ 0.54	-
<b>WF1</b>	42.04 $\pm$ 0.66	40.49 $\pm$ 1.25	6.07 $\pm$ 0.09	4.96 $\pm$ 0.19
<b>WF2</b>	43.74 $\pm$ 1.59	44.36 $\pm$ 0.53	10.12 $\pm$ 0.33	10.16 $\pm$ 0.75
<b>WF3</b>	47.09 $\pm$ 1.10	46.60 $\pm$ 0.27	11.58 $\pm$ 0.94	11.33 $\pm$ 0.48
<b>WF4</b>	39.52 $\pm$ 0.29	39.13 $\pm$ 0.65	5.74 $\pm$ 0.47	4.02 $\pm$ 0.16
<b>WF5</b>	41.00 $\pm$ 1.08	38.42 $\pm$ 0.65	8.18 $\pm$ 0.75	4.47 $\pm$ 0.54
<b>WF6</b>	41.23 $\pm$ 0.19	38.14 $\pm$ 0.78	9.61 $\pm$ 0.75	5.84 $\pm$ 0.47
<b>WF7</b>	31.72 $\pm$ 0.33	34.34 $\pm$ 0.21	17.43 $\pm$ 0.21	11.27 $\pm$ 0.68
<b>WF8</b>	32.16 $\pm$ 0.46	33.47 $\pm$ 0.92	18.22 $\pm$ 0.28	10.82 $\pm$ 0.98
<b>WF9</b>	32.13 $\pm$ 1.30	34.12 $\pm$ 0.26	19.69 $\pm$ 0.33	12.11 $\pm$ 0.19
<b>WF10</b>	29.80 $\pm$ 0.36	32.48 $\pm$ 0.53	24.55 $\pm$ 0.24	22.57 $\pm$ 0.24
<b>WF11</b>	28.59 $\pm$ 0.65	30.41 $\pm$ 0.67	27.29 $\pm$ 0.36	23.86 $\pm$ 0.34
<b>WF12</b>	29.44 $\pm$ 0.29	29.62 $\pm$ 0.82	28.62 $\pm$ 0.15	24.40 $\pm$ 0.20
<b>WF13</b>	36.22 $\pm$ 1.43	32.56 $\pm$ 1.11	45.93 $\pm$ 0.74	44.22 $\pm$ 0.50
<b>WF14</b>	30.69 $\pm$ 0.39	27.27 $\pm$ 0.71	47.97 $\pm$ 0.33	45.95 $\pm$ 0.25
<b>WF15</b>	22.27 $\pm$ 1.25	21.16 $\pm$ 0.42	50.11 $\pm$ 0.11	46.39 $\pm$ 0.21
<b>WF17</b>	-	13.22 $\pm$ 0.63	-	4.16 $\pm$ 0.61
<b>WF18</b>	-	24.48 $\pm$ 0.70	-	4.22 $\pm$ 0.35
<b>WF20</b>	-	38.24 $\pm$ 1.43	-	14.40 $\pm$ 0.34
<b>WF21</b>	-	25.80 $\pm$ 2.09	-	27.82 $\pm$ 2.02
<b>WF23</b>	-	29.40 $\pm$ 0.78	-	11.95 $\pm$ 0.36
<b>WF24</b>	-	41.19 $\pm$ 0.69	-	8.24 $\pm$ 0.24
<b>WF25</b>	-	17.42 $\pm$ 1.24	-	22.32 $\pm$ 0.47
<b>WF26</b>	-	43.15 $\pm$ 0.57	-	7.93 $\pm$ 0.33

<b>WF27</b>	-	5.46 ± 0.36	-	30.96 ± 0.45
<b>WF28</b>	-	43.46 ± 0.71	-	11.24 ± 0.52
<b>WF29</b>	-	-12.61 ± 2.12	-	40.87 ± 1.36
<b>WF30</b>	-	42.37 ± 0.98	-	8.34 ± 0.12
<b>WF31</b>	-	25.34 ± 0.46	-	16.89 ± 0.65
<b>WF32</b>	-	39.86 ± 0.87	-	5.93 ± 0.44
<b>WF33</b>	-	12.65 ± 0.21	-	24.70 ± 0.99
<b>WF34</b>	-	41.60 ± 1.13	-	20.00 ± 0.43
<b>WF35</b>	-	32.46 ± 0.55	-	14.99 ± 0.23
<b>WF36</b>	-	27.06 ± 1.78	-	24.70 ± 0.86
<b>WF37</b>	-	32.95 ± 0.54	-	45.64 ± 0.32
<b>WF39</b>	-	-18.22 ± 1.73	-	30.56 ± 0.34
<b>WF40</b>	-	-19.54 ± 0.85	-	45.99 ± 0.05

SR and SF were determined with the view to acquire information on the behaviour of the photocrosslinked structures upon prolonged contact with physiological fluids. This is particularly important because, differently from most conventional tablets, SLA 3D printed dosage forms do not disintegrate in the GI tract. Rather, such drug delivery devices behave as swellable matrices, releasing their drug content by diffusion (Colombo *et al.*, 2000). More specifically, due to their highly crosslinked nature, they can be defined as swelling-controlled release systems, where swelling continues until the achievement of thermodynamic equilibrium with the medium, and the drug release mechanism is based on relaxation-dependent diffusion (Peppas, 1984; Lee and Peppas, 1987).

3D printed tablets made from PEGDA 700 (TF1, WF1-WF6) showed high SR values, with formulation WF3 featuring the highest SR (47.09% in water, 46.60% in BioRelevant media). The inclusion of PG led to a decrease in SR, with formulations WF39-WF40 showing negative SR as a result of PG dissolution in the medium. SR of formulations containing solid fillers (WF23-WF34) showed high variability, likely resulting from the partial disintegration of the 3D printed dosage forms. In fact, while the other formulations swelled and remained intact during dissolution testing, formulations WF23-WF34 partially broke down into fragments, as described in paragraph 4.4.13 (figures 4.56-4.57).

Sol-fraction of the 3D printed formulations was also assessed to evaluate the mass fraction of the dissolved or dispersed material, resulting from the crosslinking process typically originating during SLA 3D printing (Alemán *et al.*, 2007). SF determination also provides an indication of the degree of crosslinking, as a SF of 100% indicating that the sample does not feature a crosslinked structure. On the contrary, a sol fraction close to 0% indicates that the sample has completely crosslinked (Print Parameter Optimization Guide | Support - Allevi, 2020).

For drug loaded 3D printed dosage forms, a certain extent of SF is related to the API dissolution in the medium. It was observed that the increase in liquid fillers led as expectable to an increase in SF, with WF15 showing a SF of 50.11% in water and 46.39 in BioRelevant media. Similarly, formulations WF37 and WF40, respectively including high concentrations of PEG300 and PG, had a SF of 45.64% and 45.99%, respectively, demonstrating the migration of liquid fillers from the crosslinked polymeric tablet matrix to the aqueous medium. This was also visually observed by the tablets' volume shrinkage after drying (figure 4.53). On the contrary, 3DP dosage forms only containing the photoreactive oligomers PEGDA 700 and TGDA had very low SF values, indicating a highly crosslinked structure from which little material can be dissolved or dispersed, including the API (figure 4.52).

Formulations containing solid fillers (WF23-WF34) showed high variability in the determined SF, similarly to the SR. As previously suggested, this could be due to the partial and variable entity of tablet fragmentation induced by the solubilisation of potassium bicarbonate and sodium chloride.

#### ***4.4.14 Determination of liquid fillers leachates***

It has been widely reported in the scientific literature that artefacts manufactured using vat photopolymerisation 3D printing techniques such as SLA can release over time unreacted

liquid mono/oligomers which have been associated to a certain cytotoxicity (Oesterreicher *et al.*, 2016; Oskui *et al.*, 2016; Rogers *et al.*, 2021).

However, reports of leakage of liquid fillers commonly used in SLA 3D printed dosage forms are lacking. It is known that when liquid fillers such as PEG 300 are included in a photopolymer resin, they are released during dissolution testing bringing to a visible size reduction of the 3D printed dosage forms (Wang *et al.*, 2016).

The potential release of PG (WF9, WF12 and WF15) and PEG 300 (WF35, WF36 and WF37) contained in different concentrations in SLA 3D printed dosage forms was investigated over a period of one week. The results were compared to 3D printed dosage forms (WF6) not containing any liquid filler and are reported in table 4.20.

**Table 4.20.** Percent weight and volume variation, and estimated drug loss resulting from leaching liquid fillers. Measurements were taken immediately after 3D printing and after 1 week (n = 3). Dosage forms were kept at room condition, protected from light.

<b>Formulation</b>	<b>% Weight variation <math>\pm</math> SD</b>	<b>% Volume variation <math>\pm</math> SD</b>	<b>Drug loss (mg) <math>\pm</math> SD</b>
<b>WF6</b>	1.71 $\pm$ 0.46	1.75 $\pm$ 3.43	0.00 $\pm$ 0.00
<b>WF9</b>	-5.23 $\pm$ 0.91	-10.84 $\pm$ 11.03	0.00 $\pm$ 0.00
<b>WF12</b>	-4.81 $\pm$ 0.63	-11.51 $\pm$ 19.54	0.01 $\pm$ 0.01
<b>WF15</b>	-7.37 $\pm$ 0.06	-9.43 $\pm$ 2.79	0.02 $\pm$ 0.01
<b>WF35</b>	1.01 $\pm$ 0.26	-3.52 $\pm$ 1.40	0.40 $\pm$ 0.11
<b>WF36</b>	-3.50 $\pm$ 0.31	-7.99 $\pm$ 1.65	1.63 $\pm$ 0.12
<b>WF37</b>	-2.05 $\pm$ 0.71	-9.28 $\pm$ 3.12	1.51 $\pm$ 0.36

According to the data presented in table 4.20, all 3D printed formulations containing liquid fillers, except WF35 (12.5% w/w PEG300), showed a weight reduction, more evident when increased concentrations of PG were used. Such weight reduction was also associated to a decrease in volume. 3D printed formulation WF6, used as a control, exhibited minor weight gain and volume increase, potentially resulting from environmental moisture uptake.

Potential drug loss was also investigated, and no leached warfarin sodium was detected from WF6 and WF9. On the contrary, API loss from formulations WF12 and WF15, containing increasing amounts of PG, was quantified in 0.01 mg and 0.02 mg, respectively. Alarming, 0.40 mg, 1.63 mg and 1.51 mg of warfarin sodium were respectively quantified from the leachate of formulations WF35, WF36 and WF37, indicating a theoretical % drug loss of 8%, 32.6% and 30.2%, respectively.

It is clear that such results require further attention, and that in-depth knowledge of the mechanisms causing leaching issues is needed. More factors, including a wider range of liquid fillers, photopolymer formulations, and different print and post-processing settings should be investigated to improve quality, safety and efficacy of SLA 3D printed dosage forms.

#### ***4.4.15 Weight uniformity determination of manually split tablets***

Commercially available 1 mg and 5 mg warfarin sodium tablets were manually split into halves and quarters (figure 4.59), to demonstrate the potential risk of dosage inaccuracy linked to such practice. Indeed, as widely reported in the medical community, tablet splitting can be associated with large dose deviations or weight losses that could result in serious clinical consequences, especially in the case of narrow therapeutic index drugs such as warfarin (McDevitt, Gurst and Chen, 1998; Peek, Al-Achi and J. Coombs, 2002; Verrue *et al.*, 2011).



**Figure 4.59.** 1 mg (**top**) and 5 mg (**bottom**) commercially available warfarin sodium manually split tablets.

Tablet weight was recorded on whole tablets ( $\text{weight}_1$ ), halves ( $\text{weight}_2$ ) and quarters ( $\text{weight}_3$ ). Results are reported in table 4.21. Percent weight loss and dose accuracy data of tablet halves and quarters are shown in tables 4.22-4.23.

**Table 4.21.** Weight accuracy of whole tablets ( $\text{weight}_1$ ), halves ( $\text{weight}_2$ ) and quarters ( $\text{weight}_3$ ). Results are expressed as mean weight  $\pm$  standard deviation (SD) and relative standard deviation (RSD).

Formulation	Tablet weight <sub>1</sub> mean $\pm$ SD	% RSD	Tablet weight <sub>2</sub> mean $\pm$ SD	% RSD	Tablet weight <sub>3</sub> mean $\pm$ SD	% RSD
WaNa 1 mg	159.46 $\pm$ 4.36	2.74	79.63 $\pm$ 8.33	10.46	39.64 $\pm$ 10.86	27.40
WaNa 5 mg	161.33 $\pm$ 3.72	2.30	80.54 $\pm$ 7.00	8.69	40.70 $\pm$ 7.04	17.30

**Table 4.22.** Percent weight loss of tablet halves and quarters. Results are expressed as mean % weight loss  $\pm$  standard deviation (SD) and relative standard deviation (RSD).

Formulation	% Weight loss (halves) $\pm$ SD	% RSD	% Weight loss (quarters) $\pm$ SD	% RSD
WaNa 1 mg	0.12 $\pm$ 0.10	77.58	0.51 $\pm$ 0.12	24.14
WaNa 5 mg	0.16 $\pm$ 0.10	65.40	0.33 $\pm$ 0.04	11.06

**Table 4.23.** Percent dose accuracy calculated for tablet halves and quarters. Results are expressed as mean % dose accuracy and relative standard deviation (RSD).

Formulation	% Dose accuracy (halves)	% RSD	% Dose accuracy (quarters)	% RSD
WaNa 1 mg	99.88	10.08	99.49	27.13
WaNa 5 mg	99.84	8.33	101.31	17.05

According to the data presented in table 4.21, the weight of whole tablets was relatively uniform and a RSD of 2.74% and 2.30% was recorded for 1 mg and 5 mg tablets, respectively. On the contrary, weight uniformity of tablet halves decreased sharply and a RSD of 10.46% and 8.69% was observed for 1 mg and 5 mg tablet halves, respectively. Weight uniformity worsened substantially in tablet quarters, where a RSD of 27.40% and 17.30% was calculated for 1 mg and 5 mg warfarin sodium formulations, respectively. Obviously, such results can cause high dose variability, as shown in table 4.23.

Indeed, neither tablet halves nor quarters showed a RSD for dose accuracy within acceptable limits ( $RSD \leq 6\%$ ) (Teng *et al.*, 2002), hence highlighting the risk of lack of dose uniformity associated with manual tablet splitting. Also, it should not be neglected that manual splitting is also associated with weight loss (table 4.22), which could result in the further risk of underdosing.

It is clear that these results underline the need for novel manufacturing platforms able to deliver dose flexibility in a convenient yet reliable way, requirements making pharmaceutical 3D printing a potential frontrunner (Cui *et al.*, 2021).

#### ***4.4.16 Fourier-transform infrared spectroscopy***

A major drawback of SLA 3DP is related to the presence of uncured monomers and/or oligomers in the final product generating toxicity concerns (Curti, Kirby and Russell, 2020). Indeed, it is widely reported that (meth)acrylates used in SLA have a low degree of conversion (DC) after the 3D printing process, generally between 60 – 90 %, (Oesterreicher *et al.*, 2016; Xu *et al.*, 2021), and that the uncured photoreactive molecules still present in

the 3D printed part will then be able to leach out of the crosslinked structure (Oskui *et al.*, 2016). As a result, it is a priority to investigate the DC after printing and to assess the potential presence of unreacted molecules.

FTIR spectroscopy has been widely used for such purpose (Shin *et al.*, 1993; Galvão *et al.*, 2013), and lately applied to photopolymerised 3D printed dosage forms (Clark *et al.*, 2017a; Kadry *et al.*, 2019). In this research, FTIR was used to investigate the presence of unreacted PEGDA 700 in the 3D printed tablets.

Dosage forms produced from formulations WF3, WF6, WF9, WF12, WF15, WF35, WF36 and WF37 were analysed and FTIR spectra are shown in figures 4.60-4.62.

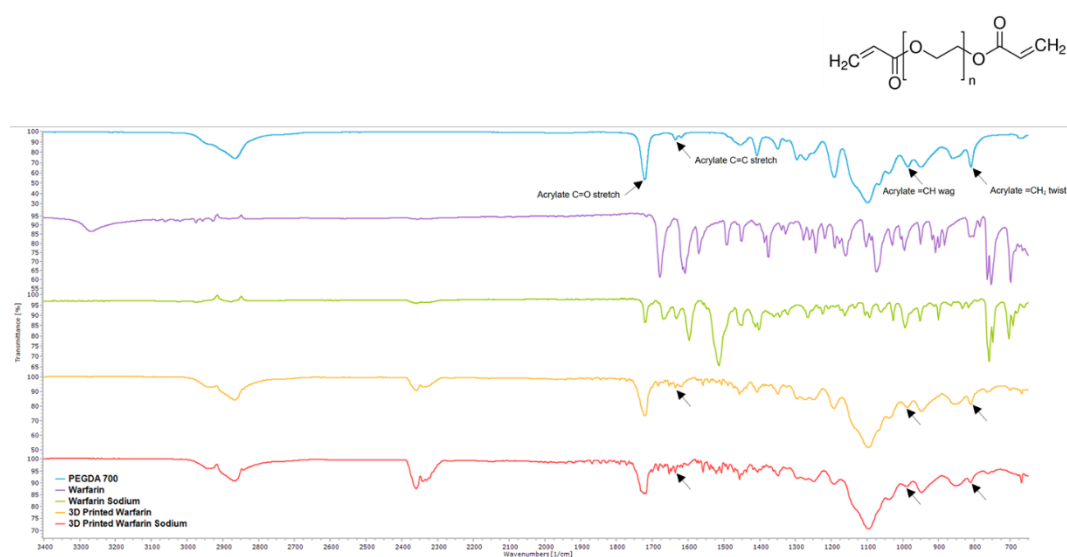


**Figure 4.60.** From top to bottom: FTIR spectra of uncured PEGDA 700, warfarin, warfarin sodium, 3D printed warfarin (WF3), 3D printed warfarin sodium (WF6). PEGDA chemical structure is reported in the top-right corner as a reference.

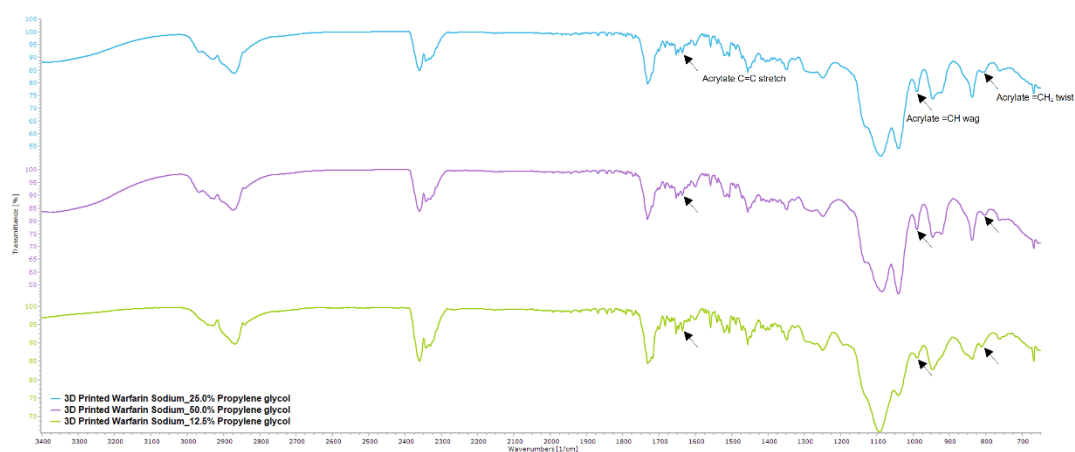


**Figure 4.61.** From top to bottom: FTIR spectra of 3D printed WF9, WF12 and WF15.

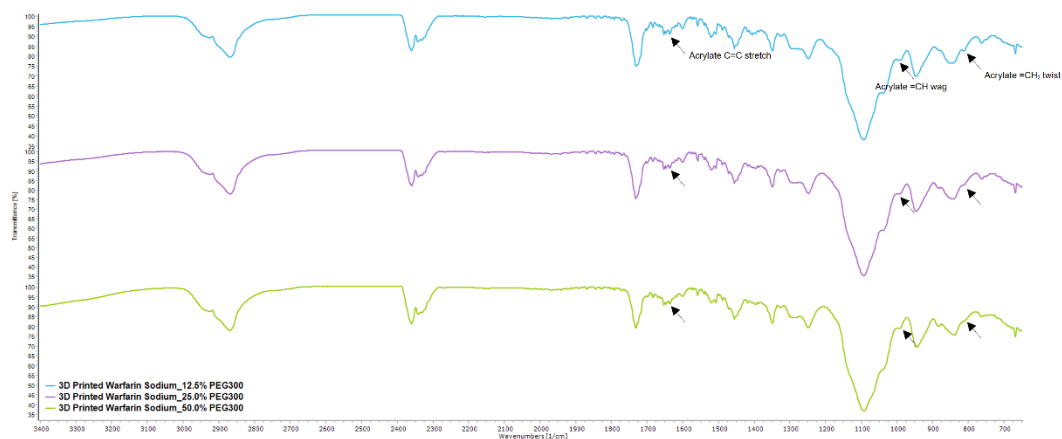


**Figure 4.62.** From top to bottom: FTIR spectra of 3D printed WF35, WF36 and WF37.

Figure 4.60 shows typical peaks of PEGDA at  $1720\text{ cm}^{-1}$  (acrylate C=O stretching),  $1635\text{ cm}^{-1}$  (acrylate C=C stretching),  $985\text{ cm}^{-1}$  (=CH wag) and  $810\text{ cm}^{-1}$  (=CH<sub>2</sub> twist) (Lin-Vien *et al.*, 1991; Hwang *et al.*, 2015). Interestingly, signals related to such peaks could be detected in all 3D printed formulations, suggesting that uncured PEGDA residues could still be present (figures 4.61-4.62). These peaks should not be attributed to warfarin, which exhibits characteristic bands at  $2954\text{--}2922\text{ cm}^{-1}$  (asymmetric -CH<sub>2</sub> stretching),  $1681\text{ cm}^{-1}$  (lactone C=O stretching),  $1617\text{ cm}^{-1}$  and  $1570\text{ cm}^{-1}$  (phenyl rings C=C stretching),  $1451\text{ cm}^{-1}$  and  $1327\text{ cm}^{-1}$  (asymmetric and symmetric -CH<sub>3</sub> bending), at  $882\text{ cm}^{-1}$ ,  $764\text{ cm}^{-1}$  and

700  $\text{cm}^{-1}$  (phenyl rings -CH bending), and at 1222  $\text{cm}^{-1}$  (hemiketal hydroxyl in-plane bending) (Rodig, 1963; Amalanathan, Joe and Kostova, 2010; Khalil *et al.*, 2012; Parfenyuk and Dolinina, 2017). These results, in contrast with previous works from Kadry *et al.*, 2019 and Clark *et al.*, 2017, underline the importance of further investigation required to precisely evaluate the DC and the quantification of uncured residues. It could be hypothesised that the low amount of photoinitiator used (0.05 % w/w) and the lack of UV or thermal post-curing have not allowed a total conversion of the C=C in PEGDA. Moreover, it may be speculated that propylene glycol (WF9, WF12, WF15) and PEG 300 (WF35-WF37), used as liquid fillers, might have acted as a reservoir of unreacted PEGDA molecules by mixing and surrounding the reactive photopolymer. Also, as it has been previously proved that liquid fillers leach out from 3D printed dosage forms over time, it could be possible that they also act as carriers of unreacted residues.

It is clear that such issue requires more attention, and the application of accurate techniques, such as Raman spectroscopy (Shin *et al.*, 1993; Gauthier *et al.*, 2005), can be particularly helpful to tackle the undetected presence of uncured (meth)acrylates in SLA 3D printed devices.

In fact, leaching of uncured residues can be particularly evident in the case of solid oral dosage forms, due to the presence of physiological fluids and movements in the gastrointestinal tract that may promote such phenomenon. This should be avoided due to the high reactivity of (meth)acrylates present in photopolymerisable resins, expressing their cytotoxicity by reacting towards amino- and thiol-groups of proteins and DNA (Oesterreicher *et al.*, 2016).

Ways of reducing the potential toxicity of SLA 3D printed devices are available, and are mainly based on increasing the DC by post-processing either using UV light or heat (Oskui *et al.*, 2016; Xu *et al.*, 2021). However, while post-processing can be done on certain types of products, particular attention should be paid in the case of drug loaded devices due to the risk of degrading the APIs or to alter core features such as drug release (Xu *et al.*, 2021).

#### 4.4.17 Differential scanning calorimetry

Thermal analysis was carried out on pure warfarin and warfarin sodium, and on drug loaded 3D printed dosage forms fabricated from formulations WF3 and WF6 to investigate samples' physical state. DSC thermograms of samples analysed are shown in figure 4.63.

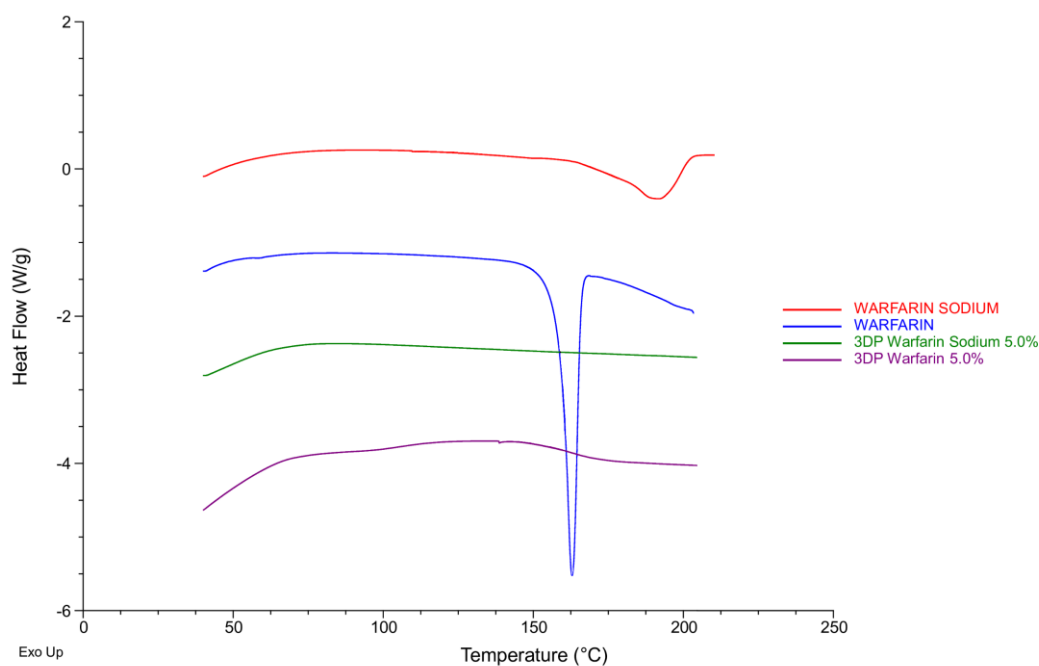


**Figure 4.63.** DSC thermograms of warfarin sodium, warfarin, 3D printed 5.0% w/v warfarin sodium (WF6) and 3D printed 5.0% w/v warfarin (WF3).

Pure warfarin DSC thermogram features a sharply defined melting peak at  $T = 162.96\text{ }^{\circ}\text{C}$  as reported in literature, thus confirming its crystalline state (Babhair, Tariq and Al-Badr, 1985; Parfenyuk and Dolinina, 2017).

A broad shoulder endothermic peak at  $T_{\text{onset}} (\Delta H_f) = 191.89\text{ }^{\circ}\text{C}$  was observed in the DSC thermogram of pure warfarin sodium, indicating that the API was in the crystalline state so it could be detected by DSC (Gao and Maurin, 2001; Vuddanda *et al.*, 2018; Sjöholm and Sandler, 2019).

3D printed warfarin (WF3) thermogram features a small endothermic peak, suggesting that some API is present in the crystalline state. This would be expected, considering that

warfarin in formulation WF3 did not fully dissolve due to its low solubility in PEGDA (table 4.12) and suspended particles remained both in the liquid photopolymer resin and in the 3D printed dosage form.

No melting peak could be observed in the DSC thermogram of 3D printed warfarin sodium (WF6), thus indicating that the API was fully dissolved in the liquid resin and remained in its amorphous state after the 3D printing process. Such a finding is particularly interesting because it reveals that SLA 3D printing can enable drug amorphisation, a successful strategy to improve the bioavailability of poorly water-soluble APIs (Buyukgoz, Kossor and Davé, 2021).

DSC results were further corroborated by the application of X-ray powder diffractometry.

#### ***4.4.18 X-ray powder diffractometry***

X-ray powder diffraction analysis was performed in order to investigate any changes in the physical form of the APIs resulting from the SLA 3DP process. XRPD data were collected on pure as received warfarin and warfarin sodium, on a drug free SLA 3D printed tablet used as reference, and on drug loaded dosage forms containing warfarin and warfarin sodium in three different concentrations (WF1-WF6) (figure 4.64).

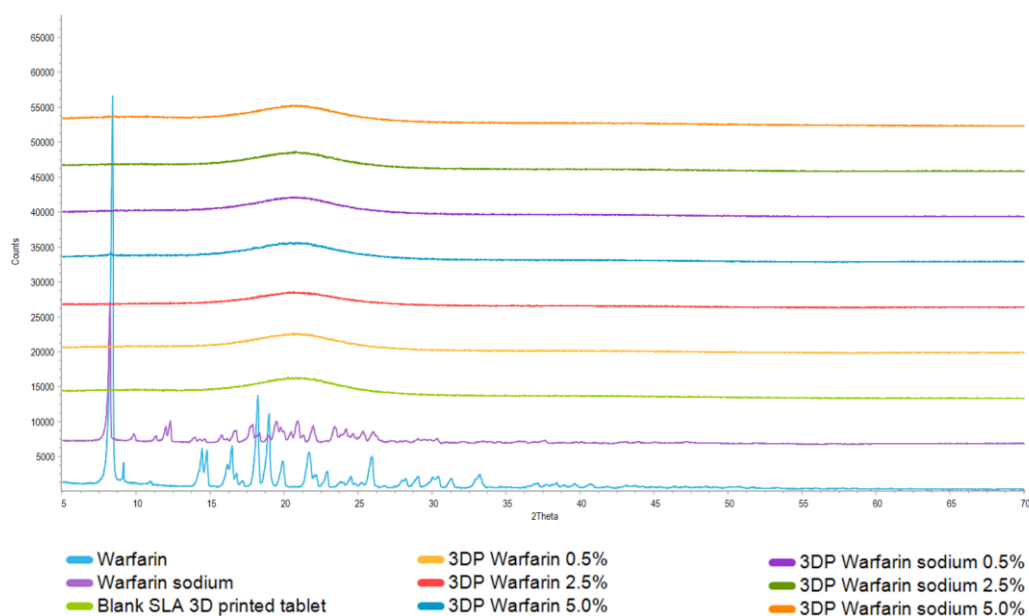


**Figure 4.64.** X-ray powder diffractograms of pure warfarin and warfarin sodium and 3D printed dosage forms. Signals were acquired over a  $2\theta$  range of 5-70 degrees.

XRPD patterns of warfarin and warfarin sodium match well with those reported in the literature (Nguyenpho *et al.*, 2015; Siddiqui *et al.*, 2015), with a characteristic peak visible at  $8.25^\circ 2\theta$ . The absence of such peak in the diffractograms of drug loaded SLA 3D printed dosage forms would suggest that the APIs are present in the amorphous state and that no recrystallisation occurred after photopolymerisation. Such results were expected, as the APIs were fully solubilised into the liquid photopolymer resin prior 3D printing.

The diffractogram of 3D printed formulation WF3, containing suspended warfarin particles, showed a low intensity peak at  $8.25^\circ 2\theta$ , suggesting that warfarin was present, to some extent, in the crystalline form.

#### 4.4.19 Scanning electron microscopy imaging

SEM imaging was employed to reveal the internal structure of a selected pool of SLA 3D printed formulations.

Images of dosage forms 3D printed from formulations WF3 and WF6 were taken to visualise any differences in the internal structure, as a potential result of the presence of suspended warfarin particles in formulation WF3 (figures 4.65-4.66). In figure 4.65A-B, particles of warfarin can be seen dispersed in the photocrosslinked structure. On the contrary, the internal surface shown in figure 4.66A-B appears much smoother, with no evidence of drug particles. Interestingly, both figures 4.65D and 4.66D reveal the presence of a network of fractures only visible at a magnification of  $\times 5000$ , which could be caused by shrinkage stress during the fast radical chain growth polymerisation (Oesterreicher *et al.*, 2016; Li, Cui and Li, 2021).

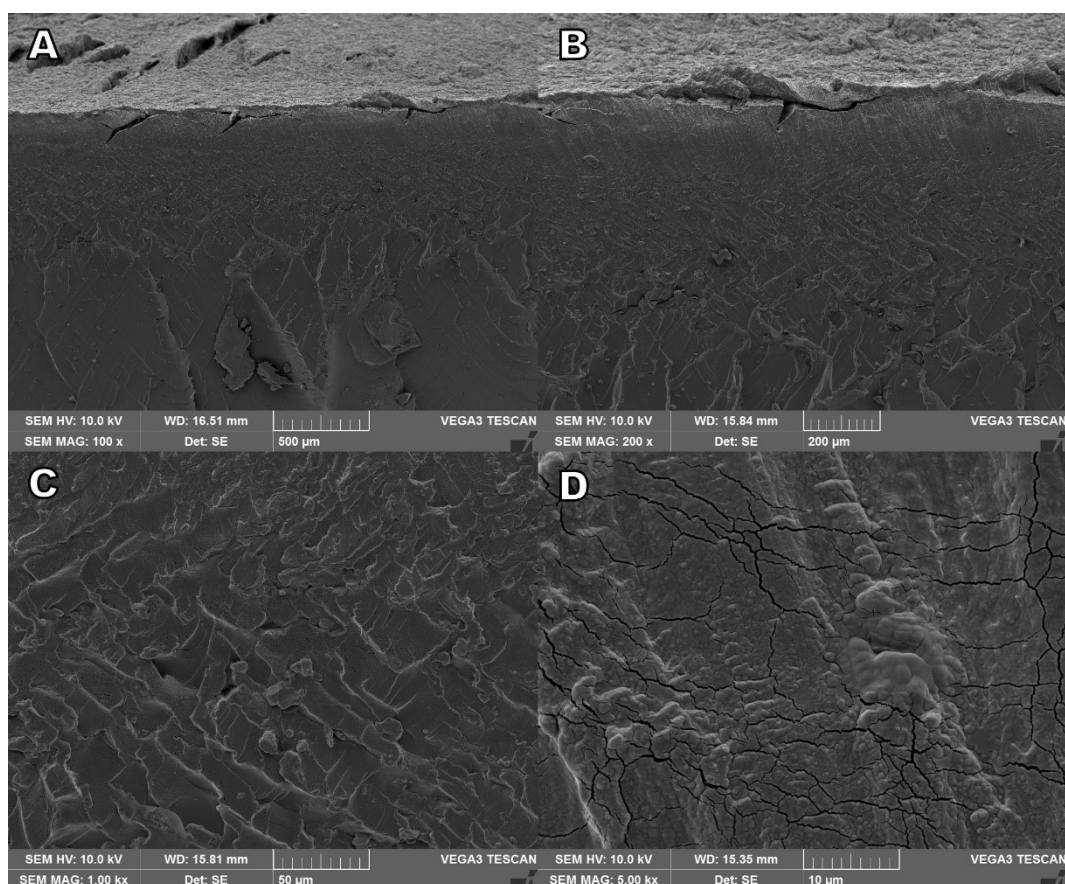


**Figure 4.65.** SEM images of cross-sectional view of a dosage form 3D printed from WF3.

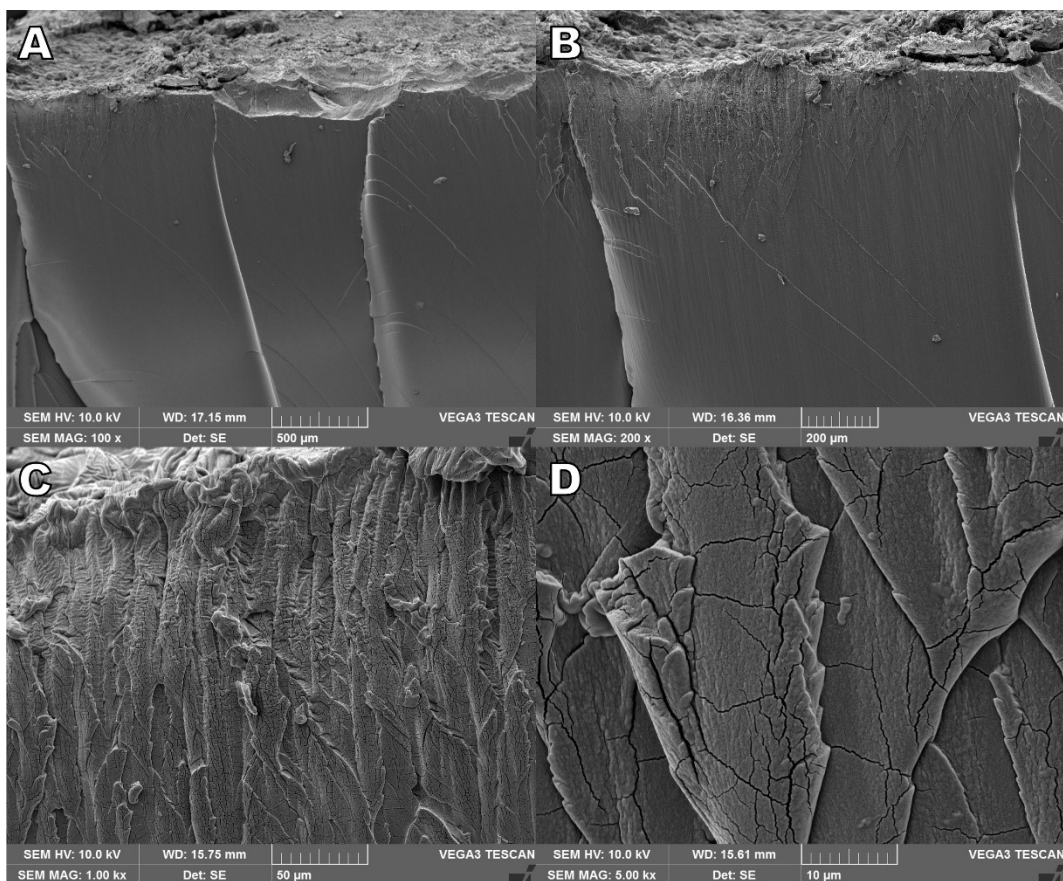


**Figure 4.66.** SEM images of cross-sectional view of a dosage form 3D printed from WF6.

SEM images of 3D printed formulation WF25 allowed to visualise structural changes after dissolution testing as a result of the effervescence of coarse potassium bicarbonate in the simulated gastric fluid. As visible in figure 4.67C-D, dosage form surface appears porous and fractured after dissolution, with visible signs of fragments detachment. Similarly, the internal section revealed the presence of fractures and small pores (figure 4.68).

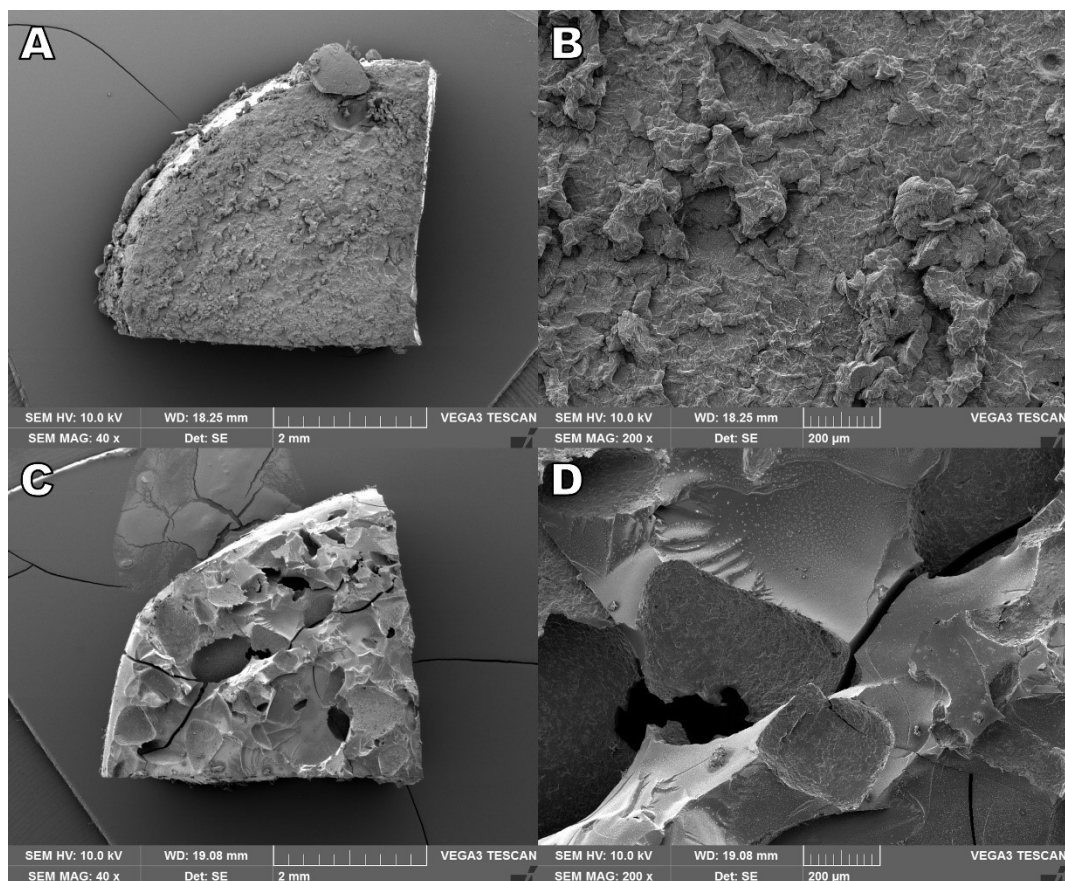


**Figure 4.67.** SEM images of top view of a dosage form 3D printed from WF25 before (A-B) and after (C-D) dissolution testing.

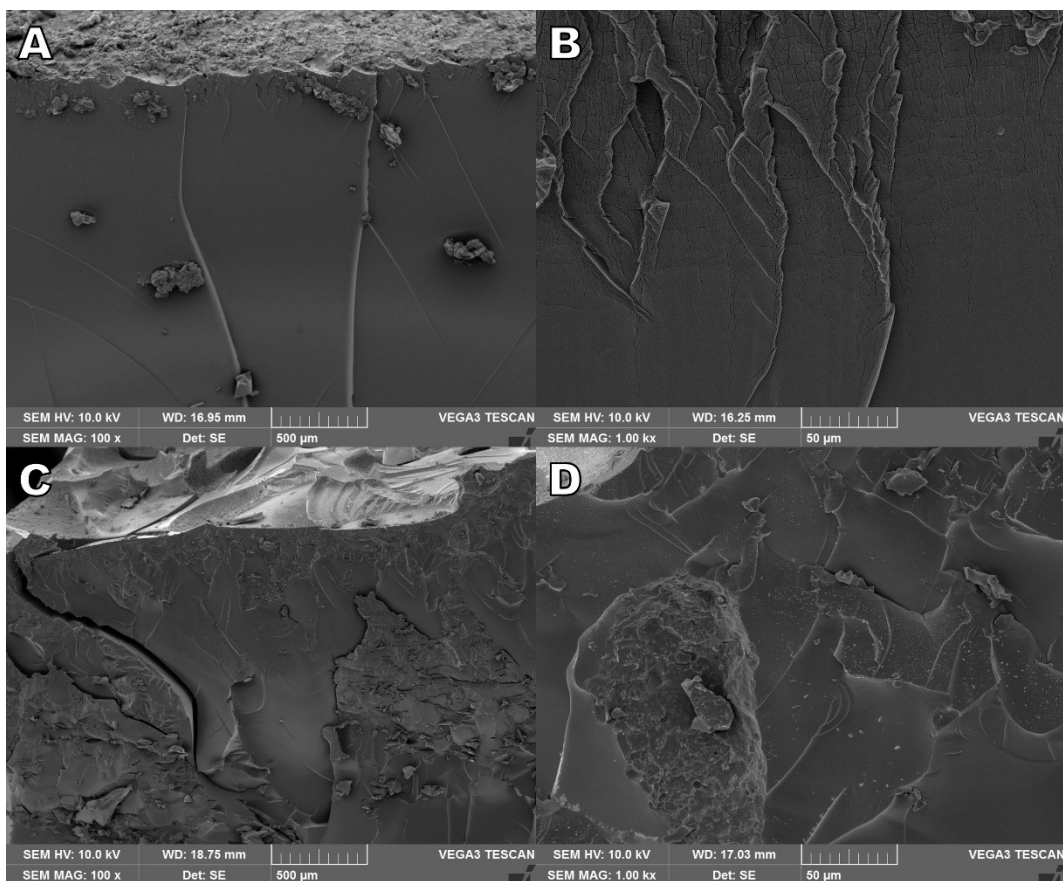


**Figure 4.68.** SEM images of cross-sectional view of a dosage form 3D printed from WF25 before (A-B) and after (C-D) dissolution testing.

In comparison with WF25, SEM images of 3D printed formulation WF28, containing milled potassium bicarbonate, showed a highly fractured surface and the presence of multiple pores after dissolution (figures 4.69-4.70).

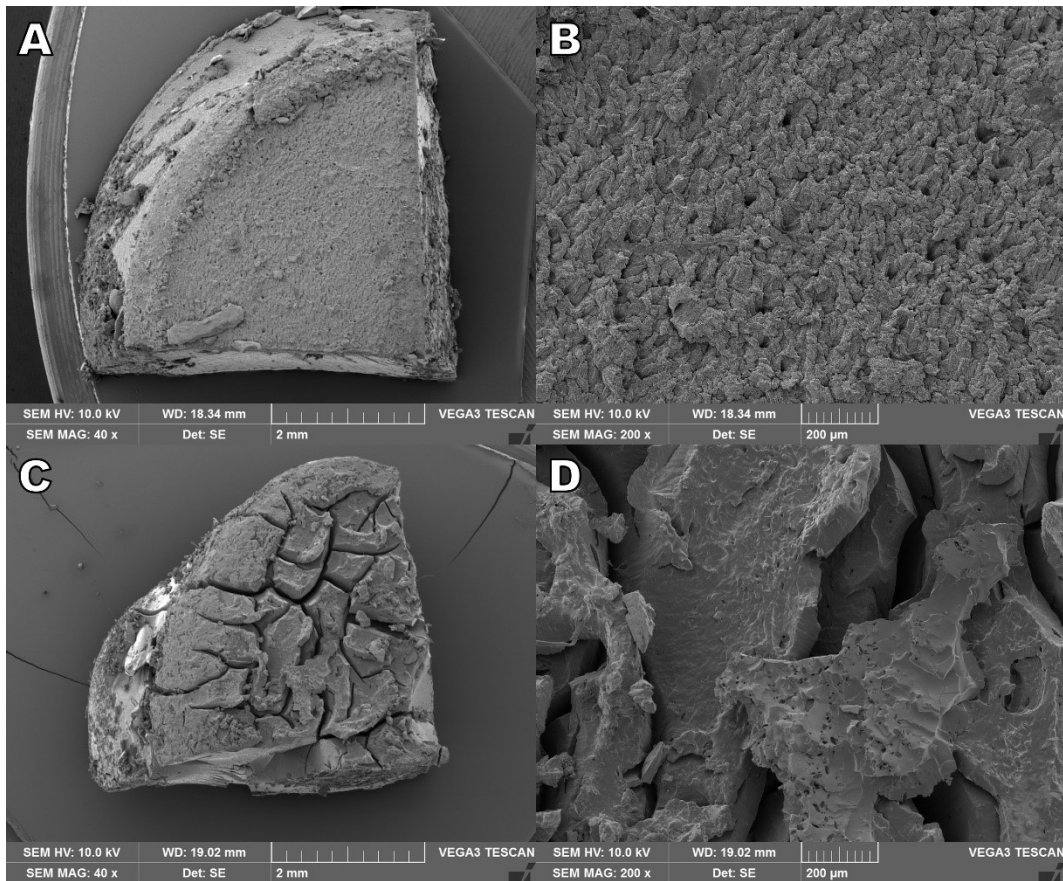


**Figure 4.69.** SEM images of top view of a dosage form 3D printed from WF28 before (A-B) and after (C-D) dissolution testing.

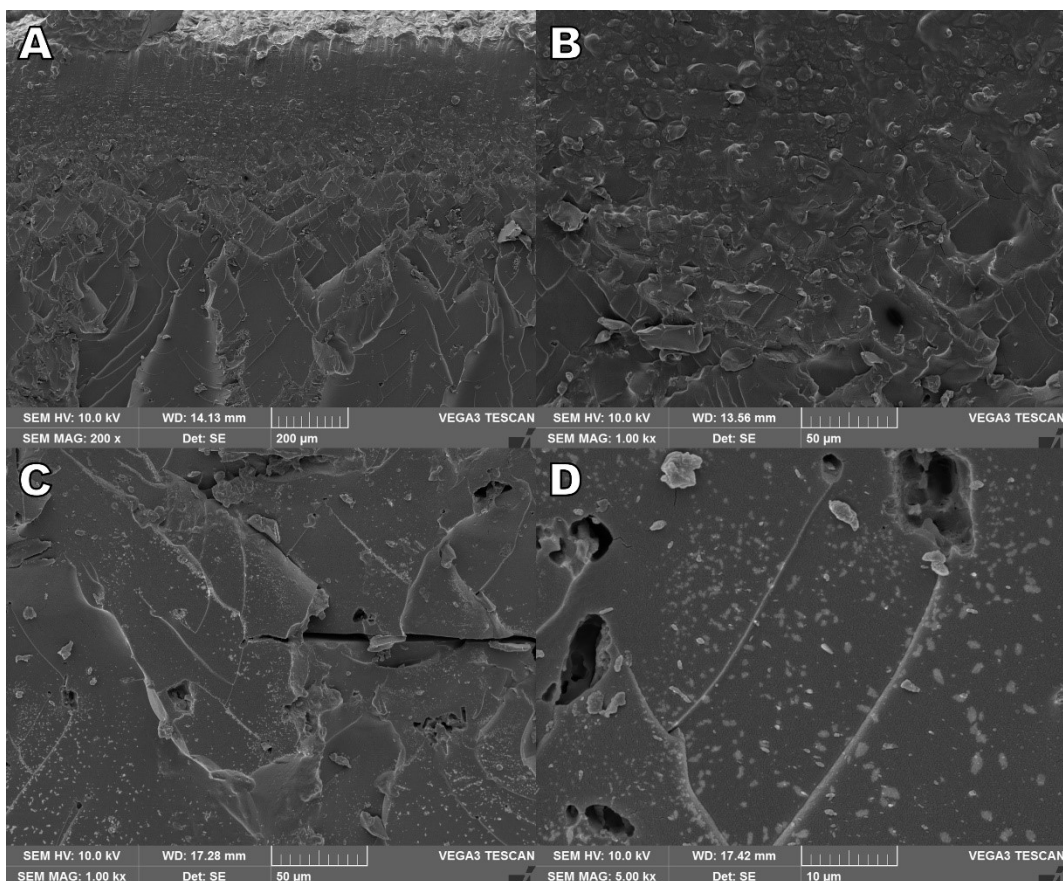


**Figure 4.70.** SEM images of cross-sectional view of a dosage form 3D printed from WF28 before (A-B) and after (C-D) dissolution testing.

SEM images of 3D printed formulation WF31 allowed to visualise structural changes after dissolution testing as a result of the solubilisation of coarse sodium chloride in the dissolution medium. As visible in figure 4.71C-D, dosage form surface appears fractured after dissolution, while only minor fractures could be observed in the internal section (figure 4.72).

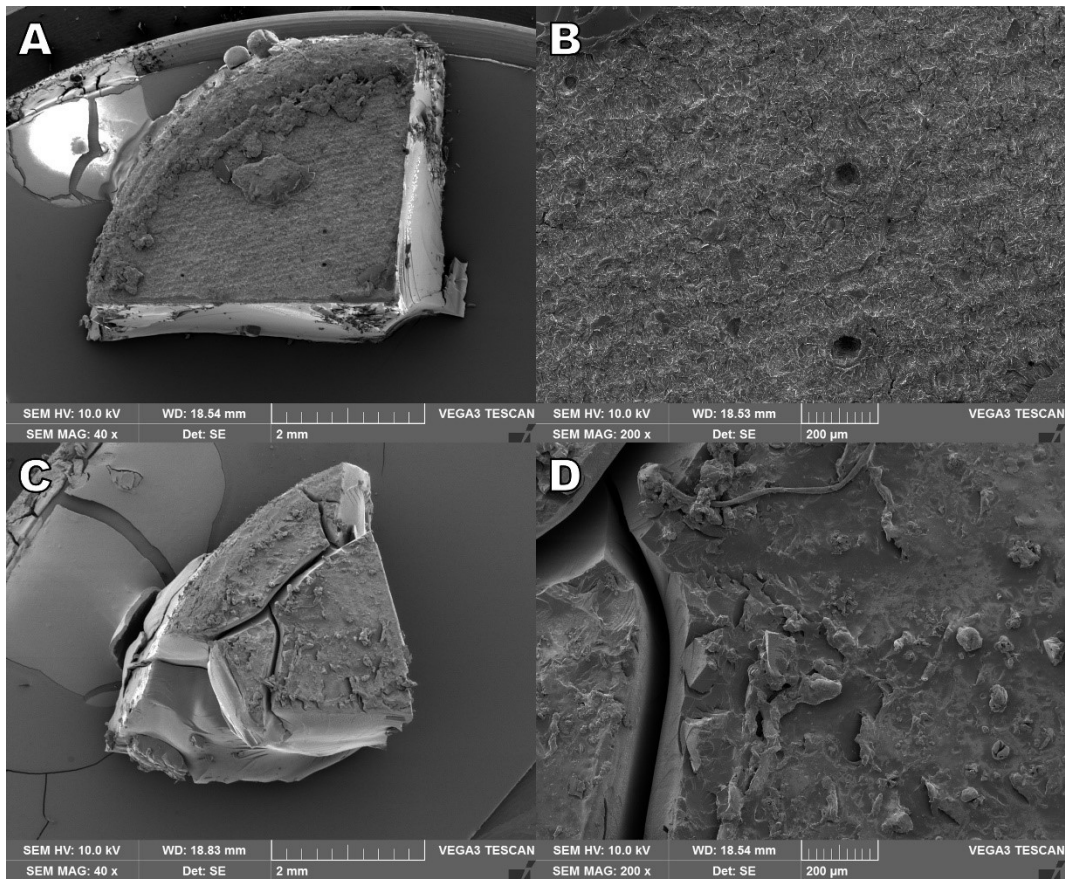


**Figure 4.71.** SEM images of top view of a dosage form 3D printed from WF31 before (A-B) and after (C-D) dissolution testing.

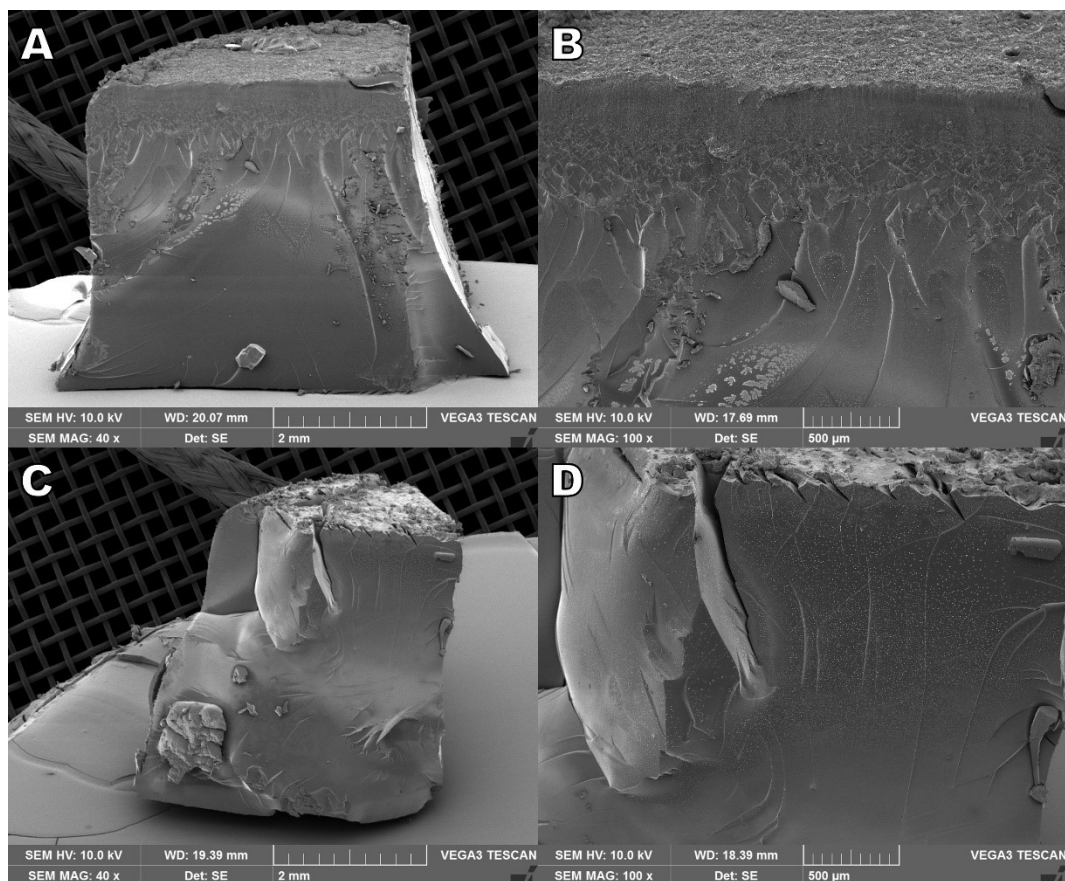


**Figure 4.72.** SEM images of cross-sectional view of a dosage form 3D printed from WF31 before (A-B) and after (C-D) dissolution testing.

In comparison with WF31, SEM images of 3D printed formulation WF34, containing milled sodium chloride, showed a highly fractured surface and the internal presence of minor fractures and pores after dissolution (figures 4.73-4.74).

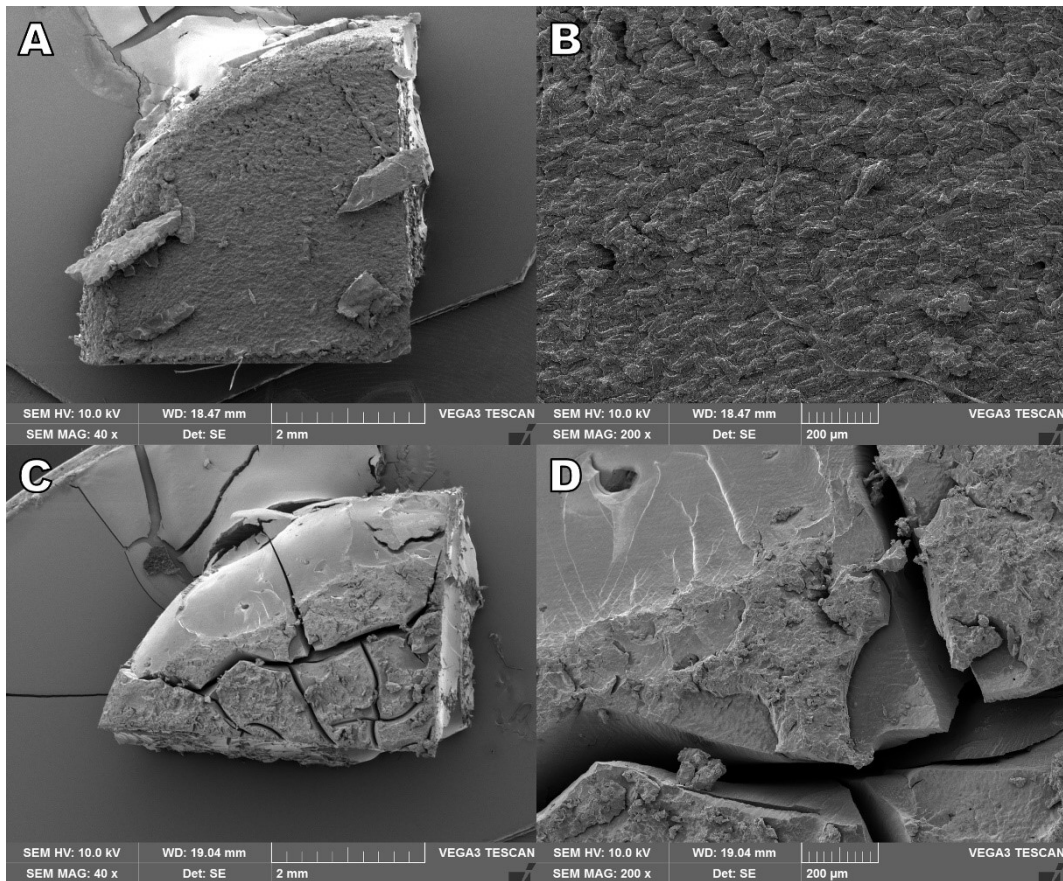


**Figure 4.73.** SEM images of top view of a dosage form 3D printed from WF34 before (A-B) and after (C-D) dissolution testing.

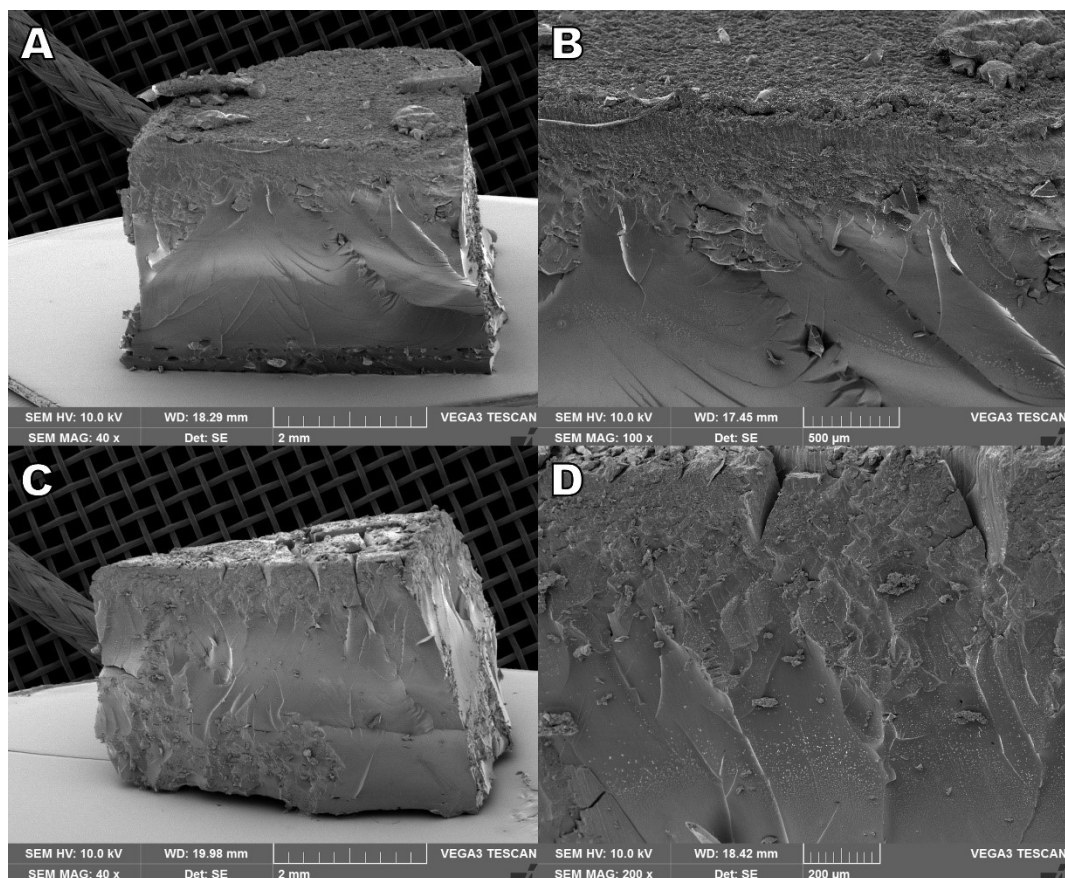


**Figure 4.74.** SEM images of cross-sectional view of a dosage form 3D printed from WF34 before (A-B) and after (C-D) dissolution testing.

#### *4.4.20 Raman spectroscopy imaging*

Raman spectroscopy was used to map the surface and the core of SLA 3D printed dosage forms before and after dissolution testing to investigate the mechanism of drug release. In fact, the limited drug release previously described would suggest that, due to the highly crosslinked nature of SLA 3D printed dosage forms and their inability to disintegrate, the API near the tablet surface would easily diffuse out, while the drug at the core of the tablet could remain trapped.

Prior to map the drug loaded dosage forms, reference spectra for warfarin sodium and a drug free PEGDA 700 3D printed tablet were collected (figure 4.75).

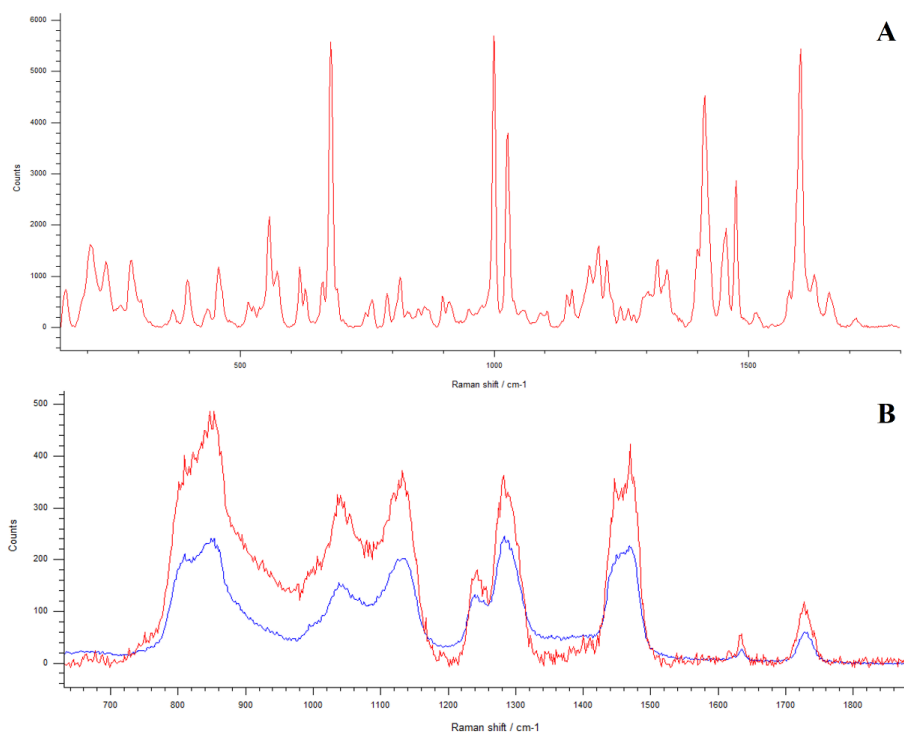


**Figure 4.75.** Raman spectra of (A) pure warfarin sodium and (B) drug free PEGDA 700 SLA 3D printed tablet (red) compared to PEGDA spectrum from Renishaw database (blue).

Raman maps of surface and core of an SLA 3D printed dosage unit produced using formulation WF6 were collected before dissolution testing, revealing the presence of the API in both areas investigated (figures 4.76-4.77).

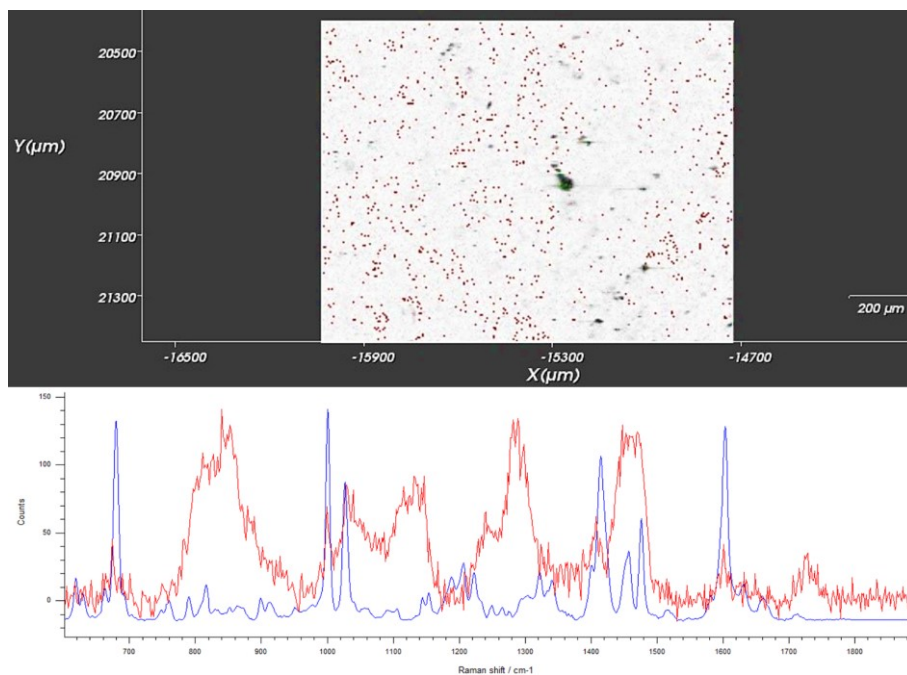


**Figure 4.76.** Raman map (**top**) and spectra (**bottom**) collected from the surface of a warfarin sodium loaded SLA 3D printed tablet before dissolution testing. Warfarin sodium and PEGDA 700 spectra are coloured in blue and red, respectively.

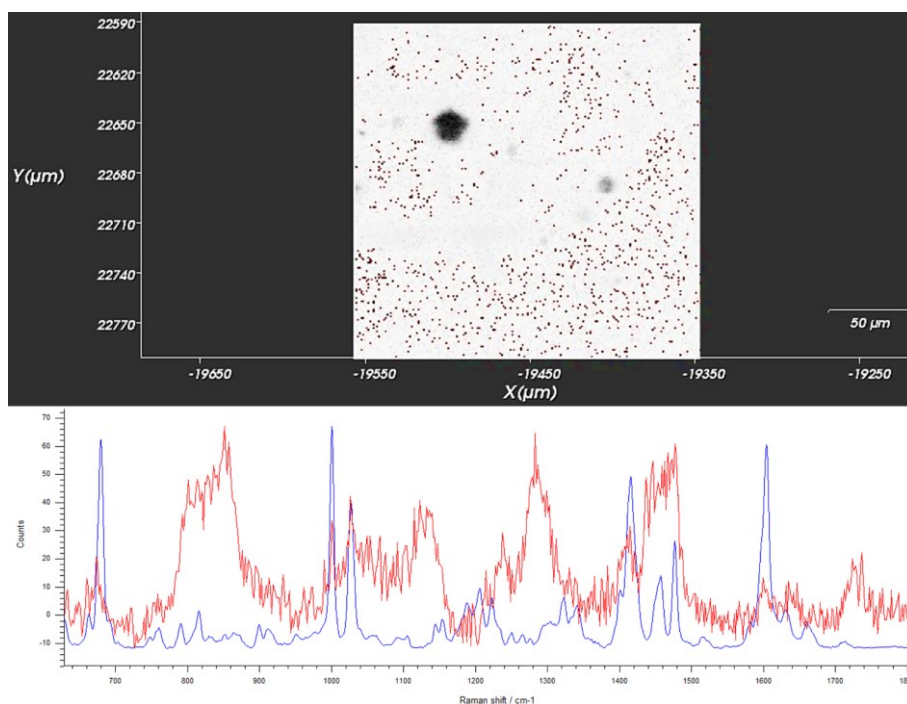


**Figure 4.77.** Raman map (**top**) and spectra (**bottom**) collected from the core of a warfarin sodium loaded SLA 3D printed tablet before dissolution testing. Warfarin sodium and PEGDA 700 spectra are coloured in blue and red, respectively.

As shown in figure 4.78, repeating Raman mapping of the tablet surface after dissolution testing in water for 24 hours revealed no API at the surface of the dosage form, thus indicating that warfarin sodium present on the surface had completely diffused out in the dissolution medium. NNLS component analysis allowed to quantify a concentration estimate of the drug at the surface as 0.06%.

On the contrary, mapping tablet core allowed to visualise a certain amount of warfarin sodium (figure 4.79), thus confirming the hypothesis of a limited drug release due to entrapment of the API at the core of the photocrosslinked tablet matrix. A concentration estimate of such drug amount was quantified through NNLS component analysis as 0.69%.

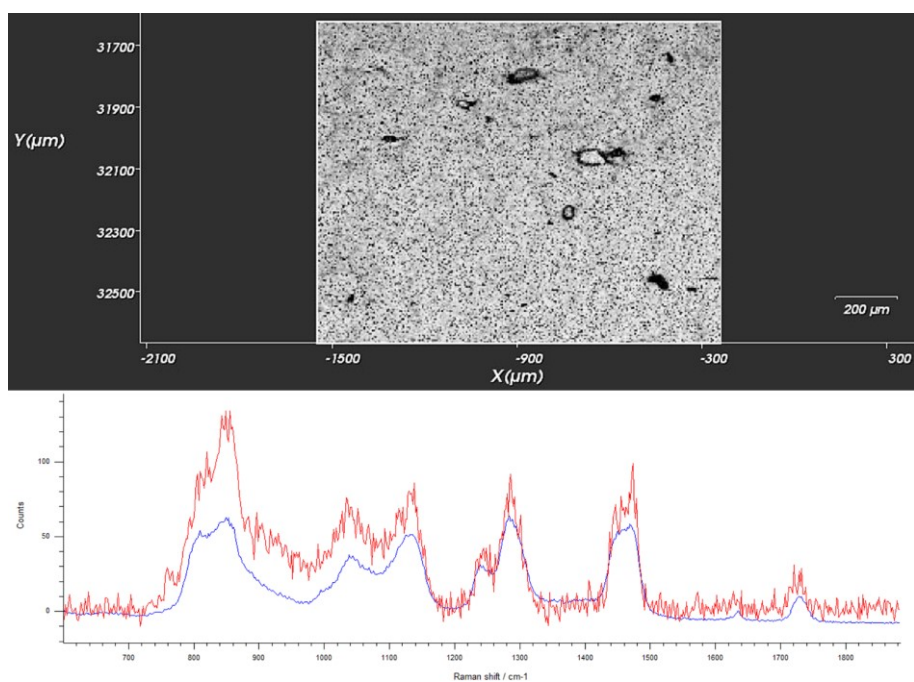


**Figure 4.78.** Raman map (**top**) and spectra (**bottom**) collected from the surface of a warfarin sodium loaded SLA 3D printed tablet after dissolution testing. PEGDA 700 spectrum (red) was compared to PEGDA reference spectrum from Renishaw database (blue).

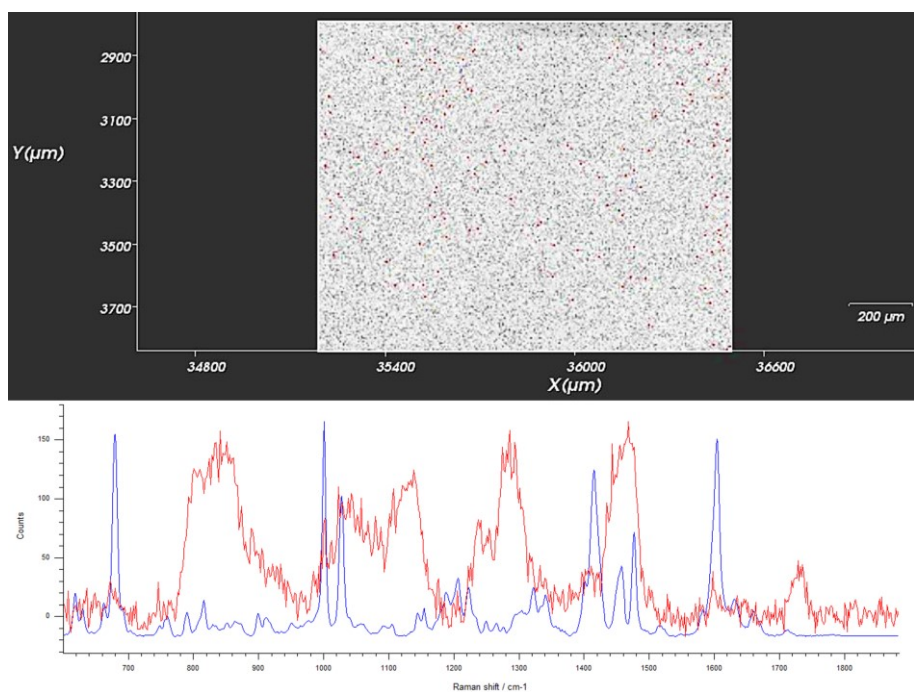


**Figure 4.79.** Raman map (**top**) and spectra (**bottom**) collected from the core of a warfarin sodium loaded SLA 3D printed tablet before dissolution testing. Warfarin sodium and PEGDA 700 spectra are coloured in blue and red, respectively.

## 4.5 Conclusion

In summary, this Chapter reports the design of 43 drug loaded photopolymer formulations for SLA 3DP including theophylline, warfarin, or warfarin sodium as APIs. Of these, 34 were successfully 3D printed into solid oral dosage forms, demonstrating the suitability of low concentrations of PI to produce drug loaded tablets with sufficient crosslinking.

Theophylline formulations with clinically relevant dosages were not printable, while warfarin did not show such limitation. In particular, warfarin sodium provided better printability outcomes due to its higher solubility in the photopolymer resin.

The investigation of dosage forms hardness and friability provided understanding of the mechanical properties of such 3D printed devices, which met the Pharmacopoeia requirements for conventional solid oral dosage forms.

Drug release from the SLA 3D printed tablets in biorelevant media was found to be incomplete after 8 hours, highlighting the need for future development and optimisation. Among the various agents investigated for their drug release-tuning properties, solid fillers such as sodium chloride and potassium bicarbonate were successfully included in different concentrations and 3D printed in the dosage forms and were found to modulate drug release by dissolution and effervescence mechanisms, respectively.

FTIR analysis allowed to identify the potential presence of uncured resin in the SLA 3D printed tablets, which will require future work to investigate any toxicity implications. Moreover, preliminary data evidenced potential issues related to leaching of liquid fillers, which demand further attention.

XRPD showed that drug amorphisation occurs in the SLA 3D printed tablet, which can therefore be considered as delivery devices of low-solubility drugs.

Finally, Raman spectroscopy allowed to observe residual drug at the core of the 3D printed tablets after dissolution testing, suggesting that the API remains entrapped within the photocrosslinked matrix.

## - Chapter V -

### CLOSING COMMENTARY AND FUTURE WORK

---

The research project described in this Thesis aimed to investigate the potential of Stereolithography (SLA) 3D printing to manufacture quality solid oral dosage forms, with the view to inform about the opportunities and challenges of such technology to deliver personalised medicines in a clinical setting.

The work conducted in this research can be categorized in four main areas, namely:

1. Review of the scientific literature describing 3D printing of solid oral dosage forms, to identify challenges and areas of development of pharmaceutical SLA 3D printing.
2. Optimisation of a commercial SLA 3D printer to enhance throughput and improve formulation development cost-effectiveness.
3. Systematic screening of novel photopolymer resins for SLA 3D printing, to identify lead formulations with optimal printability for drug loading studies.
4. Development and characterisation of stereolithographic 3D printed tablets, loaded with clinically relevant drug dosages.

The literature review highlighted the lack of photopolymers available for pharmaceutical stereolithography (Wang *et al.*, 2016a; Xu *et al.*, 2021) and the need for in-depth physical characterisation of SLA 3D printed tablets (Healy *et al.*, 2019) as core areas to address from a formulation development point of view, while limitations of SLA 3D printers also emerged (Kadry *et al.*, 2019a).

Therefore, prior to conduct a systematic printability screening of photopolymer resins, a novel SLA apparatus was designed to optimise throughput and cost-effectiveness of the process. Such apparatus was developed by reshaping the resin tank and the build platform thus enabling to simultaneously use up to 12 different photopolymer resins. Moreover, the

compartmentalization of the resin tank allowed to drastically reduce the amount of formulation required from 200 mL to 10 mL.

The capability of the novel SLA apparatus was fully exploited by carrying out the systematic printability screening of 156 photopolymer formulations, which was completed in 96.42 hours using 1.56 L of sample worth £292.21. In contrast, the original SLA apparatus would have required 1157 hours to complete the screening and 31.20 L of sample worth £5844.19, undoubtedly resulting less cost-efficient in comparison with its improved version (Curti, Kirby and Russell, 2021).

The printability screening allowed to identify PEGDA 700 as the best performing photopolymer, and propylene glycol as the liquid filler providing best printability outcomes at concentrations of 12.5%, 25%, and 50% w/w. Therefore, these materials were selected as main excipients to assemble drug loaded photopolymer resins in combination with the photoinitiator TPO, which was found most effective when used as 0.05% w/w. Other materials, namely glycerol and N-vinyl pyrrolidone, were found unsuitable for SLA 3D printing and were consequently excluded from further investigation.

Finally, oral anticoagulant drugs warfarin and warfarin sodium were loaded as 0.5%, 2.5%, and 5.0% w/v in liquid photopolymer resins enabling to fabricate SLA 3D printed solid oral dosage forms with a final theoretical dosage of 1, 5, and 10 mg, respectively. A total of 40 formulations containing warfarin or warfarin sodium were prepared, and 36 resulted successfully printable. Alongside PEGDA 700 and propylene glycol, other materials were also used; these included the reactive monomer triglycerol diacrylate (TGDA), the liquid fillers polyethylene glycol 300 (PEG 300) and polyethylene glycol dimethyl ether (PEGDME), and the solid fillers sodium chloride (NaCl) and potassium bicarbonate (KHCO<sub>3</sub>). Specifically, liquid and solid fillers were included in an attempt to modulate drug release from the 3D printed dosage forms, which was found to increase more when NaCl and KHCO<sub>3</sub> were used. This is particularly promising, as NaCl and KHCO<sub>3</sub> are GRAS listed excipients (Hussien *et al.*, 2018) conventionally used in solid oral dosage

forms, and this research demonstrated their successful inclusion in photopolymer resins in concentrations up to 4% w/w.

Nevertheless, drug release in biorelevant media over 8 hours was limited, indicating that further optimisation is needed. Moreover, while warfarin and warfarin sodium loading were adequate to 3D print tablets with clinically relevant dosages, limitations appeared when theophylline was instead used, resulting unprintable when loaded as 5.0% and 50% w/v. Furthermore, the detection of leachates from 3D printed tablets aroused toxicity concerns that need to be thoroughly addressed before SLA 3D printing of pharmaceuticals can be safely implemented in clinical settings.

The following sections will provide an overview of the areas of development identified from this research project that may deserve to be investigated in the future, as well as a general comment on the regulatory challenges of 3D printed drug products.

### **Cytocompatibility assessment of SLA 3D printed dosage forms**

Despite the demonstrated advantages of SLA 3DP in the pharmaceutical field, the safety profile of solid oral dosage forms produced with such technique remains unaddressed (Xu *et al.*, 2021). Indeed, unreacted mono/oligomers residues still present after the 3DP process represent a concern because of the cytotoxicity induced from their reaction towards amino and/or thiol groups of proteins and DNA (Oesterreicher *et al.*, 2016). Furthermore, the free-radical polymerisation process requires photoinitiator molecules to generate radical species, whose safety also needs to be investigated.

In this research, it was found that liquid fillers used in SLA 3D printed dosage forms tended to leach out over time, acting as carriers for drug molecules; therefore, it can be hypothesised that liquid unreacted mono/oligomers may leach out in a similar way, triggering cytotoxicity reactions. It is obvious that any toxicity-related issues must be addressed to allow SLA 3DP to be implemented in clinical practice. This must include a

thorough study of the effect on the GI tissues of fragments originating from the 3D printed tablets.

Based on the work started in this project, the application of analytical techniques, such as HPLC, to accurately quantify unreacted mono/oligomers in SLA 3D printed tablets and leachates, can provide preliminary indications the toxicity induced by such chemicals (Bural *et al.*, 2011; Moldovan *et al.*, 2019).

It is also imperative to assess the cytocompatibility of SLA 3D printed dosage forms via cell-culture studies, which would represent the natural continuation of this research project. A number of methods have been already applied for cytotoxicity testing of SLA 3D printed samples, including direct contact techniques (ISO 10993-5) (Warr *et al.*, 2020) and cell viability and proliferation assays (Glass *et al.*, 2018; Tang *et al.*, 2019; González *et al.*, 2020).

### **Raman spectroscopy analysis to determinate the degree of conversion**

Raman spectroscopy is a powerful tool in pharmaceutical analysis (Verde *et al.*, 2021), and its use in determining the degree of C=C double-bond conversion in SLA 3D printed structures has been investigated (Shin *et al.*, 1993; Gauthier *et al.*, 2005). More recently, Raman spectroscopy has been used to determinate the degree of conversion (DC) in 3D printed tablets (Clark *et al.*, 2017b), and it has been proposed as a frontrunner analytical technology to couple with vat photopolymerisation 3DP to assess safety and quality of 3D printed dosage forms (Xu *et al.*, 2021). Indeed, the low DC (60%-90%) typical of acrylate resins (Xu *et al.*, 2021) would cause the presence of unreacted mono/oligomers, whose potential toxicity has been previously discussed. Despite some methods based on washing and post-curing of the 3D printed tablets have been described (Januskaite *et al.*, 2020), reports on the determination of the DC in SLA 3D printed dosage forms are lacking. According to this, Raman spectroscopy could be used to develop and validate reliable methods to quantify the DC in SLA 3D printed tablets, thus enabling the systematic

evaluation of factors such as type and amount of photoinitiator and liquid fillers, or process parameters, on the final presence of unreacted material.

### **Development of machine learning tools to predict printability of medicines**

Artificial intelligence has emerged in the pharmaceutical field thanks to its ability to analyse and constantly examine large datasets, thus reshaping formulation development (Elbadawi *et al.*, 2020). SLA 3D printing can largely benefit from the application of machine learning techniques to develop tools able to predict printability outcomes of novel photopolymer formulations and various drug molecules. This is of particular importance since the lack of materials available for pharmaceutical SLA 3DP (Curti, Kirby and Russell, 2021), making necessary to screen large formulation sets.

### **Software development for multi-material pharmaceutical SLA 3D printing**

The novel, multi-material SLA apparatus described in this Thesis is controlled by the proprietary software PreForm, which doesn't allow to adapt process parameters to the different photopolymer formulations used at the same time. Hence, a significant improvement would consist in the development of a novel software allowing the operator to tune process parameters to the characteristics of each single photopolymer resin contained in the different tanks. This could allow to optimise printability while offering an unrivalled manufacturing flexibility.

### **The regulatory framework**

Currently, no regulatory pathway for personalised 3D printed medicines is established (Curti, Kirby and Russell, 2020). Although Aprelia Pharmaceuticals introduced 3DP as a novel manufacturing process, their 3D printed medicine Spritam® is not considered a personalised product but rather it is mass manufactured similarly to conventional tablets.

Therefore, even though 3DP can meet the requirements for pharmaceuticals manufacture, it seems that approval can only be granted when the process is intended for mass production. However, current research on 3DP in pharmaceuticals is mainly focused on personalised medicine, targeting the fabrication of dosage forms with properties varying from batch to batch. This is inherently in conflict with the requirements of pharmaceutical production processes, for which the inter-batch variability must be guaranteed to a minimum. Given such limitations caused by legislation, it will likely take time for 3DP processes to be awarded widespread regulatory approval, as changes in regulation will likely be implemented incrementally. For the present, it is likely that the manufacture of 3D printed medicines will be limited to fixed dose units as has proven successful in the case of Spritam® (Brandessence Market Research Company, 2019) and, more recently, of T19 (Everett, 2021).

A further observation regarding the on-demand manufacturing of a wide range of medicines, for example in hospital pharmacies, highlights the need of appropriate and accurate analytical procedures to ensure final product quality. Within this context, process analytical technologies such as near-infrared spectroscopy have demonstrated their potential as valid techniques for the intended purpose (Trenfield *et al.*, 2018a), as they can be easily implemented in GMP pharmaceutical 3D printers (Algorri *et al.*, 2021).

In conclusion, although it is necessary for the scientific community to build a solid knowledge background to understand and improve the whole manufacturing process from dosage form design to the relative quality control, it is also essential that regulatory agencies issue guidelines that can promote development and safe application of 3D printing technology in clinical scenarios.

## - List of References -

---

- Acosta-Vélez, G. F. et al. (2018) 'Photocurable poly(ethylene glycol) as a bioink for the inkjet 3D pharming of hydrophobic drugs', *International Journal of Pharmaceutics*, 546(1–2), pp. 145–153.
- Ahmat, N., Ugail, H. and Castro, G. G. (2011) 'Method of modelling the compaction behaviour of cylindrical pharmaceutical tablets', *International Journal of Pharmaceutics*, 405(1–2), pp. 113–121.
- Ahrendt, C. et al. (2020) 'Microplastic ingestion cause intestinal lesions in the intertidal fish *Girella laevis*', *Marine Pollution Bulletin*, 151, p. 110795.
- El Aita, I. et al. (2020) '3D-Printing with precise layer-wise dose adjustments for paediatric use via pressure-assisted microsyringe printing', *European Journal of Pharmaceutics and Biopharmaceutics*, 157, pp. 59–65.
- El Aita, I., Breitzkreutz, J. and Quodbach, J. (2019) 'On-demand manufacturing of immediate release levetiracetam tablets using pressure-assisted microsyringe printing', *European Journal of Pharmaceutics and Biopharmaceutics*, 134, pp. 29–36.
- El Aita, I., Breitzkreutz, J. and Quodbach, J. (2020) 'Investigation of semi-solid formulations for 3D printing of drugs after prolonged storage to mimic real-life applications', *European Journal of Pharmaceutical Sciences*, 146, p. 105266.
- Alemán, J. et al. (2007) 'Definitions of terms relating to the structure and processing of sols, gels, networks, and inorganic-organic hybrid materials (IUPAC recommendations 2007)', *Pure and Applied Chemistry*, 79(10), pp. 1801–1829.
- AlfaAesar (2015) 'Acetophenone SDS', pp. 1–4.
- Algorri, M. et al. (2021) 'Re-Envisioning Pharmaceutical Manufacturing: Increasing Agility for Global Patient Access', *Journal of Pharmaceutical Sciences*
- Alhnan, M. A. et al. (2016) 'Emergence of 3D Printed Dosage Forms: Opportunities and Challenges', *Pharmaceutical Research*, 33(8), pp. 1817–1832.
- Allahham, N. et al. (2020) 'Selective laser sintering 3D printing of orally disintegrating printlets containing ondansetron', *Pharmaceutics*, 12(2), pp. 1–13.
- Alqahtani, M. S., Kazi, M., Alsenaidy, M. A., & Ahmad, M. Z. (2021). Advances in oral drug delivery. *Frontiers in Pharmacology*, 62.
- Alshammari, J. et al. (2021) 'Survival of *Salmonella* and *Enterococcus faecium* in high fructose corn syrup and honey at room temperature (22 °C)', *Food Control*, 123, p. 107765.
- Amalanathan, M., Joe, I. H. and Kostova, I. (2010) 'Density functional theory calculation and vibrational spectral analysis of 4-hydroxy-3-(3-oxo-1-phenylbutyl)-2H-1-benzopyran-2-one', *Journal of Raman Spectroscopy*, 41(9), pp. 1076–1084.
- Amorosa, M. (1986) *Principi di tecnica farmaceutica*. Libreria Universitaria L. Tinarelli, Bologna, Italy.
- Antic, A. et al. (2021) 'Screening pharmaceutical excipient powders for use in commercial 3D binder jetting printers', *Advanced Powder Technology*, 32(7), pp. 2469–2483.
- Arafat, B., Wojsz, M., et al. (2018) 'Tablet fragmentation without a disintegrant: A novel design approach for accelerating disintegration and drug release from 3D printed cellulosic tablets', *European Journal of Pharmaceutical Sciences*, 118, pp. 191–199.

- Arafat, B., Qinna, N., et al. (2018) 'Tailored on demand anti-coagulant dosing: An in vitro and in vivo evaluation of 3D printed purpose-designed oral dosage forms', *European Journal of Pharmaceutics and Biopharmaceutics*, 128, pp. 282–289.
- Arhan, P., Devroede, G., Jehannin, B., Lanza, M., Faverdin, C., Dornic, C., ... & Pellerin, D. (1981). Segmental colonic transit time. *Diseases of the Colon & Rectum*, 24(8), 625-629.
- Augsburger, L. and Hoag, S. (2008) *Pharmaceutical Dosage Forms - Tablets*. Rational Design and Formulation. CRC Press, Boca Raton, FL, USA.
- Aulton, M. E. and Taylor, K. M. G. (2017) *Pharmaceutics: the Design and Manufacture of Medicines*. Elsevier, Amsterdam, Netherlands.
- Awad, A., Trenfield, Sarah J., et al. (2018) '3D printed medicines: A new branch of digital healthcare', *International Journal of Pharmaceutics*, 548(1), pp. 586–596.
- Awad, A., Trenfield, Sarah J, et al. (2018) 'Reshaping drug development using 3D printing', *Drug Discovery Today*, 23(8), pp. 1547–1555.
- Awad, A. et al. (2019) '3D printed pellets (Miniprintlets): A novel, multi-drug, controlled release platform technology', *Pharmaceutics*, 11(4), p. 148.
- Awad, A. et al. (2020) '3D printed tablets (Printlets) with braille and moon patterns for visually impaired patients', *Pharmaceutics*, 12(2), pp. 1–14.
- Ayyoubi, S., Cerda, J. R., Fernández-García, R., Knief, P., Lalatsa, A., Healy, A. M., et al. (2021) '3D printed spherical mini-tablets: Geometry versus composition effects in controlling dissolution from personalised solid dosage forms', *International Journal of Pharmaceutics*, 597, p. 120336.
- Babhair, S. A., Tariq, M. and Al-Badr, A. A. (1985) 'Warfarin', *Analytical Profiles of Drug Substances and Excipients*, 14(C), pp. 423–452.
- Bagheri, A. and Jin, J. (2019) 'Photopolymerization in 3D Printing', *ACS Applied Polymer Materials*, 1(4), pp. 593–611.
- Basit, A. W. and Gaisford, S. (2018) *3D Printing of Pharmaceuticals*, Volume 31. Springer International Publishing AG, Gewerbestrasse, Switzerland.
- Basulto, D. (2015) 'Why it matters that the FDA just approved the first 3D-printed drug - The Washington Post', *The Washington Post*. Available at: [https://www.washingtonpost.com/news/innovations/wp/2015/08/11/why-it-matters-that-the-fda-just-approved-the-first-3d-printed-drug/?utm\\_term=.a94e48e32de1](https://www.washingtonpost.com/news/innovations/wp/2015/08/11/why-it-matters-that-the-fda-just-approved-the-first-3d-printed-drug/?utm_term=.a94e48e32de1).
- Berg, S. et al. (2021) 'In Vitro and In Vivo Evaluation of 3D Printed Capsules with Pressure Triggered Release Mechanism for Oral Peptide Delivery', *Journal of Pharmaceutical Sciences*, 110(1), pp. 228–238.
- Bertolotti, S. G. et al. (1999) 'Riboflavin/triethanolamine as photoinitiator system of vinyl polymerization. A mechanistic study by laser flash photolysis', *Macromolecules*, 32(9), pp. 2920–2924.
- Bilbault, T. et al. (2016) 'Buccal mucosal irritation studies of sublingual apomorphine film (APL-130277) in Syrian golden hamsters', *Therapeutic Delivery*, 7(9), pp. 611–618.
- Boudriau, S. et al. (2016) 'Randomized Comparative Bioavailability of a Novel Three-Dimensional Printed Fast-Melt Formulation of Levetiracetam Following the Administration of a Single 1000-mg Dose to Healthy Human Volunteers Under Fasting and Fed Conditions', *Drugs in R&D*, 16(2), pp. 229–238.
- Brandessence Market Research Company (2019) *3D Printed Drugs Market 2019 Top Key Players are 3D Printing Systems, Aprelia Pharmaceuticals, Hewlett Packard Enterprise*,

Hewlett Packard Enterprise, GLAXOSMITHKLINE PLC and Forecast to 2025. Medgadget, Inc. Available at: <https://www.medgadget.com/2019/09/3d-printed-drugs-market-2019-top-key-players-are-3d-printing-systems-aprecia-pharmaceuticals-hewlett-packard-enterprise-hewlett-packard-enterprise-glaxosmithkline-plc-and-forecast-to-2025.html>.

British Pharmacopoeia, Appendix XVII G; Friability of Uncoated Tablets; Ph. Eur. method (2.9.7) (2011).

Brocchi, E., Corazza, G. R., Caletti, G., Treggiari, E. A., Barbara, L., & Gasbarrini, G. (1988). Endoscopic demonstration of loss of duodenal folds in the diagnosis of celiac disease. *New England Journal of Medicine*, 319(12), 741-744.

Bural, C. et al. (2011) 'Effect of post-polymerization heat-treatments on degree of conversion, leaching residual MMA and in vitro cytotoxicity of autopolymerizing acrylic repair resin', *Dental Materials*, 27(11), pp. 1135–1143.

Buyukgoz, G. G., Kossor, C. G. and Davé, R. N. (2021) 'Enhanced supersaturation via fusion-assisted amorphization during fdm 3d printing of crystalline poorly soluble drug loaded filaments', *Pharmaceutics*, 13(11), pp. 28–33.

Carstensen, J. T. (1988) 'Effect of Moisture on the Stability of Solid Dosage Forms', *Drug Development and Industrial Pharmacy*, 14(14), pp. 1927–1969.

Chai, X. et al. (2017) 'Fused deposition modeling (FDM) 3D printed tablets for intragastric floating delivery of domperidone', *Scientific Reports*, 7(1), pp. 1–9.

Channer, K. S., & Virjee, J. P. (1985). The effect of formulation on oesophageal transit. *Journal of pharmacy and pharmacology*, 37(2), 126-129.

Chen, D. et al. (2020) 'Preparation and In vitro Evaluation of FDM 3D-Printed Ellipsoid-Shaped Gastric Floating Tablets with Low Infill Percentages', *AAPS PharmSciTech*, 21(1), pp. 1–13.

Chen, H., Aburub, A. and Sun, C. C. (2019) 'Direct Compression Tablet Containing 99% Active Ingredient—A Tale of Spherical Crystallization', *Journal of Pharmaceutical Sciences*, 108(4), pp. 1396–1400.

Cheng, Y. et al. (2020) '3D printing of extended-release tablets of theophylline using hydroxypropyl methylcellulose (HPMC) hydrogels', *International Journal of Pharmaceutics*, 591, p. 119983.

Clark, E. A. et al. (2017) '3D printing of tablets using inkjet with UV photoinitiation', *International Journal of Pharmaceutics*, 529(1–2), pp. 523–530.

Colombo, P. et al. (2000) 'Swellable matrices for controlled drug delivery: Gel-layer behaviour, mechanisms and optimal performance', *Pharmaceutical Science and Technology Today*, 3(6), pp. 198–204.

Conceição, J. et al. (2019) 'Hydroxypropyl- $\beta$ -cyclodextrin-based fast dissolving carbamazepine printlets prepared by semisolid extrusion 3D printing', *Carbohydrate Polymers*, 221, pp. 55–62.

Conesa, A., Shen, S. and Coronas, A. (1998) 'Liquid Densities, Kinematic Viscosities, and Heat Capacities of Some Ethylene Glycol Dimethyl Ethers at Temperatures from 283.15 to 423.15 K', *International Journal of Thermophysics*, 19(5), pp. 1343-1358.

Conte, U. et al. (1993) 'Multi-layered hydrophilic matrices as constant release devices (Geomatrix™ Systems)', *Journal of Controlled Release*, 26(1), pp. 39–47.

Croitoru-Sadger, T. et al. (2019) 'Two-component cross-linkable gels for fabrication of solid oral dosage forms', *Journal of Controlled Release*, 303, pp. 274–280.

- Crump, S. S. (1992) 'Apparatus and method for creating three-dimensional objects', United States Patent, (19), p. US 005121329A.
- Cui, M., Yang, Y., et al. (2019) 'Effect of novel internal structures on printability and drug release behavior of 3D printed tablets', *Journal of Drug Delivery Science and Technology*, 49, pp. 14–23.
- Cui, M., Li, Y., et al. (2019) 'Exploration and Preparation of a Dose-Flexible Regulation System for Levetiracetam Tablets via Novel Semi-Solid Extrusion Three-Dimensional Printing', *Journal of Pharmaceutical Sciences*, 108(2), pp. 977–986.
- Cui, M. et al. (2020) 'Fabrication of high drug loading levetiracetam tablets using semi-solid extrusion 3D printing', *Journal of Drug Delivery Science and Technology*, 57, p. 101683.
- Cui, M. et al. (2021) 'Exploration and evaluation of dynamic dose-control platform for pediatric medicine based on Drop-on-Powder 3D printing technology', *International Journal of Pharmaceutics*, 596, p. 120201.
- Curti, C., Kirby, D. J. and Russell, C. A. (2020) 'Current formulation approaches in design and development of solid oral dosage forms through three-dimensional printing', *Progress in Additive Manufacturing*, 5(2), pp. 111–123.
- Curti, C., Kirby, D. J. and Russell, C. A. (2021) 'Stereolithography apparatus evolution: Enhancing throughput and efficiency of pharmaceutical formulation development', *Pharmaceutics*, 13(5), p. 616.
- Dumpa, N. et al. (2021) '3D printing in personalized drug delivery : An overview of hot-melt extrusion-based fused deposition modeling', *International Journal of Pharmaceutics*, 600, p. 120501.
- Eibel, A., Fast, D. E. and Gescheidt, G. (2018) 'Choosing the ideal photoinitiator for free radical photopolymerizations: Predictions based on simulations using established data', *Polymer Chemistry. Royal Society of Chemistry*, 9(41), pp. 5107–5115.
- Elbadawi, M. et al. (2020) 'M3DISEEN: A novel machine learning approach for predicting the 3D printability of medicines', *International Journal of Pharmaceutics*, 590, p. 119837.
- Epstein, R. S. et al. (2010) 'Warfarin Genotyping Reduces Hospitalization Rates. Results From the MM-WES (Medco-Mayo Warfarin Effectiveness Study)', *Journal of the American College of Cardiology. Elsevier Inc.*, 55(25), pp. 2804–2812.
- Everett, H. (2021) Triastek receives FDA IND clearance for 3D printed drug to treat rheumatoid arthritis - 3D Printing Industry. Available at: <https://3dprintingindustry.com/news/triastek-receives-fda-ind-clearance-for-3d-printed-drug-to-treat-rheumatoid-arthritis-184159/> (Accessed: 15 February 2021).
- Feng, X. et al. (2017) 'Lignin-coated cellulose nanocrystal filled methacrylate composites prepared via 3D stereolithography printing: Mechanical reinforcement and thermal stabilization', *Carbohydrate Polymers. Elsevier Ltd*, 169, pp. 272–281.
- Fina, F. et al. (2017) 'Selective laser sintering (SLS) 3D printing of medicines', *International Journal of Pharmaceutics. Elsevier B.V.*, 529(1–2), pp. 285–293.
- Fina, F., Goyanes, A., et al. (2018) '3D printing of drug-loaded gyroid lattices using selective laser sintering', *International Journal of Pharmaceutics*, 547(1–2), pp. 44–52.
- Fina, F., Madla, C. M., et al. (2018) 'Fabricating 3D printed orally disintegrating printlets using selective laser sintering', *International Journal of Pharmaceutics. Elsevier*, 541(1–2), pp. 101–107.
- Fina, F. et al. (2020) '3D printing of tunable zero-order release printlets', *Polymers*, 12(8), pp. 17-69.

- Fitzgerald S (2015) 'FDA Approves First 3D-Printed Epilepsy Drug', *Neurology Today*, 15(18), pp. 26-27.
- FormLabs (2021) What Does Resolution Mean in 3D Printing? Available at: <https://formlabs.com/blog/3d-printer-resolution-meaning/> (Accessed: 5 October 2021).
- Formlabs Inc. (2016) 'Clear Photoreactive Resin for Form 1, Form 1+, Form 2 SAFETY DATA SHEET', [Www.Formlabs.Com](http://www.formlabs.com), pp. 1–8. Available at: [https://formlabs.com/media/upload/Clear-SDS\\_u324bsC.pdf](https://formlabs.com/media/upload/Clear-SDS_u324bsC.pdf).
- Fouassier, J. P., Allonas, X. and Burget, D. (2003) 'Photopolymerization reactions under visible lights: Principle, mechanisms and examples of applications', *Progress in Organic Coatings*, 47(1), pp. 16–36.
- Fuenmayor, E. et al. (2019) 'Comparison of fused- filament fabrication to direct compression and injection molding in the manufacture of oral tablets', *International Journal of Pharmaceutics*. Elsevier, 558(January), pp. 328–340.
- Galvão, M. R. et al. (2013) 'Evaluation of degree of conversion and hardness of dental composites photoactivated with different light guide tips', *European Journal of Dentistry*, 7(1), pp. 86–93.
- Gao, D. and Maurin, M. B. (2001) 'Physical chemical stability of warfarin sodium', *AAPS Journal*, 3(1).
- Gardan, J. (2016) 'Additive manufacturing technologies: State of the art and trends', *International Journal of Production Research*. Taylor & Francis, 54(10), pp. 3118–3132.
- Gauthier, M. A. et al. (2005) 'A new method for quantifying the intensity of the C=C band of dimethacrylate dental monomers in their FTIR and Raman spectra', *Biomaterials*, 26(33), pp. 6440–6448.
- Glass, S. et al. (2018) 'TiO<sub>2</sub> as photosensitizer and photoinitiator for synthesis of photoactive TiO<sub>2</sub>-PEGDA hydrogel without organic photoinitiator', *Frontiers in Chemistry*, 6, pp. 1–9.
- Goh, W. J. et al. (2021) '3D printing of four-in-one oral polypill with multiple release profiles for personalized delivery of caffeine and vitamin B analogues', *International Journal of Pharmaceutics*. Elsevier B.V., 598(January), p. 120360.
- Gokhale, A. (2014) 'Achieving Zero-Order Release Kinetics Using Multi-Step Diffusion-Based Drug Delivery', *Pharmaceutical Technology*, 38(5). Available at: <http://www.pharmtech.com/achieving-zero-order-release-kinetics-using-multi-step-diffusion-based-drug-delivery>.
- González, G. et al. (2020) 'Materials testing for the development of biocompatible devices through vat-polymerization 3d printing', *Nanomaterials*, 10(9), pp. 1–13.
- Goole, J. and Amighi, K. (2016) '3D printing in pharmaceutics: A new tool for designing customized drug delivery systems', *International Journal of Pharmaceutics*. Elsevier B.V., 499(1–2), pp. 376–394.
- Goyanes, A. et al. (2014) 'Fused-filament 3D printing (3DP) for fabrication of tablets', *International Journal of Pharmaceutics*, 476(1), pp. 88–92.
- Goyanes, A., Wang, J., et al. (2015) '3D Printing of Medicines: Engineering Novel Oral Devices with Unique Design and Drug Release Characteristics', *Molecular Pharmaceutics*, 12(11), pp. 4077–4084.
- Goyanes, A., Buanz, A. B. M., et al. (2015) '3D printing of modified-release aminosalicylate (4-ASA and 5-ASA) tablets', *European Journal of Pharmaceutics and Biopharmaceutics*. Elsevier, 89, pp. 157–162.

- Goyanes, A., Robles Martinez, P., et al. (2015) 'Effect of geometry on drug release from 3D printed tablets', *International Journal of Pharmaceutics*. Elsevier B.V., 494(2), pp. 657–663.
- Goyanes, A., Chang, H., et al. (2015) 'Fabrication of controlled-release budesonide tablets via desktop (FDM) 3D printing', *International Journal of Pharmaceutics*. Elsevier B.V., 496(2), pp. 414–420.
- Goyanes, A., Fina, F., et al. (2017) 'Development of modified release 3D printed tablets (printlets) with pharmaceutical excipients using additive manufacturing', *International Journal of Pharmaceutics*. Elsevier B.V., 527(1–2), pp. 21–30.
- Goyanes, A., Scarpa, M., et al. (2017) 'Patient acceptability of 3D printed medicines', *International Journal of Pharmaceutics*. Elsevier B.V., 530(1–2), pp. 71–78.
- Goyanes, A. et al. (2019) 'Automated therapy preparation of isoleucine formulations using 3D printing for the treatment of MSUD: First single-centre, prospective, crossover study in patients', *International Journal of Pharmaceutics*. Elsevier, 567(June), p. 118497.
- Graham, E. (2016) 'Improving Outcomes Through Personalised Medicine', NHS England, pp. 6–10. Available at: <https://www.england.nhs.uk/wp-content/uploads/2016/09/improving-outcomes-personalised-medicine.pdf>.
- Gueche, Y. A. et al. (2021) 'Selective Laser Sintering of Solid Oral Dosage Forms with Copovidone and Paracetamol Using a CO2 Laser', *Pharmaceutics*. MDPI AG, 13(2), p. 160.
- Guhmann, M. et al. (2015) 'Design, development and in-vitro evaluation of diclofenac taste-masked orodispersible tablet formulations', *Drug Development and Industrial Pharmacy*, 41(4), pp. 540–551.
- Hajjar, E. R., Cafiero, A. C. and Hanlon, J. T. (2007) 'Polypharmacy in elderly patients', *The American Journal of Geriatric Pharmacotherapy*, 5(4), pp. 345–351.
- Haring, A. P. et al. (2018) 'Programming of Multicomponent Temporal Release Profiles in 3D Printed Polypills via Core–Shell, Multilayer, and Gradient Concentration Profiles', *Advanced Healthcare Materials*.
- de Hazan, Y. and Penner, D. (2017) 'SiC and SiOC ceramic articles produced by stereolithography of acrylate modified polycarbosilane systems', *Journal of the European Ceramic Society*, 37(16), pp. 5205–5212.
- Healy, A. V. et al. (2019) 'Additive manufacturing of personalized pharmaceutical dosage forms via stereolithography', *Pharmaceutics*, 11(12), pp. 13–15.
- Herrada-Manchón, H. et al. (2020) '3D printed gummies: Personalized drug dosage in a safe and appealing way', *International Journal of Pharmaceutics*, 587, p. 119687.
- Herting, M. G., & Kleinebudde, P. (2007). Roll compaction/dry granulation: Effect of raw material particle size on granule and tablet properties. *International journal of pharmaceutics*, 338(1-2), 110-118.
- Van Den Heuvel, K. A., De Wit, M. T. W. and Dickhoff, B. H. J. (2021) 'Evaluation of lactose based 3D powder bed printed pharmaceutical drug product tablets', *Powder Technology*, 390, pp. 97–102.
- Hirani, J. J., Rathod, D. A. and Vadalía, K. R. (2009) 'Orally disintegrating tablets: A review', *Tropical Journal of Pharmaceutical Research*, 8(2), pp. 161–172.
- Hirt, N. and Body-Malapel, M. (2020) 'Immunotoxicity and intestinal effects of nano- and microplastics: a review of the literature', *Particle and Fibre Toxicology*, 17(1), pp. 1–22.

- Holbrook, A. M. et al. (2005) 'Systematic Overview of Warfarin and Its Drug and Food Interactions', *Archives of Internal Medicine*, 165(10), p. 1095.
- Hong, X. et al. (2021) 'Binder Jet 3D Printing of Compound LEV-PN Dispersible Tablets : An Innovative Approach for Fabricating Drug Systems with Multicompartmental Structures', *Pharmaceutics*, 13(11), p. 1780
- Van Hoogevest, P. and Wendel, A. (2014) 'The use of natural and synthetic phospholipids as pharmaceutical excipients', *European Journal of Lipid Science and Technology*, 116(9), pp. 1088–1107.
- Hopkinson, N. and Dickens, P. (2003) 'Analysis of rapid manufacturing — using layer manufacturing processes for production', 217, pp. 31–39.
- Horie, K. et al. (2004) 'Definitions of terms relating to reactions of polymers and to functional polymeric materials: (IUPAC Recommendations 2003)', *Pure and Applied Chemistry*, 76(4), pp. 889–906.
- Hounnou, G. et al. (2002) 'Anatomical study of the length of the human intestine', *Surgical and Radiologic Anatomy*, 24(5), pp. 290–294.
- Hua, S. (2020) 'Advances in Oral Drug Delivery for Regional Targeting in the Gastrointestinal Tract - Influence of Physiological, Pathophysiological and Pharmaceutical Factors', *Frontiers in Pharmacology*, 11(April), pp. 1–22.
- Huang, J. N. et al. (2020) 'Exposure to microplastics impairs digestive performance, stimulates immune response and induces microbiota dysbiosis in the gut of juvenile guppy (*Poecilia reticulata*)', *Science of the Total Environment*. Elsevier B.V., 733, p. 138929.
- Hull, C. W. (1984) 'Apparatus for production of three-dimensional objects by stereolithography'. Available at: <https://patents.google.com/patent/US4575330A/en> (Accessed: 8 October 2018).
- Hussien, A. et al. (2018) 'Evaluation of different salt-amended electrolysed water to control postharvest moulds of citrus', *Tropical Plant Pathology*, 43(1), pp. 10–20.
- Hwang, J. W. et al. (2015) 'Gelation and crosslinking characteristics of photopolymerized poly(ethylene glycol) hydrogels', *Journal of Applied Polymer Science*, 132(22), pp. 1–6.
- ICH (2005) 'ICH harmonised tripartite guideline validation of analytical procedures: text and methodology Q2(R1)', The, 1994(November 1996), p. 17. doi: [http://www.ich.org/fileadmin/Public\\_Web\\_Site/ICH\\_Products/Guidelines/Quality/Q2\\_R1/Step4/Q2\\_R1\\_Guideline.pdf](http://www.ich.org/fileadmin/Public_Web_Site/ICH_Products/Guidelines/Quality/Q2_R1/Step4/Q2_R1_Guideline.pdf).
- ICH Q3C (R6) (2016) 'Guideline for Residual Solvents', International Council on Harmonisation, Step 4(October 20), p. 22. Available at: <http://www.ich.org/products/guidelines/quality/article/quality-guidelines.html>.
- Infanger, S. et al. (2019) 'Powder bed 3D-printing of highly loaded drug delivery devices with hydroxypropyl cellulose as solid binder', *International Journal of Pharmaceutics*. Elsevier, 555, pp. 198–206.
- Invernizzi, M. et al. (2020) 'Near-visible stereolithography of a low shrinkage cationic/free-radical photopolymer blend and its nanocomposite', *Journal of Applied Polymer Science*, 137(5), p. 48333.
- Jacobs, P. F. (1996) *Stereolithography and other RP&M Technologies*. Society of Manufacturing Engineers, USA.
- Jadhav, N. R., Bhosale, S. P., Bhosale, S. S., Mali, S. D., Toraskar, P. B., & Kadam, T. S. (2021). Ionic liquids: Formulation avenues, drug delivery and therapeutic updates. *Journal of Drug Delivery Science and Technology*, 65, 102694.

- Januskaite, P. et al. (2020) 'I Spy with My Little Eye: A Paediatric Visual Preferences Survey of 3D Printed Tablets', *Pharmaceutics*, 12(11), p. 1100.
- Jiang, J., Lou, J. and Hu, G. (2019) 'Effect of support on printed properties in fused deposition modelling processes', *Virtual and Physical Prototyping*, 14(4), pp. 308–315.
- Jivraj, M., Martini, L. G. and Thomson, C. M. (2000) 'An overview of the different excipients useful for the direct compression of tablets', *Pharmaceutical Science and Technology Today*, 3(2), pp. 58–63.
- Joint Formulary Committee (2020) Theophylline. 80th edn, *British National Formulary 80*. September 2020 - March 2021. 80th edn. BMJ Group and Pharmaceutical Press.
- Jones, R. et al. (2011) 'RepRap – the replicating rapid prototyper', *Robotica*. Cambridge University Press, 29(1), pp. 177–191. doi: 10.1017/S026357471000069X.
- Kadry, H. et al. (2019) 'Digital light processing (DLP) 3D-printing technology and photoreactive polymers in fabrication of modified-release tablets', *European Journal of Pharmaceutical Sciences*, 135, pp. 60–67.
- Kamoun, E. A. et al. (2016) 'Carboxylated camphorquinone as visible-light photoinitiator for biomedical application: Synthesis, characterization, and application Carboxylated camphorquinone as visible-light photoinitiator', *Arabian Journal of Chemistry*, 9(5), pp. 745–754.
- Kanakal, M. et al. (2014) 'Buffer-Free High Performance Liquid Chromatography Method for the Determination of Theophylline in Pharmaceutical Dosage Forms', *Tropical Journal of Pharmaceutical Research*, 13(1), p. 149.
- Karakurt, I. et al. (2020) 'Stereolithography (SLA) 3D printing of ascorbic acid loaded hydrogels: A controlled release study', *International Journal of Pharmaceutics*, 584(May), pp. 1–9.
- Karavasili, C. et al. (2020) 'Pediatric-friendly chocolate-based dosage forms for the oral administration of both hydrophilic and lipophilic drugs fabricated with extrusion-based 3D printing', *European Journal of Pharmaceutical Sciences*. Elsevier, 147(March), p. 105291.
- Katsiotis, C. S. et al. (2021) '3D-Printed Mesoporous Carrier System for Delivery of Poorly Soluble Drugs', *Pharmaceutics*, 13(7), p. 1096.
- Katstra, W. . et al. (2000) 'Oral dosage forms fabricated by Three Dimensional Printing™', *Journal of Controlled Release*, 66(1), pp. 1–9.
- Khaled, S. A. et al. (2014) 'Desktop 3D printing of controlled release pharmaceutical bilayer tablets', *International Journal of Pharmaceutics*, 461(1–2), pp. 105–111.
- Khaled, S. A. et al. (2015a) '3D printing of five-in-one dose combination polypill with defined immediate and sustained release profiles', *Journal of Controlled Release*, 217, pp. 308–314.
- Khaled, S. A. et al. (2015b) '3D printing of tablets containing multiple drugs with defined release profiles', *International Journal of Pharmaceutics*, 494(2), pp. 643–650.
- Khaled, S. A., Alexander, M. R., Wildman, R. D., et al. (2018) '3D extrusion printing of high drug loading immediate release paracetamol tablets', *International Journal of Pharmaceutics*, 538(1–2), pp. 223–230.
- Khaled, S. A., Alexander, M. R., Irvine, D. J., et al. (2018) 'Extrusion 3D Printing of Paracetamol Tablets from a Single Formulation with Tunable Release Profiles Through Control of Tablet Geometry', *AAPS PharmSciTech*, 19(8), pp. 3403–3413.

- Khalil, S. K. H. et al. (2012) 'Preparation and evaluation of warfarin- $\beta$ -cyclodextrin loaded chitosan nanoparticles for transdermal delivery', *Carbohydrate Polymers*, 90(3), pp. 1244–1253.
- Khanna, R., Agarwal, S. P. and Ahuja, A. (1996) 'Preparation and evaluation of bioerodible buccal tablets containing clotrimazole', *International Journal of Pharmaceutics*, 138(1), pp. 67–73.
- Kochhar, J. S. et al. (2012) 'Protein encapsulation in polymeric microneedles by photolithography', *International Journal of Nanomedicine*, 7, pp. 3143–3154.
- Kozakiewicz, M. et al. (2021) 'Binder jetting 3D printing of challenging medicines: from low dose tablets to hydrophobic molecules', *European Journal of Pharmaceutics and Biopharmaceutics*.
- Krause, W. J. (2000) 'Brunner's glands: A structural, histochemical and pathological profile', *Progress in Histochemistry and Cytochemistry*, 35(4), pp. 255–367.
- Krkobabić, M. et al. (2019) 'Hydrophilic excipients in digital light processing (DLP) printing of sustained release tablets: Impact on internal structure and drug dissolution rate', *International Journal of Pharmaceutics*, p. 118790.
- Kulinowski, P. et al. (2021) 'Selective laser sintering (SLS) technique for pharmaceutical applications—Development of high dose controlled release printlets', *Additive Manufacturing*, 38, p. 101761
- Kumar, R. and Philip, A. (2007) 'Gastroretentive dosage forms for prolonging gastric residence time', *International Journal of Pharmaceutical Medicine*, 21(2), pp. 157–171.
- Lajoinie, A. et al. (2017) 'Assessing the effects of solid versus liquid dosage forms of oral medications on adherence and acceptability in children', *Cochrane Database of Systematic Reviews*, 2017(9).
- Lee, P. I. and Peppas, N. A. (1987) 'Prediction of polymer dissolution in swellable controlled-release systems', *Solutions*, 6, pp. 207–215.
- Leong, K. F. et al. (2007) 'Characterization of a Poly- $\epsilon$ -Caprolactone Polymeric Drug Delivery Device Built by Selective Laser Sintering', *Bio-Medical Materials and Engineering*, 17(3), pp. 147–157.
- Li, Q. et al. (2018) 'Preparation and investigation of novel gastro-floating tablets with 3D extrusion-based printing', *International Journal of Pharmaceutics*, 535(1–2), pp. 325–332.
- Li, S., Cui, Y. and Li, J. (2021) 'Thiol-terminated hyperbranched polymer for DLP 3D printing: Performance evaluation of a low shrinkage photosensitive resin', *Journal of Applied Polymer Science*, 138(22), pp. 1–10.
- Ligon, S. C. et al. (2017) 'Polymers for 3D Printing and Customized Additive Manufacturing', *Chemical Reviews*, 117(15), pp. 10212–10290.
- Lin-Vien, D. et al. (1991) *The Handbook of Infrared and Raman Characteristic Frequencies of Organic Molecules*.
- Madžarevi, M. (2021) 'Understanding the Effect of Energy Density and Formulation Factors on the Printability and Characteristics of SLS Irbesartan Tablets — Application of the Decision Tree Model', *Pharmaceutics*, 13, p. 1969.
- Madžarević, M. and Ibrić, S. (2021) 'Evaluation of exposure time and visible light irradiation in LCD 3D printing of ibuprofen extended release tablets', *European Journal of Pharmaceutical Sciences*, 158, p. 105688.
- Malone, E. and Lipson, H. (2007) 'Fab@Home: The personal desktop fabricator kit', *Rapid Prototyping Journal*, 13(4), pp. 245–255. doi: 10.1108/13552540710776197.

- Martin, R. (2003) GRAS Notice 000141: Polyvinyl alcohol. Available at: <https://www.fda.gov/downloads/Food/IngredientsPackagingLabeling/GRAS/NoticeInventory/ucm267720.pdf>.
- Martinez, P. R. et al. (2017) 'Fabrication of drug-loaded hydrogels with stereolithographic 3D printing', *International Journal of Pharmaceutics*, 532(1), pp. 313–317.
- Martinez, P. R. et al. (2018) 'Influence of Geometry on the Drug Release Profiles of Stereolithographic (SLA) 3D-Printed Tablets', *AAPS PharmSciTech*, 19(8), pp. 3355–3361.
- McDevitt, J. T., Gurst, A. H. and Chen, Y. (1998) 'Accuracy of tablet splitting.', *Pharmacotherapy*, 18(1), pp. 193–7.
- Meereis, C. T. W. et al. (2014) 'BAPO as an alternative photoinitiator for the radical polymerization of dental resins', *Dental Materials*, 30(9), pp. 945–953.
- Melocchi, A. et al. (2016) 'Hot-melt extruded filaments based on pharmaceutical grade polymers for 3D printing by fused deposition modeling', *International Journal of Pharmaceutics*, 509(1–2), pp. 255–263.
- Merck (2021) Poly(ethylene glycol) - Safety Data Sheet.
- Mohammed, A. R. and Russell, C. A. (2012) 'Drug Development and Delivery', in *Pharmaceutics*. Oxford University Press.
- Moldovan, M. et al. (2019) 'Evaluation of the degree of conversion, residual monomers and mechanical properties of some light-cured dental resin composites', *Materials*, 12(13), pp. 1–14.
- Nasereddin, J. M. et al. (2018) 'Development of a Simple Mechanical Screening Method for Predicting the Feedability of a Pharmaceutical FDM 3D Printing Filament', *Pharmaceutical Research*, 35(8), p. 151.
- Nguyenpho, A. et al. (2015) 'Evaluation of In-Use Stability of Anticoagulant Drug Products: Warfarin Sodium', *Journal of Pharmaceutical Sciences*, 104(12), pp. 4232–4240.
- NHS (2020) Warfarin: a blood-thinning medicine to treat and prevent blood clots - NHS. Available at: <https://www.nhs.uk/medicines/warfarin/> (Accessed: 20 December 2021).
- Nilawar, S., Wankhade, V. and Badnag, D. (2013) 'An emerging trend on bilayer tablets', *International Journal of Pharmacy and Pharmaceutical Science Research*, 3(1), pp. 15–21.
- Nukala, P. K., Palekar, S., Patki, M., et al. (2019) 'Abuse Deterrent Immediate Release Egg-Shaped Tablet ( Egglets ) Using 3D Printing Technology : Quality by Design to Optimize Drug Release and Extraction', *AAPS PharmSciTech*, 20(2), pp. 1-12.
- Nukala, P. K., Palekar, S., Solanki, N., et al. (2019) 'Investigating the application of fused deposition modeling 3D printing pattern in preparation of patient-tailored dosage forms', *Journal of 3D printing in medicine*, 3(1), pp. 23-37.
- Nutan, M. T. H. and Reddy, I. K. (2010) *General Principles of Suspensions, Pharmaceutical Suspensions: From Formulation Development to Manufacturing*, Springer, New York, NY, USA.
- Öblom, H. et al. (2019) '3D-Printed Isoniazid Tablets for the Treatment and Prevention of Tuberculosis — Personalized Dosing and Drug Release', *AAPS PharmSciTech*, 2, pp. 1–13.
- Oesterreicher, A. et al. (2016) 'Tough and degradable photopolymers derived from alkyne monomers for 3D printing of biomedical materials', *Polymer Chemistry*, 7(32), pp. 5169–5180.

- Ohmori, S. et al. (2004) 'Development and evaluation of the tablets coated with the novel formulation termed thin-layer sugarless coated tablets', *International Journal of Pharmaceutics*, 278(2), pp. 459–469.
- Okwuosa, T. C. et al. (2018) 'On demand manufacturing of patient-specific liquid capsules via co-ordinated 3D printing and liquid dispensing', *European Journal of Pharmaceutical Sciences*, 118, pp. 134-143.
- Okwuosa, T. C. et al. (2021) 'Can filaments be stored as a shelf-item for on-demand manufacturing of oral 3D printed tablets? An initial stability assessment', *International Journal of Pharmaceutics*, 600, p. 120442.
- Osei-Yeboah, F. and Sun, C. C. (2015) 'Validation and applications of an expedited tablet friability method', *International Journal of Pharmaceutics*, 484(1–2), pp. 146–155.
- Oskui, S. M. et al. (2016) 'Assessing and Reducing the Toxicity of 3D-Printed Parts', *Environmental Science and Technology Letters*, 3(1), pp. 1–6.
- Ozturk, S. S. et al. (1988) 'Kinetics of Release from Enteric-Coated Tablets', *Pharmaceutical Research: An Official Journal of the American Association of Pharmaceutical Scientists*, pp. 550–565.
- Paarakh, M. P. et al. (2018) 'Release Kinetics – Concepts And Applications', *International Journal of Pharmacy Research & Technology*, 8, pp. 12–20.
- Parfenyuk, E. V. and Dolinina, E. S. (2017) 'Development of Novel Warfarin-Silica Composite for Controlled Drug Release', *Pharmaceutical Research*, 34(4), pp. 825–835.
- Patel, N. K., Kennon, L. L. O. Y. D., & Levinson, R. S. (1986). *Pharmaceutical suspensions. The Theory and Practice of Industrial Pharmacy*, 3, 479-501.
- Peek, B. T., Al-Achi, A. and J. Coombs, S. (2002) 'Accuracy of Tablet Splitting by Elderly Patients', *Journal of the American Medical Association*, 288(4), pp. 451-452.
- Peppas, N. A. (1984) 'Release Of Bioactive Agents From Swellable Polymers: Theory And Experiments'. In: Anderson J.M., Kim S.W. (eds) *Recent Advances in Drug Delivery Systems*. Springer, Boston, MA, USA.
- Pereira, B. C. et al. (2019) 'Temporary Plasticiser: A novel solution to fabricate 3D printed patient-centred cardiovascular "Polypill" architectures', *European Journal of Pharmaceutics and Biopharmaceutics*, 135, pp. 94–103.
- Phenomenex (2010) 'HPLC Column Protection Guide Version 0610', pp. 18–19. Available at: <https://phenomenex.blob.core.windows.net/documents/fa038833-ce35-4234-9df2-8792da3a2f41.pdf?returnURL=/Search>.
- Podczeczek, F. and Jones, B. E. (2007) *Pharmaceutical Capsules*. Pharmaceutical Press. London, UK.
- Prescott, J. and Barnum, R. (2000) 'On powder flowability', *Pharmaceutical technology*, 24, pp. 60–84.
- Print Parameter Optimization Guide | Support - Allevi (2020). Available at: <https://www.allevi3d.com/print-parameter-optimization/> (Accessed: 22 September 2021).
- Pritchard, D. E. et al. (2017) 'Strategies for integrating personalized medicine into healthcare practice', *Personalized Medicine. Future Medicine Ltd London, UK*, 14(2), pp. 141–152.
- Qian, C. et al. (2021) 'The effect of light scattering in stereolithography ceramic manufacturing', *Journal of the European Ceramic Society*, 41(14), pp. 7141–7154.

- Rautamo, M. et al. (2020) 'Benefits and Prerequisites Associated with the Adoption of Oral 3D-Printed Medicines for Pediatric Patients: A Focus Group Study among Healthcare Professionals', *Pharmaceutics*, 12(3), p. 229.
- Real, J. P. et al. (2020) 'Design of novel oral ricobendazole formulation applying melting solidification printing process (MESO-PP): An innovative solvent-free alternative method for 3D printing using a simplified concept and low temperature', *International Journal of Pharmaceutics*, 587, p. 119653.
- Reisfield, G. M. and Wilson, G. R. (2007) 'Rational use of sublingual opioids in palliative medicine', *Journal of Palliative Medicine*, 10(2), pp. 465–475.
- Robles Martinez, P. et al. (2019) '3D Printing of a Multi-Layered Polypill Containing Six Drugs Using a Novel Stereolithographic Method', *Pharmaceutics*, 11(6), p. 274.
- Rodig, O. R. (1963) 'Spectrometric Identification of Organic Compounds', *Journal of Medicinal Chemistry*, 6(6), pp. 826–827.
- Rogers, H. B. et al. (2021) 'Dental resins used in 3D printing technologies release ovotoxic leachates', *Chemosphere*, 270, p. 129003.
- Rossi, M., Nardinocchi, P. and Wallmersperger, T. (2019) 'Swelling and shrinking in prestressed polymer gels: An incremental stress-diffusion analysis', *Proceedings of the Royal Society A: Mathematical, Physical and Engineering Sciences*, 475(2230).
- Rosted, E., Schultz, M. and Sanders, S. (2016) 'Frailty and polypharmacy in elderly patients are associated with a high readmission risk', *Danish Medical Journal*, 63(9), pp. 1–6.
- Rowe, C. . et al. (2000) 'Multimechanism oral dosage forms fabricated by three dimensional printing™', *Journal of Controlled Release*, 66(1), pp. 11–17.
- Rycerz, K. et al. (2019) 'Embedded 3D printing of novel bespoke soft dosage form concept for pediatrics', *Pharmaceutics*, 11(12), pp. 1–15.
- Rygnestad, T., Zahlsen, K. and Samdal, F. A. (2000) 'Absorption of effervescent paracetamol tablets relative to ordinary paracetamol tablets in healthy volunteers', *European Journal of Clinical Pharmacology*, 56(2), pp. 141–143.
- Sadia, M. et al. (2016) 'Adaptation of pharmaceutical excipients to FDM 3D printing for the fabrication of patient-tailored immediate release tablets', *International Journal of Pharmaceutics*, 513(1–2), pp. 659–668.
- Sadia, M. et al. (2018) 'Channelled tablets: An innovative approach to accelerating drug release from 3D printed tablets', *Journal of Controlled Release*, 269, pp. 355–363.
- Sagdeev, D. I., Fomina, M. G. and Abdulagatov, I. M. (2017) 'Density and viscosity of propylene glycol at high temperatures and high pressures', *Fluid Phase Equilibria.*, 450, pp. 99–111.
- Sandle, G. I. (1998). Salt and water absorption in the human colon: a modern appraisal. *Gut*, 43(2), 294-299.
- Sastry, S., Nyshadham, J. and Fix, J. (2000) 'Recent technological advances in oral drug delivery - a review', *Pharmaceutical science & technology today*, 3(4), pp. 138–145.
- Schubert, M. L. (2016). Gastric acid secretion. *Current opinion in gastroenterology*, 32(6), 452-460.
- Scoutaris, N., Ross, S. A. and Douroumis, D. (2018) '3D Printed "Starmix" Drug Loaded Dosage Forms for Paediatric Applications', *Pharmaceutical Research*, 35(2), pp. 1–11.
- Seedher, N. and Bhatia, S. (2003) 'Solubility enhancement of cox-2 inhibitors using various solvent systems', *AAPS PharmSciTech*, 4(3), pp. 1–9.

- Seoane-Viaño, I. et al. (2021) 'Semi-solid extrusion 3D printing in drug delivery and biomedicine: Personalised solutions for healthcare challenges', *Journal of Controlled Release*, 332, pp. 367–389.
- Shariff, Z. et al. (2020) 'Patient-centric medicine design: key characteristics of oral solid dosage forms that improve adherence and acceptance in older people', *Pharmaceutics*, 12(10), pp. 1–15.
- Shariff, Z. B. et al. (2020) 'Does the Formulation of Oral Solid Dosage Forms Affect Acceptance and Adherence in Older Patients? A Mixed Methods Systematic Review', *Journal of the American Medical Directors Association*, 21(8), pp. 1015-1023.
- Shi, K. et al. (2021) 'Role of release modifiers to modulate drug release from fused deposition modelling (FDM) 3D printed tablets', *International Journal of Pharmaceutics*, 597, p. 120315.
- Shin, W. S. et al. (1993) 'Determination of the degree of cure of dental resins using Raman and FT-Raman spectroscopy', *Dental Materials*, 9(5), pp. 317–324.
- Siddiqui, A. et al. (2015) 'Development and validation of X-ray diffraction method for quantitative determination of crystallinity in warfarin sodium products', *International Journal of Pharmaceutics*, 493(1–2), pp. 1–6.
- Siepmann, F. et al. (2010) 'Modeling drug release from PVAc/PVP matrix tablets', *Journal of Controlled Release*, 141(2), pp. 216–222.
- SIGMA-ALDRICH (2015) 'TEAOH SDS', pp. 1–4.
- SIGMA-ALDRICH (2018a) '2-Hydroxy-2-methylpropiophenone SDS', (1907), pp. 1–7.
- SIGMA-ALDRICH (2018b) '2-Hydroxy-4'-(2-hydroxyethoxy)-2-methylpropiophenone SDS', (1907), pp. 1–5.
- SIGMA-ALDRICH (2018d) 'Riboflavin SDS', (1907), pp. 1–7.
- SIGMA-ALDRICH (2018e) 'TPO SDS', (1907), pp. 1–8.
- SIGMA-ALDRICH (2020) HPLC Analysis of Warfarin TM Anticoagulant on Ascentis® C18. Available at: <https://www.sigmaaldrich.com/GB/en/technical-documents/protocol/analytical-chemistry/small-molecule-hplc/hplc-analysis-of-warfarin-anticoagulant> (Accessed: 20 September 2021).
- Siyawamwaya, M. et al. (2018) '3D printed, controlled release, tritherapeutic tablet matrix for advanced anti-HIV-1 drug delivery', *European Journal of Pharmaceutics and Biopharmaceutics*, 138, pp. 99-110.
- Sjöholm, E. and Sandler, N. (2019) 'Additive manufacturing of personalized orodispersible warfarin films', *International Journal of Pharmaceutics*, 564, pp. 117–123.
- Skowyra, J., Pietrzak, K. and Alhnan, M. A. (2015) 'Fabrication of extended-release patient-tailored prednisolone tablets via fused deposition modelling (FDM) 3D printing', *European Journal of Pharmaceutical Sciences*, 68, pp. 11–17.
- Sluggett, G. W. et al. (1995) '(2,4,6-Trimethylbenzoyl)diphenylphosphine Oxide Photochemistry. A Direct Time-Resolved Spectroscopic Study of Both Radical Fragments', *Journal of the American Chemical Society*, 117(18), pp. 5148–5153.
- Solanki, N. G. et al. (2018) 'Formulation of 3D Printed Tablet for Rapid Drug Release by Fused Deposition Modeling: Screening Polymers for Drug Release, Drug-Polymer Miscibility and Printability', *Journal of Pharmaceutical Sciences*, 107(1), pp. 390–401.
- Stranzinger, S. et al. (2021) 'Review of sensing technologies for measuring powder density variations during pharmaceutical solid dosage form manufacturing', *TrAC - Trends in Analytical Chemistry*, 135, p. 116147.

- Tagami, T. et al. (2017) '3D Printing Factors Important for the Fabrication of Polyvinylalcohol Filament-Based Tablets', *Biological & Pharmaceutical Bulletin*, 40(3), pp. 357–364.
- Tagami, T., Nagata, N., et al. (2018) 'Defined drug release from 3D-printed composite tablets consisting of drug-loaded polyvinylalcohol and a water-soluble or water-insoluble polymer filler', *International Journal of Pharmaceutics*, 543(1–2), pp. 361–367.
- Tagami, T., Ando, M., et al. (2018) 'Fabrication of Naftopidil-Loaded Tablets Using a Semisolid Extrusion-Type 3D Printer and the Characteristics of the Printed Hydrogel and Resulting Tablets', *Journal of Pharmaceutical Sciences*, pp. 1–7.
- Tagami, T. et al. (2021) '3D printing of gummy drug formulations composed of gelatin and an HPMC-based hydrogel for pediatric use', *International Journal of Pharmaceutics*. Elsevier B.V., 594(September 2020), p. 120118.
- Tang, A. et al. (2019) 'Nanocellulose PEGDA aerogel scaffolds with tunable modulus prepared by stereolithography for three-dimensional cell culture', *Journal of Biomaterials Science, Polymer Edition*, 30(10), pp. 797–814.
- Teng, J. et al. (2002) 'Lack of medication dose uniformity in commonly split tablets', *Journal of the American Pharmaceutical Association*, 42(2), pp. 195–199.
- Thakkar, R. et al. (2021) 'Impact of laser speed and drug particle size on selective laser sintering 3d printing of amorphous solid dispersions', *Pharmaceutics*, 13(8), pp. 1–19.
- Tian, P. et al. (2018) 'Oral disintegrating patient-tailored tablets of warfarin sodium produced by 3D printing', *Drug Development and Industrial Pharmacy*. Taylor & Francis, 44(12), pp. 1918–1923..
- Tomeckova, V. and Halloran, J. W. (2010) 'Cure depth for photopolymerization of ceramic suspensions', *Journal of the European Ceramic Society*, 30(15), pp. 3023–3033.
- Trenfield, S. J. et al. (2018) '3D Printing Pharmaceuticals: Drug Development to Frontline Care', *Trends in Pharmacological Sciences*, 39(5), pp. 440–451.
- Trenfield, S. J. et al. (2018a) '3D printed drug products : Non-destructive dose verification using a rapid point-and-shoot approach', *International Journal of Pharmaceutics*, 549(1-2), pp. 283–292.
- U.S. Pharmacopoeial Convention (2011) *Reagents, indicators, solutions*.
- Uguzdogan, E. (2013) 'Synthesis and characterization of hydrophilic and spherical poly(glycerol dimethacrylate-co-glycerol-1,3-diglycerolate diacrylate) microbeads', *Designed Monomers and Polymers*, 16(3), pp. 250–262.
- United States Pharmacopoeial Convention (2011) 'U.S. Pharmacopoeial guidelines Dissolution', <711> *Dissolution*, 1, pp. 1–8.
- United States Pharmacopoeial Convention (2012) '<1216> Tablet friability', *United States Pharmacopoeia* 35, pp. 868–870.
- Venâncio, N. et al. (2021) 'Influence of the Infill Geometry of 3D-Printed Tablets on Drug Dissolution', *Medical Sciences Forum*, 5(1), p. 15.
- Verde, A. et al. (2021) 'SERS Sensing of Bacterial Endotoxin on Gold Nanoparticles', *Frontiers in Immunology*, 12, pp. 1–12.
- Verrue, C. et al. (2011) 'Tablet-splitting: A common yet not so innocent practice', *Journal of Advanced Nursing*, 67(1), pp. 26–32.
- Vithani, K. et al. (2019) 'An Overview of 3D Printing Technologies for Soft Materials and Potential Opportunities for Lipid-based Drug Delivery Systems', *Pharmaceutical Research*, 36(1), pp. 1–20.

- Vo, A. Q. et al. (2020) 'Hot melt extrusion paired fused deposition modeling 3D printing to develop hydroxypropyl cellulose based floating tablets of cinnarizine', *Carbohydrate Polymers*, 246, p. 116519.
- Voet, V. S. D. et al. (2018) 'Biobased Acrylate Photocurable Resin Formulation for Stereolithography 3D Printing', *ACS Omega*, 3(2), pp. 1403–1408.
- Voet, V. S. D., Guit, J. and Loos, K. (2021) 'Sustainable Photopolymers in 3D Printing: A Review on Biobased, Biodegradable, and Recyclable Alternatives', *Macromolecular Rapid Communications*, 42(3), pp. 1–11.
- Vuddanda, P. R. et al. (2018) 'Personalisation of warfarin therapy using thermal ink-jet printing', *European Journal of Pharmaceutical Sciences*, 117, pp. 80–87.
- Vuksanović, J. M., Kijevčanin, M. L. and Radović, I. R. (2018) 'Poly(ethylene glycol) diacrylate as a novel chaotropic compound for design of aqueous biphasic systems', *Journal of Molecular Liquids*, 261, pp. 250–264.
- Wadelius, M. et al. (2005) 'Common VKORC1 and GGCX polymorphisms associated with warfarin dose', *Pharmacogenomics Journal*, 5(4), pp. 262–270.
- Wang, J. et al. (2016) 'Stereolithographic (SLA) 3D printing of oral modified-release dosage forms', *International Journal of Pharmaceutics*, 503(1–2), pp. 207–212.
- Wang, Z. et al. (2021) 'Taste Masking Study Based on an Electronic Tongue: the Formulation Design of 3D Printed Levetiracetam Instant-Dissolving Tablets', *Pharmaceutical Research*, 38(5), pp. 831–842.
- Warr, C. et al. (2020) 'Biocompatible PEGDA Resin for 3D Printing', *ACS Applied Bio Materials*, 3(4), pp. 2239–2244.
- Williams, C. G. et al. (2005) 'Variable cytocompatibility of six cell lines with photoinitiators used for polymerizing hydrogels and cell encapsulation', *Biomaterials*, 26(11), pp. 1211–1218.
- Wu, B. M. et al. (1996) 'Solid free-form fabrication of drug delivery devices', *Journal of Controlled Release*, 40(1–2), pp. 77–87.
- Xu, X. et al. (2020) 'Stereolithography (SLA) 3D printing of an antihypertensive polyprintlet: Case study of an unexpected photopolymer-drug reaction', *Additive Manufacturing*, 33, p. 101071.
- Xu, X. et al. (2021) 'Vat photopolymerization 3D printing for advanced drug delivery and medical device applications', *Journal of Controlled Release*, 329, pp. 743–757.
- Yang, Y. et al. (2018) '3D printed tablets with internal scaffold structure using ethyl cellulose to achieve sustained ibuprofen release', *European Journal of Pharmaceutical Sciences*, 115, pp. 11–18.
- Yang, Y. et al. (2020) 'A tunable extruded 3D printing platform using thermo-sensitive pastes', *International Journal of Pharmaceutics*, 583, p. 119360.
- Yao, M. et al. (2021) 'Significantly improve the photoinitiation ability of hydroxyalkyl-derived polymerizable  $\alpha$ -hydroxyalkylacetophenone photoinitiators by blocking hyperconjugation', *Journal of Photochemistry and Photobiology A: Chemistry*.
- Yoder, S. et al. (2014) 'Physical Appearance Preferences for Oral Solid Dosage Formulations', *AAPS Poster*, 2018, pp. 1–4.
- Yu, D. G. et al. (2007) 'Tablets With Material Gradients Fabricated by Three-Dimensional Printing', *Journal of Pharmaceutical Sciences*, 96(9), pp. 2446–2456.

- Yu, D. G., Branford-White, C., et al. (2009) 'Novel drug delivery devices for providing linear release profiles fabricated by 3DP', *International Journal of Pharmaceutics*, 370(1–2), pp. 160–166.
- Yu, D. G., Shen, X.-X., et al. (2009) 'Novel oral fast-disintegrating drug delivery devices with predefined inner structure fabricated by Three-Dimensional Printing', *Journal of Pharmacy and Pharmacology*, 61(3), pp. 323–329.
- Yun, J. S. et al. (2016) 'Development of ceramic-reinforced photopolymers for SLA 3D printing technology', *Applied Physics A: Materials Science and Processing*. Springer Berlin Heidelberg, 122(6), pp. 1–6.
- Zakeri, S., Vippola, M. and Levänen, E. (2020) 'A comprehensive review of the photopolymerization of ceramic resins used in stereolithography', *Additive Manufacturing*, 35, p. 101177.
- Zhang, J. et al. (2017) 'Coupling 3D printing with hot-melt extrusion to produce controlled-release tablets', *International Journal of Pharmaceutics*, 519(1–2), pp. 186–197.
- Zheng, Z. et al. (2020) 'Preparation and application of subdivided tablets using 3D printing for precise hospital dispensing', *European Journal of Pharmaceutical Sciences*, 149, p. 105293.
- Zingone, G. and Rubessa, F. (2005) 'Preformulation study of the inclusion complex warfarin- $\beta$ -cyclodextrin', *International Journal of Pharmaceutics*, 291(1-2), pp. 3–10.